



RESEARCH & DEVELOPMENT

Training and Case Studies for UAV-based LIDAR and Imaging Systems

**Zhen Zhu, PhD
George Wang, PhD
Shanyue Guan, PhD
College of Engineering and Technology
East Carolina University**

NCDOT Project 2020-35

FHWA/NC/20YY-NN

July 2022

| | | | |
|---|--|--|---------------------------------|
| 1. Report No. <i>Fill in number assigned by NCDOT, near end of project (e.g. FHWA/NC/2002-006)</i> | 2. Government Accession No. | 3. Recipient's Catalog No. | |
| 4. Title and Subtitle Training and Case Studies for UAV-based LIDAR and Imaging Systems | | 5. Report Date July 31, 2022 | 6. Performing Organization Code |
| | | 8. Performing Organization Report No. | |
| 7. Author(s) Zhen Zhu, George Wang, Shanyue Guan | | 10. Work Unit No. (TRAIS) | |
| 9. Performing Organization Name and Address East Carolina University, 1000 E. 5th St. Greenville, NC 27858-4353 | | 11. Contract or Grant No. | |
| | | 13. Type of Report and Period Covered Final Report 08/01/2019-07/31/2022 | |
| 12. Sponsoring Agency Name and Address North Carolina Department of Transportation Research and Development Unit 1020 Birch Ridge Drive Raleigh, North Carolina 27610 | | 14. Sponsoring Agency Code 2020-35 | |
| | | Supplementary Notes: | |
| 16. Abstract When equipped with appropriate sensors, small UAS has been proven extremely cost-effective and efficient in surveying large areas, and creating 3D point cloud, models and maps. In North Carolina, the construction industry and government agencies have started to use small UAVs in construction-related activities and disaster management. For the state agencies to better manage and oversee these activities, it is imperative for the state engineers in various units and offices to get more familiar with the UAS-based sensing technologies. Case studies and a workshop have been developed in this project for applications of small UAS and the affiliated sensors. The technology transferred to NCDOT will enable significant savings in managing current and future projects, and will further help NCDOT revise and update regulations and guidelines for UAV applications in the State of North Carolina. Through this project, North Carolina will be able to take a leading position in regulating and managing construction and infrastructure-related applications of small UAS in the country. | | | |
| 17. Key Words Unmanned aircraft systems; LIDAR; camera | | 18. Distribution Statement | |
| 19. Security Classif. (of this report) Unclassified | 20. Security Classif. (of this page) Unclassified | 21. No. of Pages 286 | 22. Price |

DISCLAIMER

The contents of this report reflect the views of the author(s) and not necessarily the views of the University. The author(s) are responsible for the facts and the accuracy of the data presented herein. The contents do not necessarily reflect the official views or policies of either the North Carolina Department of Transportation or the Federal Highway Administration at the time of publication. This report does not constitute a standard, specification, or regulation.

Table of Contents

| | |
|---|----|
| Ch 1 Introduction | 6 |
| Ch 2 Literature review..... | 6 |
| 2.1 Introduction to UAS-based sensing systems | 6 |
| 2.2 Applications on Construction Management and Disaster Management..... | 9 |
| 2.3 Safety Considerations..... | 10 |
| Ch 3 UAS-based LIDAR and Camera Systems..... | 12 |
| 3.1 A Downward-Looking UAS-based LIDAR System..... | 12 |
| 3.1.1 Hardware components..... | 13 |
| 3.1.2 System Synchronization..... | 14 |
| 3.1.3 Navigation Measurements | 15 |
| 3.1.4 Pre-Processed Point Clouds | 15 |
| 3.1.5 Error Model..... | 16 |
| 3.1.6 Example of Error Prediction Model..... | 18 |
| 3.1.7 Error Validation..... | 20 |
| 3.2 A Side-View UAS-based LIDAR System..... | 27 |
| 3.2.1 Hardware components..... | 27 |
| 3.2.2 Error Model..... | 29 |
| 3.3 Structure from Motion System with known Camera Pose..... | 30 |
| Ch 4 Case Studies for Construction Management..... | 32 |
| 4.1 Flight, Data Collection and Processing | 32 |
| 4.2 Buildings | 34 |
| 4.3 Pit and Piles in Havelock, NC..... | 39 |
| 4.4 Volumetric Measurements of Piles at Pitt County Maintenance Yard..... | 42 |
| 4.4.1 Dataset 1 (Oct 2020)..... | 42 |
| 4.4.2 Dataset 2 (Feb 2021)..... | 44 |
| 4.4.3 Dataset 3 (March 2022)..... | 50 |
| 4.5 Summary..... | 53 |
| Ch 5 Case Studies for Disaster Management..... | 54 |
| 5.1 Seashores and Water Surface..... | 54 |
| 5.2 Road Surface..... | 55 |
| 5.3 Riverbed..... | 57 |
| 5.4 Bridge..... | 59 |
| 5.5 Summary..... | 64 |
| Ch 6 Emerging Technologies | 65 |
| 6.1 SFM with Precise Camera Position | 65 |
| 6.1.1 Open Interface System | 65 |

| | |
|---|----|
| 6.1.2 Performance..... | 68 |
| 6.2 Comparison of SFM and UAS-LIDAR Point Clouds | 70 |
| 6.3 Integration of SFM and UAS-LIDAR Point Clouds | 72 |
| Ch 7 Recommendations to NCDOT | 73 |
| 7.1 Comparison Among Different Technologies..... | 73 |
| 7.2 UAS-LIDAR Recommendations..... | 75 |
| 7.2.1 Hardware..... | 75 |
| 7.2.2 Flight Control..... | 77 |
| 7.2.3 Processing and Dissemination..... | 81 |
| 7.3 Measuring Pile Volume..... | 81 |
| References | 83 |
| Appendix..... | 87 |

Ch 1 Introduction

Small Unmanned Aerial Vehicles (UAVs) or Unmanned aircraft systems (UASs) are often used in mapping, modeling, aerial surveying, jobsite surveillance and real-time inspections. It has been proven that small UAS can be extremely cost-effective in surveying large areas and creating 3D measurements. Rapid advances in imaging, sensing, avionics, battery and navigation technologies help make small UASs more affordable, capable, reliable and user-friendly.

There are two types of UAS-based sensing technologies commonly used in construction and other industries, 1) photogrammetric (camera-based) Structure From Motion (SFM) and 2) Light Detection and Ranging (LIDAR). While both can be used to create the 3D map of a jobsite, they prefer different flight control and data processing strategies. With an airborne HD camera, multiple overlapping images will be captured from a loitering UAS, which are then used to reconstruct the 3D model of a target area in the SFM software. The performance of SFM has been well studied in literature.

By contrast, UAS-based LIDAR has received less attention. LIDAR does not rely on images. Instead, it can directly measure a dense 3D point cloud from an overhead flight. A UAS LIDAR is typically more expensive than a camera, but the flight plan and data processing are more straightforward. LIDAR point cloud will be compared against that of SFM via quantitative analysis and case studies in this work. Based on that, the potential applications in construction management and disaster management of both technologies will be discussed in this report. A workshop is offered to NCDOT personnel to demonstrate the findings of this study.

Ch 2 Literature review

UAS-based photogrammetry and UAS-based LIDAR system are covered in this review. This chapter includes a summary of the original literature review, which has been attached to this document. The ECU team has also included part of the literature review in [Guan22a] and [Guan22b], which have also been attached.

2.1 Introduction to UAS-based sensing systems

UAS-based photogrammetry is based on imagery collected with small onboard cameras. It typically requires ground control points (GCPs) with surveyed locations, and can benefit from recorded location and orientation of the camera. A 3D point cloud of the target area can be estimated via indirect or direct geo-referencing.

Indirect georeferencing refers to the methods that world-frame coordinates to 3D measurements collected in a relative reference frame. One of the most popularly used UAS-based georeferencing solution is SFM. It has been proven to be superior to conventional handheld surveying methods in certain environments, such as in projects with low vegetation, GPS availability and substantial sunlight [DJI19]. Multiple 2D images over the same area are combined and the point features are matched across them. These images are expected to have great overlap areas (80%). The 3D locations of these points are then estimated in the camera frame, which are then used to form a 3D model or point cloud. However, the camera pose (position and orientation) isn't always precisely known in a

world frame (GPS frame, for example) when a small commercial UAS is used. Therefore, the 3D model created with structure from motion with a small UAS is typically dimensionless, and cannot be directly georeferenced. It requires additional GCPs to relate back to the world frame. The absolute accuracy of this model depends on both image processing and the GCPs. It is also susceptible to camera calibration and settings, surface texture, flight pattern and vibration, light condition, etc.

Users of SFM software are typically advised to place GCPs throughout the target site, on the edge of the worksite and in the center [Pix4D17]. The locations of GCPs can be surveyed using GNSS-based Real Time Kinematic (RTK), Post-Processed Kinematic (PPK) or Precise Point Positioning (PPP) solutions [GCPS19], Total Station Survey or Terrestrial Laser Scanner (TLS) [Shaw19]. PPP is post processed GNSS positioning that do not need a local reference station like RTK and PPK do, and could be less accurate. The best performance of GCP is likely from a PPK survey, which typically has positioning error around 1 centimeter, 1 sigma. [Sanz-Ablanedo18] provided a systematic overview of accuracy in point cloud involving GCPs. With a sufficient number of GCPs (more than 2 GCPs per 100 images as specified in this work), the error of point cloud could approach double of the GCP error. If fewer GCPs were used, this paper reported that the point cloud error would be as high as 4-8 times the GCP error, which was still in the centimeter range. Vertical errors were approximately 2.5 times the error of horizontal components.

As an emerging technology, small UAS can become capable of recording the camera location and orientation for each of the images taken during a flight. In that case, camera-based direct georeferencing is possible. It can be achieved by raytracing from a single image to a known surface (such as DEM or other *a priori* terrain models), or triangulation from multiple overlapped images, or a combination of both. Since no ground control is necessary, the accuracy of 3D modeling is primarily determined the accuracy of camera timing, orientation and location. However, a small UAS that is not capable of carrying high-quality navigation sensor cannot be used for direct geo-referencing. Therefore, direct geo-referencing has not been commonly used in small UAS yet.

If only inaccurate position and orientation are available from low-quality navigation sensors, they can also be optimized in the SFM software. For UAS that have precise location, through RTK, PPK or PPP, without orientation, SFM can still be used to estimate the 3D point cloud. It can be done with few or no GCPs.

Modern SFM software would take known camera calibration, position or orientation as inputs if they are available. Commercial software is available from Agisoft [Agisoft19], Trimble [Trimble19], Pix4D [Pix4D19], and open-source software such as [Furukawa19] has also been used in scientific communities.

Alternatively, camera systems can be combined with, or replaced by a direct ranging sensor, such as a UAS-LIDAR system, on some larger-sized UASs. LIDARs are less sensitive to natural light condition and other constraints in the environment. They may provide measurements in operational conditions which prohibits camera operation (such as low light). Some researchers also suggested that LIDAR could be more reliable than photogrammetry over weakly textured surfaces (such as sand). An airborne LIDAR directly measures point cloud in the sensor frame. The point cloud will be transformed into the world frame by knowing precise location

and orientation of the LIDAR. Very much like camera direct georeferencing, airborne LIDAR point cloud accuracy is also sensitive to timing/synchronization, LIDAR orientation and location. Furthermore, airborne LIDAR sensors available today are still more expensive, more power-hungry and heavier than cameras in general.

An airborne or UAS-LIDAR system typically includes three types of sensors, a ranging sensor (2D scanning LIDAR, 3D scanning LIDAR or 3D imager); a positioning sensor (such as GPS or GNSS receiver) and an inertial sensor that measures acceleration, rotation, velocity and orientation. These three sensors are integrated in the data collection system and in the 3D modeling procedure. The GNSS and inertial sensors are typically tightly coupled together to provide precise and smooth pose of the LIDAR. It is a common practice that the positioning sensor is also responsible for accurate 3D positioning and synchronization of an onboard antenna (optional).

It is well known that a ground-based LIDAR system, such as a TLS, can provide a dense and accurate point cloud for construction measurements. The same however does not apply to UAS-based LIDAR, because the position and orientation of UAS constantly change during a flight. As a result, the point clouds captured by LIDAR cannot be geo-referenced as that of a stationary TLS. Instead, raw point cloud measurements from the airborne LIDAR must be integrated and synchronized with the UAS navigation measurements during pre-processing, which is typically a challenge and roadblock. The accuracy of geo-registration in airborne LIDAR point cloud has been studied for large, manned aircraft systems. It has been recognized that the errors in the navigation system, LIDAR installation, laser beam and ranging can all contribute to the geo-registration error [Schaer07]. The general error model can also apply to UAS-based system [Pilarska16]. A UAS typically flies at a lower altitude, and has a lower-grade navigation system than manned aircraft. The LIDAR equipped on a UAS can have lower power and shorter range as well. Therefore, the error in a UAS-LIDAR point cloud may manifest itself in a way that is slightly different from ALS. In practice, the observed error magnitude and pattern is related to the target application as well. For example, errors have been assessed for forestry [Wallace11], meadow steppe [Zhao22], mountainous area [Muller21], flood plain [Chen21] and different vegetation levels [Salach18].

In these recent publications, a consensus was formed that:

- a) LIDAR provides a more accurate point cloud when vegetation is present.
- b) LIDAR could be more reliable than photogrammetry over weakly textured surfaces.
- c) LIDAR provides coverage on where SFM or GCPs are not available.
- d) LIDAR does NOT seem to provide better accuracy than SFM.
- e) LIDAR data can be collected and processed faster than photogrammetry.

Efficiency is a feature of UAS-LIDAR that is often over-looked by the construction industry. SFM needs overlapped imagery from multiple perspective. Therefore, it will take longer to cover the same area with UAS photogrammetry than LIDAR. Data processing is also more straightforward with direct geo-referencing. With a worksite of limited size, the difference in data collection and processing time may be insignificant. However, it

would make a more significant difference for large areas, which is typical for disaster management applications. Furthermore, for these applications, time and efficiency may be of a greater concern than monitoring construction worksites.

2.2 Applications on Construction Management and Disaster Management

UAS-based imagery has been widely used in construction management. [de Melo17] discussed applications for safety inspection on construction sites. UAS-imagery could be used to identify the non-compliances with the safety requirements established. Structural damage assessment could be done with 2D or 3D imagery [Eschmann14] [Fernandaz15]. Construction progress monitoring could also benefit from using small UAS [Moeini17] [Hamledari18].

3D mapping with UAS photogrammetry is the main application to be covered in this review. A review of relevant technologies can be found in [Remondino11]. In general, UAS photogrammetry can reduce the cost and the risks in mapping and surveying tasks in harsh environments. Centimeter-level accuracy is achievable, and rotatory-wing UAS are better choices for small sites. [Siebert14] demonstrated the use of UAS imagery and SFM on modeling the surface and volume of earth work in a field-realistic environment. [Álvares18] compared the efficacy of 3D mapping in terms of the easiness of model development, data quality, usefulness and limitations on two typical building cases. [Khaloo18] demonstrated the use of UAS for augmenting bridge inspections, using the Placer River Trail Bridge in Alaska as an example.

LIDAR-based solutions are raising some interests within the construction industry as well [Knight19]. UAS-based LIDAR is a relatively new technology for construction management. As of the time of this report, users in this industry are more familiar with terrestrial laser scanners (TLS), mobile laser scanners (MLS) mounted on ground vehicles and airborne laser scanners (ALS) mounted on large manned aircraft.

Similar to the applications in construction industry, SFM and UAS photogrammetry have been used successfully for data collection in environmental applications and disaster management, especially in coastal settings. The use of UAS has been found to be a convenient, low-cost, and less environmentally invasive technique to capture coastal data. It was also found that the number and distribution of GCPs play an important role in reducing the errors in the point cloud. Most substantial errors have been associated with areas of vegetation.

Among the different types of natural disasters, floods are the most devastating, widespread, and frequent [Hashemi-Beni18]. This study investigated the quality of UAS-based DEM and evaluated the extent of a flood event in Princeville, North Carolina during Hurricane Matthew. Comparison against the US Geologic Survey (USGS) stream gauge station and LIDAR data showed that the SFM error is less than 30 centimeters. [Ruessink18] collected geomorphic change data of a foredune system between May 2013 and April 2016 at Dutch National Park Zuid-Kennemerland, Netherlands. The over-all accuracy of the SFM point cloud was between .04m and .05m. (Root mean square was between .015m-.025m in the xy direction and .03m for the z direction.) [Jaud19] showed

long-term monitoring of Porsmilin Beach using SFM. The accuracy was reported to be 3 centimeters in the vertical and horizontal directions, which was consistent with other work reported in literature. Similar accuracy were achieved in [Papakonstantinou16], which used UAS photogrammetry and SFM to map the Greece coastlines. It has been concluded that centimeter-level accuracy is achievable in UAS photogrammetry-based point cloud that is used to model environmental changes in coastal areas with a reputable SFM software.

UAS-LIDAR has found applications in disaster management as well. [Assenbaum18] discussed the use of UAS LIDAR on the French Mediterranean coast. It was a complex natural environment where geology, climate and the sea interact and continuously reshape the landscape. Coastal erosion and the availability of drinking water were two major coastal management issues that necessitate precise monitoring of the morphological changes to the shoreline. A comparison between the land survey and the LIDAR point cloud revealed an average bias of 4.0 centimeters and a standard deviation of 9.5 centimeters in the vertical direction. The expected performance was 2.5 to 5.0 centimeters on hard, well-defined surfaces like roads or concrete.

[Shaw19] directly compared UAS LIDAR with SFM in analyzing coastal changes pre- and post-storm events at Wamboro Sound, Safety Bay Australia. Either method was able to produce accurate point cloud. SFM accuracy as at centimeter level. However, adding LIDAR to SFM helped cover the gap in SFM point cloud where GCPs could not be surveyed with GNSS-RTK, Total Station or TLS. [Populus19] argued that the main reason for using LIDAR in the coastal zone is its capacity of rapidly covering large areas. UAS typically cover about 20 km² and over 50 km² per hour or more for hydrographic and topographic modes, respectively. It would be crucial for applications that only have a short time window.

2.3 Safety Considerations

Risks of small UAS could result from a number of technical reasons, including (but not limited to) power, communications, navigation and control. UAS operations may be autonomous, semi-autonomous or remote controlled [Wang16]. In a fully autonomous or semi-autonomous operation, the low-level control is governed by the on-board flight controller and navigator, which relies on GNSS (or an equivalent sensor) as afore mentioned. If the UAS follows a pre-loaded flight plan without the need of human intervention, it is considered fully autonomous. In a semi-autonomous operation, sometimes also referred to as a GNSS-assisted operation, the UAS follows the guidance of a remote controller, with commands transmitted via a communication channel. In a remote-controlled operation, the user directly performs low-level control functions, such as attitude or velocity control, without using on-board GNSS.

When a UAS is close to a building or other structure, it may lose communications with the operator. Quality of GNSS positioning in the vicinity of a construction site could also suffer from blockage and multipath. In an autonomous operation where GNSS has been corrupted, the on-board flight controller could command erroneous operations. A properly designed UAS will attempt to stop the operation, by landing or returning to the home location, upon the loss of communications or GNSS. Without the ability to “sense and avoid”, the UAS

could potentially cause damages during this process. An obvious way to prevent communication loss is for users to remain in line-of-sight when operating UAS, as often required in various regulations including FAA part 107 [FAA16]. Autonomous operations should be enabled only when GNSS (or equivalence) is available.

Small UAS with redundant navigation systems, payload capabilities, redundant rotors and battery capability in case of a rotary wing UAS provide additional safety protection. Furthermore, small UAS with GNSS-denied and indoor navigation capability, sense and avoid capability, are also available now.

A list of State and Federal UAS regulations can be found in the attached literature review.

Ch 3 UAS-based LIDAR and Camera Systems

This chapter presents the design of low-cost UAS-based LIDAR and SFM systems that have been used in case studies. After this project had started in 2019, similar commercial systems had become available on the market (such as systems made by DJI). As of the time of this report, the cost of these systems remains prohibitively high. Unlike the commercial systems, the LIDAR and Camera systems designed by the ECU team keep interfaces open between different components. Any intermediate data products, such as navigation data, imagery and raw point cloud, are available for post-processing and analysis. High-quality navigation, laser and camera sensors have been used in these systems. The total cost of building and operating these systems is substantially lower than the commercial options. A generic error model will be discussed for the UAS-LIDAR point cloud, which will be validated using an ECU LIDAR system. On the other hand, the SFM point cloud errors are highly dependent on the surface texture and image quality. Instead of an analytical error model, the performance reported in literature for different SFM applications will be used in the comparison against LIDAR in this report.

3.1 A Downward-Looking UAS-based LIDAR System

The first UAS-LIDAR system uses a commercial rotary-wing small UAS, DJI Matrice 600 Pro, equipped an auxiliary sensing system. The sensing system mainly consists of a video camera, an industrial image camera, a LIDAR sensor, a GNSS receiver, an Inertial Measurement Unit (IMU), and three embedded computers. The following components are included:

- A GoPro Hero 5 video camera
- An IDS uEye industrial RGB image camera
- A SICK LD-MRS LIDAR sensor
- A NovAtel SPAN GNSS receiver with an integrated IMU
- Three Raspberry Pi III embedded computers
- A rigid lightweight cage to mount all the components above

In addition, the GNSS receiver is paired with an onsite GNSS base station (NovAtel OEM 6 receiver) for post-processed navigation measurements. A close-up look of the major components of the sensing system is shown in Figure 1.

Using this system as an example, a generic error prediction model for UAS-LIDAR is developed. With this model, systematic and random error components have been estimated respectively. The model shows that the random error is the dominant component for a low-flying UAS-based LIDAR, and the error level is

tolerable for construction applications such as excavation and bulk pile measurements. The random errors in the vertical direction could be further reduced in post processing.

3.1.1 Hardware components

The cage attached to the bottom of the airframe is made of a rigid resin board supported by carbon fiber and 3D printed components. The system components are mounted on both sides of the board to conserve space and at the same time improve the rigidity of lever arms between the sensors. The total weight of the sensing system is approximately 3.6 kg and the maximum flight time of the UAS with this configuration is approximately 17 minutes.

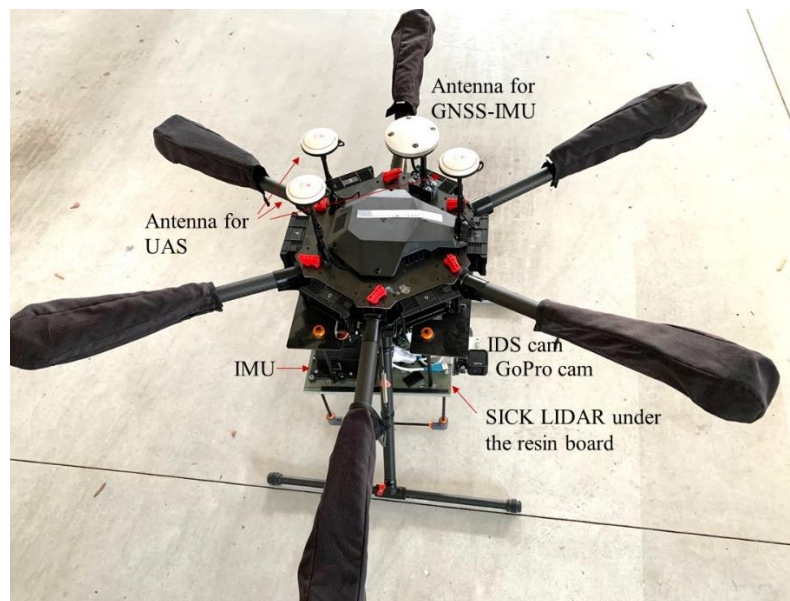


Figure 1 Major Components of the UAS Sensing System

Two lightweight cameras are mounted onboard, a GoPro video camera and an IDS industrial RGB image camera. The video camera captures continuous video frames of the flight that can be used for 2D imaging and 3D mapping via Structure from Motion (SfM), which operates independently from the other sensors. By contrast, the image camera is tightly integrated with navigation and LIDAR sensors. The image camera collects images with a global shutter triggered by the navigation system, which is also synchronized to the LIDAR. Consequently, the image camera is effectively synchronized to the LIDAR and provides 2D imagery of the point cloud observed by it. The imagery was only used to identify targets from the LIDAR point cloud and was therefore not incorporated into the point cloud in the results reported in this work.

The LIDAR is a SICK LD-MRS unit capable of scanning 4 layers simultaneously with a field of view of approximately 110° facing downwards at the ground. The aperture size is no greater than $\pm 0.4^\circ$ in one direction and $\pm 0.04^\circ$ in the other, corresponding to 0.23° and 0.023° in standard deviations, respectively. The LIDAR scans at 0.125° of angular resolution with a frequency of 12.5 Hz, and it takes approximately 10 ms to

complete one sweep of the field of view, collecting around 3,000 ground points. It is assumed that all points from a single scan will be collected simultaneously, which is timestamped by the navigation system through a synchronization mechanism, although the precise scanning time of each point could be retrieved if needed. Therefore, the potential discrepancy in timing is up to ± 5 ms for each point and is considered part of the error sources. SICK provides an estimation of nominal ranging accuracy for the LD-MRS unit, which includes a noise level of a single point at $\sigma_R \approx 0.1$ m (quantization step 0.04 m) and a systematic bias ≈ 0.3 m (estimated ahead of time and removed from the data). It is noted from field testing that the specified noise level is rather conservative compared with results from actual observations, which ranges between 0.04 m and 0.1 m.

The NovAtel SPAN GNSS-inertial integrated receiver is used as the primary navigation system for data collection over the native flight control system of Matrice 600 Pro, due to the superior performance in limiting potential systematic error [Guan19]. The GNSS receiver is paired with a GNSS base station to record raw data for accurate post-processing without relying on a live Real-Time Kinematic (RTK) solution, while the integrated IMU enables accurate orientation estimation. Nevertheless, any uncertainty in position and orientation from the GNSS-IMU will propagate to raw data of all the attached sensors, which becomes part of the systematic error. Figure 1 shows four GNSS antennas mounted on top of the airframe, of which three are used by the UAS for the redundancy and safety of flight control, and the fourth is part of the GNSS-IMU system.

3.1.2 System Synchronization

The time synchronization function is the core mechanism of sensor integration in the UAS-LIDAR system, as shown in Figure 2. Naturally, GNSS is synchronous to GPS time, which also enables additional timing services via input and output triggers to the receiver. The GNSS receiver in the UAS-LIDAR system triggers the shutter of the image camera and receives a timing trigger from the LIDAR. Raw data with corresponding timing information recorded by the image camera, LIDAR, and GNSS-IMU are streamed into three onboard Raspberry Pi embedded computers, which also control and initialize all the sensors. Due to the time-sensitivity of data collection, each computer records the raw data from only one sensor and stores it into a separate SD card for post-processing, avoiding onboard processing to allow sufficient throughput capability.

The configuration of the sensing system can be easily adjusted for other applications. As illustrated in Figure 2, the various sensors use a parallel configuration: the GNSS-IMU sensors establish accurate position, orientation, and timing, which is essential to the system, whereas other sensors can be either replaced or expanded as long as they can be synchronized via a triggering mechanism.

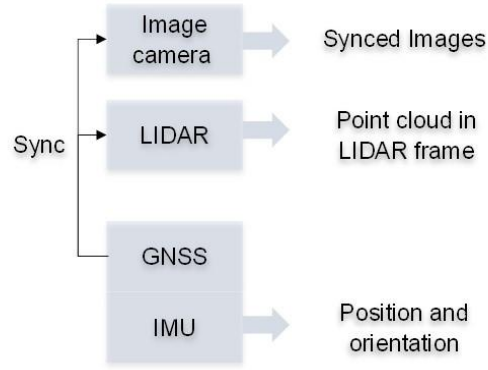


Figure 2 Synchronization Schematics of the UAS-LIDAR System

3.1.3 Navigation Measurements

The NovAtel Inertial Explorer software was used to process the raw data recorded by the GNSS and IMU sensors. GNSS carrier phase-based differential solution needs to be computed with respect to a nearby reference GNSS station, which could be either an onsite setup or from a local reference station, such as a Continuously Operating Reference Station (CORS). In this study, an onsite GNSS base station was set up and the positioning accuracy was defined based on the uncertainty of absolute positioning, which refers to the position geo-registered in a global frame. The positioning error from post-processing typically does not exceed centimeter level. The orientation accuracy was computed separately and differently. While the roll and pitch angles from the IMU are typically accurate and stable, the accuracy of true heading (geographic north instead of magnetic north), however, depends on the flight trajectory of the UAS. Since the IMU used in this work cannot directly sense the true heading, it must be inferred from an accurate position measurement while the UAS is moving. Therefore, the UAS must perform specific maneuvers at the beginning of each data collection flight to gain an accurate heading.

3.1.4 Pre-Processed Point Clouds

The point clouds collected by the LIDAR are referenced in the LIDAR body frame (L frame), which is constructed with Forward, Right, Down (FRD) directions. Since the LIDAR is constantly moving and rotating in the air, the point clouds cannot be directly geo-referenced in a global frame (G frame). The conversion between the two frames relies on the accurate position, orientation, and true heading of the LIDAR, as well as the accuracy in relative timing between each LIDAR scan point and the GNSS receiver.

When a LIDAR point in the L frame is synchronized to GNSS time, it can be geo-referenced into a G frame based on the reference GNSS station. For example, if the reference station is located with World Geodetic System (such as WGS-84) coordinates, the G frame will use local North, East, Down (NED) coordinates based on the WGS-84 coordinates. The potential positioning error in the reference station is ignored in this study.

The following algorithm of frame conversion was implemented in a custom code in MATLAB.

1. Record the 3D position of a static ground point x in L frame, $\mathbf{P}_x^L(t)$, at time t . The position error $\boldsymbol{\varepsilon}\mathbf{P}_x^L(t)$ is caused by LIDAR ranging error and beam angular error (aperture size).
2. Convert $\mathbf{P}_x^L(t)$ into the G frame:

$$\mathbf{P}_x^G = \mathbf{C}_L^G(t')\mathbf{P}_x^L(t) + \mathbf{P}_L^G(t') \quad (1)$$

where \mathbf{P}_x^G is the static position of this point in the G frame (no longer a function of time), \mathbf{C}_L^G reflects the rotation from L frame to G frame, and \mathbf{P}_L^G stands for the LIDAR position.

t' is the time of measurement of this LIDAR point perceived by the system, which could be slightly different from the actual time of measurement t . This time difference exists because the position and rotation of the LIDAR are computed based on measurements from the GNSS and IMU sensors at t' instead of t . The LIDAR timing error is thus specified as $\boldsymbol{\varepsilon}t = t' - t$ and could be up to 5 ms in a single scan point in the presented UAS-LIDAR system, as noted before.

\mathbf{C}_L^G is not directly measurable and is computed via the real-time IMU orientation and relative orientation of LIDAR from the IMU, also known as boresighting [May07]:

$$\mathbf{C}_L^G(t') = \mathbf{C}_V^G(t')\mathbf{C}_L^V \quad (2)$$

where \mathbf{C}_L^V is the fixed rotation from L frame to the vehicle frame (V) and $\mathbf{C}_V^G(t')$ reflects the rotation from the vehicle frame (IMU in this system) to G frame.

\mathbf{P}_L^G is not directly measurable either. The GNSS antenna location on the UAS \mathbf{P}_{ant}^G is measured at time t' , and the lever arm between the antenna and the LIDAR is measured in the vehicle frame as $\mathbf{P}_L^V - \mathbf{P}_{ant}^V$. Thus,

$$\mathbf{P}_L^G(t') = \mathbf{C}_V^G(t')[\mathbf{P}_L^V - \mathbf{P}_{ant}^V] + \mathbf{P}_{ant}^G(t') \quad (3)$$

3. Finally, the geo-referenced location of point x is found using

$$\mathbf{P}_x^G = \mathbf{C}_V^G(t')\mathbf{C}_L^V\mathbf{P}_x^L(t) + \mathbf{C}_V^G(t')[\mathbf{P}_L^V - \mathbf{P}_{ant}^V] + \mathbf{P}_{ant}^G(t') \quad (4)$$

3.1.5 Error Model

Errors in t' , $\mathbf{C}_V^G(t')$, \mathbf{C}_L^V , $\mathbf{P}_L^V - \mathbf{P}_{ant}^V$ and $\mathbf{P}_{ant}^G(t')$ can contribute to the overall system error. It is further assumed in this study that with a rigorous calibration procedure in place, errors such as the ones found in boresighting are at least one order of magnitude smaller than those from IMU orientation. For simplicity of

analysis, boresighting errors were not modeled in this study. Similarly, it is assumed that the lever arm error is also negligible. Therefore, the contributions of UAS orientation, positioning, timing, and LIDAR are considered in the error prediction model.

First, smaller angular errors in UAS roll ($\varepsilon\varphi$), pitch ($\varepsilon\theta$), and heading ($\varepsilon\psi$) angles are considered. In addition, a rotating or vibrating airframe will experience additional angular errors due to uncertainties in time, such that

$$\Delta^T = [\varepsilon\varphi \ \varepsilon\theta \ \varepsilon\psi] + \left[\frac{d\varphi}{dt} \ \frac{d\theta}{dt} \ \frac{d\psi}{dt} \right] \varepsilon t \quad (5)$$

$$\varepsilon C_V^G(t') = \Delta_{\times} C_V^G(t) \quad (6)$$

where Δ_{\times} is a skew-symmetric matrix. Ideally, $\varepsilon\psi$ is at a sub-degree level for the sensor used in the system, whereas $\varepsilon\varphi$ and $\varepsilon\theta$ are substantially smaller.

Next, the UAS position error, including the impact from the timing uncertainties, is represented with $\varepsilon t \frac{d\mathbf{P}_{ant}^G(t)}{dt} + \varepsilon \mathbf{P}_{ant}^G(t)$, where $\frac{d\mathbf{P}_{ant}^G(t)}{dt}$ is the velocity of the antenna in the G frame.

Finally, $\varepsilon \mathbf{P}_x^L$ is considered in the L frame in forward, right, and down directions. Since the LIDAR is pointing to the ground, the LIDAR forward direction is the vehicle down direction. The position error without timing error is

$$\varepsilon \mathbf{P}_x^L(t) = [0 \ \delta_r \ \delta_d]_{\times} \mathbf{P}_x^L(t) + \varepsilon R \frac{\mathbf{P}_x^L(t)}{|\mathbf{P}_x^L(t)|} \quad (7)$$

where $\varepsilon R \frac{\mathbf{P}_x^L(t)}{|\mathbf{P}_x^L(t)|}$ represents the LIDAR ranging error projected onto the direction of point x . δ_r and δ_d indicate right and downward angular errors with respect to LIDAR.

The error in x is thus modeled with

$$\varepsilon \mathbf{P}_x^G = [\varepsilon C_V^G(t')] C_L^V \mathbf{P}_x^L(t) + [\varepsilon C_V^G(t')] [\mathbf{P}_L^V - \mathbf{P}_{ant}^V] + C_V^G(t) C_L^V \cdot [\varepsilon \mathbf{P}_x^L(t)] + \varepsilon \mathbf{P}_{ant}^G(t) + \varepsilon t \frac{d\mathbf{P}_{ant}^G(t)}{dt} \quad (8)$$

Equation (8) can be used to predict the 3D error magnitude in a global frame for individual scan points. Noticeably, the LIDAR errors (δ_r , δ_d , and εR) are not considered systematic errors. Instead, $\varepsilon \mathbf{P}_x^L$ from Equation (7) is modeled as a random process, which is uncorrelated either among multiple points within the same scan or among repeated scans of the same point from a moving LIDAR. The other components from Equation (8) may

be correlated among the points within the same scan, but are likely uncorrelated among repeated scans. Therefore, the total errors in $\varepsilon \mathbf{P}_x^G$ are expected to include a major component of random errors and a minor component of systematic errors. Since the random error component is caused by the LIDAR, it is considered a relative error, whereas the systematic error component was largely related to errors in the G frame, which is an absolute error.

In a set of points \mathbf{X} that are approximately collocated in the G frame horizontally, the vertical dimension can be estimated based on all the points, \mathbf{P}_x^G . In this study, the points were computed with a mean or median value. Therefore, a dense raw point cloud could be preprocessed, decimated, and turned into a more accurate elevation model. The expected accuracy can be significantly improved with the number of points. For example, the down-sampled point $\mathbf{P}_{x,v}^G$ could be an average of all the points, as shown in Equation (9).

$$\mathbf{P}_{x,v}^G = \text{mean}\{\mathbf{P}_{x,v}^G, \forall x \in \mathbf{X}\} \quad (9)$$

The standard deviation of vertical errors in $\mathbf{P}_{x,v}^G$ is reduced by the square root of the number of points in \mathbf{X} . With a sufficiently large number of points in \mathbf{X} , the random and relative errors in $\mathbf{P}_{x,v}^G$ will approach zero, and therefore the systematic and absolute errors will dominate.

Alternatively, $\mathbf{P}_{x,v}^G$ can be calculated based on the median value of all the points in \mathbf{X} . Median values are less likely to be affected by outliers in the set. An implicit assumption is made such that all the points in the set share similar heights in a small horizontal neighborhood (centimeter to decimeter level), which is a valid assumption for most smooth surfaces. The median value shown in Equation (10) is expected to be a robust estimation. To better find all the points, some optimization methods will be applied as future work (Tao et al., 2019).

$$\mathbf{P}_{x,v}^G = \text{median}\{\mathbf{P}_{x,v}^G, \forall x \in \mathbf{X}\} \quad (10)$$

While the error model can predict horizontal and vertical errors separately, it is independent of the target surface. The texture, smoothness, and slope of a surface can contribute to the errors in the point cloud. For instance, a horizontal error can be perceived as a vertical error in a sloped surface. Vegetation on the surface could also result in additional uncertainty, and as a result, the optimal choice of the down-sampling method, i.e., mean vs. median values, may be dependent on the target surface. In general, the UAS-LIDAR system can measure a smooth, flat surface that is not covered by any vegetation with lower errors.

Furthermore, this error model is generic, and would be applicable to any UAS-LIDAR system that has LIDAR synchronized to an onboard navigation system. However, in order to implement Equation (8), it does require intermediate data such as the error models of navigation and synchronization, which may not be available from a commercial system.

3.1.6 Example of Error Prediction Model

The presented error model helps with the quantification of the contribution of individual error sources in a single point in a LIDAR point cloud. As an illustrative example, consider a typical slow and smooth flight (speed

= 5 m/s, no vibration or vertical velocity considered) where the UAS holds a constant altitude of 15 m above ground. Based on the typical performance of the UAS sensors in the system, it is assumed that $[\varepsilon\varphi \ \varepsilon\theta \ \varepsilon\psi] = [0.01, 0.01, 0.1]^\circ$ (1 standard deviation) and $\varepsilon\mathbf{P}_{ant}^G = [0.01, 0.01, 0.02]m$ for positioning errors (1 standard deviation). The lever arm between the LIDAR and the antenna $|\mathbf{P}_L^V - \mathbf{P}_{ant}^V| = 0.17m$. The LIDAR is pointing

downward, thus $C_L^V = \begin{bmatrix} 0 & 0 & -1 \\ 0 & 1 & 0 \\ 1 & 0 & 0 \end{bmatrix}$. It is further assumed that the UAS is leveled and facing north, thus $C_V^G(t) =$

$\begin{bmatrix} 1 & 0 & 0 \\ 0 & 1 & 0 \\ 0 & 0 & 1 \end{bmatrix}$. The error magnitude on a ground point x right underneath the LIDAR ($\mathbf{P}_x^L(t) = [15m, 0, 0]^T$) is

analyzed and illustrated below:

Let $\varepsilon\mathbf{P}_{x,\Delta}^G$ represent the error component contributed by the orientation uncertainty. In a leveled flight with little vibration, it is assumed that there is unsensed orientation change within εt such that $\left[\frac{d\varphi}{dt} \ \frac{d\theta}{dt} \ \frac{d\psi}{dt}\right] \varepsilon t = 0$. Although this assumption may be too optimistic for the UAS in some practical flight conditions, it would be acceptable for the presented sensing system since the vibration of the sensing system could be damped or separated from the vibration of the UAS airframe. In this case, the orientation error has a simplified model $\Delta^T = [\varepsilon\varphi \ \varepsilon\theta \ \varepsilon\psi]$.

Since the distance between x and the LIDAR is much greater than the lever arm, i.e., $|\mathbf{P}_x^L(t)| \gg |\mathbf{P}_L^V - \mathbf{P}_{ant}^V|$, the main contribution from the orientation error will be based on the term $[\varepsilon C_V^G(t')] C_L^V \mathbf{P}_x^L(t)$. Recall that $\varepsilon C_V^G(t') = \Delta_x C_V^G(t)$, therefore,

$$\varepsilon\mathbf{P}_{x,\Delta}^G = \Delta_x C_V^G(t) C_L^V \mathbf{P}_x^L(t) = [0.0026, -0.0026, 0]^T m. \quad (11)$$

where $\varepsilon\mathbf{P}_{x,\Delta}^G$ is a component of the overall error, $\varepsilon\mathbf{P}_x^G$, which is caused by the orientation uncertainty Δ . The errors are provided in North, East, and vertical directions, respectively.

Similarly, the error component caused by UAS positioning can be estimated by

$$\varepsilon\mathbf{P}_{x,P}^G = \varepsilon\mathbf{P}_{ant}^G = [0.010, 0.010, 0.020]^T m. \quad (12)$$

In this simplified model, the contribution of timing error is purely horizontal and is only proportional to UAS velocity. The magnitude is limited by

$$|\varepsilon\mathbf{P}_{x,t}^G| = \left| \frac{d\mathbf{P}_{ant}^G(t)}{dt} \cdot \varepsilon t \right| \leq 0.025 \text{ m}. \quad (13)$$

A greater contribution comes from LIDAR error $\varepsilon \mathbf{P}_x^L(t)$. As aforementioned, $\delta_r = 0.023^\circ$, $\delta_d = 0.23^\circ$ and $\varepsilon R = 0.1m$ (a conservative error level) are assumed for this LIDAR.

$$\varepsilon \mathbf{P}_x^L(t) = [0 \ \delta_r \ \delta_d]_{\times} \mathbf{P}_x^L(t) + \varepsilon R \frac{\mathbf{P}_x^L(t)}{|\mathbf{P}_x^L(t)|} = [0.10, 0.06, -0.006]^T m \quad (14)$$

which contributes to the overall error via

$$\varepsilon \mathbf{P}_x^G = C_V^G(t) C_L^V \cdot [\varepsilon \mathbf{P}_x^L(t)] = [0.006, 0.06, 0.10]^T m. \quad (15)$$

It is evident from comparing Equations (11) to (15) that the LIDAR is the dominant error source ($\varepsilon \mathbf{P}_x^L$) for point x . Since the majority of $\varepsilon \mathbf{P}_x^G$ is considered a random process that is independent among points, as mentioned earlier, the integration and synchronization with the navigation measurements does not introduce substantial systematic errors in the LIDAR point. As a result, the error magnitude is on the order of 0.1 m for both horizontal and vertical directions in a typical low-altitude flight. It agrees with the performance reported in literature, as discussed in Chapter 2.

3.1.7 Error Validation

The vertical and horizontal performance of raw point measurements \mathbf{P}_x^G can be validated with customized calibration targets. The error prediction model was first validated for random errors with a flat surface cardboard box that measures 1.24 m (Width) by 0.94 m (Depth) by 0.95 m (Height). The box target was placed on flat paved ground with a reference GNSS antenna next to it to record raw data for post-processing. The UAS scanned the target at different heights from 20 m to 40 m above the target (~ 21 m to ~ 41 m above ground) with 5 m intervals. Figure 3 illustrates the raw point cloud collected at 20 m above target with both the target and the reference antenna.

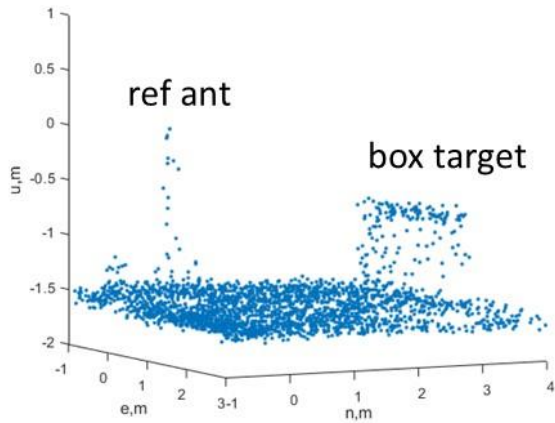


Figure 3 Left: Raw Point Cloud of Box Target and Reference GNSS Antenna. Right: Image from Onboard Camera. Collected at 20 m above target (~21 m above ground)

To improve the heading accuracy, the UAS performed initialization maneuvers immediately after taking off. After the flight, raw data were retrieved from the SD cards from both the UAS and the reference receivers. The data were post-processed, and the accuracy has been summarized in Table 1.

Table 1 Post-Processed Error Level for Flat Surfaces, Averaged over the Entire Flight

| Error Level | Positioning | | | Orientation | | |
|-------------|-------------|---------|---------|---------------|---------------|--------------|
| | North | East | Down | Roll | Pitch | Heading |
| 1σ | 0.006 m | 0.007 m | 0.008 m | 0.006° | 0.007° | 0.02° |

The vertical and horizontal errors in \mathbf{P}_x^G were assessed with the consistency of raw point cloud data collected from the top surface and one side surface of the box target, which contains mainly random and relative errors. As aforementioned, the vertical Root Mean Square Error (RMSE) of the raw point cloud is expected to be between 0.04 m and 0.1 m regardless of the height above the target, which was verified with results presented in Figure 4. On the other hand, Equation (8) indicates that the horizontal error would grow proportionally with the distance to target as it is mainly contributed to by angular uncertainties. As demonstrated in Figure 5, the observed RMSE in the horizontal direction closely follows the estimated nominal error level.

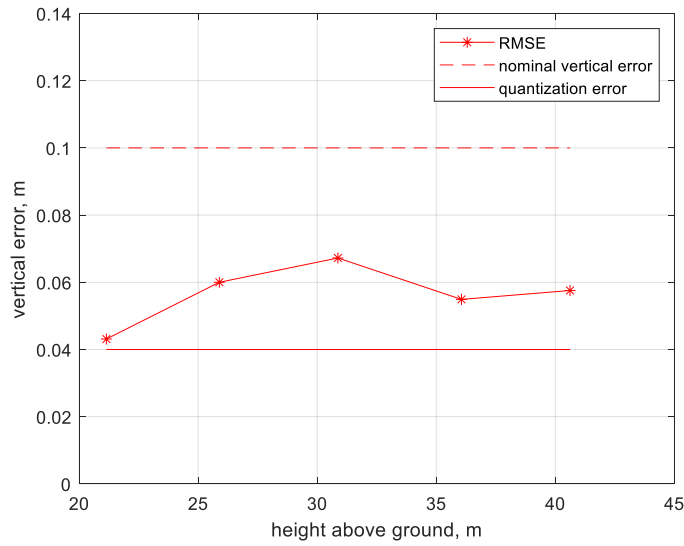


Figure 4 Vertical Error of Raw Point Cloud of the Box Target

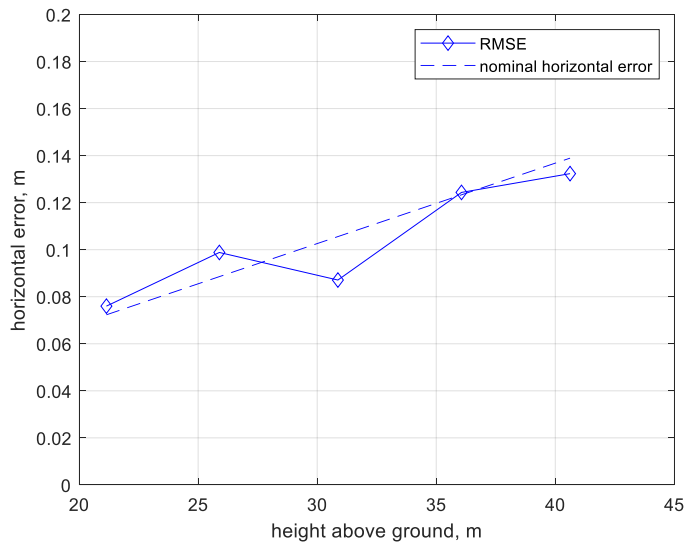


Figure 5 Horizontal Error of Raw Point Cloud of the Box Target

The box target used to validate the single point error model described in Equation (8) has known flat surfaces that are either vertical or horizontal. The error magnitude presented in Figures 4 and 5 is representative of the vertical and horizontal error components of individual scan points, which are dominated by random errors contributed to by the LIDAR. Figure 4, however, does not include the potential contribution of horizontal errors. On a box-shaped target, the horizontal errors of points on the edge of a surface could result in greater vertical errors, which will be discussed next.

Next, the magnitude of random and systematic errors was validated respectively, using a point cloud dataset with slope surfaces and survey points. Two tent-shape target objects were placed on flat paved

ground, each with two smooth planar surfaces covered by white canvas, as shown in Figure 6. The UAS hovered at approximately 15 m to 17 m above the ground and scanned the targets multiple times. The navigation data were post-processed, and the accuracy has been summarized in Table 2. The accuracy level in this table is typical in a UAS flight.



Figure 6 Experimental Setup for Model Validation with Tent Targets

Table 2 Post-Processed Error Level for Slope Surfaces, Averaged over the Entire Flight

| Error Level | Positioning | | | Orientation | | |
|-------------|-------------|---------|--------|---------------|---------------|--------------|
| | North | East | Down | Roll | Pitch | Heading |
| 1σ | 0.007 m | 0.006 m | 0.01 m | 0.007° | 0.008° | 0.07° |

The raw LIDAR point cloud georeferenced in a G frame (NED) is shown in Figure 7, and Figure 8 provides a zoomed-in view with the two corners of both tent targets marked, which were surveyed separately by post-processed GNSS with an accuracy of 0.005 m, 0.005 m, 0.01 m in NED.

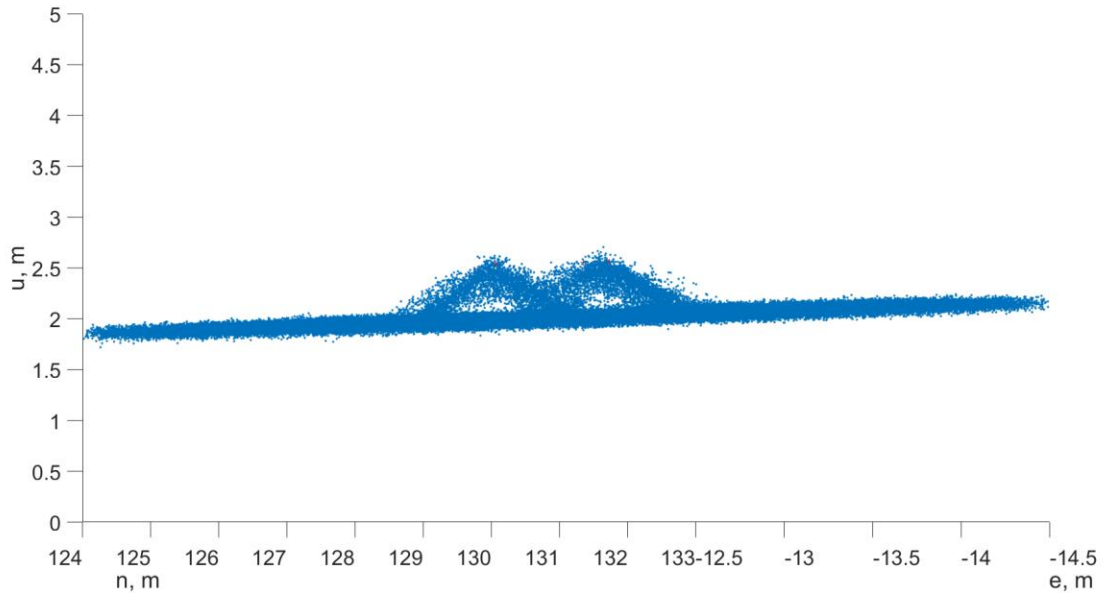


Figure 7 Raw Point Cloud of Tent Targets, Georeferenced in A Local G Frame (NED)

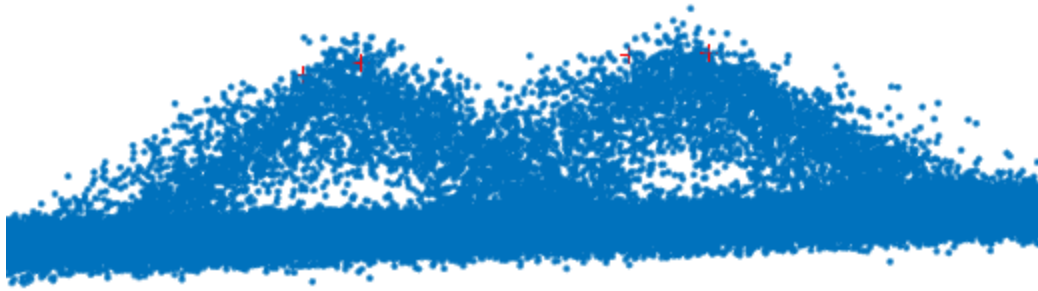


Figure 8 Zoomed-In View of Raw Point Cloud of Tent Targets with Four Survey Points Marked

In this dataset, raw point cloud ($\mathbf{P}_{x,v}^G$) reports 0.04 m relative vertical error (1σ) on a flat ground surface, which is consistent with the results reported in Figure 4. However, the vertical error observed on the tent targets was expected to be greater. Since the slope on both sides of the targets is approximately 45° , a portion of the horizontal errors was mapped onto the vertical direction at a 1:1 ratio. In other words, the observed vertical error from a raw LIDAR point cloud would be a combination of the actual horizontal and vertical error components. As a result, the absolute vertical error of raw point cloud on slope surfaces is approximately 0.1 m (1σ), which is also consistent with the error prediction model in Equation (8).

Although the UAS-LIDAR system can collect relatively dense point clouds, it is not guaranteed that all surfaces of the target will be captured directly in the raw point cloud during a flight. As a result, it should not be assumed that the entire target will be included in the raw point cloud. Instead, the system is able to

extract the geometry of targets from the raw point cloud in addition to measurements. The systematic error component of the point cloud can be estimated by using known geometric information of the target, such as shape and dimensions, and the target location from GNSS surveys. The geometric features of the target, such as planar surfaces, can then be extracted from a partial point cloud, and it is more convenient and robust to identify and extract planar features than point features on small-scale objects.

The average height of an object can be estimated from two planar features that are extracted from all points measured by the UAS-LIDAR system, and the absolute positioning error on a point reflects the magnitude of systematic and absolute error. The measurements from one of the two tent targets are validated here as a demonstration. Figure 9 illustrates 8,280 points from Target 2 that are projected onto a 2D plane perpendicular to the ridgeline of the target. These points form the cross-section shape of the tent target as a triangle, and its left side and right side, colored in red and blue, respectively, represent all the points from both planar surfaces. An orthogonal linear fit is applied to each side to recover the shape of the triangle, the top of which is then compared against its GNSS survey reference projected onto the same plane. As shown in Table 3, the LIDAR measurement of the height of Target 2 is 2.504 m whereas the GNSS measurement is 2.512 m (averaged between two corners), resulting in a vertical difference of 0.008 m. Since this difference is smaller than the GNSS survey accuracy of 0.01 m, it may not accurately represent the actual vertical error. Nonetheless, the absolute systematic error is indeed much smaller than the overall vertical error of 0.1 m, as predicted in Equation (8).

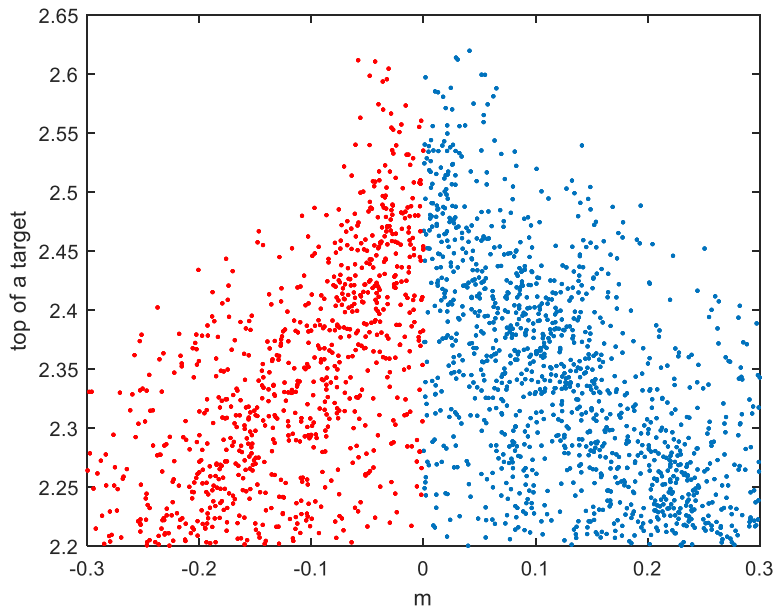


Figure 9 Raw Point Cloud of Tent Target 2 Projected onto A 2D Perpendicular Plane

Table 3 Height of Tent Target 2 by Measured by LLDAR and GNSS Survey

| Target 2 | LIDAR | GNSS Survey | Difference | GNSS Accuracy (1σ) |
|----------|---------|-------------|------------|-----------------------------|
| Height | 2.504 m | 2.512 m | 0.008 m | 0.01 m |

LIDAR measurements of bulk piles will face the same challenges as the tent targets, and it would be impractical to directly extract the height, surface, and volume from a noisy raw point cloud. Instead, an averaged, down-sampled point cloud will be more reliable, assuming that the errors on single points are mostly independent of each other, which has been validated in this dataset. The vertical errors can be effectively reduced by pre-processing based on mean or median values introduced in Equations (9) and (10). As a demonstration, the pre-processed point cloud of the tent targets shown in Figure 10 appears much less noisy than the raw data point cloud in Figure 7.

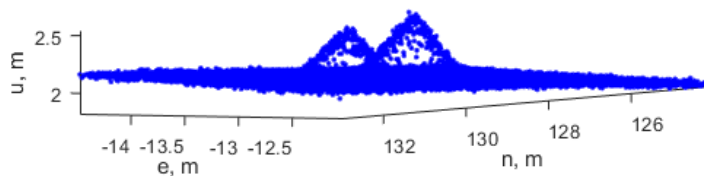


Figure 10 Pre-Processed Point Cloud of Tent Targets

A robust error model was developed for a generic UAS-LIDAR system to predict the horizontal and vertical errors of single point geo-registration. The contributions of errors from different components, such as navigation, timing and LIDAR are all considered. This model was validated for the proposed UAS-LIDAR system with calibration targets and real-world data from three different measurement scenarios: a box target with smooth flat surfaces for random error validation, targets of known sloped surfaces for systematic error validation, and a test site rock stair pile for bulk measurement validation. The test results indicated that the random errors from raw LIDAR point cloud reach approximately 0.1m in the horizontal and vertical directions respectively during typical low-altitude flight conditions. Systematic errors, such as those caused by navigation and timing components are at or below centimeter-level in these flights, suggesting that the presented UAS-LIDAR had introduced negligible systematic errors. In addition, pre-processing of the raw point cloud can further reduce the random errors.

If substantial systematic error does exist, it will result in inconsistency within the point cloud. The points collected from the same object with the same UAS-LIDAR from different positions, angles and time will not agree with each other. Figure 11 illustrates a hypothetical case of vertical systematic error. The actual object, a black pile, can be observed with positive or negative vertical biases, which depends on the orientation

and the position of the LIDAR. Even if the red and blue represent the same LIDAR in the same flight, both partial point clouds (red and blue) would not agree with each other. Either one of them can represent the pile precisely, but they cannot be directly merged. They will have to be registered to each other through manual correction or a specialized software solution. Luckily, the systematic bias is expected to be small based on the analysis of this system. However, it can still be visible in some of the datasets to be discussed in Chapter 4.

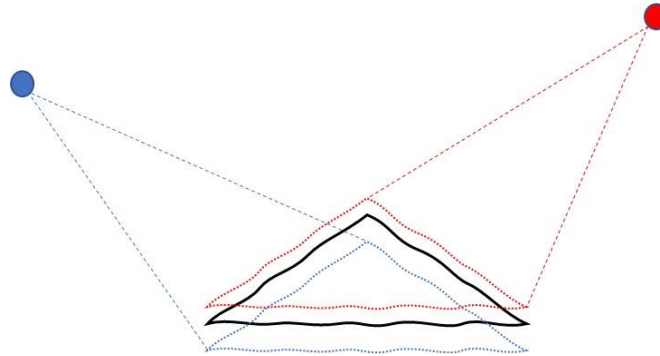


Figure 11 Impact of Vertical Systematic Error (Black = True Object; Blue = LIDAR Point Cloud from Left; Red = LIDAR Point Cloud from Right)

3.2 A Side-View UAS-based LIDAR System

3.2.1 Hardware components

It has been verified that the downward-looking LIDAR could scan ground objects, such as piles very effectively. However, it is not convenient to scan vertical objects and structures, such as bridges. The second UAS-LIDAR system was constructed by the ECU team to provide point cloud from a horizontal side view. Similar to the system shown in Figure 1, it is also using the DJI Matrice 600 Pro airframe, equipped an auxiliary sensing system including the following components:

- A Velodyne PUCK-16 LIDAR sensor
- A Garmin GPS receiver
- A NovAtel SPAN GNSS receiver with an integrated Inertial Measurement Unit (IMU)
- Two Raspberry Pi III embedded computers
- A rigid lightweight cage to mount all the components above

The Velodyne LIDAR is installed horizontally in this system, as can be seen in Figure 12. It has 16 layers of laser beams (covering a 30° vertical field of view). It has an operational range of 100 m, with a 3 cm 1 sigma accuracy. It can scan 360° around the sensor body with 0.2° resolution. The timing mechanism of this unit is different from the one used in the downward-looking system. The manufacturer recommended that the

LIDAR data be synchronized to GPS time using a small Garmin receiver. Therefore, an additional Garmin receiver is added to the system for synchronization only. The data from the Garmin receiver is not used to compute the position and orientation of the UAS. Since the receiver is compact and light-weighted, it is not considered a substantial burden in the UAS payload.



Figure 12 Velodyne LIDAR Installed in a Cage on Matrice 600 Pro

The side-view LIDAR can scan large vertical structures very efficiently. Since the target is no longer on the ground, it may be as far as 100 m away from the UAS with this LIDAR, even if the UAS maintains a 15 m height above ground. It can create up to 300,000 points per second. Within few minutes, it can model a large area or object with dense point cloud. A segment of a bridge is shown in Figure 13. The point cloud was obtained within several seconds.

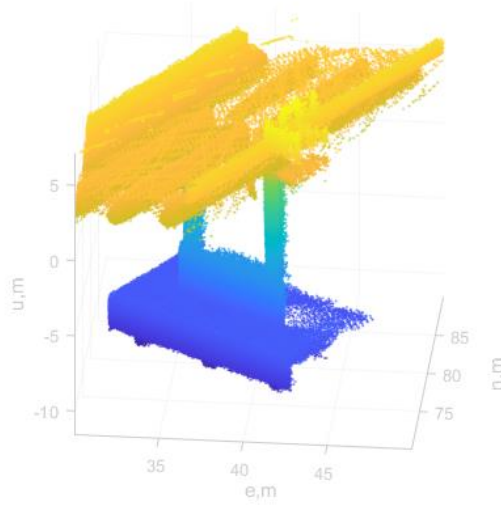


Figure 13 Sample Point Cloud Data from the Side-View LIDAR

3.2.2 Error Model

The error model defined in Equation (8) can also be used to predict the 3D error magnitude in a global frame for individual scan points for the side-view LIDAR. Similar to the downward-looking LIDAR, the errors in this system will also have random, relative errors and systematic, absolute errors. However, there are two major differences: the relative geometry and the distance to the targets.

The LIDAR is pointing forward instead of downward, thus $C_L^V = \begin{bmatrix} 1 & 0 & 0 \\ 0 & 1 & 0 \\ 0 & 0 & 0 \end{bmatrix}$. Also assume that the UAS is leveled and facing north, thus $C_V^G(t) = \begin{bmatrix} 1 & 0 & 0 \\ 0 & 1 & 0 \\ 0 & 0 & 1 \end{bmatrix}$. The error magnitude on a target point x at 100 m way forward ($\mathbf{P}_x^L(t) = [100m, 0, 0]^T$) will have a substantial error level. With the orientation error has a simplified model $\Delta^T = [\varepsilon\varphi \ \varepsilon\theta \ \varepsilon\psi]$. Using $[\varepsilon\varphi \ \varepsilon\theta \ \varepsilon\psi] = [0.01, 0.01, 0.1]^\circ$, the error due to UAS orientation is thus

$$\varepsilon\mathbf{P}_{x,\Delta}^G = \Delta_x C_V^G(t) C_L^V \mathbf{P}_x^L(t) = [0 \ 0.524 \ 0.0524]^T m. \quad (16)$$

The heading error of 0.1° (caused by navigation or boresighting) is responsible for a significant horizontal error of 0.524 m. The error magnitude is much greater than that observed in equation 11. It is mainly contributed to by the longer distance to the target (100 m vs 15 m) and a different geometric relationship. Since the orientation error may be observed as a bias, equation (16) reflects a potential systematic error in the side-view LIDAR. It will dominate the overall error in $\varepsilon\mathbf{P}_x^G$, which is considerable larger than the one shown in equation (15). Clearly, centimeter-level error on single LIDAR points can no longer be guaranteed in this system due to orientation, especially heading errors. Further, the systematic error component could be greater than the

random error component. It indicates that the side-view LIDAR could produce precise dimensional measurements, but the geo-registration of the point cloud may have a small offset in a global coordinate system. The impact of horizontal systematic error is illustrated in Figure 14. Similar to the vertical systematic error show in Figure 11, the horizontal systematic error also causes both partial point clouds (red and blue) to disagree with each other in the horizontal direction. In this case, it is primarily due to heading errors in UAS-LIDAR.

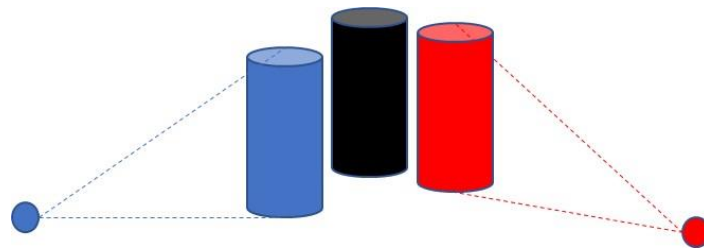


Figure 14 Impact of Horizontal Systematic Error (Black = True Object; Blue = LIDAR Point Cloud from Left; Red = LIDAR Point Cloud from Right)

In order to limit the error magnitude, the absolute heading error $\epsilon\psi$ has to be constrained. It can be achieved by a more rigorous calibration procedure of boresighting before flight and calibration of heading during every flight. Furthermore, the target distance can be limited despite the sensor capability. In other words, only points measured within a certain distance (for example, 50 m) can be used in the final data product.

3.3 Structure from Motion System with known Camera Pose

Since the traditional UAS-based SFM system has been well studied in literature and discussed in chapter 2 of this report, it will not be repeated here.

Precise position and orientation (pose) of the camera recorded in a world coordinate system can be used to estimate a 3D model geo-registered in the same coordinate system. Precise camera location can be achieved using GNSS, more particularly, RTK and PPK technologies. While generally considered expensive, newer technologies are reducing the cost of RTK and PPK. Orientation of a camera can be sensed using an IMU that is typically integrated with a satellite navigation system on a small UAS. Precise camera position and orientation are crucial to proper scaling, orientation and geo-registration of the 3D model in the world frame. However, the high-quality IMUs required for geo-registration are not commonly available for small UAS yet. Even if the orientation measurement is not available to small UAS, geo-registration can still benefit from precise positioning alone.

A SFM with precise location from GNSS RTK and a camera synchronized with GNSS is constructed in this project. The system is not based on a costly commercial solution. Instead, it is based on a combination of low-cost UAS, GNSS receiver and camera, with open and interchangeable interfaces between components.

It has been verified that with precise location alone, SFM can achieve precise relative measurements with the correct scale, without using GCPs. The details of this system will be discussed in Chapter 6.

Ch 4 Case Studies for Construction Management

There were two main goals the ECU team had for the UAS-LIDAR data collection in construction and management projects.

1. Accurate geo-registration of LIDAR points. The absolute vertical error of every individual point should be below 0.1 m, 1 sigma.
2. Data presentation and visualization with a standard coordinate system (such as NC state plane), format (such as “.las” files) and ideally with imagery texture.

Based on the analysis presented in Chapter 3, the accuracy is related to UAS flight pattern, hardware calibration and synchronization, and post processing steps. Therefore, the corresponding requirements for flight, data collection hardware and software, and data processing procedures have been provided in this chapter.

4.1 Flight, Data Collection and Processing

The following hardware is needed for data collection. Examples used in this project are included.

1. UAS frame, DJI Matrice 600 Pro
2. Navigation system, NovAtel OEM 6 + NovAtel IGM A1
3. Downward-looking LIDAR synchronous to GPS time, SICK LD-MRS420201
4. Ground reference GNSS antenna and receiver, with tripod (optional), NovAtel OEM 6
5. Calibration targets (optional)
6. Camera synchronized to GPS time (optional), IDS uEye

The following software components are needed for post processing:

1. Post processed position and orientation solution, NovAtel Inertial Explorer
2. LIDAR point extraction and geo-registration, Custom MATLAB code for synchronization, geo-registration and exporting LIDAR points
3. Reference system conversion (optional), NOAA Vdatum
4. Point Cloud data viewing and file type conversion (optional), Lastools
5. Custom MATLAB code, for integrating imagery (optional)

The requirements for the UAS flight include:

1. A safe, low-altitude and steady flight over the target area
2. Sufficient initialization maneuvers to reduce navigation error (especially heading)
3. Dense point cloud collected over the target area

4. Dense point cloud collected over calibration targets at known locations to verify the performance in each flight

A typical flight includes the following major steps

1. Take off and hover at ~15 m above ground.
2. Initialization maneuvers for ~ 3 min: including accelerations in horizontal directions. Make circular and figure-8 patterns.
3. Fly over calibration targets (optional). The target can be the antenna and the tripod of the ground reference GNSS receiver.
4. Fly over worksite, ~15 m above target, ~5 m/s.
5. Fly over calibration targets (optional).
6. Land.

The LIDAR can collect a relatively dense point cloud during a flight (~37.5 K points per second). As discussed in Chapter 3, the error in the LIDAR point cloud heavily depends on the error in the navigation system. However, the performance of the navigation system cannot be reported in real time. Although the GNSS receivers have predictable performance with RTK or PPK, the accuracy of orientation measurements is harder to predict with the IMU device available on small UAS.

The orientation accuracy specified by the manufacturer can be achieved based on certain assumptions of the UAS operation. Sufficient initialization maneuver is necessary, but it cannot always guarantee the orientation accuracy. In some cases, it may even be challenging for the post-processing software to estimate the orientation and its accuracy. It is possible for the post-processing software to be overly optimistic or pessimistic about the orientation.

Therefore, the most reliable way to assess the accuracy of point cloud and the navigation solution is to directly observe one or few calibration targets with known location in the point cloud.

The raw point cloud data will be retrieved from the UAS and post processed.

1. Post-process GNSS position and orientation.
2. Synchronize LIDAR and camera to GPS time.
3. Geo-registered raw point cloud in local ENU frame by integrating LIDAR, GNSS and Inertial data.
4. Down sampling to desired horizontal resolution; outliers removed.
5. Convert the coordinates of the data points to target frame.
6. Convert the data file into a desired format.
7. Add imagery texture if available.

4.2 Buildings

The first case reported here is with data collected over an NCDOT site in Butler, NC. This location includes several buildings and ground targets pre-surveyed by NCDOT. In this dataset, the target area includes a building and a pre-surveyed target. This dataset demonstrates the workflow defined in section 4.1, the efficacy of UAS-LIDAR in scanning buildings and the accuracy verified with independent survey results.



Figure 15 Butler Site with Surveyed Locations

A ground reference GNSS antenna and receiver and two calibration targets were used. A picture of both can be found in Figure 6. The locations of both targets were surveyed using GNSS onsite, as shown in Figure 16. These locations were computed in the NovAtel Inertial Explore software with a PPK solution with respect to the Durham CORS site (DURH). The antenna location was computed in NAD2011 as:

- ECEF: 1004835.436 -5058567.965 3740131.122 (m)
- LLH 36° 07' 57.30411" -78° 45' 53.98576" 80.597 (m)
- NCSP 2069399.74, 867245.54, 361.86 (US Survey ft)
- Expected accuracy 0.004 m horizontal and 0.009m vertical

The antenna was set up on top of a tripod, which is located on a pre-surveyed target (monument). Compared against the truth reference provided by NCDOT, the difference was

- 0.0140 -0.0340 -0.0200 (ft), or approximately 0.004, -0.01, -0.006 m.

which agrees with the expected accuracy of the PPK solution. Notice that at this stage, these coordinates were not extracted from the UAS-LIDAR yet. The locations of the targets are geo-referenced relative to the antenna, as illustrated in Figure 16.

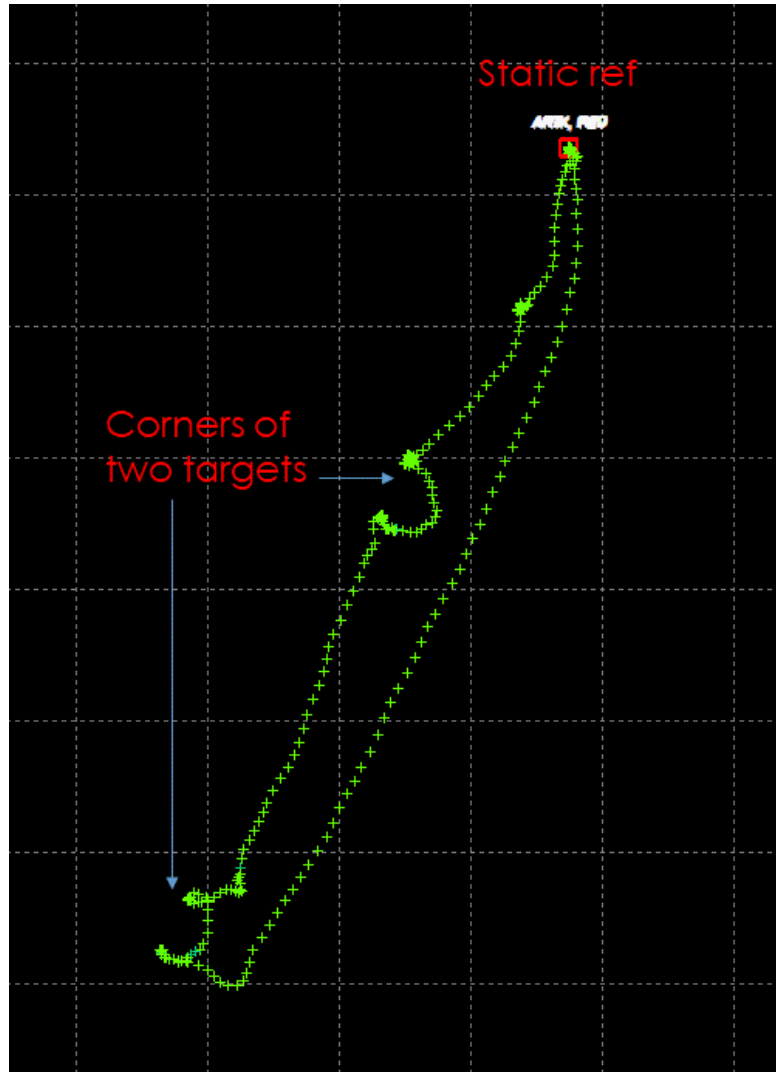


Figure 16 Ground Survey of Calibration Targets from the Butner, NC Dataset

Following the UAS flight steps listed in section 4.1, the UAS flew over the antenna and the calibration targets several times, to capture a dense point cloud. The ground track of the UAS can be found in Figure 17. Since each of the points has its unique coordinates, the location of the antenna and the calibration targets can be directly extracted from the point cloud. The point cloud of the antenna is shown in Figure 18, and the targets in Figure 19.

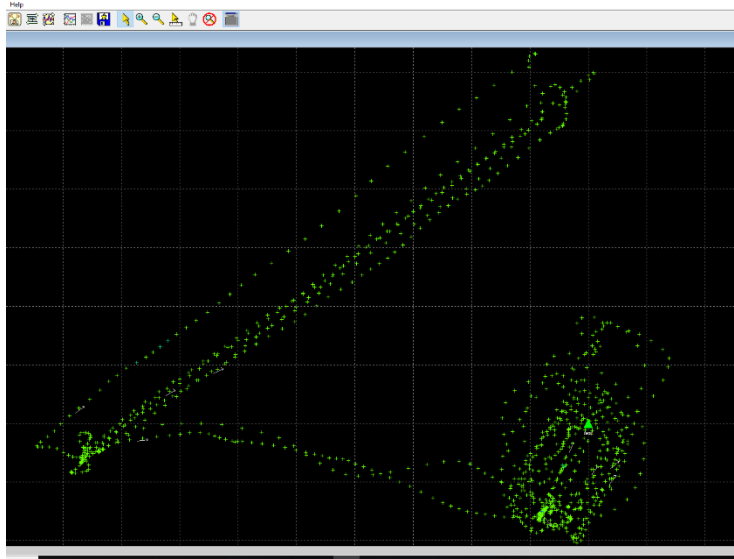


Figure 17 Ground Track of UAS Flight from the Butner, NC Dataset

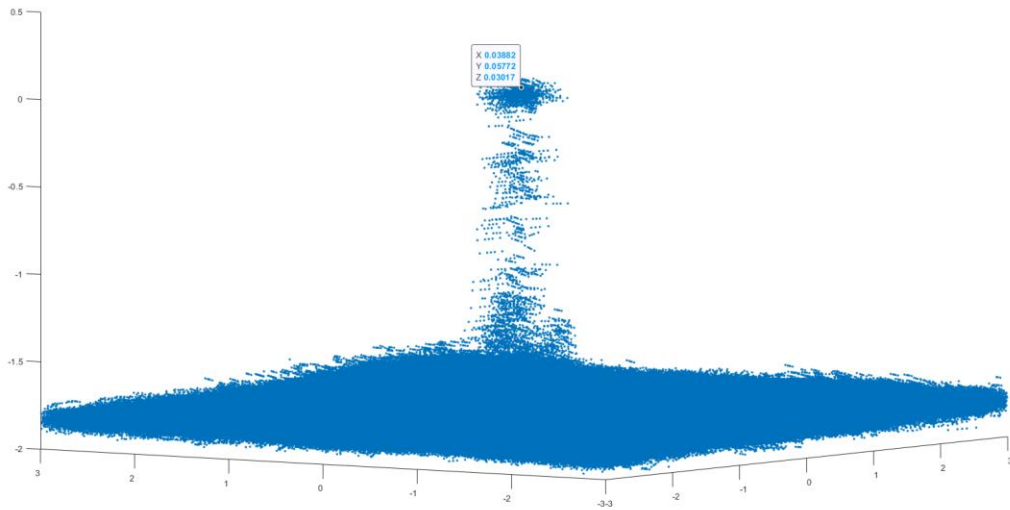


Figure 18 Dense Point Cloud of Reference Antenna from the Butner, NC Dataset

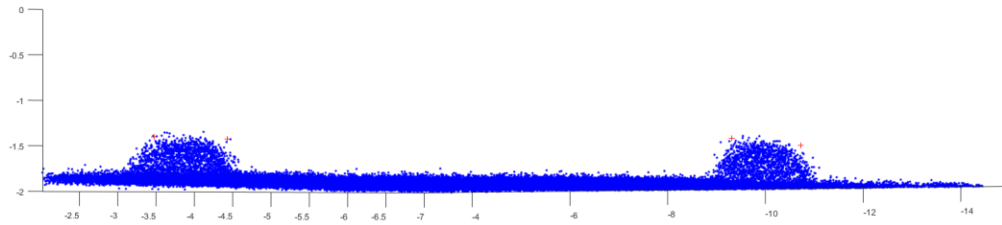


Figure 19 Dense Point Cloud of Calibration Targets from the Butner, NC Dataset

Relative to the antenna location computed by ECU survey, the antenna location extracted from the point cloud is [0.039, 0.058 0.03] m. The original data is illustrated in Figure 18. The error is within the budget discussed in Chapter 3. Similar results can be found from the calibration targets. The vertical error observed as 0.03 m, 1 sigma. The point cloud of the antenna and the calibration targets clearly validates the performance of the point cloud and the navigation system.

An imagery map of the building complex can be found in Figure 20. The UAS flew over the building in less than 10 minutes. A dense point cloud of the building is created in the customized software, shown in Figure 21. The point cloud can be converted into a “.las” file in Lastools, shown in Figure 22.



Figure 20 Building Complex from the Butner, NC Dataset

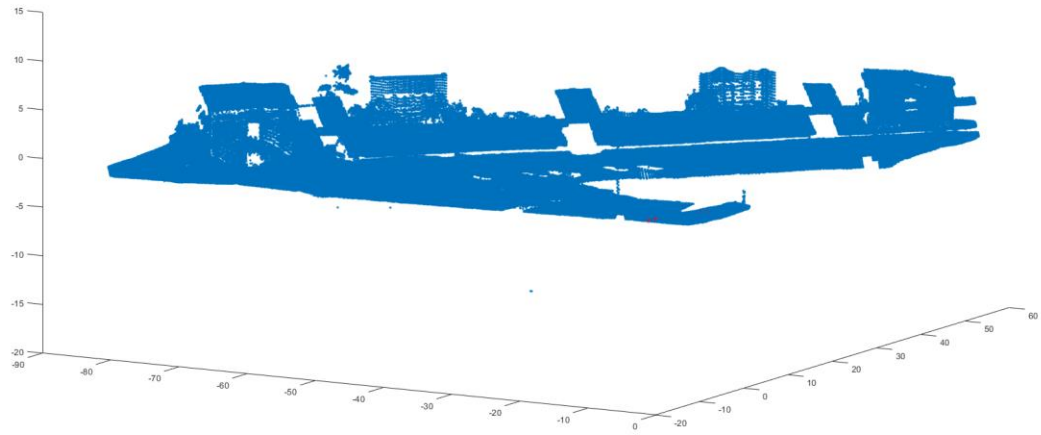


Figure 21 Point Cloud of the Building Complex from the Butner, NC Dataset

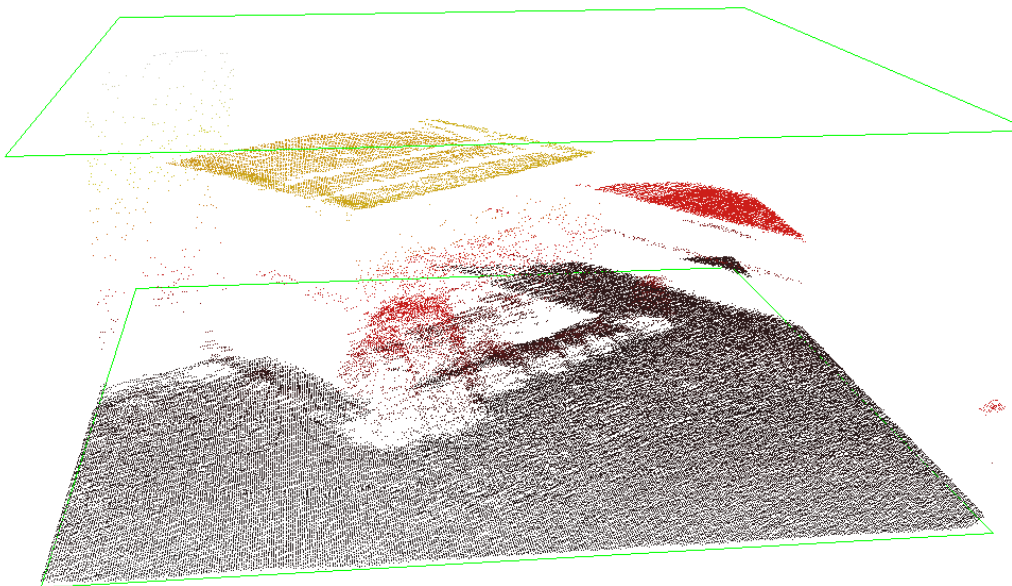


Figure 22 Point Cloud of the Building Complex from the Butner, NC Dataset, Viewed in Lastools

It can be seen from this dataset that the absolute geo-registration accuracy of the UAS-LIDAR point cloud can be predicted and over-bounded by the analysis presented in Chapter 3. Centimeter-level accuracy is observed from calibration targets and the reference antenna. It appears that the accuracy validation can be achieved by using the antenna alone, although it was also validated using both calibration targets in this dataset.

Following the flight plan defined in section 4.1, the UAS can scan a building complex (approximately 100m by 100 m) in a single flight, within minutes. The data can be converted into a desired format and coordinate system with the post-processing workflow.

4.3 Pit and Piles in Havelock, NC

The second case included in this report is with data collected over a site in Havelock, NC, suggested by NCDOT. This location includes piles and pits filled with water. Contractor Balfour Beatty had been working on this site when the dataset was collected. Figure 23 provide an overall image of the site. Two flights of the UAS-LIDAR system were performed.



Figure 23 Imagery of the Havelock, NC Site (34° 48'59.7"N 76°52'00.2"W, near Newport Loop),
Courtesy from Balfour Beatty

The image was collected several days before the UAS-LIDAR flight. A greater part of the pit area had been filled with water when the UAS flight took place. The point cloud of the UAS-LIDAR of the pit area (highlighted in a blue circle in Figure 23) can be found in Figure 24. Figure 25 shows the airborne imagery collected with the video camera on board the UAS. It corresponds to the section in Figure 24 highlighted in a red circle.

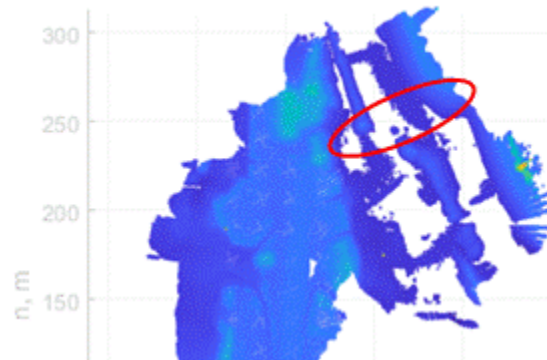


Figure 24 UAS LIDAR Point Cloud of the Havelock, NC Site



Figure 25 Imagery from a Camera onboard the UAS-LIDAR System

Water in the pit was relatively still with a very smooth surface. There were few returns from the LIDAR, which could not form a meaningful point cloud. As expected, LIDAR is not a good choice for measuring a smooth water surface. It can still effectively measure piles and empty pits on this site.

The first flight covered most of the dry land at approximately 12 m above ground. The second flight was higher to avoid obstacles. It covered most of the pit area, at approximately 24 m above ground. Due to the operational environment, there was no reference antenna or calibration target in the point cloud of Flight 2. There was a small overlap between both point clouds. On average, there is a 0.1 m difference between both flights. As discussed in Chapter 3, systematic errors are likely due to errors in navigation solution. Although the navigation solutions of both flights were reported with good quality in the post-processing software, one or both of them could still be overly optimistic. However, since flight 2 did not have a validation point (antenna or targets), it becomes difficult to independently verify the performance of this flight. The bias between overlapped point clouds will have to be manually corrected, which is not ideal. However, the relative precision of either point cloud is still well within the expected range.

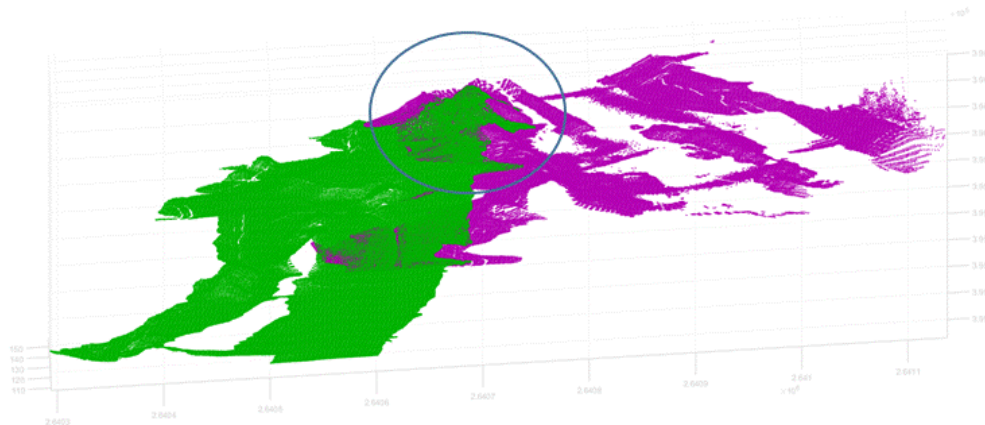


Figure 26 Point Cloud from the Havelock, NC Dataset, Green: Flight 1; Red: Flight 2

Balfour Beatty also measured the area using SFM. However, due to a few operational reasons (weather forecast, permission to fly etc.) both teams could not fly on the same day. The changes in the area made it infeasible to compare SFM point cloud with UAS-LIDAR. However, a few observations were made regarding both technologies in this case:

1. SFM needs a lot of GCPs. UAS-LIDAR will need one or two calibration targets, such as the antenna itself.

2. UAS-LIDAR has a clear advantage over SFM in areas where GCPs cannot be placed, such as on sites involving pits and piles.
3. It is more convenient to visualize SFM point cloud (LIDAR needs additional imagery which will be discussed in the following section).
4. Still water surfaces could not be measured with either SFM or LIDAR.
5. LIDAR seems to get some returns from water surface, which will be further explored in the following chapter.
6. The LIDAR used in this project has a wide laser beam, which works properly in a dusty environment.

4.4 Volumetric Measurements of Piles at Pitt County Maintenance Yard

The third case is about volumetric measurements of piles. The NCDOT Pitt County Maintenance Yard is located near the Pitt County Airport. The area of interest is approximately 80m by 160m. There are several piles of different materials on the yard. As requested by the airport, the UAS flights at this location were kept at a low altitude (<60 ft above ground). Each flight lasts ~15 minutes, although it only needs 5 minutes to scan all the piles. No GCPs or calibration targets other than the antenna itself were used in any of the flights.

4.4.1 Dataset 1 (Oct 2020)

The first dataset was collected in October 2020. The dataset collected in the first flight was used to demonstrate volumetric measurements and expected accuracy. It also established a baseline 3D model of all the piles. The 3D point cloud can be found in

Figure 27. The point cloud of each individual pile has been listed in Table 4 together with an image obtained with an onboard camera.

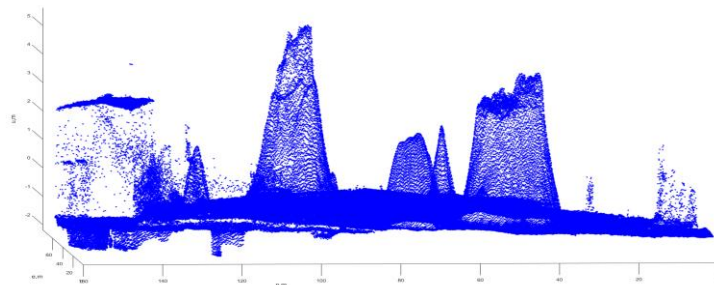
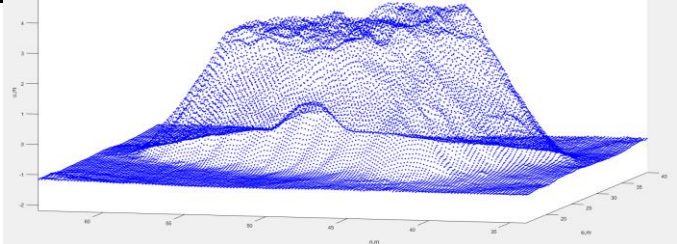
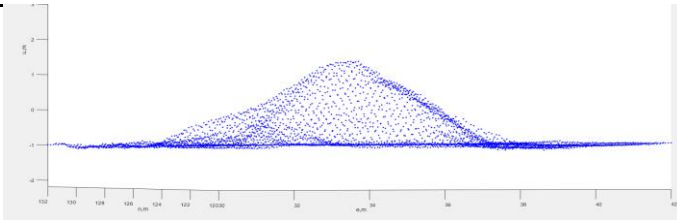
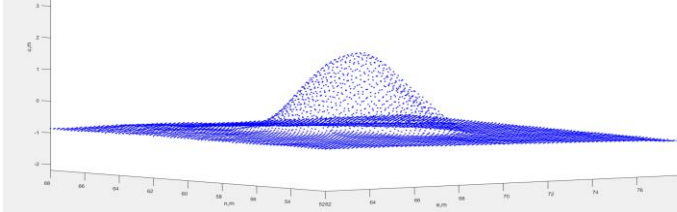
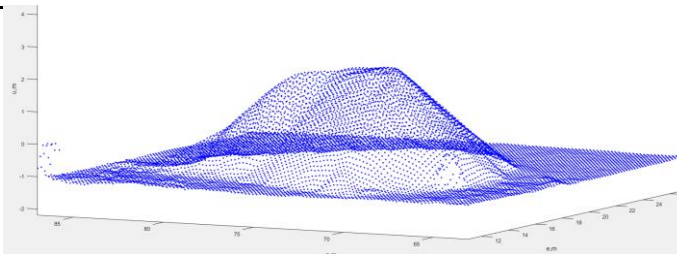
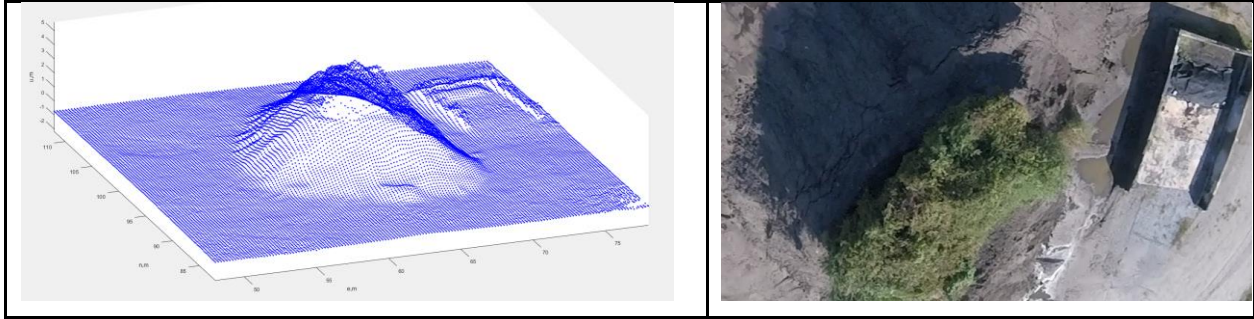


Figure 27 Point Cloud of Pitt County Maintenance Yard, Dataset 1 (Oct 2020)

Table 4 Point Cloud and Imagery of Piles

| | |
|---|--|
|  |  |
|  |  |
|  |  |
|  |  |



The point cloud accuracy of every flight had been validated with the reference antenna. As discussed in Chapter 3, the random error of individual points can be as high as 0.1m (vertical, 1 sigma). However, after down sampling in post processing, it can be greatly reduced. It has been observed that the random vertical error is typically 0.01-0.02m 1 sigma with a grid size of 0.1 m.

4.4.2 Dataset 2 (Feb 2021)

As suggested by NCDOT, a second dataset was collected in February 2021, when all the piles were measured using a traditional GNSS-based survey. Figure 28 illustrates the six piles measured by NCDOT on a satellite image. Notice that the piles in the satellite image have different sizes than what was measured. The image should only be used to locate and identify the piles.



Figure 28 Location of 6 Piles in Dataset 2, courtesy of NCDOT

Figure 29 shows the UAS-LIDAR point cloud with a top-down view. It was oriented in the same direction as the satellite imagery for convenience. All the coordinates were East-North based on the reference antenna used in Dataset 2, which is also used to identify the piles.

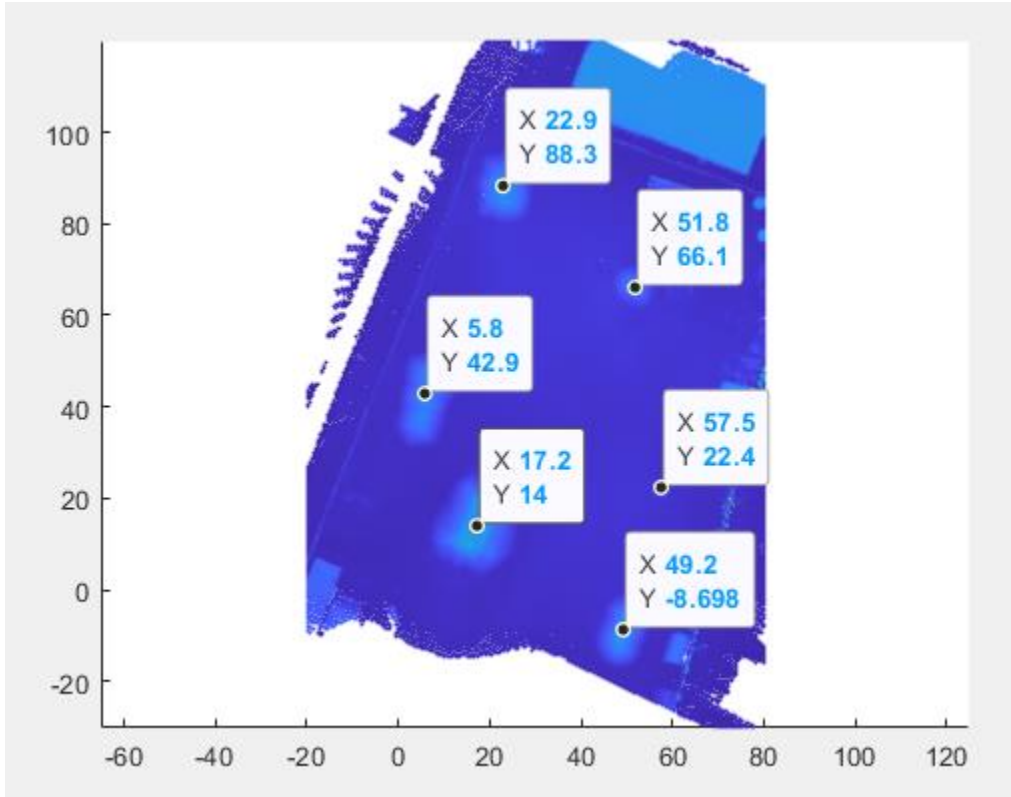


Figure 29 Point Cloud of 6 Piles in Dataset 2, Top View

For volumetric measurements, a simplified model is used for this dataset, which will be updated in the next dataset. Assuming that the point cloud of a pile has been downsized with a fixed grid size, A . h_i stands for the vertical measurement of grid i . The total volume is computed using

$$V = \sum_i A \cdot h_i. \quad (17)$$

The number of grids depends on the grid size and the size of the pile. If a pile has a base of 3m by 3m, it will result in 900 grids with a grid size of 0.1m. The LIDAR vertical error is normally 0.1m 1 sigma, and the majority of it is random error. After the summing over 900 grids in Equation (17), the contribution of random error to the overall volumetric error is usually negligible.

As shown in Chapter 3, the vertical systematic error is typically on the order of $b = 0.01\text{m}$. In the worst case scenario, it may present as a bias in all h_i measurements, which leaves a bias in V . As shown in Equation

(18), the fractional volumetric bias is proportional to the bias over the average height \bar{h}_i . For a pile that has an average height of at least 1m, the fractional volumetric bias would be smaller than 1%.

$$\Delta V/V = \frac{b}{\bar{h}_i}. \quad (18)$$

Since the systematic error is bounded, the fractional volumetric bias becomes even smaller with larger piles. Therefore, UAS-LIDAR system causes minimal error in volumetric measurements. It is a highly precise and efficient tool for bulk measurements.

However, the vertical h_i is measured against a ground reference. Normally the ground under a pile would not be measured ahead of time. Therefore, the actual ground model is always unknown in practice. In the case, the ground is estimated based on the points around the pile. For example, the points around Pile A can be found in Figure 30. It may appear a flat ground, and it is in fact possible fit a 2D plane to these points, from which h_i is calculated. However, a zoomed in look from Figure 31 reveals that the ground is far from flat. In addition to the obvious slope, there is undulation on the order of 0.1m to 0.2m. As a result, the error introduced by an uneven ground would be greater than the LIDAR error described in Equation (18).

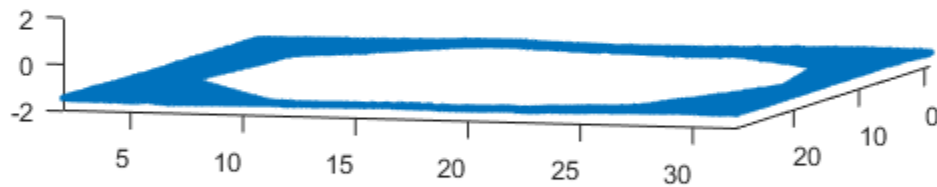


Figure 30 Points around Pile A, with the Pile Removed

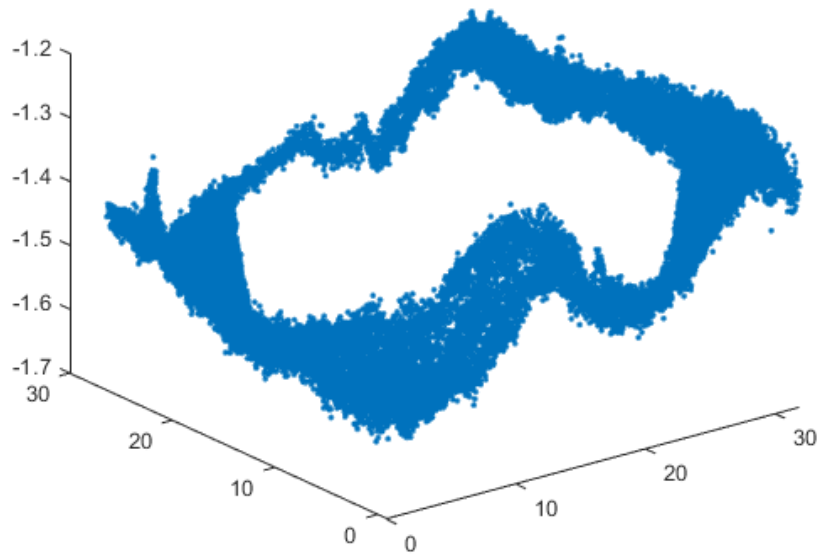


Figure 31 Points around Pile A (zoomed in), with the Pile Removed

The uneven ground would be a dominating error source to any absolute volumetric measurement, but it is not a unique error to UAS-LIDAR. Commercial software (such as Bentley MicroStation) does not rely on a flat ground assumption with sparse GNSS survey points. There have been different models developed to account for that, which can apply to UAS-LIDAR point cloud as well. More details will be provided in the following section.

Without accounting for the ground model difference, the Volumetric Measurements between GNSS Survey (reported by NCDOT) and UAS-LIDAR have been listed in Table 5. The difference can be as large as 6% from the greatest pile.

Table 5 Volumetric Measurements of Piles

| Pile | Survey | UAS-LIDAR | Diff % |
|------|--------|-----------|--------|
| A | 360.83 | 370.81 | 2.8 |
| B | 453.40 | 461.69 | 1.8 |
| C | 97.72 | 95.95 | -1.8 |
| D | 13.60 | 13.23 | -2.7 |
| E | 343.59 | 346.54 | 0.86 |
| F | 920.83 | 865.75 | -5.98 |

The UAS-LIDAR results from Table 5 are based on using a 0.1 m grid size. As aforementioned, even with a small pile (3m by 3m base), it results in 900 grids. Although it causes little extra effort to process in automatic programs, it could be a significant burden in any manual operations, such as user input into commercial software, are required. Therefore, it is of interest to NCDOT to test the same method with larger grid size and fewer grids. As shown in Figure 32, a 0.5m grid size results far less (25 times) samples.

As expected, a larger grid size affects the smaller piles more. Table 6 shows that Pile D sees the greatest difference between two grid sizes, which is the smallest pile. Figure 33 further elaborates the differences among different grid sizes. With a 0.5m grid size, the error can be as large as 1.8% in a small pile (~13 cubic yards).

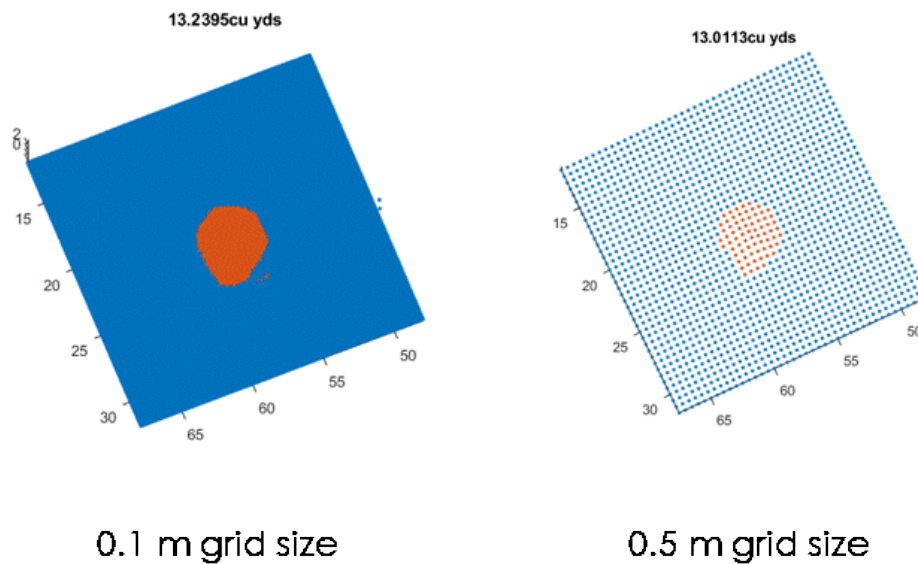


Figure 32 Sampling a Pile with Different Grid Size 0.1m vs 0.5m

Table 6 Volumetric Measurements of Piles with Different Grid Sizes

| Pile | UAS-LIDAR | Diff% (0.5 m vs. 0.1m) |
|------|-----------|------------------------|
| A | 370.81 | 0.48 |
| B | 461.69 | 0.006 |
| C | 95.95 | 0.15 |
| D | 13.23 | 1.8 |
| E | 346.54 | 0.017 |
| F | 865.75 | 0.03 |

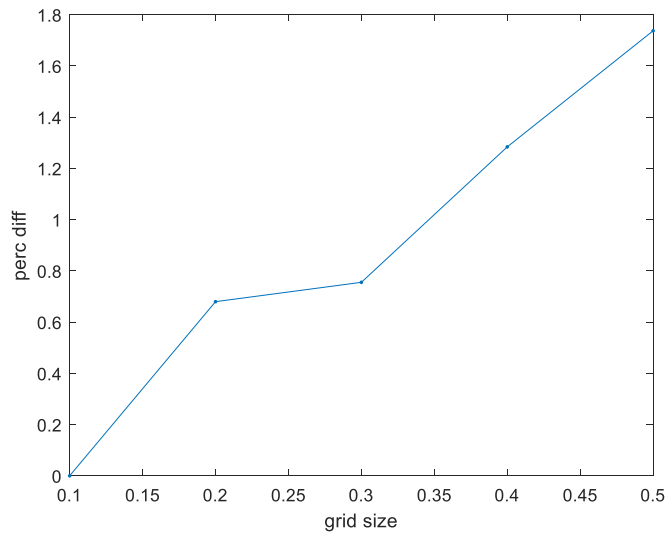


Figure 33 Difference in Volume of Pile D with Different Grid Sizes

The point clouds from 2020 and 2021 have been illustrated in Figure 34, with 2020 in green and 2021 in red. On fixed structures, such as the buildings on the back, both point clouds agree with each other within the nominal error level (centimeter-level). It indicates that there is minimal systematic bias in year-to-year comparison. The change of all the piles can be observed with different colors. Both point clouds have been converted into the NC State Plane system, and can be viewed and compared in Lastools or MATLAB.

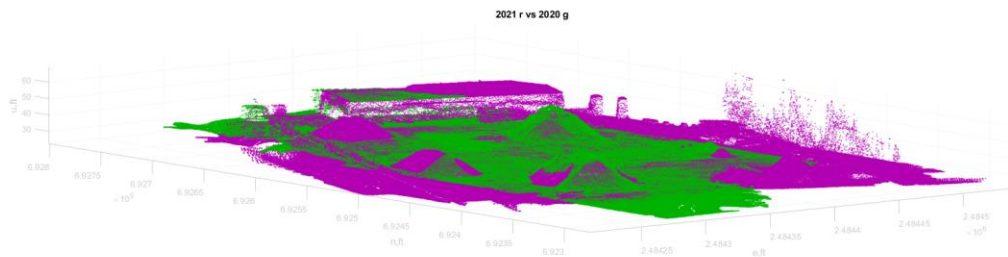
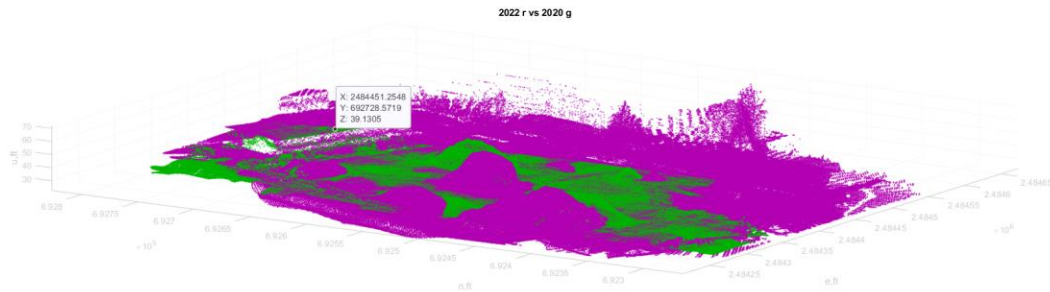


Figure 34 Difference in Point Cloud (2021 Red vs. 2020 Green, NCPS, ft)

4.4.3 Dataset 3 (March 2022)

As suggested by NCDOT, a third dataset was collected in March 2022. This dataset is used as an additional data point to illustrate the change of volume of piles, and to better understand the differences between UAS-LIDAR and GNSS survey.

Similar to Figure 34, the comparison of 2022 vs. 2020 can be found in Figure 35. It is also verified that the point clouds agree with each other on fixed structures within the nominal error level (centimeter-level), which means minimal systematic error from 2020 to 2022.



which only took a few seconds to collect in the flight. When all the LIDAR points were used to compute the volume in TIN model, the result was 310.45 cubic yards (10% smaller).

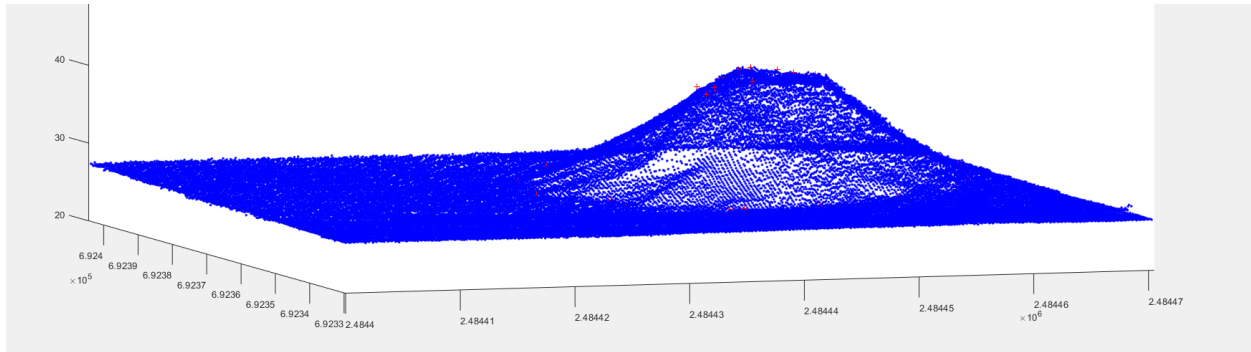


Figure 36 NCDOT GNSS Survey (Red Dots) vs. UAS-LIDAR Point Cloud (NCPS, ft)

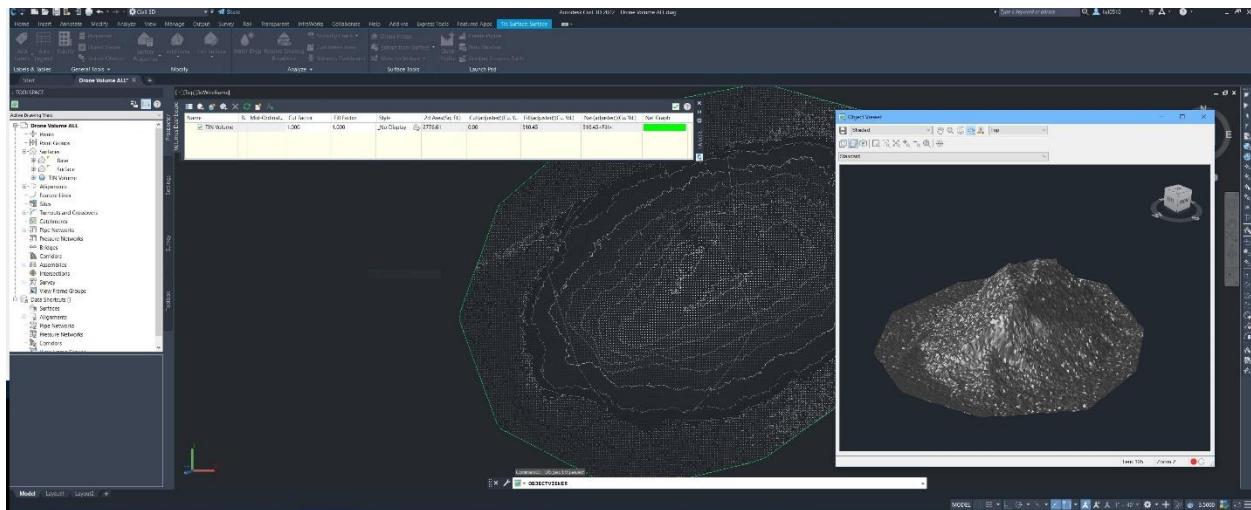


Figure 37 TIN Model in Civil 3D (Courtesy from Dr. Yilei Huang, ECU)

Although volumetric measurements do not rely on imagery of the piles, it was suggested by NCDOT that it would be much more convenient for users to have imagery-based surface or texture in addition to a 3D point cloud or model. The low-cost LIDARs onboard small UAS typically do not have color-based returns, which means a colored surface would not be directly available on these point clouds. However, there is a synchronous IDS uEye camera onboard the ECU UAS system. As discussed in Chapter 3, every image from this camera has a GPS time tag, which means that the position and orientation of the UAS and the camera is known at the moment where each image was taken. For example, an image from the IDS camera collected as

part of dataset 3 can be found in Figure 38. It shows pipes piled near the fence of the maintenance yard. Pipes instead of piles are used in this example since they are more visually distinguished than piles.



Figure 38 Image over the Pitt County Maintenance Yard, from Synchronous Camera

The IDS camera and lens had been calibrated ahead of the flight. With known location and orientation of the camera, the image can be directly mapped onto the 3D point cloud of the pipes. Each point in Figure 39 has 3D coordinates in East, North, Up directions, referenced to the GNSS antenna on the ground, and a RGB color extracted from the image.

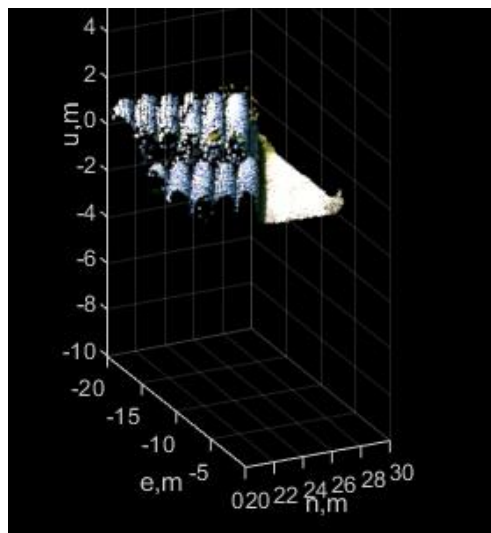


Figure 39 3D Point Cloud with Imagery Texture Superimposed

4.5 Summary

- UAS-LIDAR is very effective at measuring volume of piles.
 - The geo-registration accuracy is more than enough for volumetric measurements. (1% volume error for small piles, less error for larger piles)
 - Data collection is quick. (a few seconds each pile)
 - There is little systematic bias from a low flight.
 - UAS-LIDAR can provide precise measurement on change of volume over a long time.
 - Imagery-surface can be super imposed on the point cloud if available.
 - UAS could fly at higher altitude or higher speed, since less points or greater grid size are acceptable.
 - Absolute accuracy depends on the model used.
- UAS-LIDAR can measure buildings and pits effectively as well.
 - It cannot measure surface of still water.
- UAS-LIDAR can measure road surfaces as well (to be included in the next chapter).
- UAS-LIDAR vs. GNSS-based survey.
 - Both offer similar measurements and accuracy on individual points.
 - UAS-LIDAR data collection is much faster.
 - UAS-LIDAR point cloud is much denser, and can lead to different volume estimates (10%).
- UAS-LIDAR vs. SFM
 - UAS-LIDAR does not require any GCPs over the worksite, but can benefit from having one or few for validation purposes.
 - UAS-LIDAR data collection is faster.
 - UAS-LIDAR can collect data over low-texture surfaces (sand or soil).
 - Usually UAS-LIDAR does not create an imagery surface.
 - Image can be superimposed on point cloud.

Ch 5 Case Studies for Disaster Management

Applications of both the downward-looking and the side-view UAS-LIDAR systems were explored in disaster management applications. Since the performance of the systems are well understood from the construction-related projects, these case studies are more focused on potential applications of the UAS-LIDAR technology, and less on error analysis. The first three cases were based on the downward-looking system and the last one is with the side-view system. The flight, data collection and processing procedures have been defined in Chapter 4, and will not be repeated in this chapter.

5.1 Seashores and Water Surface

As discussed in Chapter 2, UAS-LIDAR is expected to be an efficient tool for scanning a long seashore. It is expected capture all the land-based features, such as structures or trees with the accuracy discussed in Chapter 3. However, whether it can capture any water surface was unclear. Chapter 4 showed that UAS-LIDAR did not get good returns from a smooth water surface. It was likely due to reflection of the laser beam. It was realized that the reflection of a single laser beam over water depends on the following aspects:

- 1) Roughness of water surface
- 2) Water turbidity
- 3) Laser beam size and footprint size of a single beam
- 4) Laser beam incidence angle
- 5) Laser power and distance

In other words, it is possible for UAS-LIDAR to measure sea water surface with waves. However, there is a tradeoff in terms of UAS altitude. A high-flying UAS-LIDAR would have a wider footprint, but lower power density. There have been few studies in literature on whether a UAS-LIDAR can measure the sea water surface or waves in practice.

Luckily, the SICK LIDAR used in the ECU system has a wide laser beam (0.4°), since it was designed to work in a dusty environment. At a distance of 42m, it has a footprint of approximately 1 ft. For a very calm sea surface with wave size as small as 1 ft, the LIDAR needs to be at least 42m above the water so that an entire wavelength can be covered by the footprint. It helps to capture returns from the water surface. For waves with greater roughness on the surface, the flight altitude can be lower.

In September 2021, the ECU team attempted a flight over open water in Albemarle Sound, NC. The UAS took off and scanned the seashore area first. It then flew into the sound and hovered over the water at 40-60m above water. It scanned the water surface in a circular flight pattern before returned to launch position. An airborne image collected with the UAS can be found in Figure 40. A narrow canal leads into the sound in this area. The canal has relatively calm water, which could not be measured by the LIDAR. Figure 41 shows the point cloud that includes the canal (blank), the seashore, the trees and the water surface in the sound. The

wave height forecast of the sound was 1 ft. A dense point cloud can be found over the water surface. Therefore, it confirms that the UAS-LIDAR can in fact scan a water surface with small waves.

The 3D point cloud combined with the imagery can be used to estimate change in water level and any damage to the seashore after major disasters.



Figure 40 UAS Image over Albemarle Sound, NC

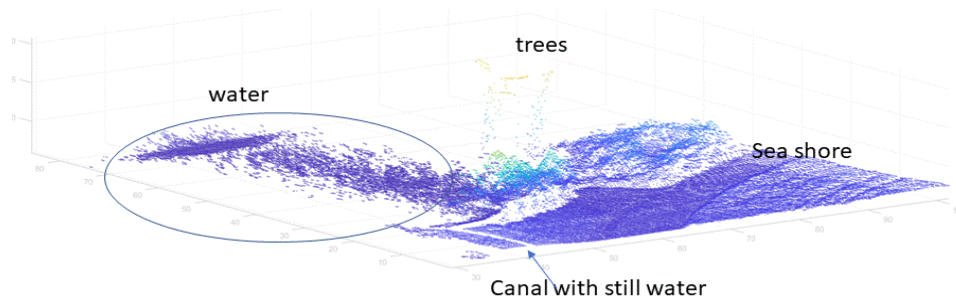


Figure 41 3D Point Cloud over Albemarle Sound, NC

5.2 Road Surface

The UAS-LIDAR can also scan road surfaces efficiently. Even with a smooth steady flight pattern suggested in Chapter 3, the UAS can still scan the road surface while moving at 5m/s. The dataset was collected over a part of a rural road (approximately 100 m long) on the campus of East Carolina University, in Greenville, NC, as shown in Figure 42. The point cloud can be found in Figure 43. It has been rotated to reflect the surface of the road in Figure 44.

The point cloud is relatively precise. It was observed in this dataset that the random error before down sampling had 1 sigma of 5cm. The largest error magnitude observed as 0.14m. After down sampling, the error has 1 sigma of 1-2cm typically.

Therefore, it is possible to detect centimeter-level elevation changes on the road surface with UAS-LIDAR. The 3D point cloud combined with the imagery can be used to estimate any damage to the road surface after major disasters.



Figure 42 Image of a Rural Road in Greenville, NC

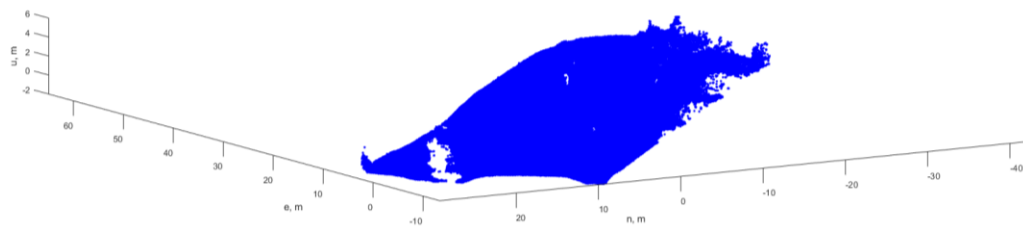


Figure 43 3D Point Cloud of a Rural Road in Greenville, NC

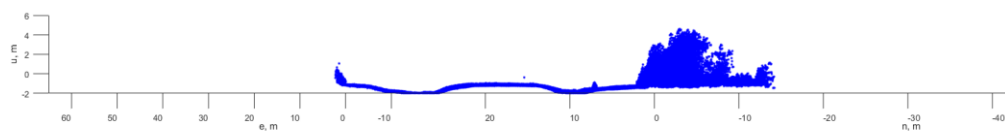


Figure 44 3D Point Cloud of a Rural Road in Greenville, NC, Side View of the Road Surface

5.3 Riverbed

The third case was based on data collected near Town Creek in Greenville, North Carolina. The UAS-LIDAR system scanned a stretch of the creek (approximately 100 m long) multiple times, where a pile of rock stairs was built on a dry riverbed as part of the creek drainage system. An image of the test site from the UAS camera is shown in Figure 45.



Figure 45 UAS Image of Town Creek

In this dataset, the collected raw point cloud was down sampled using a grid size of 0.05 m, to gain a more detailed view of the creek drainage system. The processed point cloud of the site with rock stairs is presented in Figure 46.

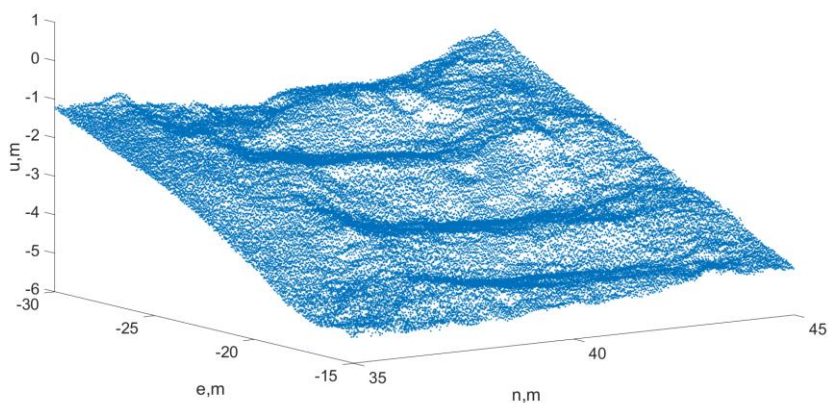


Figure 46 Point Cloud of Rock Stairs at Town Creek

In other datasets included in this report, the point cloud of the reference antenna has always been used as a truth reference to assess the accuracy and validate the point cloud. Such validation is usually sufficient for smooth surfaces, such as piles and road surfaces. However, the surface of the riverbed and the creek drainage system is more complex. The rock stairs have irregular surfaces, which could lead to additional errors in UAS-

LIDAR. Therefore, additional truth reference on the rock stairs will be provided. A TLS scan of the test site was performed separately, reported in [Cooper21], where a Leica ScanStation P40 with a 3 mm (1σ) accuracy at 50 m was used. The TLS point cloud was used as a true reference for the comparison with a vertical profile of down-sampled UAS-LIDAR point cloud. As shown in Table 7, the difference between the measurements from the two sensors was 0.055 m in 1σ with a 0.064 m mean, and the maximum observed difference was 0.24 m. The vertical profiles measured by the TLS and UAS-LIDAR are illustrated in Figure 47, where deviation between the two profiles can be seen at a few locations. It is likely due to the changes in horizontal locations that can contribute to vertical errors in UAS-LIDAR measurements, as previously discussed. At this test site, the rock stairs have irregular rock shapes with steep slopes on the edge, resulting in a substantial level of mean and maximum error. Nevertheless, the overall error is still consistent with the error model from Chapter 3.

Table 7 Measurements Difference of Rock Stairs between TLS and UAS-LIDAR

| TLS-UAS Difference | Mean | 1σ | Max |
|--------------------|---------|------------|--------|
| Rock Stairs | 0.055 m | 0.064 m | 0.24 m |

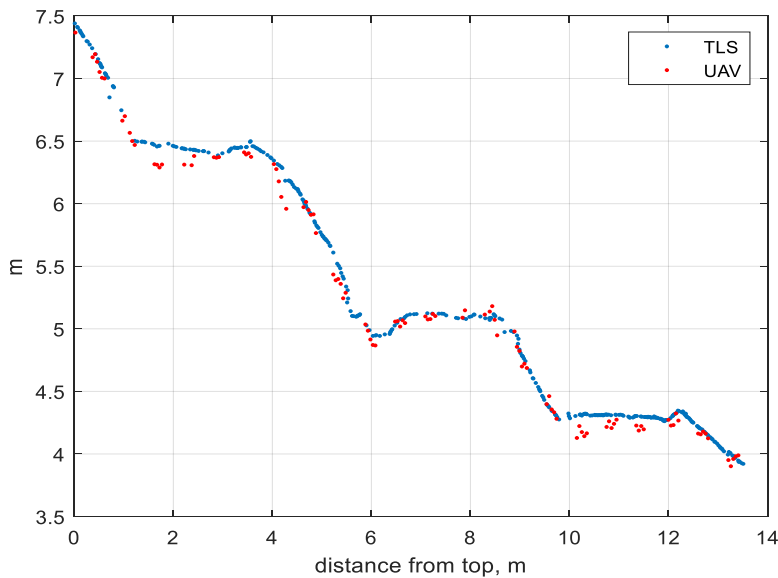


Figure 47 Comparison of Point Cloud Vertical Profile of Rock Stairs between TLS and UAS-LIDAR Measurements

The 3D point cloud combined with the imagery can be used to estimate any change to the riverbed and drainage system after major disasters, although it may not be able to observe the water surface in the river.

5.4 Bridge

The last case is unique, as the data was collected using the side-view UAS-LIDAR system. As aforementioned, this system was designed to scan vertical targets, such as bridges. The dataset was obtained from scanning a rural bridge in Pitt County, NC, suggested by NCDOT, in November 2021. An image of the bridge can be found in Figure 48. An area in the middle of the bridge is highlighted in this figure. Point clouds from this area will be shown in this section.

The side-view system can produce a dense point cloud at 300,000 points per second, which is even more efficiently than the downward-looking system. In practice, it takes less than a minute to get a dense point cloud of the 20m by 20m area.

As discussed in section 3.2, since it provides a side-view point cloud at a great range, it can be more sensitive to systematic errors caused by heading errors. Even if the heading error is within the spec of the navigation device, such as a 0.1° , it may still cause substantial horizontal errors. Additional steps have been taken to limit such errors, such as reducing the range from 100m to 50m, and more rigorous calibration procedure of boresighting and heading. In addition, the 3D point cloud of the reference antenna can provide additional validation of the accuracy. As shown in Figure 49, centimeter-level accuracy was observed on the antenna. Figure 50 illustrates the point cloud of the bridge collected during the flight. The structure of the bridge is clearly visible in the point cloud. Since it is geo-registered, the dimension and location of any components of the bridge, such as the beam and the piers, can be directly measured.

The point cloud is precise, since the random errors are expected to be at centimeter-level in both horizontal and vertical directions. However, the potential heading angle bias could leave a small horizontal systematic error, which is at or above centimeter-level. For example, with 0.1° heading error there will be a 0.087m horizontal bias at 50m away. The bias will only be 0.035m at 20m away. Since it is feasible for the UAS-LIDAR to fly relatively close to the bridge, it is possible to limit the systematic error.

The ECU team also tested the downward looking system on the same bridge. This system had to fly over the bridge. To ensure the safety of the UAS and the vehicles on the bridge, the UAS altitude was at least ~ 20 m over the bridge. It could only measure the surface of the bridge with moving vehicles on it. As shown in Figure 51, it does not provide much information about the structure.



Figure 48 Bridge on South Grimesland Bridge Road, over Tar River in Pitt County, NC (Google Map)

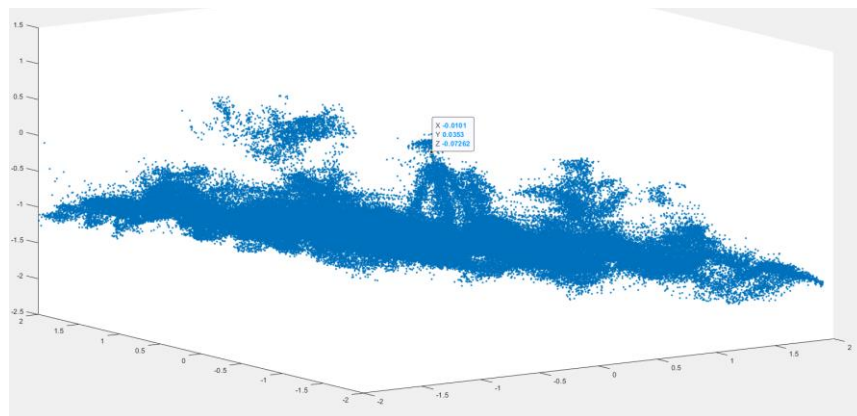


Figure 49 Point Cloud of Antenna, for Validation

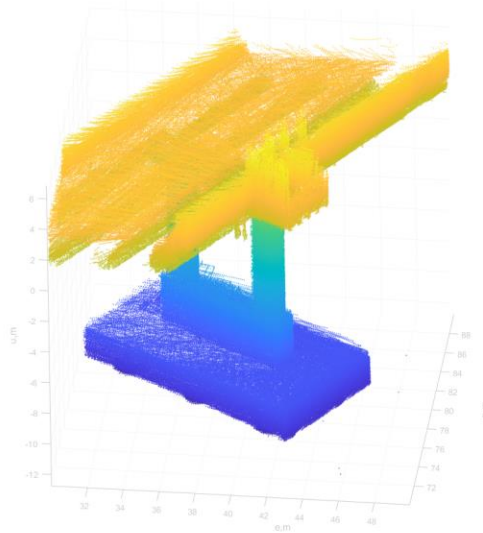


Figure 50 Point Cloud from the Side-View UAS-LIDAR, Flight Part 1

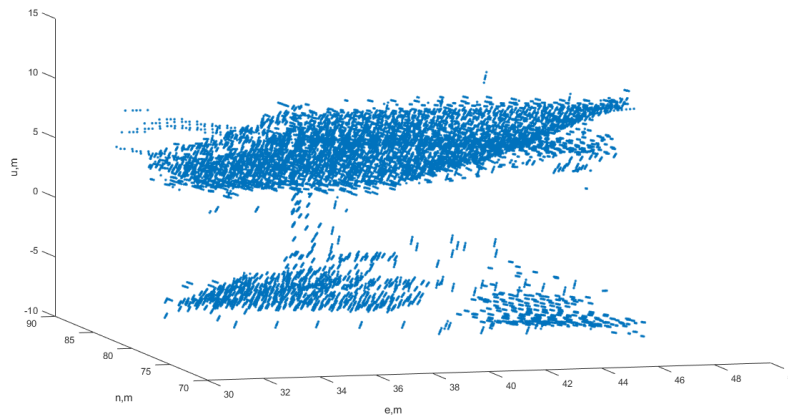


Figure 51 Point Cloud from the Downward Looking UAS-LIDAR

After correction, all the points from the whole flight can be integrated into one point cloud, as shown in Figure 52. The 2D view of the columns and the pier can be extracted from this point cloud, which can be found in Figure 53 and Figure 54 respectively. They are compared against the structure design of the bridge. As shown in Figure 55, the distance between the centers of both columns is designed to be 20 ft. The columns in Figure 53 are measured in the point cloud, which are 6.125 m or 20.09 ft apart. The distance between the centers of the left and the right piers is 33 ft. The piers in Figure 54 are 10.099 m or 33.13 ft apart, as measured

in the point cloud. The estimated systematic horizontal error is 3 cm, 1 sigma, after correction. The estimated random horizontal error is also at 3 cm, 1 sigma, based on the LIDAR performance. The difference between LIDAR point cloud and the design document is within LIDAR error budget.

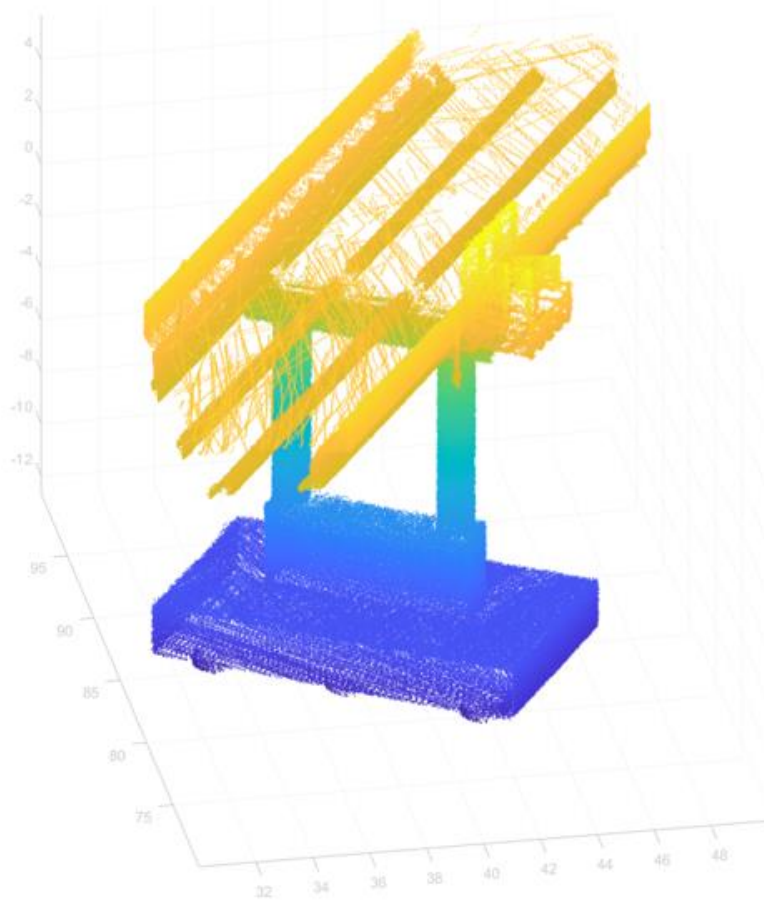


Figure 52 Point Cloud from the Side-View UAS-LIDAR, whole flight

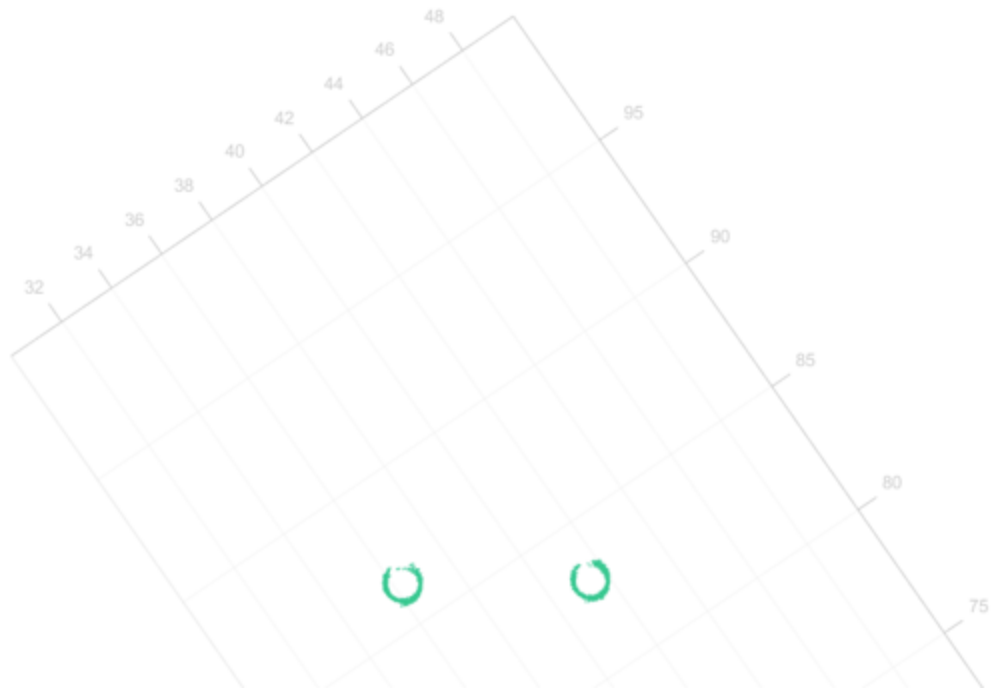


Figure 53 Point Cloud of columns

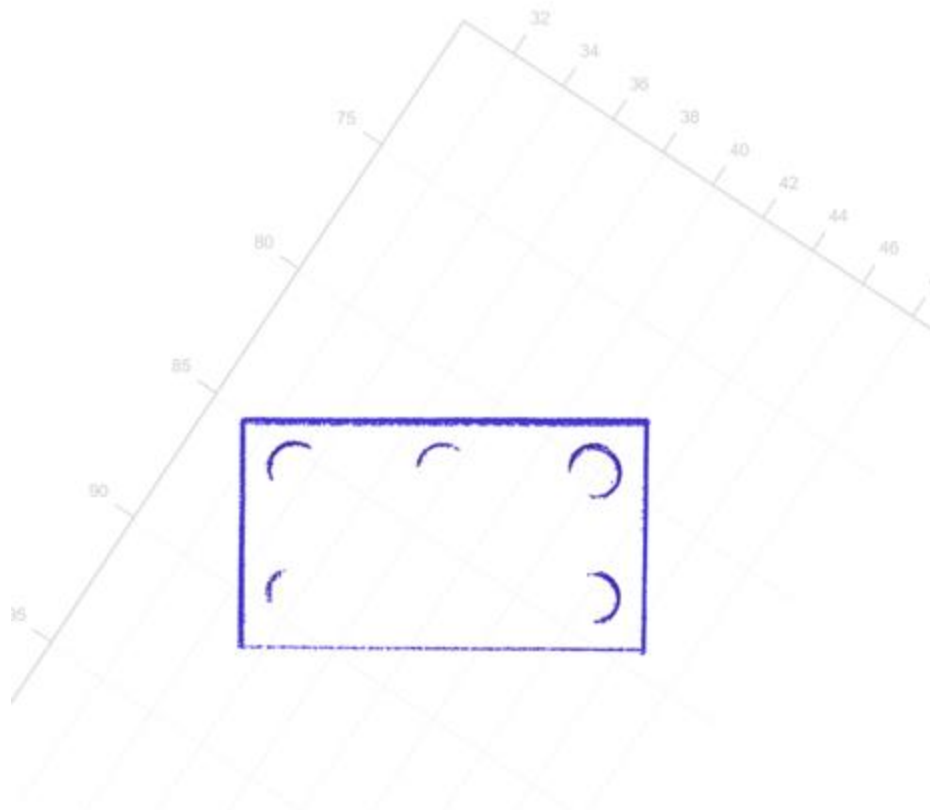


Figure 54 Point Cloud from the Side-View UAS-LIDAR, Flight Part 1

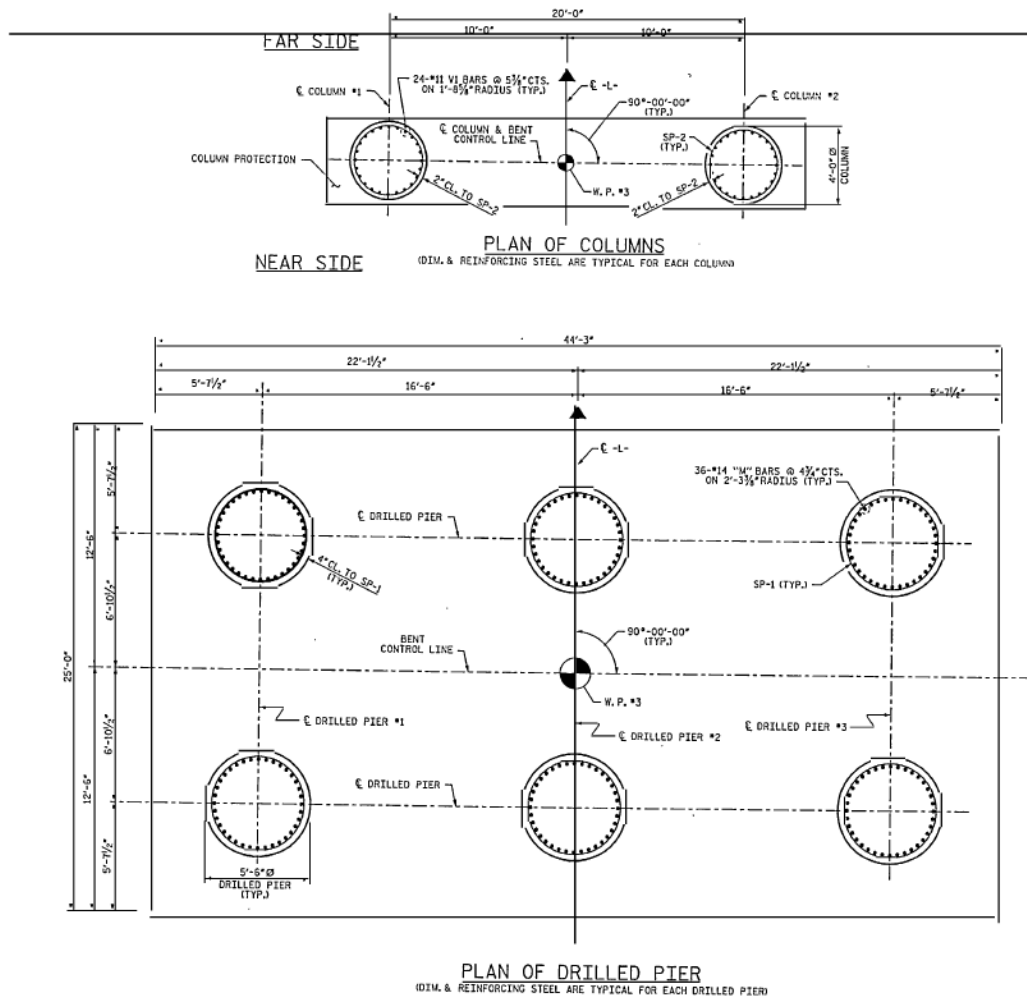


Figure 55 Dimensions of pier and columns, courtesy of NCDOT

5.5 Summary

The downward-looking UAS-LIDAR system can be used to measure 3D models of water level (with waves), road surface and riverbed/drainage systems. It may be used to detect changes caused by major disasters. However, the side-view system is more effective in taking 3D measurements of horizontal structures, such as bridges.

Ch 6 Emerging Technologies

Although camera/SFM has been the most popular UAS-based sensing technology in construction management and disaster management, a major challenge still remains, which is the dependence on GCPs. The quality of SFM point cloud is directly related to the density and accuracy of GCPs. A dense network of GCPs (such as 40 per squared kilometer) have to be established and surveyed ahead of the flight, to ensure the accuracy of geo-registration.

With today's technologies, small UAS could carry high-quality GNSS receivers that are capable of RTK on the fly, or recording data for post processing. Post-Processed position through PPK or PPP could be used to help improve the accuracy with limited GCPs. [Pix4D17] noted that RTK and PPK could both produce centimeter-level accuracy. The data with PPK was more accurate than that of RTK, but less than using GCPs, especially on the vertical direction.

Although the approaches above claimed that GCPs were not necessary if PPK position were available for the cameras, the point cloud could not be directly registered with any GCPs. SFM with PPK can produce precise point cloud only in the camera body frame. Since high-quality IMUs have not been commonly available for small UAS, these systems cannot directly place the point cloud in a world frame. An additional step is needed to align the point cloud in the correct direction, often by using a few GCPs.

In terms of geo-registration, the main focus is to reduce the number of GCPs with RTK and PPK, not to eliminate them.

6.1 SFM with Precise Camera Position

The main manufacturer of commercial UAS DJI has followed the strategy of fewer GCPs, since it reduces set-up time [DJI19]. The new UAS solution supports both RTK and PPK. However, since the commercial DJI UAS is closed-interface proprietary system with a high cost, it has not been used in the project. Instead, a low-cost open-interface system was built for research and demonstration purposes.

6.1.1 Open Interface System

The ECU team constructed an open-interface system that includes:

1. A video camera
2. PPK-capable GNSS receiver and antenna (onboard)
3. PPK-capable GNSS receiver and antenna (ground, optional)
4. A synchronization mechanism (onboard)
5. Airframe with a sensor enclosure.
6. PPK software
7. SFM software

The camera is required to capture and save images at a high frame rate. A GoPro Hero 7 was selected for this purpose. It is equipped with a fisheye lens to capture larger areas. It has a 240 frame per second (FPS) rate, which had been independently verified using LED-based timing circuitry by the ECU team.

The onboard and ground GNSS receivers were the U-blox F9P chip embedded on the U-blox C099-F9P development board. They are low-cost and capable of RTK/PPK. In practice, only PPK solution generated from recorded data is needed. The PPK solution was produced in an open-source library RTKLIB. More details of the algorithm behind the GNSS PPK solution can be found in [Krebs22]. GNSS data were recorded using Raspberry Pi III computers. The whole system was supported by 3.7V lithium batteries, which are independent of the UAS power supply.

The images were synchronized to GPS time via an onboard timing mechanism, which is based on LEDs driven by the GNSS receiver. The details of this system can be found in [Hill22].

A 3D-printed enclosure is used to house all the onboard components (Figure 56). It can be attached to any UAS with sufficient payload capability. As shown in (Figure 57), it has been attached to a DJI Inspire Pro 2.

The SFM software selected is the Agisoft Metashape, although other commercial and open-source options are available as well.

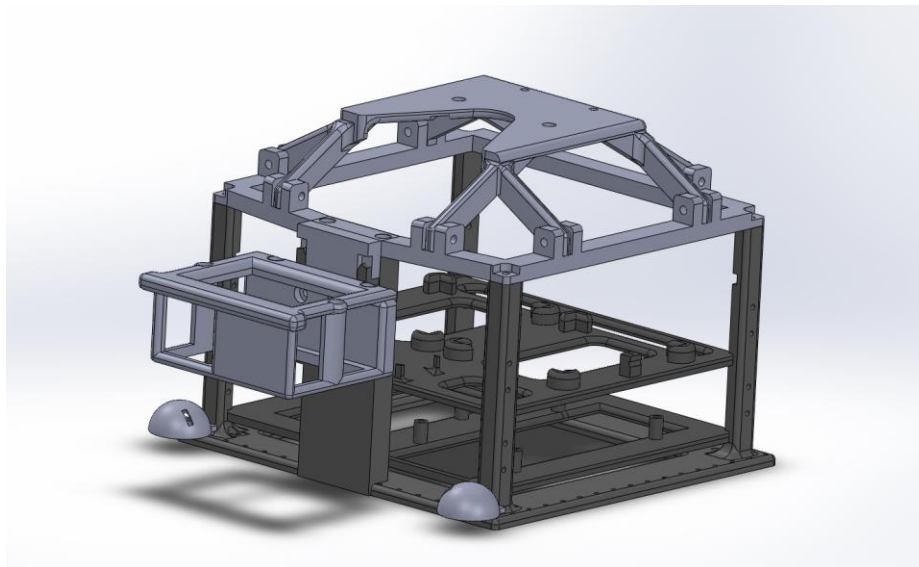


Figure 56 UAS Enclosure for SFM



Figure 57 Sensor Enclosure Attached to a DJI Inspire Pro 2

6.1.2 Performance

To validate the geo-registration accuracy, a test flight was performed in March, 2022. The canvas targets introduced in Chapter 3 were modified to have checker board-like patterns on the surface. Both targets are placed at a short distance away from one another. Both are identified with different colors, one in black and one in blue, as shown in Figure 58 and Figure 59 respectively. The point cloud was processed in Agisoft Metashape. Figure 60 shows the screenshot of an intermediate step from Agisoft, which displays the pose of camera from all the images used in SFM. The position of the camera was measured with PPK and provided to Agisoft, whereas the orientation was calculated by Agisoft. As aforementioned, the orientation of the camera and the point cloud is relative, and does not represent the actual orientation in a world frame.

The checker board pattern included a lot of corners, which are used as point features. The location, physical dimensions and patterns (corners) of both targets were carefully measured and used as a truth reference. Based on that, the performance of the point cloud, including accuracy and precision were evaluated. For example, Figure 61 illustrates the points identified on the corners of the checker board pattern.

The location of all the points from SFM were compared against that from truth reference. It was found that the position error all these points range from 4mm to 8mm (1σ). They are consistent with the precision reported in literature, as discussed in Chapter 2. However, this only reflects relative precision of the measurements. Since there is no GCPs involved at this stage, the point cloud could not be directly registered to a world frame. If a user is only interested in relative measurements, such as dimensions and sizes, SFM from this system alone is sufficient. Otherwise, GCPs have to be introduced.



Figure 58 UAS and Calibration Targets.

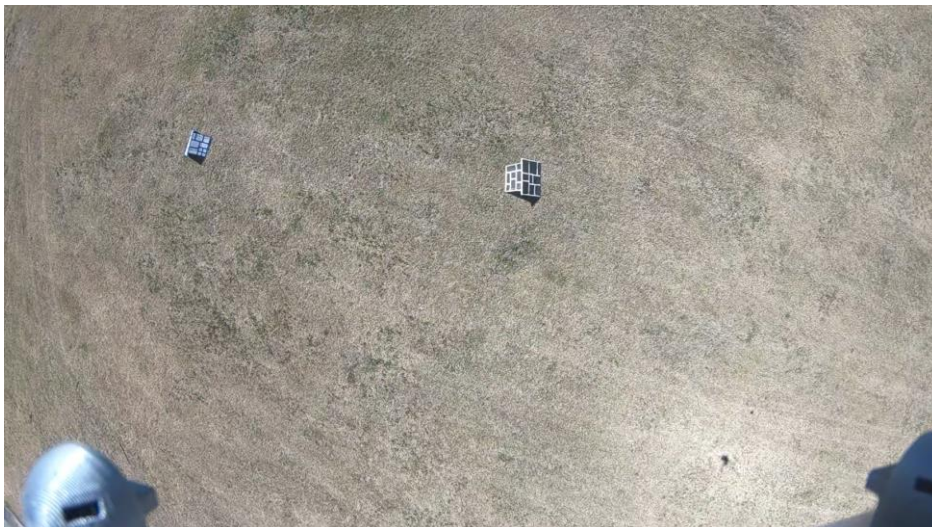


Figure 59 Targets as Seen by UAS

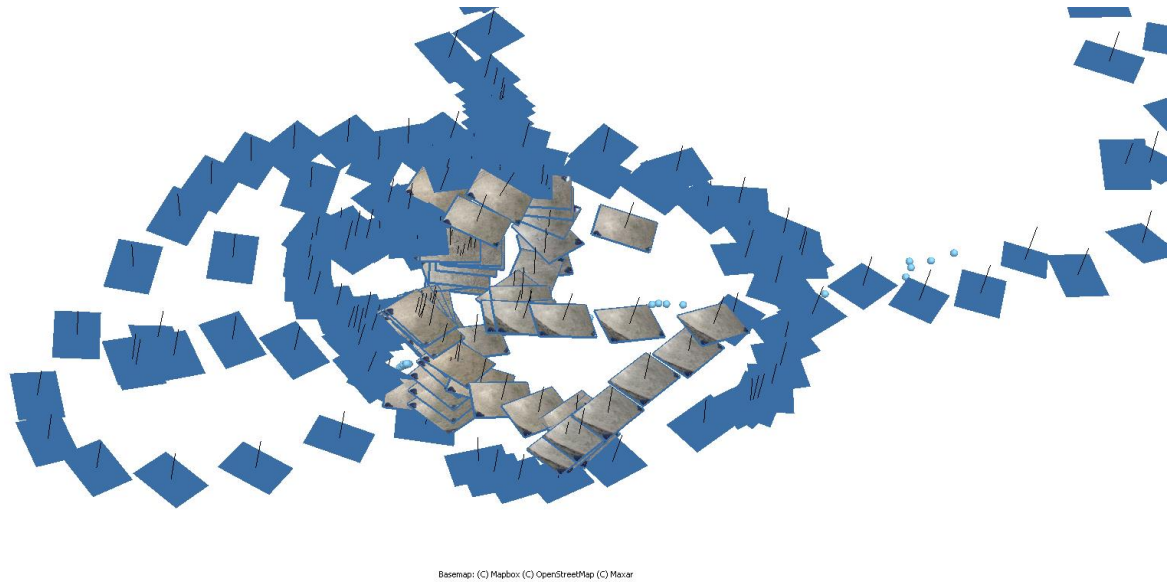


Figure 60 Location of Camera Estimated by Agisoft Metashape

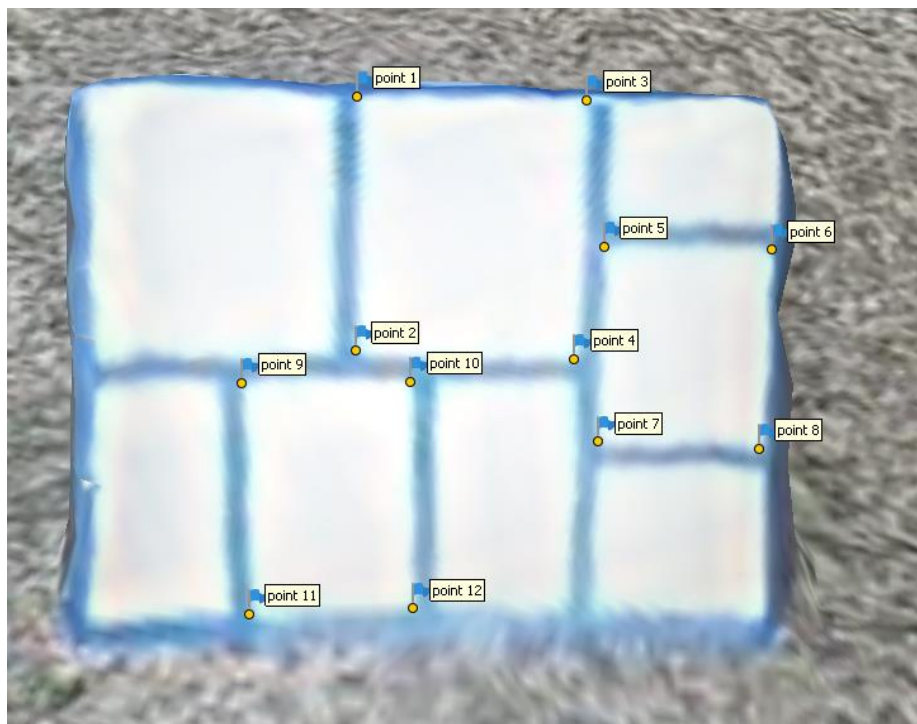


Figure 61 Target One (Side A) Points Selected for Analysis.

6.2 Comparison of SFM and UAS-LIDAR Point Clouds

In addition to SFM, the downward-looking UAS-LIDAR was also used to collect a point cloud. The point cloud of a target from both systems can be found in Figure 62. The geo-registration error for a target has

a standard deviation of approximately 0.04 m, which is close to the UAS-LIDAR ranging noise level. Therefore, it is concluded that there is a strong agreement between SFM and UAS-LIDAR models for each target after geo-registration. In general, the SFM point cloud has higher density and resolution than UAS-LIDAR. The targets in the SFM point cloud have smoother surfaces than those from UAS-LIDAR, which indicates that SFM offers higher relative precision as well. For example, the SFM relative error estimated in this flight test is below 0.01m, whereas the UAS-LIDAR error estimated in Chapter 3 is below 0.1m.

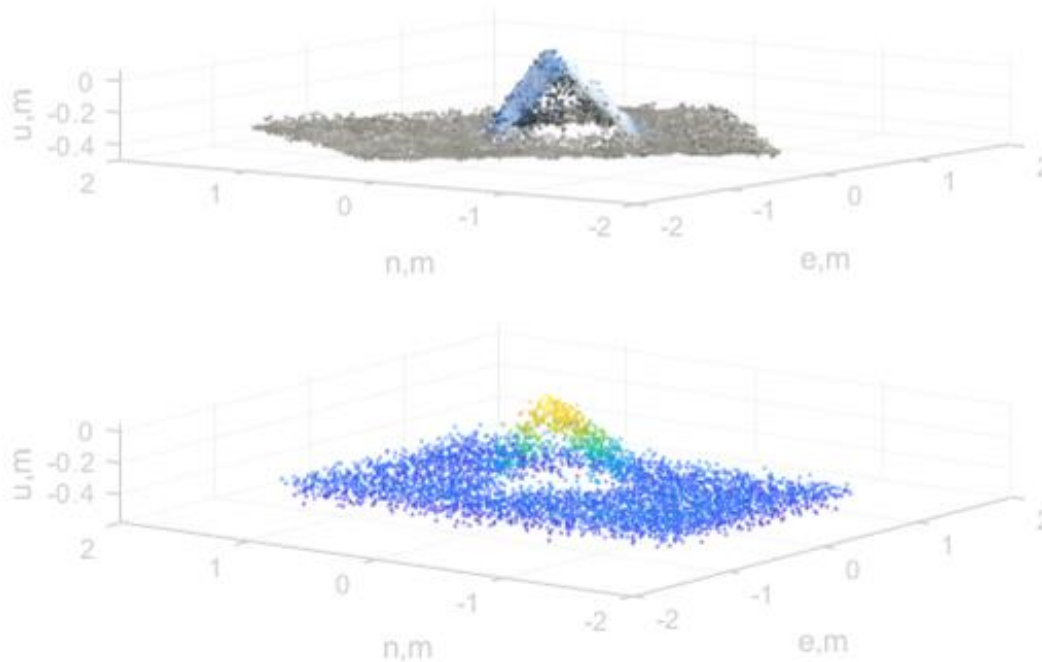


Figure 62 SFM (Top) vs. UAS-LIDAR (Bottom) Point Cloud

The limitation of SFM is also obvious. Even with PPK, it would still need GCPs. In this case, the UAS-LIDAR point cloud can be used as GCPs to geo-locate the SFM point cloud. However, if both targets are used simultaneously as GCPs, the comparison shows a drift between both targets in the SFM point cloud. One of the targets would have a horizontal bias of approximately 0.1 m in geo-registration. Since the UAS-LIDAR does not have large systematic errors, as proved in Chapter 3, the horizontal bias is likely in the SFM point cloud. It is likely because there is a large gap between both targets covered by grass, as can be seen in Figure 59. This space does not have clear visible texture like the checker board, which results in less accurate point cloud. The SFM point cloud could be improved by adding more texture and GCPs between the targets. It is noted from this dataset that SFM with PPK may still need a few GCPs for practical reasons.

6.3 Integration of SFM and UAS-LIDAR Point Clouds

The integration of SFM (with or without PPK) and UAS-LIDAR can be accomplished using commercially available software. The following steps have been defined for Agisoft and Lastools, but are applicable to other options as well:

- 1) Use Agisoft Metashape to align images and prepare them for a 3D point cloud.
- 2) Use Lastools to pre-process the UAV LIDAR point cloud.
- 3) Create markers (geo-referenced targets) from LIDAR and import them into Agisoft.
- 4) Use Agisoft to geo-register 3D imagery point cloud.

Ch 7 Recommendations to NCDOT

7.1 Comparison Among Different Technologies

The following Tables demonstrate the comparison among three technologies, UAS-LIDAR, traditional SFM and SFM with RTK/PPK. The quality of data product (mainly the point cloud); the requirement and constraints on flight pattern, environment and the surface; the cost to acquire and to operate them; and potential applications. They are based on discoveries made with cases and literature review studied in this project. In the following tables, **green** = advantageous; **red** = disadvantageous; black or blank = neutral.

Table 8 Data quality

| | UAS-LIDAR | SFM | SFM-RTK(PPK) |
|---|---------------------|-----------------|-----------------|
| Relative precision (typical values, 1 sigma) | <0.1m | Depends on GCPs | <0.01m |
| Absolute accuracy (typical values, 1 sigma) | <0.1m | Depends on GCPs | Depends on GCPs |
| Resolution / point density | Medium | High | High |
| Visualization | Need external image | Yes | Yes |

UAS-LIDAR is accurate in a world frame (absolute accuracy), but has lower precision and resolution than SFM in general. SFM-RTK(PPK) can be very precise even without GCPs.

Table 9 Requirements on Flight for Data Collection

| | UAS-LIDAR | SFM | SFM-RTK(PPK) |
|-----------------------|------------------|----------|--------------|
| Flight duration | Short | Long | Long |
| Flight pattern | Straight (short) | Circles | Circles |
| Desired flight height | Low | Multiple | Multiple |
| In flight calibration | Yes | No | No |

UAS-LIDAR can cover a large area in a short amount of time, but prefers lower flight. UAS-LIDAR does also benefit from some circular flight patterns, especially during initialization. Long and straight flights should be avoided as they increase systematic error. The requirement for flight for SFM with and without RTK is the same.

Table 10 Constraints on Environment and Surface

| | UAS-LIDAR | SFM | SFM-RTK(PPK) |
|---------------------------------|----------------------------|------------------------|------------------------|
| GCPs or ground reference points | Few, optional | Dense, onsite | Sparse, onsite |
| Light condition | Not sensitive | Sensitive | Sensitive |
| Shadow | Not sensitive | Sensitive | Sensitive |
| Surface texture | Not sensitive | Sensitive [#] | Sensitive [#] |
| Vegetation on surface | Not sensitive [*] | Sensitive | Sensitive |
| Dusty or foggy environment | Not sensitive [*] | Sensitive | Sensitive |
| Still water surface | No | No | No |
| Moving water surface | Yes ⁺ | No | No |

^{*}Wide laser beam and multiple returns are helpful.

⁺Wide laser beam is helpful.

[#]High camera resolution is helpful.

In general, UAS-LIDAR is less sensitive to the environment or the surface texture than SFM. Therefore, it should be considered for low-texture surfaces, such as sand dunes. High-resolution cameras can be used in SFM to compensate for low textures.

Table 11 Cost

| | UAS-LIDAR | SFM | SFM-RTK(PPK) |
|-------------------------|--------------|--------------|--------------------|
| Hardware (typical cost) | High(>\$20K) | Low (<\$10K) | Medium (\$10K~20K) |
| Software | Medium | High | High |
| Operation (Labor) | Low | High | High |
| Post-processing (Labor) | Medium | High | High |

The cost assessment is based on commercial proprietary solutions. The ECU systems have a different cost base. The UAS-LIDAR equipment is more expensive, but may cost less to operate in a long run.

Table 12 Recommended Applications

| | UAS-LIDAR | SFM | SFM-RTK(PPK) |
|----------------------|-----------|-----|--------------|
| Piles | Yes | Yes | Yes |
| Pit with no water | Yes | Yes | Yes |
| Pit with water | No | No | No |
| Buildings | Yes | Yes | Yes |
| Bridge | Yes | No | TBD |
| Road | Yes | Yes | Yes |
| Beach and sand dunes | Yes | Yes | Yes |
| Seashore/riverbank | Yes | Yes | Yes |
| Sea/river water | Yes | No | No |

This table does not include a complete list of applications that NCDOT may be interested in. It is mainly based on the case studies performed in this project. All three systems have limited application over water surface.

7.2 UAS-LIDAR Recommendations

7.2.1 Hardware

The navigation system includes an IMU and a GNSS receiver. Commercial UAS-LIDAR system available today often uses a navigation system that is very similar to the one installed on the ECU system. The typical performance in orientation and position solution can be found in this table:

Table 13 Typical Performance of Navigation System (with GNSS, after PPK)

| | Roll | Pitch | Heading | East | North | Up |
|---------|-------|-------|---------|-------|-------|-------|
| 1 sigma | 0.01° | 0.01° | 0.1° | 0.01m | 0.01m | 0.02m |

There is greater variety in LIDAR, in terms of maximum range, field of view and speed of scan. This table includes the expected performance in terms of synchronization error (vs GNSS), ranging error (centimeter-level) and laser beam angular uncertainty (due to laser aperture, for example). The installation and calibration of LIDAR also affects the quality of data. The lever arm and boresighting between LIDAR and IMU is also considered in this table.

Table 14 Expected Performance of LIDAR, Installation/Calibration and Synchronization

| | Synchronization error | Range error | Beam angular uncertainty | Lever arm X | Lever arm Y | Lever arm Z |
|---------|-----------------------|-------------|--------------------------|-------------|------------------|-------------|
| 1 sigma | 1ms | 0.05m | 0.1°+ | 0.001m | 0.001m | 0.001m |
| | Boresighting Roll | | Boresighting Pitch | | Boresighting Yaw | |
| 1 sigma | 0.01° | | 0.01° | | 0.1° | |

+SICK LD-MRS420201 LIDAR actually has a wider laser beam since it was designed to work in a dusty environment.

The point cloud accuracy is significantly affected by the configuration even with the identify LIDAR and navigation system. There are two factors to be considered: 1) angular errors caused by boresighting and the navigation solution often result in systematic errors or biases in the point cloud; 2) the error in the heading (yaw) direction tends to be greater, both from navigation solution and boresighting. In order to limit biases in point cloud, it would be ideal to avoid the impact of the angular errors as much as possible. The boresighting error levels introduced in Table 14 are similar to those from the navigation system. These levels can be achieved by using calibration targets on the ground.

The downward-looking LIDAR used in this work is a SICK LD-MRS420201 unit, and the side-view LIDAR is Velodyne Puck VLP-16. The SICK LIDAR has approximately 90° field of view. The vertical accuracy of the downward-looking SICK LIDAR is mainly sensitive to laser ranging error and the surface texture, and it is less sensitive to angular errors, especially the heading. Therefore, the downward-looking configuration presented in this work provides reliable vertical measurement with little bias, as shown in Chapter 3. In some cases, the horizontal errors can be mapped into the vertical direction due to slope and texture of the surface.

In theory, both LIDARs can be installed as downward-looking or side-view. However, since the VLP-16 has a 360° field of view, it is a better choice as a side-view LIDAR. The vertical accuracy is only sensitive to errors in roll and pitch angles, which is usually much smaller than the heading errors in boresighting and the navigation solution. The horizontal error, however, can still be significant. As suggested in Chapter 3, the user would need a more rigorous calibration procedure of boresighting before flight, and careful calibration of heading during every flight. Furthermore, the target distance can be limited despite the sensor capability. In other words, only points measured within a certain distance (for example, 50 m) can be used in the final data product.

The impact of UAS flight on these errors will be further explained in the follow subsection.

Table 15 Point Cloud Accuracy of Downward and Sideview UAS-LIDAR

| | Downward (90° field of view) | Side-view (360° field of view) |
|--|------------------------------|--------------------------------|
| | | |

| | | |
|----------------------------------|--------------------------------------|---------------------------------|
| Vertical accuracy sensitive to | Laser ranging, surface texture, roll | roll, pitch |
| Horizontal accuracy sensitive to | roll, pitch, heading | heading, laser ranging, texture |

As shown in the table below, RTK or PPK can be used for UAS-LIDAR. PPK is a better option unless precise position is needed in real time.

Table 16 RTK or PPK for UAS-LIDAR (also applicable to SFM)

| | RTK | PPK (Post Processed RTK) |
|--------------------------------|------|--------------------------|
| Base station | Yes | Optional |
| Datalink required | Yes | No |
| Results available in real time | Yes | No |
| Accuracy | Good | Best |

7.2.2 Flight Control

UAS-LIDAR can cover a large area in a short amount of time. It can be controlled manually or with a pre-configured flight plan. Since a downward-looking UAS-LIDAR can better cover a horizontal worksite, which is more common in NCDOT applications, the flight control of this system will be discussed here.

Table 17 Flight Control of UAS-LIDAR (Downward-Looking)

| | Manual control | Pre-planned |
|-----------|----------------------|-------------|
| Height | <30m | >30m |
| Worksite | Small (100m by 100m) | Large |
| Waypoints | No | Yes |

A manual flight is feasible for a small worksite or at low altitude. At a low altitude, it may be convenient to control the UAS manually, to avoid potential obstacles and hazards (such as trees and buildings). The UAS can directly fly over the worksite, as shown in Figure 63, if LIDAR footprint is wide enough to cover the entire site.

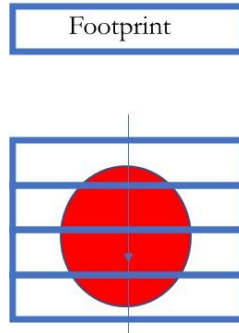


Figure 63 Flight Path over a Single Worksite (Red)

For manual flight, the following steps may be helpful:

Pre-flight

1. Survey the target area.
2. Estimate flight height above ground and above target. Estimate the boundaries of flight ground track.

Onsite

3. Place visual observers on boundaries.
4. Take off and hover at ~15 m above ground.
5. Initialization maneuvers for 3 min: including accelerations in horizontal directions. Make a straightforward flight followed by circular and figure-8 patterns.
6. Fly over calibration targets (optional). The target can be the antenna and the tripod of the ground reference GNSS receiver.
7. Fly over worksite, ~15 m above target, ~5 m/s. Use live camera link if available.
8. Fly over calibration targets (optional).
9. Land and retrieve data.

The UAS can initialize a rough heading from a straightforward flight first. When the UAS is flying in circular (in both directions) and figure-8 patterns, as shown in Figure 64, it exercises acceleration in all horizontal directions (forward, back, left and right). These patterns can be repeated with rotating heading angle and fixed heading angle. With acceleration in horizontal directions, heading error can be corrected with GNSS-PPK. Therefore, it is recommended that the UAS complete initialization maneuvers, which will help improve the initial heading accuracy.



Figure 64 Circular and Figure-8 Patterns

If feasible, the UAS should exercise acceleration in horizontal directions during the entire flight. Heading errors cannot be corrected during maneuvers such as straight steady flight, hovering and rotations. Therefore, these maneuvers should be avoided as much as possible during manual or planned flights. Circular and figure-8 flight patterns will help keep the heading error low through the flight.

If calibration targets, such as the ground reference antenna (as shown in Chapter 4), are available, the UAS could fly over them at the same height as the rest of the flight. Ideally, the UAS can fly over them twice, at the beginning and at the end. If both partial point clouds from the beginning and the end agree with the truth reference (GNSS), they can be used to validate the performance of the entire point cloud.

For pre-planned flight

Pre-flight

1. Survey the target area.
2. Program waypoints and heading, including initial maneuvers and flight over calibration targets.
Fly over worksite, ~15 m above target, ~5 m/s.

Onsite

3. Place visual observer.
4. Take off and hover at ~15 m above ground.
5. Execute flight plan.
6. Land and retrieve data.

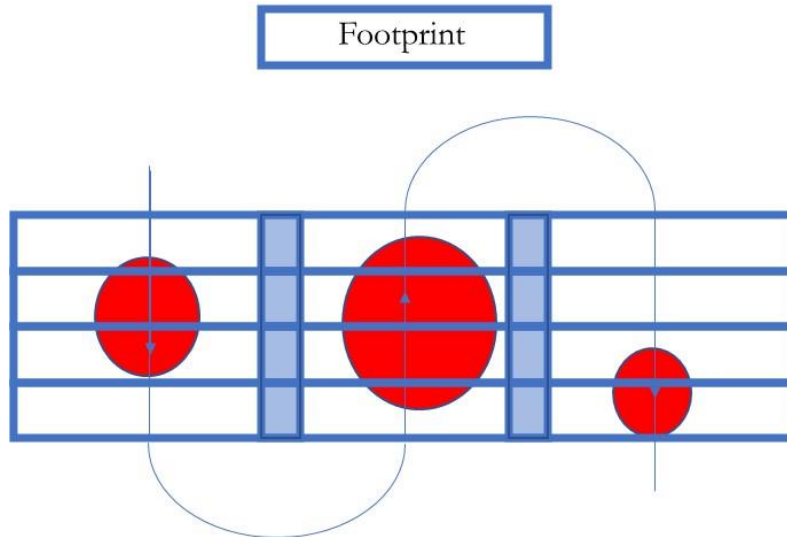


Figure 65 Flight Path over Multiple Worksite (Red) with Overlapped Footprint (Blue Shade)

If there is a large area to cover, possibly with multiple sites, and the UAS can fly at a higher altitude, a pre-planned flight may be more convenient. The flight altitude should be high enough to avoid any obstacles while taking into consideration the ground undulation. The LIDAR footprint on the ground should be calculated ahead of time, based on the altitude and LIDAR orientation. The flight should be planned so that there is small overlap of the LIDAR footprints between adjacent segments, as shown in Figure 65. It is important to keep these overlaps especially when the UAS altitude is high.

Using the error model in Chapter 3, it can be found that the systematic angular errors are mapped onto the point cloud error via distance. Systematic errors are related to UAS orientation, position and time, which means that the errors would be different between different segments of the UAS flight. There could be a bias between the partial point cloud from the same area scanned in two segments of the UAS flight. As shown in Chapter 4, both the downward-looking and the side-view UAS-LIDAR systems could have biases.

The bias could exist in vertical and horizontal directions. They can be observed in the overlapped area between two flight segments. The magnitude of the bias can be used to assess the actual accuracy of point cloud geo-registration. If the biases are constant, they could potentially be corrected.

Although UAS-LIDAR and SFM are often carried by rotary-wing airframes, they can be carried by fixed-wing airframes as well. Although a rotary-wing UAS may be less efficient in carrying payload, which results in less payload capability and shorter distance, it is easier to take off, land in a smaller space, and easier to maneuver at low altitude. Therefore, it is a preferred choice for SFM and LIDAR.

Table 18 Airframe

| | Fixed-wing | Rotary-wing |
|-----------------|------------|-------------|
| Takeoff/landing | Hard | Easy |
| Distance | Long | Short |
| Height | High | Various |
| Maneuverability | Low | High |
| Payload | High | Low |

7.2.3 Processing and Dissemination

The post processing steps are the same for both manual and pre-planned flights, as reported in Chapter

4.

1. Post-process GNSS position and orientation.
2. Synchronize LIDAR and camera to GPS time.
3. Geo-registered raw point cloud in local ENU frame by integrating LIDAR, GNSS and Inertial data.
4. Down sampling to desired horizontal resolution; outliers removed.
5. Convert the coordinates of the data points to target frame
6. Convert the data file into a desired format.
7. Add imagery texture if available.

7.3 Measuring Pile Volume

It was shown in Chapter 4 that the UAS-LIDAR accuracy and resolution is more than enough for volumetric measurements. It is very efficient. It takes seconds to scan a single pile, and only minutes to scan an area of 100m by 100m. It would take 30 min total onsite time for a 2-person team, regardless of the number of piles. It can be even more efficient if the UAS can fly at a higher altitude and a higher speed. After the point cloud is converted into the desired format and coordinate system, the points can be used to calculate the volume of a pile. Here is a potential workflow:

1. Visually select a boundary for the pile in the LIDAR processing software.
2. Export the data of the points inside the boundary.
3. Import the data to calculate volume, for example, in Civil 3D.
4. Choose a model, such as the TIN model in the software.
5. Compute the volume in the software.

Table 19 LIDAR or GNSS

| | UAS-LIDAR | GNSS-Survey |
|-----------------------|---|--------------------------------------|
| Point density | Thousands per pile | Tens per pile |
| Data collection speed | Minutes for a site with multiple piles; 2-person team | Hours for a site with multiple piles |
| Accuracy | centimeter-level | centimeter-level |
| Difference in volume | ~10%, due to point density | |

Based on the cases studied in this work, it is summarized that:

1. UAS-LIDAR is more efficient than GNSS-based survey, with much higher density (resolution) and similar single point accuracy. The total volumetric measurements will be more accurate with UAS-LIDAR because of the density.
2. The comparison between UAS-LIDAR and SFM can be found in section 7.1.
3. Since it can be difficult to place visual observers in UAS-LIDAR flight, the UAS operator can benefit from a live downward video link if available.
4. Since the UAS-LIDAR provides sufficient accuracy and resolution, it can fly at a higher altitude (30m) and a higher speed (>5m/s) to cover a larger area.
5. UAS-LIDAR can measure absolute volume and relative volume change over time. The absolute accuracy depends on the choice of ground model. The relative accuracy can be achieved as long as the same ground model is used over time.

References

1. Agisoft(2019), Tutorial (Beginner level): Orthomosaic and DEM Generation with Agisoft PhotoScan Pro 1.3 (with GCPs). available: [https://www.agisoft.com/pdf/PS_1.3%20-Tutorial%20\(BL\)%20-%20Orthophoto,%20DEM%20\(GCPs\).pdf](https://www.agisoft.com/pdf/PS_1.3%20-Tutorial%20(BL)%20-%20Orthophoto,%20DEM%20(GCPs).pdf)
2. Álvares, J. S., Costa, D. B., & Melo Roseneia Rodrigues, S. d. (2018). Exploratory study of using unmanned aerial system imagery for construction site 3D mapping. *Construction Innovation*, 18(3), 301-320. doi:http://dx.doi.org/10.1108/CI-05-2017-0049
3. Assenbaum, M.. (2018). Monitoring coastal erosion with UAS LIDAR. GIM International. 32. 18-21.
4. Chen, Z., Li, J. and Yang, B., 2021. A strip adjustment method of UAV-borne lidar point cloud based on DEM features for mountainous area. *Sensors*, 21(8), p.2782.
5. Cooper, H.M., Wasklewicz, T., Zhu, Z., Lewis, W., LeCompte, K., Heffentrager, M., Smaby, R., Brady, J., & Howard, R. (2021). Evaluating the ability of multi-sensor techniques to capture topographic complexity. *Sensors*, 21(6), 2105.
6. de Melo RR, Costa DB, Álvares JS, Irizarry J. (2017). Applicability of unmanned aerial system (UAS) for safety inspection on construction sites. *Safety science*. Oct 1;98:174-85.
7. DJI. (2019). Next Generation Mapping – Saving Time in Construction Surveying With Drones. Available: <https://enterprise.dji.com/news/detail/next-generation-mapping>
8. Eschmann C, Kuo C, Kuo C, Boller C, "Unmanned aircraft systems for remote building inspection and monitoring," Proceedings of the 6th European Workshop on Structural Health Monitoring, Dresden, Germany. Vol. 36, 2012
9. FAA. (2016) Part 107 of the Federal Aviation Regulations.
10. Fernandez Galarreta J, Kerle N, Gerke M. UAS-based urban structural damage assessment using object-based image analysis and semantic reasoning. *Natural hazards and earth system sciences*. 2015 Jun 1;15(6):1087-101.
11. Furukawa, Yasutaka. Ponce, Jean. (2019) CMVS. Available: <https://github.com/pmoulon/CMVS-PMVS>
12. GCPS. (2019). Creating Quality GCPs for Mapping Contour Lines. Available: <https://www.groundcontrolpoints.com/mapping-contour-lines-using-gcps>
13. Guan, S. Zhu, Z. (2019) UAS-Based 3D Reconstruction Imagery Error Analysis, *Structural Health Monitoring 2019*, 2019
14. Guan, S.; Zhu, Z.; Wang, G. A Review on UAV-Based Remote Sensing Technologies for Construction and Civil Applications. *Drones* 2022, 6, 117. <https://doi.org/10.3390/drones6050117>
15. Guan, S.; Sirianni, H.; Wang, G.; Zhu, Z. sUAS Monitoring of Coastal Environments: A Review of Best Practices from Field to Lab. *Drones* 2022, 6, 142. <https://doi.org/10.3390/drones6060142>

16. Hashemi-Beni, L.; Jones, J.; Thompson, G.; Johnson, C.; Gebrehiwot, A. (2018). Challenges and opportunities for UAS-based digital elevation model generation for flood-risk management: A case of princeville, north carolina. *Sensors* 2018, 18, 3843.
17. Hamledari, H, Davari, S, Azar, E, McCabe, B, Flager, F, Fischer, M (2018) “UAS-Enabled Site-to-BIM Automation: Aerial Robotic-and Computer Vision-Based Development of As-Built/As-Is BIMs and Quality Control”, Available:
<https://cife.stanford.edu/TR230>
18. Hill, Nicholas. (2022). LOW-COST PHOTOGRAMMETRY SYSTEM FOR GEOREFERENCED STRUCTURE FROM MOTION, MS Thesis, East Carolina University.
19. Howard, John & Murashov, Vladimir & Branche, Christine. (2017). Unmanned aerial vehicles in construction and worker safety. *American Journal of Industrial Medicine*. 61. 10.1002/ajim.22782.
20. James, Mike & Ilic, S. & Ružić, Igor. (2013). Measuring 3D coastal change with a digital camera. 2013. 893-904.
21. Jaud, M., Delacourt, C., Dantec, N. L., Allemand, P., Ammann, J., Grandjean, P., ... Floc'H, F. (2019). Diachronic UAS Photogrammetry of a Sandy Beach in Brittany (France) for a Long-Term Coastal Observatory. *ISPRS International Journal of Geo-Information*, 8(6), 267. doi: 10.3390/ijgi8060267
22. Khaloo, A., Lattanzi, D., Cunningham, K., Dell'Andrea, R., & Riley, M. (2018). Unmanned aerial vehicle inspection of the Placer River Trail Bridge through image-based 3D modelling. *Structure and Infrastructure Engineering*, 14(1), 124-136.
23. Knight, Renee. (2019) LIDAR: Going Beyond Photogrammetry. *Inside Unmanned Systems* May.
24. Krebs, A. (2022). Enhancing GNSS RTK Solutions with Random Sample Consensus, MS Thesis, East Carolina University.
25. Lee, K. W., & Park, J. K. (2019). Comparison of UAV image and UAV LiDAR for construction of 3D geospatial information. *Sensors and Materials*, 31(10), 3327. doi:10.18494/SAM.2019.2466
26. May, N. C., & Toth, C. K. (2007). Point positioning accuracy of airborne LIDAR systems: A rigorous analysis. *International Archives of Photogrammetry, Remote Sensing and Spatial Information Sciences*, Munich, Germany, 19-21.
27. Moeini, Shahab. Oudjehane, Azzeddine. Baker, Tareq. & Hawkins, Wade. (2017). Application of an interrelated UAS - BIM system for construction progress monitoring, inspection and project management.
28. Muller, A., 2021. Assessment of Vertical Accuracy from UAV-LiDAR and Structure from Motion Point Clouds in Floodplain Terrain Mapping (Doctoral dissertation, Portland State University).

29. Papakonstantinou, A., Topouzelis, K., & Pavlogeorgatos, G. (2016). Coastline Zones Identification and 3D Coastal Mapping Using UAS Spatial Data. *ISPRS International Journal of Geo-Information*, 5(6), 75. doi: 10.3390/ijgi5060075
30. Pix4D. (2017). Available: Do RTK/PPK drones give you better results than GCPs? https://assets.ctfassets.net/go54bjdzbrgi/2VpGjAxJC2aaYIpsmFswD/3bcd8d512ccfe88ff63168e15051baee/BLOG_rtk-ppk-drones-gcp-comparison.pdf
31. Pix4D. (2019). Pix4D. Available: pix4d.com
32. Pilarska, M., Ostrowski, W., Baku?a, K., G?rski, K. and Kurczy?ski, Z., 2016. The Potential of Light Laser Scanners Developed For Unmanned Aerial Vehicles-The Review And Accuracy. *International Archives of the Photogrammetry, Remote Sensing & Spatial Information Sciences*, 42.
33. Populus, Jacques. (2019): Use of LIDAR for coastal habitat mapping. Available: http://www.coastalwiki.org/wiki/Use_of_LIDAR_for_coastal_habitat_mapping
Retrieved on 12/01/2019.
34. Remondino, Fabio & Barazzetti, Luigi & Nex, Francesco & Scaioni, Marco & Sarazzi, D. (2011). UAS photogrammetry for mapping and 3D modeling-Current status and future perspectives. *ISPRS - International Archives of the Photogrammetry, Remote Sensing and Spatial Information Sciences*. XXXVIII-1/C22. 10.5194/isprsarchives-XXXVIII-1-C22-25-2011.
35. Ruessink, B., Arens, S., Kuipers, M., & Donker, J. (2018). Coastal dune dynamics in response to excavated foredune notches. *Aeolian Research*, 31, 3–17. doi: 10.1016/j.aeolia.2017.07.002
36. Salach, A., Bakula, K., Pilarska, M., Ostrowski, W., G?rski, K. and Kurczy?ski, Z., 2018. Accuracy assessment of point clouds from LiDAR and dense image matching acquired using the UAV platform for DTM creation. *ISPRS International Journal of Geo-Information*, 7(9), p.342. <https://doi.org/10.3390/ijgi7090342>
37. Schaer, P., Skaloud, J., Landtwing, S. and Legat, K., 2007. Accuracy estimation for laser point cloud including scanning geometry. In *Mobile Mapping Symposium 2007, Padova* (No. CONF).
38. Shaw, L., Helmholz, P., Belton, D., & Addy, N. (2019). Comparison Of UAS LIDAR And Imagery For Beach Monitoring. *ISPRS - International Archives of the Photogrammetry, Remote Sensing and Spatial Information Sciences*, XLII-2/W13, 589–596. doi: 10.5194/isprs-archives-xlii-2-w13-589-2019
39. Sick. (2017). Operating_instructions_LD_MRS_3D_LIDAR_sensors. Available: <https://www.sick.com/us/en/detection-and-ranging-solutions/3d-LIDAR-sensors/ldmrs/c/g91913>
40. Siebert, S., & Teizer, J. (2014). Mobile 3D mapping for surveying earthwork projects using an Unmanned Aerial Vehicle (UAS) system. *Automation in Construction*, 41, 1–14. doi:10.1016/j.autcon.2014.01.004

41. Tao, C., Watts, B., Ferraro, C. C., & Masters, F. J. (2019). A Multivariate Computational Framework to Characterize and Rate Virtual Portland Cements. *Computer-Aided Civil and Infrastructure Engineering*, 34(3), 266-278.
42. Velodyne. (2019). VLP-16 User Manual63-9243 Rev. D. Available: https://github.com/UCSD-E4E/aerial_LIDAR/blob/master/Datasheets%20and%20User%20Manuals/velodyne%20LIDAR%20datasheets/**VLP-16%20User%20Manual%20and%20Programming%20Guide%2063-9243%20Rev%20A.pdf
43. Wallace, L., Lucieer, A., Turner, D. and Watson, C., 2011. Error assessment and mitigation for hyper-temporal UAV-borne LiDAR surveys of forest inventory. *Proceedings of Silvilaser*, pp.1-13.
44. Wang, George & Hollar, Donna & Sayger, Susan & Zhu, Zhen & Buckeridge, John & Li, Jie & Chong, Jimmy & Duffield, Colin & Ryu, Dongryeol & Hu, Wei. (2016). Risk Considerations in the Use of Unmanned Aerial Vehicles in the Construction Industry. *The Journal of Risk Analysis and Crisis Response*. 6. 10.2991/jrarc.2016.6.4.1.
45. Zhao, X., Su, Y., Hu, T., Cao, M., Liu, X., Yang, Q., Guan, H., Liu, L. and Guo, Q., 2022. Analysis of UAV lidar information loss and its influence on the estimation accuracy of structural and functional traits in a meadow steppe. *Ecological Indicators*, 135, p.108515. <https://doi.org/10.1016/j.ecolind.2021.108515>

Appendix

A.1 List of Parts

A.1.1 ECU UAS System (downward looking)

Drone (UAS) System

- Make: DJI
- Model: Matrice 600 pro
- Specification sheet

<https://store.dji.com/product/matrice-600-pro>

Digital Camera

- Make: GoPro
- Model: Hero session
- Specification sheet

https://gopro.com/en/us/update/hero_session

Digital Camera (secondary, sync)

- Make: IDS
- Model: uEye USB LE
- Specification sheet

<https://en.ids-imaging.com/store/products/cameras/usb-2-0-cameras/ueye-le/show/all.html>

GNSS System

- Make: NovAtel
- Model: OEM 6
- Specification sheet

<https://www.novatel.com/assets/Documents/Papers/OEM628.pdf>

Inertial (IMU) System

- Make: Analog Devices/NovAtel
- Model: IGM A1
- Specification sheet

<https://www.novatel.com/products/span-gnss-inertial-systems/span-imus/span-mems-imus/imu-igm-a1/>

GNSS-IMU Post Processing Software

- Product: NovAtel Waypoint/inertial explorer
- Version 8.7
- Specification sheet

<https://www.novatel.com/products/software/inertial-explorer/>

LIDAR

- Make: SICK
- Model: LD-MRS420201
- Specification sheet

https://www.sick.com/us/en/detection-and-ranging-solutions/3d-LIDAR-sensors/ld-mrs/ld-mrs420201/p/p496644?ff_data=JmZmX2lkPXA0OTY2NDQmZmZfbWFzdGVySWQ9cDQ5NjY0NCZmZl90aXRsZT1MRC1NUI0MjAyMDEmZmZfcXVlcnk9JmZmX3Bvcz0xJmZmX29yaWdQb3M9MSZmZl9wYWdlPTEmZmZfcGFnZVNpemU9MjQmZmZfb3JpZ1BhZ2VTaXplPTI0JmZmX3NpbWk9OTMuMA==

A.1.2 ECU UAS System (side view)

Drone (UAS) System

- Make: DJI
- Model: Matrice 600 pro
- Specification sheet

<https://store.dji.com/product/matrice-600-pro>

GNSS + IMU System

- Make: NovAtel
- Model: pwrpak 7
- Specification sheet

<https://www.novatel.com/assets/Documents/Papers/OEM628.pdfhttps://hexagondownloads.blob.core.windows.net/public/Novatel/assets/Documents/Papers/PwrPak7-Product-Sheet/PwrPak7-Product-Sheet.pdf>

GNSS-IMU Post Processing Software

- Product: NovAtel Waypoint/inertial explorer
- Version 8.7
- Specification sheet

<https://www.novatel.com/products/software/inertial-explorer/>

LIDAR

- Make: Velodyne
- Model: Puck-16
- Specification sheet

<https://www.amtechs.co.jp/product/VLP-16-Puck.pdf>

A.1.3 ECU UAS System (SFM)

Drone (UAS) System

- Make: DJI
- Model: Inspire pro 2
- Specification sheet

<https://store.dji.com/product/matrice-600-pro> <https://www.dji.com/inspire-2>

GNSS System

- Make: U-blox
- Model: C099-F9P
- Specification sheet

<https://www.novatel.com/assets/Documents/Papers/OEM628.pdf> https://content.u-blox.com/sites/default/files/documents/C099-F9P-AppBoard_UserGuide_UBX-18063024.pdf

Camera

- Make: GoPro
- Model: Hero7
- Specification sheet

<https://gopro.com/en/us/out-of-the-box-experience/hero-7-black>

GNSS-IMU Post Processing Software

- Product: RTKLIB
- Version 2.4.3
- Specification sheet

https://github.com/rtklibexplorer/RTKLIB/blob/demo5/doc/manual_demo5.pdf

<https://www.novatel.com/products/software/inertial-explorer/>

A.2 Literature Review (v0.0, last revised January 2020)

Training and Case Studies for UAV-based LIDAR and Imaging Systems

A Literature Review Report Prepared for the

The Project Steering and Implementation Committee

RP2020-35

North Carolina Department of Transportation

By

East Carolina University Research Team

December 31, 2019

Table of Contents

| | | |
|-----|---|----|
| 1. | Introduction to UAV-based sensing systems..... | 3 |
| 2. | Data quality and error models..... | 6 |
| 2.1 | SFM and GCP errors..... | 6 |
| 2.2 | LIDAR and direct georeferencing errors | 9 |
| 2.2 | ALS corrections | 12 |
| 3. | Safety and risk considerations..... | 13 |
| 4. | Applications on construction management applications..... | 15 |
| 4.1 | UAV-based photogrammetry..... | 15 |
| 4.2 | LIDAR applications..... | 17 |
| 4.3 | Data fusion applications | 21 |
| 5. | Applications on environmental applications and disaster management..... | 23 |
| 5.1 | UAV Photogrammetry and SFM..... | 23 |
| 5.2 | UAV LIDAR..... | 26 |
| 6. | State and Federal Regulations | 29 |
| 7. | Emerging technologies..... | 41 |
| | References..... | 43 |

1. Introduction to UAV-based sensing systems

There are two types of remote sensing systems covered in this literature review: 1) Unmanned Aerial Vehicle (UAV)-based photogrammetry and 2) UAV-based LIDAR system.

UAV-based photogrammetry is primarily based on imagery collected with small onboard cameras. It typically requires ground control points (GCPs) with surveyed locations and can benefit from recorded location and orientation of the camera. A 3D point cloud of the target area can be estimated via direct or indirect geo-referencing. Indirect georeferencing refers to the methods that world-frame coordinates to 3D measurements collected in a relative reference frame. One of the most popularly used UAV-based georeferencing solution is structure from motion (SfM). It has been proven to be superior to conventional handheld surveying methods in certain environments, such as in projects with low vegetation, stable GPS availability and substantial sunlight (DJI, 2019).

Multiple 2D images over the same area can be combined and the point features are matched across them. These images are expected to have great overlap areas (~80%). The 3D locations of these points are then estimated in the camera frame, which are then used to form a 3D model or point cloud. However, the camera (position and orientation) isn't always precisely known in a world frame (GPS frame, for example) when a small commercial UAV is used. Therefore, the 3D model created with structure from motion with a small UAV is typically dimensionless and cannot be directly georeferenced. It requires additional GCPs to relate back to the world frame. The absolute accuracy of this model depends on both image processing quality and the GCPs.

Some customized and commercially off-the-shelf UAVs are capable of recording the camera location and orientation for each of the images taken during a flight. In that case, camera-based direct georeferencing is possible. It can be achieved by raytracing from a single image to a known surface (such as Digital Elevation Model (DEM) or other a priori terrain models), or triangulation from multiple overlapped images, or a combination of both. Since no ground control is necessary, the accuracy of 3D modeling is primarily determined by the accuracy of camera timing, orientation and location. However, a small UAV that is not capable of carrying high-quality navigation sensor cannot be used for direct geo-referencing. Therefore, direct geo-referencing has not been commonly used in small UAVs yet. It will be further discussed in the context of emerging technologies.

Although there existed several specialized software solutions for triangulation, it has become part of the software solution for SFM. As discussed in previous sections, SFM does not require a priori position and orientation of the camera, or the complete camera calibration model. These items can be estimated as part of the outcome of SFM. The core algorithm in SFM is typically based on bundle adjustment. A good review of the algorithm can be found in (Triggs, McLauchlan, Hartley & Fitzgibbon, 2000).

The main functions of Agisoft are listed here as examples, retrieved from (Semyonov, 2011).

- Feature matching across the photos
At the first stage Agisoft detects points in the source photos which are stable under viewpoint and lighting variations and generates a descriptor for each point based on its local neighborhood. These descriptors are used later to detect correspondences across the photos. This is similar to the well-known Scale Invariant Feature Transform (SIFT) approach (Lowe, 1999), but uses different algorithms for a little higher alignment quality.
- Solving for camera intrinsic and extrinsic orientation parameters
Agisoft uses a greedy algorithm to find approximate camera locations and refines them later using a bundle-adjustment algorithm.
- Dense surface reconstruction
At this step several processing algorithms are available. Exact, Smooth and Height-field Methods are based on pair-wise depth map computation, while Fast Method utilizes a multi-view approach.
- Texture mapping
At this stage the software parametrizes a surface possibly cutting it in smaller pieces, and then blends source photos to form a texture atlas.

Modern SFM software would take known calibration, position or orientation as input. Commercial software is available from Agisoft (Agisoft, 2019), Trimble (Trimble, 2019), Pix4D (Pix4D, 2019), and open-source software such as CMVS (Furukawa, 2019) has also been used in scientific communities. They can help improve the quality of the 3D point cloud. If only inaccurate position

and orientation are available from low-quality navigation sensors, they can also be optimized in the SFM software. Therefore, for UAVs that have precise location, through Real Time Kinematic (RTK), Post-Processed Kinematic (PPK), or post-processed Precise Point Positioning (PPP), without orientation, SFM can still be used to estimate the 3D point cloud. It can be done with few or no GCPs. PPP is post-processed GNSS positioning that does not need a local reference station like RTK and PPK do, which could be less accurate.

Alternatively, camera systems can be combined with, or replaced by a direct ranging sensor, such as a UAV LIDAR system, on some bigger-sized UAVs. LIDARs are less sensitive to natural light condition, and may provide measurements in operational conditions which prohibits camera operation (such as low light). An airborne LIDAR directly measures point cloud in the sensor frame. The point cloud will be transformed into the world frame by knowing precise location and orientation of the LIDAR. Very much like camera direct georeferencing, airborne LIDAR point cloud accuracy is also sensitive to timing/synchronization, LIDAR orientation and location. Furthermore, airborne LIDAR sensors available today are still more expensive, more power-hungry and heavier than cameras in general.

An airborne or UAV LIDAR system typically includes three types of sensors, a ranging sensor (2D scanning LIDAR, 3D scanning LIDAR or 3D imager); a positioning sensor (such as GPS or GNSS receiver) and an inertial sensor that measures acceleration, rotation, velocity and orientation. These three sensors are integrated in the data collection system and in the 3D modeling procedure. The GNSS and inertial sensors are typically tightly coupled together to provide precise and smooth pose of the LIDAR. It is a common practice that the positioning sensor is also responsible for accurate 3D positioning and synchronization of an onboard antenna (optional).

2. Data quality and error models

The data quality from UAV photogrammetry based on SFM and indirect geo-referencing is discussed here.

2.1 SFM and GCP errors

The errors modeled considered in (Nasrullah, 2016) included camera/lens calibration errors; motion blurriness; altitude, pattern and stability of flight; image overlap and distribution of GCPs.

1) Camera calibration can be estimated as part of SFM (self-calibration). However, a pre-calibrated camera/lens may be more convenient and robust. Other parameters, such as shutter speed, lens aperture, and ISO also have a considerable impact on the image quality.

2) Small UAV platforms are often sensitive to wind and vibration problems. Even mild wind during data acquisition can cause offset in camera pointing direction, and eventually insufficient image overlap. Vibration can increase the blurriness. Furthermore, light conditions during image acquisition can add to the complexity. To compensate for low light conditions, a lower shutter speed or higher ISO are used. Lowered shutter speed increase motion blurriness, while higher ISO increases noise. In most target applications, a larger area of interest will probably need multiple flight acquisition. Appearance changes, such as change of shadows, can cause another problem.

3) The impact of flight altitude on accuracy is a little more complex. Flight altitude changes the distance, image footprint, image overlap and geometry (slope) to the object. Errors tend to increase with distance and a steeper slope in SFM. Imaging the object from a steeper slope limits the variety in perspectives (view angles). Since SFM benefits from imagery from multiple perspectives, vertical accuracy decreases due to bad geometry.

Examples to quantify the findings above can be found in (Nasrullah, 2016).

Micheletti, Chandler & Lane (2013) gave specific advices for UAV SFM:

- Plan camera survey and registration or scaling method in advance.
- Capture the whole subject first, and then the detail, ensuring that occlusions are captured adequately (see item 3).

- Ensure appropriate coverage. The basic principle is that every point on the subject must appear on at least three images acquired from spatially different locations.
- Keep static scene.
- Keep consistent light.
- Avoid overexposed and underexposed images.
- Avoid blurred images – normally arising from slow shutter speed and/or camera movement.
- Avoid transparent, reflective or homogeneous surfaces.

It was also noted in (Micheletti et al., 2013) that images did not need to be acquired from the same distance or have the same scale. The authors argued that it was better to acquire **multi-scale** image sets. High altitude, large-scaled images could initially capture the whole site with fewer frames. Closer images could capture the desired detail at the required resolution and precision. It is particularly important when capturing areas of detail which are physically obscured by occlusions.

Users of SFM software are typically advised to place GCPs throughout the target site, on the edge of the worksite and in the center (Pix4D, 2017). The locations of GCPs can be surveyed using GNSS-based RTK solutions, RTK and PPK solutions (GCPS, 2019), Total Station Survey or TLS scans (Shaw, Helmholz, Belton, & Addy, 2019). PPK survey typically has positioning error around 1 cm, 1 sigma. However, to achieve centimeter-level accuracy in the point cloud, the user is required to place up to 40 GCPs per square kilometer (DJI, 2019).

Sanz-Ablanedo, Chandler, Rodríguez-Pérez & Ordóñez (2018) provided a systematic overview of accuracy in point cloud involving GCPs. With a sufficient number of GCPs (more than 2 GCPs per 100 images as specified in this work), the error of point cloud could approach double of the GCP error. If fewer GCPs were used, this paper reported that the point cloud error would be as high as 4-8 times the GCP error, which was still in the centimeter range. Vertical errors were approximately 2.5 times the error of horizontal components. It was also suggested that GCPs should be evenly distributed around the whole interest area, ideally in a triangular mesh grid. For a greater project, denser GCPs were needed to achieve the same accuracy. This is probably because of possible systematic errors in SFM, which tends to amplify with growing distance and area.

The goal of **GCP placement strategy** is to minimize the distance from point cloud to any GCP.

In many scenarios or applications, it is not possible to place GCPs with this strategy. Sanz-Ablanedo et al. (2018) also recommended the use of

- pre-calibrated cameras rather than the self-calibration;
- mixing different altitude flights;
- various degrees of image convergence; and
- known positional and orientation parameters.

They are consistent with recommendations made in other literature.

Onboard pose error for direct geo-referencing was also considered (Nasrullah, 2016). With today's technologies, small UAVs could carry high-quality GNSS receivers that are capable of RTK on the fly, or recording data for post processing. Post-Processed position through PPK or PPP could be used to help improve the accuracy with limited GCPs. Pix4D (2017) noted that RTK and PPK could both produce centimeter-level accuracy. PPK was more accurate RTK, but less than using GCPs, especially on the vertical direction. Grayson, Penna, Mills, & Grant (2018) further compared PPK with PPP. Since PPP does not need an additional local reference GNSS receiver, it is more convenient and flexible. However, it was found out that PPP produced worse accuracy on the vertical direction than RTK (10 cm error reported for PPP). Further RTK requires a live datalink between a reference station and the airborne receiver, which is not always possible or necessary.

Although the approaches above claimed that GCPs were not necessary if PPK position were available for the cameras, the point cloud could not be directly registered yet. SFM with PPK can produce precise point cloud only in the camera body frame. Since PPK position does not directly solve the **orientation** of the camera or the point cloud, an additional step is needed to align the point cloud in the correct direction.

It is practical to use a few GCPs even with PPK. (Zhang, Aldana-Jague, Clapuyt, Wilken, Vanacker & Oost, 2019) showed that a PPK–SFM solution workflow could provide consistent, repeatable point cloud over time, with an accuracy of a few centimeters. A vertical bias could be corrected using one single GCP. The results were used to estimate centimeter-level topographical change detection. PPK-SFM could accurately and quickly achieve a very high spatial and temporal resolution.

The main manufacturer of commercial small UAVs DJI also stated similar conclusions (DJI, 2019). The new UAV supports both RTK and PPK solutions. Although it could potentially reduce the required amount of GCPs to 0, DJI mentioned the use of “fewer GCPs”, and a reduction in GCP set-up time.

2.2 LIDAR and direct georeferencing errors

Although a UAV LIDAR has different sensor quality from a more capable Airborne Laser Scanner (ALS), both follow the same principle for measurements. The error analysis of ALS is based on direct geo-referencing and is largely applicable to UAV LIDAR.

LIDAR measurement error, navigation and timing error, and modeling error can all contribute to the error in the LIDAR point cloud.

At any time of measurement, the LIDAR senses the distance to a point in the 3D world based on the return of a laser beam. Since the beam would be sent at a known direction specified in the LIDAR body frame, the position of this point is therefore directly measured in the LIDAR body frame.

“LIDAR measurement error” refers to the single point position error in the body frame. It is dependent on the beam width (or divergence), the reflecting surface, the angle and the range measurement (Guan & Zhu, 2019). Beam divergence and the possible uncertainty in the scan angle are both considered angular errors in the LIDAR, whereas the reflecting surface and the measurement itself both contribute to the ranging error along the laser beam. In (May & Toth, 2007), the angular and ranging errors are both modeled as random processes. The magnitude of these errors depends on the LIDAR manufacturer. In a downward looking laser beam, ranging error primarily contributes to the **vertical** position error. In practice, ranging error could also have a systematic component, such as a bias. It needs to be calibrated or bounded.

Some LIDARs are designed with narrow beams (1 or few milliradians, 1 milliradian is approximately 0.06 degrees) to minimize this uncertainty such as (Velodyne, 2019). Some believe that a wider beam is more robust (~10 milliradians) for a UAV LIDAR. With multiple returns measured on the same beam, a wide beam may get returns on the target or the ground after it hits occlusion due to dust, rain and other objects (Webber, 2018). Therefore, it has the potential to measure distance to targets and ground in a harsh environment. The small angular error is scaled with distance to the ground,

which contributes to **horizontal** position error in a downward looking laser beam. However, since the laser beam would have a slant angle even with a downward looking LIDAR, it will also contribute to the vertical uncertainty.

The position in LIDAR body frame cannot be directly used in a 3D model if the LIDAR is mobile or airborne. The absolute position and orientation of the LIDAR in the global world frame need to be accurately measured and synchronized with the measurement time of each point in the point cloud.

The **position** of LIDAR is not directly measured. Instead, it is inferred from the location of GPS/GNSS antenna measured with RTK, PPK or PPP. The accuracy of RTK, PPK or PPP had been discussed in the previous section, in the range of 1 cm to 10 cm. It must be noted that the navigation system used for UAV LIDAR should be GPS/GNSS tightly coupled with the onboard inertial measurement unit. The post-processed GNSS and inertial solution can be less noisy than PPK or PPP alone, typical values are 1 cm horizontal and 2 cm vertical (NovAtel, 2016); or 2-5 cm (Trimble-Appianix, 2019). The actual values are sensor-specific.

The antenna position is combined with the **lever arm** between the antenna and the LIDAR center of measurement to compute the LIDAR position. Any errors in lever arm, which is typically at millimeter level, become **biases** in the point cloud.

Similarly, the navigation system measures the **orientation** of the UAV in the world frame. It is transferred into the LIDAR orientation via known boresighting of the LIDAR. Boresighting errors can be calibrated, and any residual error will contribute to the angular errors discussed below. Ravi, Lin, Elbahnasawy, Shamseldin & Habib (2018) showed that successful calibration could reduce error magnitude down to centimeter level.

The navigation system can be very accurate at measuring roll and pitch angles, typical values are much lower than 1 degree (0.008 degrees (NovAtel, 2016) or 0.015 degrees (Trimble-Appianix, 2019)). The actual values are sensor-specific.

However, the reported **true heading** angle accuracy for these sensors could be overly optimistic and misleading. The nominal accuracy, typically better than 0.1 degrees, is achieved only after maneuvers of the UAV and fine alignment of heading. The maneuvers may not always be possible for small

UAVs with a short flight time; or for the operational environment of a small urban worksite. Without that, the heading is initialized by vehicle velocity, gyro-compassing, compassing or manual input, which has the accuracy of a few degrees as reported in (Mostafa, Hutton, Reid & Hill, 2001). The heading accuracy levels with and without alignment are applicable to most high-end navigation systems that can fit on a small UAV.

True heading error of a few degrees is a **major** concern for UAV LIDAR, although it was not a big issue for SFM. As discussed above, SFM point cloud is calculated from overlapping images. The points from SFM are precisely located with respect to each other within the camera body frame, and the relative precision does not depend on the absolute orientation in the world frame. In fact, camera orientation can be precisely solved from matching point features in images (Hartley & Zisserman, 2004).

The same does **NOT** apply to LIDAR point cloud. In processing raw LIDAR data, the points are geo-located independently from each other. There is no relative precision like SFM. As a result, a large angular error, such as the heading offset, causes each point to be out of its place. A point cloud formed in this case could be distorted so much that it could no longer represent the geometric shape of the target or the terrain. Therefore, point cloud becomes meaningless with large angular errors. Smaller heading and boresighting errors would cause the points measured in different parts of a UAV flight or from different flights to be inconsistent (Toth & Grejner-Brzezinska, 2009).

Unfortunately, the operator of small UAVs may not know if the UAV has completed enough maneuvers to guarantee the desired heading accuracy. In the navigation industry, measuring true heading in real time has always been a challenge. A possible solution for airborne and ground vehicles is to use a dual-antenna system. For example, VectorNav has a dual antenna system that can measure the relative location of both antennas in the GPS coordinate frame. The vector between both antennas thus provides an absolute heading, with the error of 0.3 degrees 1 sigma (VectorNav, 2019). However, the accuracy is achieved by placing both antennas at least 1 m away from each other. Unfortunately, the heading error would be inversely proportional to the distance between both antennas. If installed on a small UAV, the maximum distance between antennas is typically much shorter than 1 meter, and the heading error approaches 1 degree 1 sigma. Therefore, the dual antenna solution could not help with a lot of small UAVs.

In addition, the timing error between the navigation system is often overlooked. Ideally, the LIDAR orientation at the exact moment of measuring every single point in the point cloud must be recorded. Sometimes process is simplified by using the same orientation for a batch of points, which leaves small uncertainty in time, at millisecond level. Any UAV rotation and vibration experienced within few milliseconds are therefore not compensated, which contributes to the overall angular error.

Finally, the LIDAR point cloud will be processed and registered. In some applications, LIDAR points will be compared against a known model; and fit with the known model (Fernandez, Kerle & Gerke, 2015). In this case, the location of the fit 3D model would not directly reflect the noise level on each point. Instead, it could be affected by the bias and systematic errors in LIDAR point cloud.

In summary, the position errors observed in the navigation system are typically limited, and the orientation errors could be significant. In an ideal case, the orientation errors would mainly affect the horizontal locations of the individual points in the LIDAR point cloud. For example, an angular error of 0.1 degrees is equivalent to horizontal errors of 5 cm at 30 m away. The expected vertical error is also around the level of several centimeters. An analytical example can be found in (Guan & Zhu, 2019), and similar behavior and performance were observed in (Graham, 2019).

2.2 ALS corrections

If the angular error magnitude or the flight altitude increases, centimeter-level accuracies cannot be guaranteed anymore. Some of the error sources are in fact systematic errors that result in bias in the point cloud with respect to the truth, and discrepancies among subsets of the LIDAR point cloud measured from different flight paths. ALS point cloud was faced with similar problems (Toth & Grejner-Brzezinska, 2009).

The lessons learned in SFM may be applicable here. Overlapped observation of the same terrain or target was not necessary to form LIDAR point cloud, but it helps correct the self-discrepancies. Overlapped area between the footprint of different flight paths (also called “strips”) can be used to correct the subsets of the point cloud, which makes the entire point cloud more precise in a relative sense. (Toth & Grejner-Brzezinska, 2009) mentioned the data-driven approach to minimize the differences between strips for a given transformation model.

Points and geometric features can be extracted from LIDAR data and matched with ground control points or features with surveyed locations. This approach would make the point cloud accurate in an absolute sense (Toth & Grejner-Brzezinska, 2009). These points and features could be calibration targets purposely distributed in the area, which makes them equivalent to GCPs; or common objects with recognizable shapes, such as sidewalks.

3. Safety and risk considerations

FAA part 107 guidelines (FAA, 2016) must be followed when operating small UAVs for these applications. Additional risks arise primarily from operating in construction applications.

Howard, Murashov & Branche (2017) noted that “about 30 incidents of near-misses or crashes leading to human injury have been reported associated with the use of recreational UAVs. Unstable flying conditions, operator errors, and faulty equipment may represent potential hazards to nearby workers from the commercial use of UAVs.” This work described the use of UAVs in construction, the potential risks of their use to workers, approaches for risk mitigation, including “prevention-through-design” for small UAVs, adequate training of operators, updating occupational safety regulations.

Risks of small UAVs could result from a number of technical reasons, including (but not limited to) power, communications, navigation and control. UAV operations may be autonomous, semi-autonomous or remote controlled (Wang, Hollar, Sayger, Zhu, Buckeridge, Li, Chong, Duffield, Ryu & Hu, 2016). In a fully autonomous or semi-autonomous operation, the low-level control is governed by the on-board flight controller and navigator, which relies on GNSS (or an equivalent sensor) as aforementioned. If the UAV follows a pre-loaded flight plan without the need of human intervention, it is considered fully autonomous. In a semi-autonomous operation, sometimes also referred to as a GNSS-assisted operation, the UAV follows the guidance of a remote controller, with commands transmitted via a communication channel. In a remote-controlled operation, the user directly performs low-level control functions, such as attitude or velocity control, without using on-board GNSS.

When a UAV is close to a building or other structure, it may lose communications with the operator. Quality of GNSS positioning in the vicinity of a construction site could also suffer from blockage and multipath. In an autonomous operation where GNSS has been corrupted, the on-board flight

controller could command erroneous operations. A properly designed UAV system will attempt to stop the operation, by landing or returning to the home location, upon the loss of communications or GNSS. Without the ability to “sense and avoid”, the UAV could potentially cause damages during this process. An obvious way to prevent communication loss is for users to remain in line-of-sight when operating UAVs, as often required in various regulations including FAA part 107 (FAA, 2016). Autonomous operations should be enabled only when GNSS (or equivalence) is available.

Small UAVs with redundant navigation systems, payload capabilities, redundant rotors and battery capability in case of a rotary wing UAV provide additional safety protection. Furthermore, small UAVs with GNSS-denied and indoor navigation capability, sense and avoid capability, are also available now.

4. Applications on construction management applications

4.1 UAV-based photogrammetry

UAV-based sensing systems have been widely used for various types of operations and applications in the construction industry. Main capabilities of UAV-based imaging system include 2D surveying, 3D mapping and modelling, progress control, onsite monitoring, inspection and assessment. They are applicable to buildings, bridges, transportation areas and other infrastructure systems. A summary of these applications can be found in (Dastgheibifard & Asnafi, 2018).

de Melo, Costa, Álvares, & Irizarry (2017) discussed applications for **safety inspection** on construction sites. UAV-imagery could be used to identify the non-compliances with the safety requirements established. With improved visualization of the working conditions, UAVs could help improve the safety inspection process on jobsites by means of a better visualization of working conditions. (de Melo et al., 2017) developed a set of procedures and guidelines for data collecting, processing and analyzing safety requirements based on 2D imagery.

Construction progress monitoring could also benefit from using small UAVs. Instead of relying on manual input and observation of each and every phase of the construction projects, which are costly and time consuming, Moeini, Oudjehane, Baker & Hawkins (2017) proposed to integrate Building Information Modeling (BIM), UAVs and real-time cloud based-data modeling and analysis. It enabled an accurate comparison between as-Planned and the UAS based As-Built states of the project. The limitation of this approach lies on the fact that the data generated is currently qualitative with a visualization of the project progress. A software approach to automatically align and compare the BIM model and the point cloud was needed to produce quantitative and measurable data for project control and performance monitoring. Hamledari, Davari, Azar, McCabe, Flager & Fischer (2018) proposed an industry foundation classes (IFC)-based solution for UAV-enabled as-built and as-is BIM development, quality control, and smart inspections. It enabled automated integration of as-built and as-is conditions into BIM. However, it was based on 2D images only.

Structural damage assessment could be done with 2D or 3D imagery. (Eschmann, Kuo & Boller, 2014) showed examples of building scanning and monitoring using a small rotary-wing UAV. 2D UAV images were stitched together to become a high-resolution imagery map. It allowed damages and cracks to be observed in the millimeter range. Additional algorithm and processing software

were developed to recognize and highlight the cracks based on 2D edge detection. In (Fernandaz et al., 2015), a 3D point cloud was formed the multi-perspective, overlapping, very high-resolution oblique images collected with UAVs. The 3-D point-cloud was collected for the entire building, and was combined with detailed object-based image analysis (OBIA) of façades and roofs. Major damages could be identified in the 3D point cloud, whereas other cases are by OBIA-based damage indicators. However, it was recognized that the 3D point cloud was collected for individual parts of the building. It required an additional algorithm to aggregate the information from these parts.

3D mapping with UAV photogrammetry is the main application to be covered in this review. A review of relevant technologies can be found in (Remondino, Barazzetti, Nex, Scaioni & Sarazzi, 2011). In general, UAV photogrammetry can reduce the cost and the risks in mapping and surveying tasks in harsh environments. Centimeter-level accuracy is achievable, and rotatory-wing UAVs are better choices for small sites. However, the durability of small UAVs may be a potential issue considering weather and wind conditions.

The principle of SFM and estimation algorithm has not changed in the last few decades. However, high-quality cameras and sensors have become more suitable for small UAVs, as they become cheaper, smaller, lighter and less power hungry. SFM software and computation hardware have been improved as well. There are more choices for commercial software and more powerful hardware available today.

Siebert & Teizer (2014) demonstrated the use of UAV imagery and SFM on modeling the **surface and volume** of earth work in a field-realistic environment. Although UAV was much more convenient than traditional methods, it was recognized that the volumetric measurements could bear large errors. The authors noted that error sources needed to be identified and mitigated. DEM of a designated area could be created from UAV imagery and SFM (Ajayi, Palmer, & Salubi, 2018). The horizontal and vertical accuracy fall within the desirable threshold according to National Standard for Spatial Data Accuracy. The DEM was used to choose a proper siting for dam construction. The authors concluded that the terrain model created in this approach was robust enough for planning purposes in construction and engineering applications.

Álvares, Costa & de Melo (2018) compared the efficacy of 3D mapping in terms of the easiness of model development, data quality, usefulness and limitations on two **typical building cases**. The

easiness of model development took into consideration the accessibility of the worksite for takeoff and landing; physical barriers for UAV flights; disruption on the worksite and software processing time. The data quality included the footprint, spatial resolution and overlap of the images, and visual inconsistency between images due to distortion, shadowing and gaps. The usefulness and limitations were defined for the users of the data product. The users interviewed in this work noted that the 3D maps were useful for logistics, monitoring work progress, planning and visualization. However, these maps could not provide details in a close range, and there were parts of the buildings that could not be modeled (such as inside and top). Due to safety considerations and regulations, the UAV flight could not cover certain parts of the site to create a full 3D point cloud.

Khaloo, Lattanzi, Cunningham, Dell'Andrea & Riley (2018) demonstrated the use of UAVs for augmenting **bridge** inspections, using the Placer River Trail Bridge in Alaska as an example. The authors produced a 3D model of the bridge using UAV imagery and a hierarchical dense SFM algorithm. The UAV design, data capture and data analysis were optimized together for a dense 3D model, and the results are compared against models generated through laser scanning. The 3D models created with UAV-imagery did provide the accuracy to resolve defects and support the needs of infrastructure managers.

In summary, UAV-based photogrammetry has found applications in pre-construction survey, mapping, volumetric measurement, monitoring and assessment.

4.2 LIDAR applications

LIDAR-based solutions are raising some interests within the construction industry as well (Knight, 2019). UAV-based LIDAR is a relatively new technology for construction management. Users in this industry are more familiar with terrestrial laser scanners (TLS), mobile laser scanners (MLS) mounted on ground vehicles and ALS mounted on large manned aircraft.

Mill, Alt & Liias (2014) showcased how **TLS** point cloud be integrated with Total Station surveying to create BIM models for existing buildings. The point cloud-based BIM model provided the ability to detect and define facade damage on buildings. It also provided the ability to detect discrepancies between the existing drawings and the real situation captured with the TLS point cloud. Limitations of this method were also pointed out, including: 1) difficulty in manipulating point cloud data; 2) lack of best fitting algorithm; 3) lack of ability to enforcing known shapes of opening such as

windows in point cloud and 4) lack of a standard in managing data. Truong-Hong & Laefer (2014) focused on TLS application on bridge inspection, on involving geometric documentation, surface defect determination, and corrosion evaluation. Workflows based on TLS data were proposed to measure cracks and vertical deflection. They could save up to 90% of time, and could detect cracks 1.6mm to 4.8mm.

TLS measures point cloud from a fixed location, which is inconvenient in a lot of applications. LIDAR can be installed on airborne and ground vehicles, and can measure point cloud while the vehicles are moving. These types of LIDARs would require high-quality navigation sensors (typically differential GPS/GNSS and inertial measurement unit (Wang, Peethambaran & Dong, 2018)) to measure the position and orientation of the LIDAR.

ALS has been widely used to survey the ground and create topographical models, although normally it would not be used to survey construction worksites, due to cost and other practical limitations. Suaraz, Ontiveros, Smith & Snape (2005) described the use of aerial photography and ALS to estimate individual tree heights in forests. The main challenge of modeling the forest-covered terrain was to differentiate the LIDAR returns from the tree and the ground. This process depended on multiple returns of the laser beam, since the first return is usually from the tree tops, and the last strong return is from the ground. However, due to the low density of ALS returns (3-4 returns per m^2) and small foot print of laser beam (10 cm^2), the tree models were not as accurate as one had hoped for with LIDAR measurements. Only meter-level accuracy was achieved.

The application of MLS is similar to that of TLS. For example, Puri & Turkan (2020) proposed to use MLS in monitoring **progress**. MLS point cloud data and 4D design models were used to identify deviations of the performed work from the planned work. The proposed framework was tested using as-built data acquired from an on-going bridge construction project. The Percentage of Completion for the as-built bridge elements were calculated and compared with the as-planned values. The differences for every element on a specific scan date were used for assessing the performance of the proposed framework. The obtained difference ranged from -7% to 6% for most elements.

Since **MLS** is mounted on ground vehicles, it can offer similar high data density as the TLS (higher than that of ALS), similar accuracy levels (millimeter to centimeter), and is more flexible than TLS.

MLS is becoming a popular choice for mapping an urban environment (Wang et al., 2018). Available commercial systems today can produce close to or more than 1 million of points per second and a few hundred-meter range. The manufacturers of these LIDARs include Faro, Velodyne, Riegl, Sick, Optech and Leica. They have been used in mapping for transportation infrastructure, building information modeling, utilities surveying, vegetation. Road markings, zebra crossings, center lines and other features could be automatically identified from the integrated LIDAR-imagery data product. The challenges identified in using MLS include 1) classification and recognition of objects 2) data integration and registration, and 3) city modeling.

The issue with **data integration and registration** is the most relevant to this work. Although MLS point cloud can be directly geo-referenced, since position and orientation of the LIDAR are measured, errors in navigation (position and orientation) can cause discrepancies among the point cloud data sets. In particular, the authors noted that “the misalignment among sensors needs to be carefully calibrated (through either indirect or direct sensor orientation), and their time needs to be rigorously synchronized”. It was because orientation and timing errors could cause great offset in the location of the point cloud. MLS point cloud could be registered with respect to other sensor data, such as a reference point cloud and imagery. Multiple sets of MLS point cloud could also be registered and stitched together. However, different data sets often had to be manually registered into the same coordinate system due to navigation errors. Special shaped artificial targets were used in the process. The precision of MLS point cloud was verified via registration, which was around 4-5 cm.

Wang et al. (2018) provided a summary on how **urban** objects could be modeled with LIDAR point cloud from TLS, MLS and ALS. Building roof and façade could be modeled with ALS or ground-based LIDAR. The modeling process could be data-driven, which extracted models from the point cloud; or model-driven, which verified a hypothetical model with point cloud; or a hybrid between the two. The choice of models was a balance between geometry, topology and semantics. Power lines could be better modeled with ALS and geometric models (a more detailed example can be found in (Zhang, Yang, Xiao, Liang, Liu, & Wang, 2019)). Road surfaces could be modeled with ALS or MLS, and with various types of models. Wang et al. (2018) called for more research into LIDAR-based bridge models.

Wang et al. (2018) also recognized that it was more challenging to model **free-form** objects, such as statues, towers, fountains and certain types of buildings. Various types of surface reconstruction methods were discussed in this work, and it was certainly possible to extract robust and accurate (centimeter level) representation from the point cloud. However, the accuracy depended on the surface characteristics and the input data.

Although there has not been much literature on the application of UAV-based ALS, the remote sensing industry has started to pay more attention to it. UAV LIDARs were developed based on adapted versions of ALS (Riegler, 2019) and MLS (Hokuyo, 2012) (Sick, 2017) (Velodyne, 2019). Like ALS and MLS, the UAV LIDARs were tightly integrated with navigation systems, such as Trimble/Trimble (Trimble-Trimble, 2019) and NovAtel (NovAtel, 2016).

Due to constraints in cost, power, size and weight, the low-cost UAV LIDAR systems had limitations in range, point cloud density, ranging accuracy and navigation accuracy. For example, Hokuyo LIDAR in (Hokuyo, 2012) has a nominal range of 30m. They are only suitable for ground vehicles and UAVs flying very low to the ground. GPS/GNSS receivers with RTK or differential corrections could produce large position errors, which translates to large 3D position errors in the point cloud. The orientation of the low-cost IMU sensors produced substantial angular errors, especially in heading. As a result, the accuracy and resolution of low-cost UAV LIDARs were rather limited. Remote sensing experts had argued that UAV LIDARs are not as effective as UAV photogrammetry in construction management not too long ago (Graham, 2018).

It is easier to obtain high-density point cloud with photogrammetry, and high-resolution cameras are much more cost effective than high-density LIDARs. More importantly, the relative precision of 3D point cloud from SFM photogrammetry is based on the consistency within imagery. It is relatively more convenient to achieve centimeter-level relative precision with sufficient imagery coverage. The absolute accuracy is dependent on GCPs. With sufficient GCPs, centimeter-level absolute accuracy can also be achieved. On the other hand, LIDAR point cloud is always using direct geo-referencing. As discussed above, the accuracy is highly dependent on the navigation sensors, especially angular measurements. As a result, the errors in 3D point cloud is amplified with distance. Limited by accuracy and range, low cost UAV LIDARs often have to take measurements close to the ground (tens of meters). Therefore, it was argued that low cost UAV LIDARs could only help when SFM or GCPs are not available (Graham, 2018).

However, it was pointed out that there could be several types of environments where UAV LIDAR would enable projects to be delivered that may not have been possible otherwise (Tompkinson, 2019). These projects included those that involved steep topography, or a linear-based survey, or sites covered by dense vegetation. LIDAR direct georeferencing minimizes the need for GCPs, and therefore are suitable in environments where it is either too expensive or impossible to place GCPs. More importantly, some LIDARs have multiple return capabilities (Sick, 2017) (Velodyne, 2019). The LIDAR beams are sometimes wide enough such that it can be reflected by multiple surfaces and objects, including dust, rain, foliage and the actual target (ground). It becomes possible for LIDAR to see through to the ground. Therefore, a main advantage of using LIDAR is potentially differentiating ground from vegetation.

Furthermore, recent development in remote sensing and navigation industries has made available higher density UAV LIDARs at a greater range (few hundred meters), and better inertial measurement units that can measure orientation more precisely. They could be used to take volumetric or topographic measurements of ground, with or without vegetation cover; model roads, cuts and other surfaces, and even buildings (Graham, 2019).

In the last few years, custom-built LIDAR systems have been reported that were specially designed for modelling the terrain or vegetation, such as (Guo, Su, Hu, Zhao, Wu, Li, ... Wang, 17). Commercial solutions are becoming more available, such as (Microdrones, 2019).

4.3 Data fusion applications

In general, UAV LIDARs are more capable of measuring terrain and surfaces, with or without vegetation cover, via direct geo-referencing. The point cloud density and accuracy decrease with distance, therefore it may not provide the same level of details that UAV imagery can. Alternatively, UAV LIDAR point cloud can be fused with available imagery to construct 3D models. The fusion will be based on direct geo-referencing and can still provide more details.

Mastin, Kepner & Fisher (2009) proposed an approach to **register** images with ALS point cloud for urban models. OpenGL and graphics hardware were used in the optimization process for efficient registration. Parmehr, Fraser, Zhang & Leach (2012) discussed a hybrid intensity-based approach that utilizes both statistical and functional relationships between images, particularly in the case of registering aerial images and 3D point clouds. Statistical dependence of Mutual Information or

functional relationships of Correlation Ratio along was not sufficient to register photos to LIDAR reliably. However, the proposed method used both of them, and performed robust registration of urban areas. Thuy, Watanabe & Wakutsu (2020) discussed registering SFM 3D point clouds, 3D meshes, and georeferenced orthophoto imagery in a fully automated manner. The data product could be used in disaster relief response and construction progress monitoring.

Kubota, Ho & Nishi (2019) focused more on **road** maintenance. This work combined TLS point cloud with UAV photogrammetry. The authors acknowledged the difficulties faced with road maintenance using TLS alone: 1) As passengers and cars use the road being surveyed during measurements, and available space for instrumentation setup is limited, it is sometimes difficult to set up TLS.

2) TLS can only provide high density measurements in a limited range (10m). Part of the road that was surveyed used UAV photogrammetry and SFM. The point cloud was combined with that from TLS, which was used to scan a bridge, including sides and lower works. The inaccuracy for the bridge was an effective length of 1.2 cm and an effective width of 1.9 cm, and the three-dimensional data described the structure of the bridge with high accuracy. The combined point cloud could be used to develop a road maintenance management system that accumulates data and refers to the inspection results and repair information in three dimensions.

The existing literature mainly covered the registration of imagery with TLS and ALS. The fusion and registration of UAV LIDAR with imagery collected by an onboard camera has not been well documented. It is one of the emerging technologies that will soon find applications in construction and civil engineering.

5. Applications on environmental applications and disaster management

Similar to the applications in the construction industry, SFM and UAV photogrammetry have been used successfully for data collection in environmental applications and disaster management, especially in coastal settings. The use of UAVs has been found to be a convenient, low-cost, and less environmentally invasive technique to capture coastal data, as well as having the ability to capture larger spatial areas and quickly without having to interpolate between points. Data analysis of coastal dunes, coastline change, and coastal cliffs have been well studied using SFM. The SFM data have been comparable to the data collected from TLS, with differences within millimeters. In most cases, researchers have used the software Agisoft to process the UAV imagery, which is also a popular choice in construction industry. It was also found that the number and distribution of GCPs play an important role in reducing the errors in the point cloud. Most substantial errors have been associated with areas of vegetation.

5.1 UAV Photogrammetry and SFM

The resolution in the point cloud has been proven to work well enough to capture small scale features within the environments, such as sand ripples. To capture the best imagery, it was also found that the camera should be set to a wide angle and fixed focal length, have low sensitivity and high depth of field, and have at least 80% overlap between images. These recommendations are similar to those found in construction applications, although the point cloud is usually constructed for a greater area. However, some of the limitations associated with UAVs are the necessity for good weather conditions and visibility, good quality control points. Some manual processing is still required.

Among the different types of natural disasters, **floods** are the most devastating, widespread, and frequent (Hashemi-Beni, Jones, Thompson, Johnson & Gebrehiwot, 2018). They account for approximately 30% of the total loss caused by natural disasters. They are also one of the biggest challenges faced in disaster management in North Carolina. The reliability and accuracy of flood assessment maps is dependent on the quality of the DEM, which could be generated with UAV photogrammetry. This study investigated the quality of UAV-based DEM and evaluated the extent of a flood event in Princeville, North Carolina during Hurricane Matthew. Comparison against the

US Geologic Survey (USGS) stream gauge station and LIDAR data showed that the SFM error is less than 30 cm.

Without direct geo-referencing, the performance of SFM is largely dependent on the **GCPs**. In (Goldstein, Oliver, Devries, Moore & Jass, 2015) UAV photogrammetry and SFM were used to analyze a coastal cliff setting in Hog Island, VA. SFM requires images to be taken of an object at different angles and then are combined to create a point cloud for analysis. The authors purposely altered the number of GCPs used from 5 to 30, and repeated SFM 10 different times Agisoft. It was found that the accuracy did not increase significantly after the use of 10 GCPs in this project. The errors with 30 GCPs are roughly the same level as that with 10. The root mean square error remained constant at 4 cm with at least 10 GCPs. Obviously the optimum number and distribution of GCPs are dependent on the actual project and the target performance. The performance reported in (Goldstein et al., 2015) seems representative for small UAVs, sufficient GCPs and Agisoft SFM.

Ruessink, Arens, Kuipers & Donker (2018) collected geomorphic change data of a foredune system between May 2013 and April 2016 at Dutch National Park Zuid-Kennemerland, Netherlands. 40 GCPs were used in the study area, all measured for accuracy using a GNSS-RTK. Agisoft was also used to analyze 700-1400 images. The over-all **accuracy** of the SFM point cloud was between 4 cm and 5 cm. (Root mean square was between 1.5 cm and 2.5 cm in the xy direction and 3 cm for the z direction.)

As afore mentioned, SFM in environmental studies is largely dependent on commercial software. (Jaud, Delacourt, Dantec, Allemand, Ammann, Grandjean, ... Floc'H, 2019) showed long-term monitoring of Porsmilin Beach using SFM. The authors originally used custom software programmed in MATLAB for data processing and analysis; but later realized that Agisoft and MicMac software was more useful. DEMs of Difference (DoD) were created to model coastal beach evolution and sediment budget changes. The **accuracy** was reported to be 3 cm in the vertical and horizontal directions, which was consistent with other work reported in literature.

Similar **accuracy** was achieved in (Papakonstantinou, Topouzelis & Pavlogeorgatos, 2016), which used UAV photogrammetry and SFM to map the Greece coastlines. This work also used Agisoft for SFM and geographic object-based image analysis for coastline detection. It was concluded that SFM point cloud fills in the gap between high-accuracy ground survey and large-scaled ALS.

In (Sturdivant, Lentz, Thieler, Farris, Weber, Remsen, ... Henderson, 2017), UAV imagery was collected over coastal features in Black Beach, MA. 250 images were collected at an altitude of 35 m and a near nadir angle. GCPs were used and surveyed in with a GNSS-RTK. Agisoft was used for SFM, while MATLAB was used to extract shorelines and foredune toe and crest positions. It was concluded that the UAV imagery was able to cover a larger spatial area and at **lower resolutions** without affecting the error negatively. However, UAVs do have some limitations such as: weather conditions and quality of control points. The GCPs had centimeter-level positioning accuracy. It reported SFM error of 6.1 cm in the horizontal and 2.8 cm in the vertical. Error increased in areas where there was more vegetation.

There are other SFM software options used in these applications. (Kim, Park, Han, Son, Lee, Han, ... Kim, 2019) reported results using **Pix4D** in monitoring coastal settings in Imiang Beach, Busan, Korea. A total of 40 GCPs were used for surveying and were measured with a GNSS-RTK and a total of 21 stations were set up for the use of the TLS. The error had a root mean square error of 4 cm.

James, Ilic, & Ružić, (2013) discussed how SFM techniques were used to analyze coastal cliff erosion in Sunderland Point, Morecambre Bay, UK. A camera with a wide angle and fixed focal length lens was used for data capture. The camera was UAV compatible, but was not actually mounted on a UAV. Two **open-source software** were used for data analysis: combination of Bundler and PMVS2 and 123D catch. Compared against TLS, the data product error is approximately 2 cm. It was noted that SFM was good at detecting small geomorphic changes and was an appropriate method for monitoring coastal changes.

In existing literature, TLS is the most commonly used tool for 3D modeling in these applications and was often used as the **truth reference** to gauge the accuracy of SFM. (Medjkane, Maquaire, Costa, Roulland, Letortu, Fauchard, ... Davidson, 2018) compared SFM to TLS data to justify its accuracy in determining areas of erosion and deposition in coastal features. The Vaches-Noires coastal cliffs located in Normandy, France were the object of study for this research to understand whether SFM would be a suitable approach for coastal monitoring. Overall, SFM approaches seem to be comparable to that of the TLS and therefore are accurate and reliable. Agisoft, Adobe, and Riscan Pro 2.0 were used for the data processing and analysis of the SFM and TLS data.

It is concluded that centimeter-level accuracy is achievable in UAV photogrammetry-based point cloud that is used to model environmental changes in coastal areas with a reputable SFM software.

5.2 UAV LIDAR

Similar to the findings by the construction industry, application of UAV LIDAR in environmental monitoring and disaster management are getting more attention recently (Terra news, 2019). Some of the literature in the previous section is also applicable to these applications and will not be repeated in this section.

Jaboyedoff, Oppikofer, Abellán, Derron, Loye, Metzger, & Pedrizzini (2012) presented a short history of laser scanner technologies in geosciences used for imaging relief by high-resolution DEMs or 3D models. A general overview of light detection and ranging (LIDAR) techniques applied to landslides was followed by a review of different applications of LIDAR for landslide, rockfall and debris-flow. These applications were classified as: 1) detection and characterization of mass movements; 2) hazard assessment and susceptibility mapping; 3) modeling; 4) monitoring. This review emphasizes how LIDAR-derived high resolution DEMs can be used to investigate any type of landslides. Although not included in this review yet, UAV LIDARs today are capable of some of the applications mentioned in this work.

Researchers started with low-cost LIDARs or MLS. For example, Nasrollahi, Bolourian, Zhu & Hammad (2018) proposed to use more affordable 2D LIDARs in the inspection and maintenance of bridges. They proposed to add additional mechanism to rotate the LIDAR and effectively turn a 2D LIDAR into a 3D LIDAR. As 3D UAV LIDARs are becoming smaller and more affordable (Sick, 2017) (Velodyne, 2019), there will be less benefit in using a 2D LIDAR.

Flener, Vaaja, Jaakkola, Krooks, Kaartinen, Kukko, Kasvi, Hyyppä, Hyyppä & Alho (2013) created high-resolution 3D models of river channels and their floodplains for a sub-arctic river by combining MLS with UAV photogrammetry. They achieved centimeter-level accuracy in the models, and were able to detect change of vertical level over a year. They used TLS as a truth reference.

Assenbaum (2018) discussed application of UAV LIDAR on the French Mediterranean coast. It was a complex natural environment where geology, climate and the sea interact and continuously reshape

the landscape. Coastal erosion and the availability of drinking water were two major coastal management issues that necessitate precise monitoring of the morphological changes to the shoreline. UAV LIDAR used in this region to produce comprehensive topographic surveys.

A comparison between the land survey and the LIDAR point cloud revealed an average bias of 4.0 cm and a standard deviation of 9.5 cm in the vertical direction. The expected performance was 2.5 to 5.0 cm on hard, well-defined surfaces like roads or concrete surfaces. These results were consistent with expected sensor capability. The 900 m study area could be surveyed by UAV LIDAR within minutes.

Populus (2019) also argued that the main reason for using LIDAR in the coastal zone is its capacity of rapidly covering large areas. UAVs typically cover about 20 km²; or over 50 km² per hour or more for hydrographic and topographic modes, respectively. It would be crucial for applications that only have a short time window.

The unique sensor setup discussed in this work also included a Hydrographic LIDAR that can provide uniform and dense data in even the shallowest water.

Shaw et al. (2019) directly compared UAV LIDAR with SFM in analyzing coastal changes pre- and post-storm events at Wamboro Sound, Safety Bay, Australia. Either method was able to produce accurate point cloud. SFM accuracy as at centimeter level. However, adding LIDAR to SFM helped cover the gap in SFM point cloud where GCPs could not be surveyed with GNSS-RTK, Total Station or TLS.

In these recent publications, a consensus was formed that:

- LIDAR provides a more accurate point cloud when **vegetation** is present, which is the case in some dune areas.

It is consistent with the findings of the construction industry.

- LIDAR provides coverage on where SFM or GCPs are not available.
- LIDAR does **NOT** seem to provide better accuracy than SFM.

- LIDAR data can be collected and processed **faster** than photogrammetry.

It is a feature of UAV LIDAR that is often over-looked by the construction industry. SFM needs overlapped imagery from multiple perspective. Therefore, it will take longer to cover the same area with UAV photogrammetry than LIDAR. Data processing is also more straightforward with direct geo-referencing.

With a worksite of limited size, the difference in data collection and processing time may be insignificant. However, it would make a more significant difference for large areas, which is typical for disaster management applications. Furthermore, for these applications, time and efficiency may be of a greater concern than monitoring construction worksites.

Some researchers also suspected that LIDAR could be more reliable than photogrammetry over weakly textured surfaces. A high-resolution camera on a low-flying UAV could compensate for that, at a potential cost of efficiency.

Finally, Serifoglu Yilmaz, Yilmaz & GÜNGÖR (2018) investigated the removal of ground covering objects including vegetation via ground filtering, in several different SFM and LIDAR processing software. This study compared the performances of seven widely used ground filtering algorithms on UAV-based point clouds in commonly used software: 1) the adaptive triangulated irregular network implemented in Agisoft, 2) the multi-scale curvature classification implemented into the commercial global mapper software, 3) the cloth simulation filtering (CSF) applied with a MATLAB script, 4) the interpolation-based Boise Centre Aerospace Laboratory-lidar algorithm embedded in the commercial environment for visualizing images software, 5) the interpolation-based gLiDAR non-commercial software, 6) the 2D progressive morphological algorithms, and 7) elevation threshold with expand window algorithms embedded in the non-commercial airborne lidar data processing and analysis tools software. The results showed that the CSF algorithm presented the best filtering results.

6. State and Federal Regulations

Since FAA published part 107 in 2016, rules and regulations before that became less relevant. This review focuses on publications after 2016.

Cracknell (2017) described the development of UAV regulations in multiple countries. This research focused on Australia and UK as models to look towards, since the UAV regulations were well defined in both countries. Most European countries already have well-developed sets of laws or regulations regarding the operation of drones in their countries. The European Union had recently released the European Aviation Safety Agency's Prototype Commission Regulation on Unmanned Aircraft Operations in 2016. With respect to international drone laws, this article mentioned how all civilian, unmanned aircraft was subject to Article 8 of the Convention on International Civil Aviation of 1944. However, Article 8 wasn't necessarily productive or useful at the current time as a result of lack of enforcement.

Stöcker, Bennett, Nex, Gerke & Zevenbergen (2017) discussed global UAV regulations as of 2017. The goal of this work was to compile an adequate list of regulations dealing with UAVs by looking through multiple data sources and using a comparative analysis. Comparisons were made between countries, in terms of applicability, technical requirements, operational limits, administrative procedures, human resource requirements, and Implementation of ethical constraints. A risk-based approach was found to be the preferred UAV regulation strategy overall in the countries studied. The regulations target the management of risks and minimization of perceived harms. Within the context of UAVs, the main harms are malfunction, mid-air collisions and consequent damages to people and property on the ground. It was found in this work that UAV regulations as of 2017 focused on targeting the regulated use of airspace by UAVs; imposing operational limitations; and the administrative procedures of flight permissions, pilot licenses and data collection authorization.

Okpala, Nnaji, & Awolusi (2019) assessed limitations to national regulations of UAVs, particularly in a construction setting. This was completed by conducting a global literature search on the standards and regulations for many of the technologies used in the construction industry, including LIDAR and UAVs. It was found at the time of this search that there were no regulations for using LIDAR in the construction industry. The researchers were also unable to find any sort of standards for UAVs that applied strictly to the construction industry besides FAA part 107.

Gheisari & Esmaceli (2019) recognized that the construction industry had the potential to greatly increase safety and efficiency on the job site, particularly in safety inspections. This article discussed the opinions of safety managers and their thoughts on the implementation of UAVs. As of 2019, the construction industry was found as the second highest economic market sector for UAVs, with agriculture in first. It was found that various monitoring tasks such as cranes in the proximity of overhead power lines, are the most important safety-related tasks that might benefit from using UAVs on a construction project. It also found three most important technical features on the UAV were the camera movability, sense-and-avoid capability, and a real-time video communication feed.

A list of state regulations can be found in (UAV coach, 2019).

Alaska

<https://uavcoach.com/drone-laws-alaska/>

This website looks at the specific federal and state drone regulations in Alaska. There are currently no state laws that relate to the hobby or commercial flying of UAVs. The one state law in Alaska relates to law enforcement, and how the save the drone images.

Arizona

<https://uavcoach.com/drone-laws-arizona/>

Arizona has one state law on drone usage. SB 1449 prohibits UAS's from interfering with police, firefighters, or manned aircraft. Drones can't be flown within dangerous proximity of people or property. UAS also can't be flown within 500 ft horizontally or 250 ft vertically to any 'critical facility'. Additionally, there must be at least one park that allows drones in cities that have more than one park. Finally, individual cities are prohibited from creating local drone laws.

Arkansas

<https://uavcoach.com/drone-laws-arkansas/>

Arkansas has multiple state drone laws. Regulation HB 1349 prohibits drones from being used to record someone who has an expectation of privacy. HB 1770 prohibits using drones to collect

information on critical infrastructure without consent. Arkansas State Parks - State Park Regulation prohibits the use of drones in the state parks without a special use permit.

California

<https://uavcoach.com/drone-laws-california/>

California has three state laws on drone usage. SB 807 protects the rights of first responders in the case that they damage an interfering UAS while providing emergency services. AB 1680 prohibits flying a drone that interferes with first responders during emergencies. AB prohibits interfering with an individual's privacy without their consent.

Colorado

<https://uavcoach.com/drone-laws-colorado/>

Colorado has two state laws relating to drone regulations. HB 1070 says that the Center of Excellence in the Department of Public Safety must determine ways to use UAS within local and state government activities relating to firefighting, search and rescue, and emergency management to name a few functions. The Colorado State Parks Regulation #100-c.24 prohibits drone use in state parks except for in the model airfields of Cheery Creek State Park and Chatfield State Park. A few additional parks have offered special use permits.

Connecticut

<https://uavcoach.com/drone-laws-connecticut/>

Regulation SB 975 prohibits the regulation of drones by municipalities but does allow water companies to regulate drone usage over public land and water supply. DEEP 23-4-1 prohibits drone flights at state parks, state forests, or any Department of Energy and Environmental Protection lands without a special use license.

Delaware

<https://uavcoach.com/drone-laws-delaware/>

Delaware has one state drone regulation. HB 195 prohibits flying drones over events with over 5,000 people. It also prohibits flying drones over critical infrastructure.

Florida

<https://uavcoach.com/drone-laws-florida/>

Florida has multiple state drone regulations. HB 1027 allows only Florida Legislature to make state drone laws, but allows local governments to make regulations for nuisance flying or other minor infractions. Flying near critical infrastructure is also illegal, as is flying a weaponized UAS. SB 766 protects the privacy of individuals and private property if there's a reasonable expectation of privacy. SB 92 limits law enforcement's use of drones. Florida Administrative Code 51-4.003 prohibits the use of drones on lands such as state parks and forests, without authorization, unless the flight is on a helispot or runway. Florida Administrative Code 40C-9.320 makes it illegal for drones to take off/land on district land without a special use authorization.

Georgia

<https://uavcoach.com/drone-laws-georgia/>

State regulation HB 481 allows state and local governments to regulate the launching and landing of UAV's on public property. Georgia Department of Natural Resources Park Rules and Regulations prohibits the use of drones at state parks or historic sites without a waiver, which are occasionally approved for professional commercial projects.

Hawaii

<https://uavcoach.com/drone-laws-hawaii/>

Hawaii has one state law regarding drone usage. SB 661 created a chief operating position for the UAS test site and created an advisory board for the test site.

Idaho

<https://uavcoach.com/drone-laws-idaho/>

Idaho has two state laws for drone usage. Idaho Code 36-1101 prohibits using drones to track animals, particularly for hunting purposes. Idaho Code 21-213 requires law enforcement to have a warrant in order to use a drone.

Illinois

<https://uavcoach.com/drone-laws-illinois/>

Illinois has multiple drone regulations specific to the state. SB 2937 allows law enforcement to use UAVs in the case where public safety is in question. HB 1652 prohibits drone use that interferes with hunter or fisherman activities. SB 1587 allows law enforcement to use drones in cases such as terrorist attacks. SB 3291 states that cities aren't able to create drone regulations unless they have a population greater than 1,000,000 people.

Indiana

<https://uavcoach.com/drone-laws-indiana/>

Indiana has five state drone laws. SB 299 prohibits sex offenders from following or contacting someone with the use of a drone. It also prohibits flying a drone in a way that interferes with public safety official's work. HB 1013 allows drone use at a traffic crash site. HB 1246 prohibits using drones to track animals while hunting. HB 1009 outlines guidelines for police use of drones. IAC 312 8-2-8 prohibits drone use on DNR land without permission.

Iowa

<https://uavcoach.com/drone-laws-iowa/>

Iowa has one state drone law. HB 2289 prohibits law enforcement from using drones to enforce traffic laws.

Kansas

<https://uavcoach.com/drone-laws-kansas/>

Kansas has one state drone regulation. SB 319 includes the use of some drones for their definition of stalking.

Kentucky

<https://uavcoach.com/drone-laws-kentucky/>

Kentucky has one state drone law. HB 540 allows airports to create maps of where UAVs are not permitted to fly.

Louisiana

<https://uavcoach.com/drone-laws-louisiana/>

Louisiana has eight state drone laws. SB 69 gives the state the power to regulate UAVs over local regulations. SB 73 prohibits interfering with police officers using a drone. HB 19 prohibits surveying school or correctional facility sites with drones. HB 335 regulates registration and license fees for UAVs. HB 635 makes using UAS for voyeurism illegal. SB 141 defines what is criminal trespass by unmanned aircraft. SB 183 regulates UAS in commercial agriculture operations. HB 1029 prohibits using drones to survey facilities without the consent of the owner.

Maine

<https://uavcoach.com/drone-laws-maine/>

The LD 25 regulation in Maine requires law enforcement to have approval before using drones. The Bureau of Parks and Lands Drone Policy prohibits drone use in state parks, historic sites, and boat launches without a special activity permit.

Maryland

<https://uavcoach.com/drone-laws-maryland/>

Maryland has one state drone law. SB 370 states that the state laws pre-empt county authority.

Michigan

<https://uavcoach.com/drone-laws-michigan/>

Michigan has two state drone laws. SB 992 prohibits local government from regulating UAVs, allows commercial and hobby drone operation, prohibits drone interference with emergency

personnel, and prohibits sex offenders from following or photographing the person they are forbidden to contact. SB 54 prohibits using a drone to harass hunters.

Minnesota

<https://uavcoach.com/drone-laws-minnesota/>

There are multiple state drone laws in Minnesota. The MN DOT Aeronautics Rules Chapter 8800 requires commercial drone operators to pay \$30 to get the Commercial Operations License. The Minnesota Statute 360.59 requires commercial operators to have drone insurance. Minnesota Statute 360.60 requires commercial and recreational drone pilots to register their drone with the MN DOT. SF 550 allots \$348,000 to use UAVs for monitoring natural resources and the moose population.

Mississippi

<https://uavcoach.com/drone-laws-mississippi/>

Mississippi has one state drone law. SB 2022 considers using drones for ‘peeping tom’ activities a felony.

Montana

<https://uavcoach.com/drone-laws-montana/>

Montana has two state laws concerning the use of drones. Hb 644 prohibits the use of UAS in interfering with wildfire suppression efforts. SB 196 limits drone information that can be used as evidence in a prosecution.

Nevada

<https://uavcoach.com/drone-laws-nevada/>

The state of Nevada has one state drone law. AB 239 prohibits weaponization of UAVs, using UAVs within a distance of critical facilities and airports, and limits UAV use by law enforcement.

New Hampshire

<https://uavcoach.com/drone-laws-new-hampshire/>

New Hampshire has one state drone law. SB 222 prohibits the use of UAS for hunting, fishing, or trapping.

New Jersey

<https://uavcoach.com/drone-laws-new-jersey/>

The regulation SB 3370 states that owners of critical infrastructure can apply to limit drones near the infrastructure, protects public safety and security, protects the rights of first responders, prohibits the operation of drones while under the influence of drugs or alcohol, and pre-empts local governments from contradicting these rules. Additionally, the New Jersey State Park Service Policy prohibits flying drones within lands and waters managed by the state park without prior approval.

New Mexico

<https://uavcoach.com/drone-laws-new-mexico/>

New Mexico has one state drone law. SB 556 prohibits using drones for unwanted surveillance.

North Carolina

<https://uavcoach.com/drone-laws-north-carolina/>

Multiple state laws on drone regulation exist in North Carolina. HB 128 prohibits flying drones near correctional facilities. HB 337 allows UAVs for emergency management activities such as search and rescue or damage assessment. SB446 allows the Chief Information Officer to buy and use a UAS by the state. NCAC 13B.1204 prohibits drones from landing or taking off within a state park without a special permit by the park. Lastly, SB 744 creates specific regulations for commercial, recreational, and government operators. Commercial regulations include that drone operators flying under part 107 or 333 exemption need to have a commercial operator's permit and must pass the NCDOT knowledge test and apply for a state permit. To get the permit, pilots need proof of a remote pilot certificate or equal alternative. Recreational pilots don't need a license or permit from the Division of Aviation, but need to follow NC UAS regulations. Government pilots need to pass the NCDOT UAS knowledge test and apply for a state permit. One example of a local regulation is the city of Raleigh- Parks, Recreation, and Cultural Resources Drone Policy. This policy outlines which parks

and recreational areas allow drones. Drone flight is not allowed in nature preserves, nature parks, wetland centers, or landing/taking off from cemeteries or over lakes.

North Dakota

<https://uavcoach.com/drone-laws-north-dakota/>

North Dakota has one state drone law. HB 1328 prohibits using lethal weapons on drones, and limits the use of UAS for surveillance.

Ohio

<https://uavcoach.com/drone-laws-ohio/>

Ohio has one state drone law. HB 292 created the aerospace and aviation technology committee.

Oklahoma

<https://uavcoach.com/drone-laws-oklahoma/>

Oklahoma has one state drone law. HB 2559 prohibits any drone within 400 feet of a critical infrastructure facility.

Oregon

<https://uavcoach.com/drone-laws-oregon/>

Oregon has four state drone laws. HB 3047 prohibits the weaponization of drones, allows law enforcement certain situations where drone use is acceptable, and flying UAVs over private property that annoys the owner. HB 4066 modifies definitions of weaponized UAVs, and prohibits drones near critical infrastructure. SB 5702 clarifies registration fees for public UAS. HB 2710 refines regulations for drones in law enforcement, requires registration of drones, refines penalties for drone weaponization, allows conditions where land owners can fly lower than 400 feet over their property, and looks at private party registration of aircraft.

Pennsylvania

<https://uavcoach.com/drone-laws-pennsylvania/>

The state of Pennsylvania has multiple laws on drone usage. Title 18 Sec 3505 people on private property from drone harassment. Title 53 Sec. 305 acts as a pre-empt which supersedes any rule regulating ownership of UAV. Drones can be used only in designated flying sites within certain state parks.

Rhode Island

<https://uavcoach.com/drone-laws-rhode-island/>

Rhode Island has one state drone law. HB7511 gives the state of Rhode and the Airport Corporation exclusive authority in UAS regulation.

South Dakota

<https://uavcoach.com/drone-laws-south-dakota/>

South Dakota has two state drone laws. SB 22 exempts UAVs weighing less than 55 from needing to follow registration requirements. SB 80 prohibits flying drones over military or correctional facilities, or intentionally invading someone's privacy.

Tennessee

<https://uavcoach.com/drone-laws-tennessee/>

Tennessee has six state drone laws. SB 2106 prohibits drones within 250 feet of critical infrastructure. HB 2376 states that UAVs can be used by people of both public and private institutions of higher education. HB 153 prohibits drones over fireworks shows. SB 1777 prohibits using drones for video surveillance of hunters and fishers without permission. SB 1892 protects privacy rights of individuals. SB 796 allows law enforcement certain occasions where drone use is permitted.

Texas

<https://uavcoach.com/drone-laws-texas/>

Texas has multiple state drone laws. SB 840 permits only law enforcement to take drone images within 25 miles of the boarder for security reasons. HB 1424 prohibits drones over correctional and

detention facilities, as well as sports venues. HB 1643 prohibits local government from regulating UAVs. HB 2167 allows individuals of certain professions to use UAVs to assist in their job. HB 1481 clarifies the height a drone must reach to be over a critical infrastructure facility. Texas Administrative code 65.152 prohibits hunting or tracking wildlife. The Texas Parks and Wildlife Policy states drones aren't allowed in state parks except in the specified zones in Lake Whitney and San Angelo state parks. Permits for other parks can be permitted by application.

Utah

<https://uavcoach.com/drone-laws-utah/>

The state of Utah has five drone laws. HB 217 prevents the harassment of livestock with drones. SB 111 defines regulations for law enforcement use of drones, prohibits weaponized drones, and protects personal privacy. HB 296 allows law enforcement to use drones to locate a missing person. SB 167 requires law enforcement to have a warrant to use data from a UAV. SB 196 requires law enforcement to have a warrant before using UAVs in areas where people have a reasonable expectation of privacy.

Vermont

<https://uavcoach.com/drone-laws-vermont/>

Vermont has one state law for drones. SB 155 regulates the use of drones by law enforcement.

Virginia

<https://uavcoach.com/drone-laws-virginia/>

Virginia has multiple state drone laws. HB 2350 makes it illegal to spy with a drone by trespassing. SB 873 allows the fire chief full authority over the airspace in an emergency. HB 412 prohibits regulation of UAS by local governments. HB 2125 makes it necessary for law enforcement to have a warrant before using a drone. Code of Virginia 4VAC5-30-400 requires a special use permit for drone use at the state parks. Only commercial or research drone operations can get a special use permit.

Washington

<https://uavcoach.com/drone-laws-washington/>

Washington has one state law for drones. WAC 352-32-130 states that permission must be granted to fly drones in the state parks.

West Virginia

<https://uavcoach.com/drone-laws-west-virginia/>

West Virginia has two state drone laws. HB 2515 prohibits hunting with UAS. HB 4607 requires permission from the State Park Superintendent to fly a drone in any state park.

Wisconsin

<https://uavcoach.com/drone-laws-wisconsin/>

Wisconsin has two state drone laws. SB 338 prohibits using drones to interfere with hunting, fishing, or trapping activities. AB 670 prohibits operating UAVs over correctional facilities.

Wyoming

<https://uavcoach.com/drone-laws-wyoming/>

Wyoming has one state drone law. SF 170 is for the Wyoming Aeronautics Commission, requiring it to regulate where UAVs can take off and land.

States with no specific state UAV regulations: Alabama; Massachusetts; Missouri; Nebraska; New York; South Carolina.

These regulations do address the legal use of UAV photos. However, states do not usually set regulations on related technologies, such as GCPs in SFM and LIDAR. Academic and industrial organizations offer recommendations on the best practices, such as (GCPS, 2019) (Coastal Wiki, 2019).

7. Emerging technologies

As can be seen in the previous sections of this review report, technologies in remote sensing, computer vision and image processing software, computational hardware, navigation and robotics have all been developed at a rapid pace in the last few years. This section focuses on the integration, visualization and applications of sensor data product.

Although the principle of SFM has been well known for decades (Triggs et al., 2000). Efficient and robust commercial solution took years of development in image processing software and computational hardware. There have been several well-known software packages available today that can register images to each other, and/or produce a dense 3D point cloud. (von Übel, 2019) provided a list of software developers, some of which had been included in this review already:

- COLMAP
- Meshroom
- MicMac
- Regard3D
- VisualSFM
- OpenMVG
- WebODM
- Agisoft
- RealityCapture
- Autodesk ReCap
- Photomodeler
- SOCET GXP
- 3DF Zephyr
- DroneDeploy
- Pix4D
- iWitnessPRO
- Bentley ContextCapture
- IMAGINE Photogrammetry

- Trimble Inpho

Some of the developers of these packages also offer software for point cloud processing. In addition, LIDAR manufactures such as Leica has their own software solution (Leica, 2019). There are fewer options to autonomously register images to 3D point cloud, and to compare or merge different sets of point cloud. Examples include (Autodesk, 2019) (Meshlab, 2019) and (Cloudcompare, 2019).

There are a few challenges in registering images with UAV LIDAR 3D point cloud. 1) The point cloud and imagery are both considered “unstructured scan” in (Autodesk, 2019). Manual input is often needed in registration with today’s software solutions. 2) The high noise level on each point in the point cloud make it difficult to register a “free form” object. (Wang et al. 2018) 3) Some UAV LIDARs are not able to produce a 3D “image”. A direct 3D image requires image-like intensity values measured in LIDAR returns, in addition to distance, and a very dense 3D point cloud. Either or both features are not available in low-cost UAV LIDARs today, although LIDARs with these features have become more affordable recently. As a result, image-based and intensity-based autonomous registration methods such as (Parmehr et al., 2012) are not applicable.

Autonomous image and 3D point cloud technology could make it a lot more convenient to fuse data from imagery, SFM, DEM, LIDARs and other data sources. The data product will provide direct geo-referenced imagery without the limitations faced with SFM or LIDAR alone. It will create 3D models with proper surface and texture representation, which is the fundamental model used to create virtual reality (VR), augmented reality (AR) (Lee & Park, 2019) and mixed reality (XR). 3D visualization with VR, AR and XR technologies will soon find more applications in construction management, environmental monitoring and disaster management.

References

1. Agisoft (2019). Tutorial (Beginner level): Orthomosaic and DEM Generation with Agisoft PhotoScan Pro 1.3 (with GCPs). Available:
[https://www.agisoft.com/pdf/PS_1.3%20-Tutorial%20\(BL\)%20-%20Orthophoto,%20DEM%20\(GCPs\).pdf](https://www.agisoft.com/pdf/PS_1.3%20-Tutorial%20(BL)%20-%20Orthophoto,%20DEM%20(GCPs).pdf)
Retrieved on 12/01/2019.
2. Ajayi, O. G., Palmer, M., & Salubi, A. A. (2018). Modelling farmland topography for suitable site selection of dam construction using unmanned aerial vehicle (UAV) photogrammetry. *Remote Sensing Applications: Society and Environment*, 11, 220-230.
3. Álvares, J. S., Costa, D. B., & de Melo, R. R. S. (2018). Exploratory study of using unmanned aerial system imagery for construction site 3D mapping. *Construction Innovation*, 18(3), 301-320.
4. Assenbaum, M. (2018). Monitoring coastal erosion with UAV lidar. *GIM International*. 32. 18-21.
5. Autodesk. (2019). Registering Unstructured Scans. Available:
<https://knowledge.autodesk.com/support/recap/learn-explore/caas/CloudHelp/cloudhelp/2018/ENU/Reality-Capture/files/GUID-AF55A2EB-FCE8-4982-B3D6-CEAD5732DF03-htm.html>
Retrieved on 12/01/2019.
6. Cloudcompare. (2019). 3D point cloud and mesh processing software. Available:
<https://www.danielgm.net/cc/>
7. Cracknell, A. (2017). UAVs: regulations and law enforcement. *International Journal of Remote Sensing* 38(8,10): 3054-3067
8. Coastal Wiki. (2019). Use of Lidar for coastal habitat mapping. Available:
http://www.coastalwiki.org/wiki/Use_of_Lidar_for_coastal_habitat_mapping

Retrieved on 12/01/2019.

9. Dastgheibifard, Soroush & Asnafi, Mahsa. (2018). A Review on Potential Applications of Unmanned Aerial Vehicle for Construction Industry. 10.26392/SSM.2018.01.02.044.
10. de Melo, RR. Costa, DB. Álvares, JS. & Irizarry, J. (2017). Applicability of unmanned aerial system (UAS) for safety inspection on construction sites. Safety science. Oct 1;98:174-85.
11. DJI. (2019). Next Generation Mapping – Saving Time in Construction Surveying With Drones. Available: <https://enterprise.dji.com/news/detail/next-generation-mapping>
Retrieved on 12/01/2019.
12. Eschmann, C. Kuo, C. & Boller, C. (2012). Unmanned aircraft systems for remote building inspection and monitoring. Proceedings of the 6th European Workshop on Structural Health Monitoring, Dresden, Germany. Vol. 36,
13. FAA. (2016) Part 107 of the Federal Aviation Regulations.
14. Fernandez, Galarreta J. Kerle, N. & Gerke, M. (2015). UAV-based urban structural damage assessment using object-based image analysis and semantic reasoning. Natural hazards and earth system sciences. 15(6):1087-101.
15. Flener, C., Vaaja, M., Jaakkola, A.; Krooks, A., Kaartinen, H., Kukko, A., Kasvi, E., Hyyppä, H., Hyyppä, J. & Alho, P. (2013). Seamless Mapping of River Channels at High Resolution Using Mobile LiDAR and UAV-Photography. Remote Sens., 5, 6382-6407.
16. Furukawa, Yasutaka. Ponce, Jean. (2019) CMVS. Available:
<https://github.com/pmoulon/CMVS-PMVS>
Retrieved on 12/01/2019.
17. GCPS. (2019). Creating Quality GCPs for Mapping Contour Lines. Available:
<https://www.groundcontrolpoints.com/mapping-contour-lines-using-gcps>

Retrieved on 12/01/2019.

18. Gheisari, M. & Esmacili, B. (2019). Applications and requirements of unmanned aerial systems (UASs) for construction safety. *Safety Science* 118(2019): 230-240
19. Goldstein, E. B., Oliver, A. R., Devries, E., Moore, L. J., & Jass, T. (2015). GCP requirements for structure-from-motion derived topography in low-slope coastal environments. doi: 10.7287/peerj.preprints.1444
20. Graham, Lewis. (2018) "Drone Mapping – SfM versus Low Precision LIDAR." Available: <https://support.geocue.com/drone-mapping-sfm-versus-low-precision-lidar/>
Retrieved on 10/24/2019.
21. Graham, Lewis. (2019) "Drone LIDAR Systems (Drone LIDAR Considerations)." Available:
<http://www.geocue.com>
Retrieved on 10/24/2019.
22. Grayson, B., Penna, N.T., Mills, J.P. & Grant, D.S. (2018), GPS precise point positioning for UAV photogrammetry. *Photogram Rec*, 33: 427-447. doi:10.1111/phor.12259
23. Guan, S. & Zhu, Z. (2019). UAS-Based 3D Reconstruction Imagery Error Analysis, *Structural Health Monitoring* 2019.
24. Guo, Q., Su, Y., Hu, T., Zhao, X., Wu, F., Li, Y., . . . Wang, X. (2017). An integrated UAV-borne lidar system for 3D habitat mapping in three forest ecosystems across china. *International Journal of Remote Sensing*, 38(8-10), 2954-2972.
doi:10.1080/01431161.2017.1285083
25. Hashemi-Beni, L. Jones, J. Thompson, G. Johnson, C. & Gebrehiwot, A. (2018). Challenges and opportunities for UAV-based digital elevation model generation for flood-risk management: A case of princeville, north carolina. *Sensors* 2018, 18, 3843.

26. Hamledari, H. Davari, S. Azar, E. McCabe, B. Flager, F. & Fischer, M. (2018). "UAV-Enabled Site-to-BIM Automation: Aerial Robotic-and Computer Vision-Based Development of As-Built/ As-Is BIMs and Quality Control", Available:
<https://cife.stanford.edu/TR230>
Retrieved on 12/01/2019.
27. Hartley, Richard & Zisserman, Andrew. (2014). Multiple View Geometry in Computer Vision, Second Edition, Cambridge University Press.
28. Hokuyo. (2012). Scanning Laser Range Finder UTM-30LX/LN Specification. Available:
<https://www.hokuyo-aut.jp/search/single.php?serial=169>
Retrieved on 09/01/2017.
29. Howard, John & Murashov, Vladimir & Branche, Christine. (2017). Unmanned aerial vehicles in construction and worker safety. *American Journal of Industrial Medicine*. 61. 10.1002/ajim.22782.
30. James, Mike & Ilic, S. & Ružić, Igor. (2013). Measuring 3D coastal change with a digital camera. 2013. 893-904.
31. Jaud, M., Delacourt, C., Dantec, N. L., Allemand, P., Ammann, J., Grandjean, P., ... Floc'H, F. (2019). Diachronic UAV Photogrammetry of a Sandy Beach in Brittany (France) for a Long-Term Coastal Observatory. *ISPRS International Journal of Geo-Information*, 8(6), 267. doi: 10.3390/ijgi8060267
32. Jaboyedoff, M., Oppikofer, T., Abellán, A., Derron, M., Loye, A., Metzger, R., & Pedrazzini, A. (2010). Use of LIDAR in landslide investigations: a review. *Natural Hazards*, 61, 5-28.
33. Karpowicz, K. (2014). The Use of Unmanned Aerial Systems for Steep Terrain Investigations

<https://dot.ca.gov/-/media/dot-media/programs/research-innovation-system-information/documents/f0016678-unmanned-aerial-systems-preliminary-investigation-rev8-14-14.pdf>

Retrieved on 12/01/2019.

34. Khaloo, A., Lattanzi, D., Cunningham, K., Dell'Andrea, R., & Riley, M. (2018). Unmanned aerial vehicle inspection of the Placer River Trail Bridge through image-based 3D modelling. *Structure and Infrastructure Engineering*, 14(1), 124-136.
35. Knight, Renee. (2019) LiDAR: Going Beyond Photogrammetry. *Inside Unmanned Systems*.
36. Kim, S., Park, S., Han, J., Son, S., Lee, S., Han, K., ... Kim, J. (2019). Feasibility of UAV Photogrammetry for Coastal Monitoring: A Case Study in Imlang Beach, South Korea. *Journal of Coastal Research*, 90(sp1), 386. doi: 10.2112/si90-049.1
37. Kubota^{1a}, S., Ho^{2b}, C., & Nishi^{2b}, K. (2019). Construction and Usage of Three-dimensional Data for Road Structures Using Terrestrial Laser Scanning and UAV with Photogrammetry. In ISARC. *Proceedings of the International Symposium on Automation and Robotics in Construction* (Vol. 36, pp. 136-143). IAARC Publications.
38. Laflamme, Simon, Turkan, Yelda & Tan, Liangyu., (2015). Bridge Structural Condition Assessment using 3D Imaging. *Civil, Construction and Environmental Engineering Conference Presentations and Proceedings*. 33.
39. Lee, K. W., & Park, J. K. (2019). Comparison of UAV image and UAV LiDAR for construction of 3D geospatial information. *Sensors and Materials*, 31(10), 3327. doi:10.18494/SAM.2019.2466
40. Leica. (2019). Cyclone 3D Point Cloud Processing Software. Available: <https://leica-geosystems.com/en-us/products/laser-scanners/software/leica-cyclone>
Retrieved on 12/01/2019.

41. Lowe, David G. (1999). "Object recognition from local scale-invariant features" (PDF). Proceedings of the International Conference on Computer Vision. 2. pp. 1150–1157. doi:10.1109/ICCV.1999.790410.
42. Mancini, F., Dubbini, M., Gattelli, M., Stecchi, F., Fabbri, S., & Gabbianelli, G. (2013). Using Unmanned Aerial Vehicles (UAV) for High-Resolution Reconstruction of Topography: The Structure from Motion Approach on Coastal Environments. Remote Sensing, 5(12), 6880–6898. doi: 10.3390/rs5126880
43. Mastin, A. Kepner J. & Fisher, J. (2009). Automatic registration of LIDAR and optical images of urban scenes. IEEE Conference on Computer Vision and Pattern Recognition, Miami, FL, pp. 2639-2646.
44. May, N., & Toth, C.K. (2007). Point Positioning Accuracy of Airborne Lidar Systems : A Rigorous Analysis. In: Stilla U et al (Eds) PIA07. International Archives of Photogrammetry, Remote Sensing and Spatial Information Sciences, 36
45. Medjkane, M., Maquaire, O., Costa, S., Roulland, T., Letortu, P., Fauchard, C., ... Davidson, R. (2018). High-resolution monitoring of complex coastal morphology changes: cross-efficiency of SfM and TLS-based survey (Vaches-Noires cliffs, Normandy, France). Landslides, 15(6), 1097–1108. doi: 10.1007/s10346-017-0942-4
46. Meshlab. (2019). Meshlab. Available: <http://www.meshlab.net/#>
Retrieved on 10/01/2018.
47. Moeini, Shahab. Oudjehane, Azzeddine. Baker, Tareq. & Hawkins, Wade. (2017). Application of an interrelated UAS - BIM system for construction progress monitoring, inspection and project management. Available:

http://pmsymposium.umd.edu/pm2017/wp-content/uploads/sites/3/2017/01/Application_of_an_interrelated_UAS_BIM-Azzeddine-Oudjehane-Mocini.pdf

Retrieved on 12/01/2019.

48. Micheletti, N., Chandler, Jim & Lane, Stuart. (2013). Structure from motion (SFM) photogrammetry. 1-12.
49. Microdrones. (2019). Fully Integrated Systems for Professionals. Available: <https://www.microdrones.com/en/integrated-systems/mdlidar/mdlidar3000dl/>
Retrieved on 12/01/2019.
50. Mill, Tarvo., Alt, Aivars & Liias, Roode. (2014). Combined 3D building surveying techniques-Terrestrial laser scanning (TLS) and total station surveying for BIM data management purposes. Journal of Civil Engineering and Management. 19. S23-S32. 10.3846/13923730.2013.795187.
51. Mostafa, Mohamed., Hutton, Joe., Reid, Blake & Hill, Richmond. (2003). GPS/IMU products -- the Applanix approach.
52. Nasrullah, Asgan Riza. (2016). Systematic Analysis of Unmanned Aerial Vehicle (UAV) Derived Product Quality. MS Thesis. University of Twente.
53. Nasrollahi, M., Bolourian, N., Zhu, Z., & Hammad, A. (2018). Designing LiDAR-equipped UAV platform for structural inspection. ISARC. Proceedings of the International Symposium on Automation and Robotics in Construction, 35, 1-8.
54. NovAtel. (2016). SPAN IMU-CPT. Available: <https://www.novatel.com/assets/Documents/Papers/IMU-CPT.pdf>
Retrieved on 10/01/2017.

55. Okpala, I., Nnaji, C. & Awolusi, I. (2019). Emerging Construction Technologies: State of Standard and Regulation Implementation. *Computing in Civil Engineering*.
doi:10.1061/9780784482438.020
56. Parmehr, E.G., Fraser, C.S., Zhang, C., & Leach, J. (2012). Automatic Registration of Aerial Images with 3D LiDAR Data Using a Hybrid Intensity-Based Method. *International Conference on Digital Image Computing Techniques and Applications (DICTA)*, Fremantle, WA, 2012, pp. 1-7.
57. Papakonstantinou, A., Topouzelis, K., & Pavlogeorgatos, G. (2016). Coastline Zones Identification and 3D Coastal Mapping Using UAV Spatial Data. *ISPRS International Journal of Geo-Information*, 5(6), 75. doi: 10.3390/ijgi5060075
58. Pix4D. (2017). Do RTK/PPK drones give you better results than GCPs? Available:
https://assets.ctfassets.net/go54bjdzbrgi/2VpGjAxJC2aaYIpsmFswD/3bcd8d512ccfe88ff63168e15051baee/BLOG_rtk-ppk-drones-gcp-comparison.pdf
Retrieved on 12/01/2019.
59. Pix4D. (2019). Pix4D. Available:
<https://pix4d.com>
Retrieved on 12/01/2019.
60. Populus, Jacques. (2019): Use of Lidar for coastal habitat mapping. Available:
http://www.coastalwiki.org/wiki/Use_of_Lidar_for_coastal_habitat_mapping
Retrieved on 12/01/2019.
61. Puri, N., & Turkan, Y. (2020). Bridge construction progress monitoring using lidar and 4D design models. *Automation in Construction*, 109, 102961.
62. Ravi, R., Lin, Y., Elbahnasawy, M., Shamseldin T. & Habib A. (2018). Bias Impact Analysis and Calibration of Terrestrial Mobile LiDAR System With Several Spinning Multibeam Laser

Scanners. IEEE Transactions on Geoscience and Remote Sensing, vol. 56, no. 9, pp. 5261-5275

63. Remondino, Fabio., Barazzetti, Luigi., Nex, Francesco., Scaioni, Marco. & Sarazzi, D. (2011). UAV photogrammetry for mapping and 3D modeling-Current status and future perspectives. ISPRS - International Archives of the Photogrammetry, Remote Sensing and Spatial Information Sciences. XXXVIII-1/C22. 10.5194/isprsarchives-XXXVIII-1-C22-25-2011.
64. Riegl. (2019). "Downward-Looking" LiDAR Sensor for Unmanned Laser Scanning". Available: <http://www.riegl.com/products/unmanned-scanning/riegl-minivux-1dl/>
Retrieved on 12/01/2019.
65. Ruessink, B., Arens, S., Kuipers, M., & Donker, J. (2018). Coastal dune dynamics in response to excavated foredune notches. *Aeolian Research*, 31, 3–17. doi:10.1016/j.aeolia.2017.07.002
66. Sanz-Ablanedo, E., Chandler, J.H., Rodríguez-Pérez, J.R. & Ordóñez, C. (2018). Accuracy of Unmanned Aerial Vehicle (UAV) and SfM Photogrammetry Survey as a Function of the Number and Location of GCPs Used. *Remote Sens.* 2018, 10, 1606
67. Serifoglu Yilmaz, C., Yilmaz, V., & Güngör, O. (2018) Investigating the performances of commercial and non-commercial software for ground filtering of UAV-based point clouds. *International Journal of Remote Sensing*, 39(15-16), 5016-5042. doi:10.1080/01431161.2017.1420942
68. Semyonov, Dmitry. (2011). Re: Algorithms used in Photoscan
Available: <https://www.agisoft.com/forum/index.php?topic=89.0>
Retrieved on 12/01/2019.
69. Shaw, L., Helmholz, P., Belton, D., & Addy, N. (2019). Comparison Of Uav Lidar And Imagery For Beach Monitoring. ISPRS - International Archives of the Photogrammetry,

Remote Sensing and Spatial Information Sciences, XLII-2/W13, 589–596. doi:
10.5194/isprs-archives-xlii-2-w13-589-2019

70. Sick. (2017). *Operating_instructions_LD_MRS_3D_LiDAR_sensors*. Available:
<https://www.sick.com/us/en/detection-and-ranging-solutions/3d-lidar-sensors/ld-mrs/c/g91913>
Retrieved on 10/01/2018.
71. Siebert, S., & Teizer, J. (2014). Mobile 3D mapping for surveying earthwork projects using an Unmanned Aerial Vehicle (UAV) system. *Automation in Construction*, 41, 1–14.
doi:10.1016/j.autcon.2014.01.004
72. Stöcker, C., Bennett, R., Nex, F., Gerke, M., & Zevenbergen, J. 2017. Review of the Current State of UAV Regulations. *Remote Sensing* 9(5): 459. DOI: 10.3390/rs9050459
73. Sturdivant, E., Lentz, E., Thieler, E. R., Farris, A., Weber, K., Remsen, D., ... Henderson, R. (2017). UAS-SfM for Coastal Research: Geomorphic Feature Extraction and Land Cover Classification from High-Resolution Elevation and Optical Imagery. *Remote Sensing*, 9(10), 1020. doi: 10.3390/rs9101020
74. Suárez, J.C., Ontiveros, C., Smith, S., & Snape, S. (2005). Use of airborne LiDAR and aerial photography in the estimation of individual tree heights in forestry. *Computers & Geosciences*, 31, 253-262.
75. Terra news. (2019). “Terra Drone Indonesia’s LiDAR mapping UAVs are helping Palu recover from 2018 double disaster.” Available:
<https://www.terra-drone.net/global/2019/05/15/terra-drone-indonesia-lidar-drones-for-disaster-recovery-palu/>
Retrieved on 12/01/2019.
76. Thuy, C. T., Watanabe, A., & Wakutsu, R. (2020). Cloud-Based 3D Data Processing and Modeling for UAV Application in Disaster Response and Construction Fields.

In Geotechnics for Sustainable Infrastructure Development (pp. 1177-1182). Springer, Singapore.

77. Trimble-Appplanix. (2019). APX-20 UAV High Performance GNSS-Inertial Solution with Dual IMU'S. Available:
https://www.appplanix.com/downloads/products/specs/APX20_UAV.pdf
Retrieved on 12/01/2019.
78. Triggs B., McLauchlan P.F., Hartley R.I., Fitzgibbon A.W. (2000) Bundle Adjustment — A Modern Synthesis. In: Triggs B., Zisserman A., Szeliski R. (eds) Vision Algorithms: Theory and Practice. IWVA 1999. Lecture Notes in Computer Science, vol 1883. Springer, Berlin, Heidelberg
79. Trimble. (2019). Trimble Inpho UASMaster. Available:
<https://geospatial.trimble.com/products-and-solutions/trimble-inpho-uasmaster>.
Retrieved on 12/01/2019.
80. Truong-Hong, Linh & Laefer, Debra. (2014). Application of Terrestrial Laser Scanner in Bridge Inspection: Review and an Opportunity. IABSE Symposium Report. 102. 10.2749/222137814814070190.
81. Tompkinson, William. (2019). Professional UAV lidar is (finally) focusing on the ground. Available:
<https://www.spar3d.com/blogs/measuring-the-value/professional-UAV-LIDAR-is-finally-focusing-on-the-ground/>
Retrieved on 12/01/2019.
82. Toth, Charles. & Grejner-Brzezinska, Dorota A. (2009). Airborne LiDAR Reflective Linear Feature Extraction for Strip Adjustment and Horizontal Accuracy Determination. Available:
<https://rosap.nsl.bts.gov/view/dot/18475>
Retrieved on 12/01/2019.

83. UAV coach. (2019). Master List of Drone Laws. Available:
<https://uavcoach.com/drone-laws/>
Retrieved on 12/01/2019.
84. von Übel, Max. (2019). Affordable and Easy 3D Scanning 2019 Best Photogrammetry Software. Available:
<https://all3dp.com/1/best-photogrammetry-software/>
Retrieved on 12/01/2019.
85. VectorNav. (2019). VectorNav Industrial Series. Available:
[https://www.vectornav.com/docs/default-source/product-brochures/industrial-series-product-brochure-\(12-0009\).pdf](https://www.vectornav.com/docs/default-source/product-brochures/industrial-series-product-brochure-(12-0009).pdf)
Retrieved on 12/01/2019.
86. Velodyne. (2019). VLP-16 User Manual63-9243 Rev. D. Available:
https://github.com/UCSD-E4E/aerial_lidar/blob/master/Datasheets%20and%20User%20Manuals/velodyne%20lidar%20datasheets/**VLP-16%20User%20Manual%20and%20Programming%20Guide%2063-9243%20Rev%20A.pdf
Retrieved on 12/01/2019.
87. Wang, George. Hollar, Donna. Sayger, Susan. Zhu, Zhen. Buckeridge, John. Li, Jie. Chong, Jimmy. Duffield, Colin. Ryu, Dongryeol. Hu, Wei. (2016). Risk Considerations in the Use of Unmanned Aerial Vehicles in the Construction Industry. The Journal of Risk Analysis and Crisis Response. 6. 10.2991/jrarc.2016.6.4.1.
88. Wang, Ruisheng & Peethambaran, Jiju & Dong, Chen. (2018). LiDAR Point Clouds to 3D Urban Models: A Review. IEEE Journal of Selected Topics in Applied Earth Observations and Remote Sensing. PP. 10.1109/JSTARS.2017.2781132.

89. Webber, Harold. (2018). Sick AG Whitepaper. Available:
https://cdn.sick.com/media/docs/2/22/322/Whitepaper_SICK_AG_Whitepaper_Select_the_best_technology_for_your_vision_application_en_IM0063322.PDF
Retrieved on 12/01/2019.
90. Zhang, He. Aldana-Jague, Emilien. Clapuyt, François. Wilken, Florian. Vanacker, Veerle & Oost, Kristof. (2019). Evaluating the potential of post-processing kinematic (PPK) georeferencing for UAV-based structure- from-motion (SfM) photogrammetry and surface change detection. *Earth Surface Dynamics*. 7. 10.5194/esurf-7-807-2019.
91. Zhang, Ruizhuo. Yang, Bisheng. Xiao, Wen. Liang, Fuxun. Liu, Yang & Wang, Ziming. (2019). Automatic Extraction of High-Voltage Power Transmission Objects from UAV Lidar Point Clouds. *Remote Sensing*. 11. 2600. 10.3390/rs11222600.

A.3 Literature Review Paper 1 (published 2022)

Review

A Review on UAV-Based Remote Sensing Technologies for Construction and Civil Applications

Shanyue Guan ^{1,*}, Zhen Zhu ^{1,*}  and George Wang ²¹ Department of Engineering, East Carolina University, Greenville, NC 27858, USA; guans18@ecu.edu² Department of Construction Management, East Carolina University, Greenville, NC 27858, USA; wangg@ecu.edu

* Correspondence: zhuz@ecu.edu

Abstract: UAV-based technologies are evolving and improving at a rapid pace. The abundance of solutions and systems available today can make it difficult to identify the best option for construction and civil projects. The purpose of this literature review is to examine the benefits and limitations of UAV-based sensing systems in the context of construction management and civil engineering, with a focus on camera-based and laser-based systems. The risk factors associated with UAV operations at construction sites are also considered.

Keywords: UAV; LIDAR; photogrammetry; construction management; literature review



Citation: Guan, S.; Zhu, Z.; Wang, G. A Review on UAV-Based Remote Sensing Technologies for Construction and Civil Applications. *Drones* **2022**, *6*, 117. <https://doi.org/10.3390/drones6050117>

Academic Editor: Sungjin Kim

Received: 11 April 2022

Accepted: 28 April 2022

Published: 6 May 2022

Publisher's Note: MDPI stays neutral with regard to jurisdictional claims in published maps and institutional affiliations.



Copyright: © 2022 by the authors. Licensee MDPI, Basel, Switzerland. This article is an open access article distributed under the terms and conditions of the Creative Commons Attribution (CC BY) license (<https://creativecommons.org/licenses/by/4.0/>).

1. Introduction

The construction industry is one of the major industries in the world. There is about USD 10 trillion spent on construction-related tasks every year. With the rapid growth of the construction industry, construction sites and tasks are becoming more complex and diverse than before. There is a strong demand for introducing automation and intelligent technologies [1] to improve operation efficiency, reduce project costs, and most importantly ensure the safety of construction workers and infrastructure. More and more cutting-edge technologies are being introduced and put into practice, improving civil and construction industry sustainability. Among all these emerging technologies, one of the most promising and widely adopted technologies to improve construction and infrastructure sustainability is unmanned aerial vehicles (UAVs). Because of their natural advantages, including accessibility, high efficiency, and reasonable cost, UAVs act as a reliable partner to address some practical challenges and have been deployed in many different areas. To better serve practical applications, UAVs have been integrated with various types of navigation, sensing, and monitoring systems. Focusing on the civil and construction industry, UAV-based sensors are used to conduct multiple types of tasks, including construction site monitoring, infrastructure assessment, and surface and volume measurements. The sensor data collected in these tasks are usually integrated and analyzed with computer software. In this paper, we summarize some of the literature about UAV-based sensing applications in civil and construction industry applications, which covers topics including sensing technology types, data product integration, data quality and error models, practical application cases, and safety-related issues.

2. UAV-Based Sensing Systems

Various types of sensing systems have been integrated with UAVs to conduct different types of tasks. The most commonly used sensors include HD cameras, light detection and ranging (LIDAR), infrared cameras, and other imaging/ranging systems. In this paper, we are going to focus on two types of sensing systems integrated with UAVs that can be used in the civil and construction industry: (1) unmanned aerial vehicle (UAV)-based photogrammetry and (2) LIDAR systems.

2.1. UAV-Based Photogrammetry

UAV-based photogrammetry is primarily based on imageries collected with small onboard cameras. It typically requires ground control points (GCPs) with surveyed locations and can benefit from the recorded location and orientation of the camera. A 3D point cloud of the target area can be estimated via direct or indirect geo-referencing. Indirect geo-referencing refers to the methods that assign world-frame coordinates to 3D measurements collected in a relative local reference frame. One of the most popularly used UAV-based geo-referencing solutions is structure from motion (SFM). It has been proven to be superior to conventional handheld surveying methods in certain environments: projects with low vegetation, stable GPS availability, and substantial sunlight [2].

Multiple 2D images over the same area can be combined and the point features are matched across them. These images are expected to have great overlap areas (~80%). The 3D locations of these points are then estimated in the camera frame, which are then used to form a 3D model or point cloud. However, the camera pose (position and orientation) is not always precisely known in a world frame (a GPS frame, for example) when a small commercial UAV is used. Therefore, the 3D model created with SFM with a small UAV is typically dimensionless and cannot be directly geo-referenced. It requires additional GCPs to relate back to the world frame. The absolute accuracy of this model depends on both the image processing quality and the GCPs.

Some customized and commercially off-the-shelf UAVs are capable of recording the camera location and/or orientation for each of the images taken during a flight. In that case, camera-based direct geo-referencing is possible. It can be achieved by raytracing from a single image to a known surface such as in the digital elevation model (DEM) or other a priori terrain models; triangulation from multiple overlapped images; or a combination of both. Since no ground control is necessary for this method, the accuracy of 3D modeling is primarily determined by the accuracy of camera timing, orientation, and location. However, a small UAV that is not capable of carrying a high-quality navigation sensor cannot be used for direct geo-referencing. Therefore, direct geo-referencing has not been commonly used in low-cost small UAVs yet.

SFM does not require an a priori position and orientation of the camera or the complete camera calibration model. In fact, they can also be estimated as part of the outcome of SFM. However, if an a priori estimation of these items is available, it can be incorporated into the SFM software to further improve the quality of the data product. The core algorithm in SFM is typically based on bundle adjustment, which is essentially a triangulation process using multiple images. Triangulation is a key component in SFM and the direct geo-referencing system. Although there are several specialized software solutions for triangulation, it is usually included as a part of a commercial software solution for SFM today. A good review of the bundle adjustment algorithm can be found in [3].

2.2. UAV-Based LIDAR System

Alternatively, camera systems can be combined with, or replaced by, a direct ranging sensor, such as a UAV LIDAR system, on some bigger-sized UAVs. The LIDAR senses the distance to a point in the 3D world based on the return of a laser beam. Since the beam would be sent at a known direction specified in the LIDAR body frame, the position of this point is therefore directly measured in the LIDAR body frame. LIDARs are less sensitive to natural light conditions and may provide measurements in operational conditions which prohibit camera operation (such as low light). An airborne LIDAR directly measures the point cloud in the sensor frame, instead of the world frame. The point cloud will be transformed into the world frame by knowing the precise location and orientation of the LIDAR. Very much like camera direct geo-referencing, airborne LIDAR point cloud accuracy is also sensitive to timing/synchronization, LIDAR orientation, and location. Furthermore, airborne LIDAR sensors available today are still more expensive, more power-hungry, and heavier than cameras in general.

An airborne or UAV LIDAR system typically includes three types of sensors: a ranging sensor (2D scanning LIDAR, 3D scanning LIDAR, or 3D imager); a positioning sensor, such as a Global Positioning System (GPS) or Global Navigation Satellite System (GNSS) receiver; and an inertial sensor that measures acceleration and rotation. These three sensors are integrated into the data collection system and in the 3D modeling procedure. The GNSS and inertial sensors are typically coupled together to provide a precise and smooth pose (position and orientation) and velocity of the LIDAR. It is a good practice that the GPS/GNSS also be responsible for the accurate time tagging and synchronization of other sensors.

3. Sensor Data Product Integration

Technologies in remote sensing, computer vision and image processing software, computational hardware, navigation, and robotics have all been developed at a rapid pace in the last few years. This section focuses on the integration, visualization, and applications of a sensor data product.

3.1. Photogrammetry Data Processing

The principle of SFM and estimation algorithms has not changed much in the last few decades. However, high-quality cameras and sensors have become more suitable for small UAVs as they become cheaper, smaller, lighter, and less power-hungry. SFM software and computation hardware have been improved as well. There are more choices for commercial software and more powerful hardware available today. Commercial software is available from, for example, Agisoft [4], Trimble [5], and Pix4D [6], and open-source software such as CMVS [7] has also been used in scientific communities. A more complete list will be discussed below. As aforementioned, modern SFM software takes known calibration, position, or orientation as inputs. However, if only inaccurate position and/or orientation are available from low-quality navigation sensors, 3D point clouds can still be optimized in the SFM software based on known error models of these measurements. Furthermore, for UAVs that have a precise location, through real-time kinematic (RTK), Post-processed kinematic (PPK), or post-processed precise point positioning (PPP), without orientation, SFM can also be used to estimate the 3D point cloud. PPP is post-processed GNSS positioning that does not need a local reference station as RTK and PPK do, which could be less accurate. In the presence of a precise camera position, SFM can be accomplished with fewer GCPs.

Although the principle of SFM has been well known for decades [3], the efficient and robust commercial solutions took years of development in image processing software and computational hardware. There are several well-known software packages available today that can register images to each other, and/or produce a dense 3D point cloud; von Übel [8] provided a list of software developers shown in Table 1.

Table 1. Photogrammetry software.

| Software Name | Type | Operating Systems |
|------------------------|---------------------|-----------------------|
| COLMAP | Aerial, Close-range | Windows, macOS, Linux |
| Meshroom | Aerial, Close-range | Windows, Linux |
| MicMac | Aerial, Close-range | Windows, macOS, Linux |
| Multi-View Environment | Aerial, Close-range | Windows, macOS |
| OpenMVG | Aerial, Close-range | Windows, macOS, Linux |
| Regard3D | Aerial, Close-range | Windows, macOS, Linux |
| VisualSFM | Aerial, Close-range | Windows, macOS, Linux |
| 3DF Zephyr | Aerial, Close-range | Windows |
| Autodesk Recap | Aerial, Close-range | Windows |

Table 1. *Cont.*

| Software Name | Type | Operating Systems |
|------------------------|---------------------|-------------------------------------|
| Agisoft Metashape | Aerial, Close-range | Windows, macOS, Linux |
| Bentley ContextCapture | Aerial, Close-range | Windows |
| Correlator3D | Aerial | Windows |
| DroneDeploy | Aerial | Windows, macOS, Linux, Android, iOS |
| Elcovision 10 | Aerial, Close-range | Windows |
| iWitnessPro | Aerial, Close-range | Windows |
| IMAGINE Photogrammetry | Aerial | Windows |
| Photomodeler | Aerial, Close-range | Windows |
| Pix4Dmapper | Aerial | Windows, macOS, Linux |
| RealityCapture | Aerial, Close-range | Windows |
| SOCET GXP | Aerial | Windows |
| Trimble Inpho | Aerial, Close-range | Windows |
| WebODM | Aerial | Windows, macOS |

Focusing on one of the most popular software products, Agisoft, as an example, the main functions of Agisoft are listed here as examples, retrieved from [9].

- Point features are acquired and matched across multiple images. The software detects point features in these images that are stable and repeatable. It then generates a descriptor for each point based on the appearance, which is often based on a small section of image centered on the point. The descriptors of all the points are then matched to detect correspondences across the images. This is similar to the well-known scale invariant feature transform (SIFT) approach [10].
- Solving for camera intrinsic and extrinsic parameters. Agisoft uses a greedy algorithm to find approximate camera parameters and refines them in the bundle adjustment algorithm. For example, the camera/lens model is considered intrinsic and camera orientation is extrinsic. Both types of parameters can be estimated in bundle adjustment.
- Dense reconstruction. Different processing algorithms are available at this step to create a dense point cloud based on all the involved images. The point cloud will be treated as a surface at this stage.
- Texture mapping. As the last step, the software models a surface by possibly cutting it into smaller pieces, and assigns color and texture extracted from images to the surface.

3.2. LIDAR Data Processing

Some of the developers of the SFM packages also offer software for point cloud processing. In addition, LIDAR manufacturers such as Leica have their own software solution [11]. There are fewer options to autonomously register images to a 3D point cloud and to compare or merge different sets of clouds. Examples include Autodesk [12], MeshLab [13], and CloudCompare [14].

There are a few challenges in registering images with UAV LIDAR 3D point cloud: (1) The point cloud and imagery are both considered an ‘unstructured scan’ in [12]. Manual input is often needed in registration with today’s software solutions. (2) The high noise level on each point in the point cloud makes it difficult to register a ‘free form’ object [15]. (3) Some UAV LIDARs are not able to produce a 3D ‘image’. A direct 3D image requires image-like intensity values measured in LIDAR returns, in addition to distance, and a very dense 3D point cloud. Either or both features are not available in low-cost UAV LIDARs today, although LIDARs with these features have become more affordable recently. As a

result, image-based and intensity-based autonomous registration methods such as in [16] are not applicable.

4. Error Models of UAV-Based Sensing

One of the most important factors to consider when using a UAV-based monitoring system is the accuracy of the point cloud product.

4.1. Photogrammetry Errors

The errors modeled in [17] included camera/lens calibration errors; motion blurriness; the altitude, pattern, and stability of flight; image overlap; and the distribution of GCPs. The main discoveries and arguments from this work include the following:

(1) Camera calibration can be estimated as part of SFM (self-calibration). However, a pre-calibrated camera/lens may be more convenient and robust. Other parameters, such as shutter speed, lens aperture, and ISO also have a considerable impact on the image quality.

(2) Small UAVs are often sensitive to wind and airframe vibration. Even mild wind during data acquisition can cause offset in the camera pointing direction, and eventually insufficient image overlap. Vibration can increase blurriness. Furthermore, light conditions during image acquisition can add to the complexity. To compensate for low light conditions, a lower shutter speed or higher ISO is used. Lowered shutter speed increases motion blurriness, while higher ISO increases noise. In most target applications, a larger area of interest will probably need multiple flight acquisitions. Appearance changes, such as changes in shadows, can cause another problem.

(3) The impact of flight altitude on accuracy is a little more complex. Flight altitude changes the distance, image footprint, image overlap, and geometry (slope) of the object. Errors tend to increase with distance and a steeper slope in SFM. Imaging the object from a steeper slope limits the variety of perspectives (view angles). Since SFM benefits from imagery from multiple perspectives, vertical accuracy decreases due to bad geometry. Examples to quantify the findings above can be found in [17].

It was also noted in [18] that images did not need to be acquired from the same distance or have the same scale. The authors argued that it was better to acquire multi-scale image sets. High altitude, large-scaled images could initially capture the whole site with fewer frames. Closer images could capture the desired detail at the required resolution and precision. It is particularly important when capturing areas of detail that are physically obscured by occlusions. Ref. [18] also gave specific advice to improve UAV SFM errors: (1) plan the mission in advance; (2) capture the whole area first before focusing on the details, but ensure that occlusions are captured adequately; (3) ensure appropriate coverage and overlap so that every point on the subject must appear on at least three images acquired from spatially different locations; (4) keep a static scene (no moving objects) and consistent light condition; (5) avoid overexposed images, underexposed images, and blurred images—normally arising from slow shutter speed and/or camera movement—and avoid transparent, reflective, or homogeneous surfaces.

Users of SFM software are typically advised to place GCPs throughout the target site, on the edge of the worksite, and in the center [19]. The locations of GCPs can be surveyed using GNSS-based RTK solutions, RTK and PPK solutions [20], and total station survey or TLS scans [21]. A PPK survey typically has positioning errors around 1 cm (1 sigma). However, to achieve centimeter-level accuracy in the point cloud, the user is required to place up to 40 GCPs per square kilometer [2].

Ref. [22] provided a systematic overview of accuracy in the point cloud involving GCPs. With a sufficient number of GCPs (more than 2 GCPs per 100 images as specified in this work), the error of the point cloud could approach double that of the GCP. If fewer GCPs were used, this paper reported that the point cloud error would be as high as 4–8 times the GCP error, which was still in the centimeter range. Vertical errors were approximately 2.5 times the error of horizontal components. It was also suggested that GCPs should be evenly distributed around the whole interest area, ideally in a triangular

mesh grid. For a greater project, denser GCPs were needed to achieve the same accuracy. This is probably because of possible systematic errors in SFM, which tend to amplify with growing distance and area.

The goal of the GCP placement strategy is to minimize the distance from the point cloud to any GCP. In many scenarios or applications, it is not possible to place GCPs with this strategy. Ref. [22] also recommended the use of (1) pre-calibrated cameras rather than the self-calibration; (2) mixing different altitude flights; (3) various degrees of image convergence; and (4) known positional and orientation parameters.

The onboard pose error for direct geo-referencing was also considered [17]. If small UAVs can carry high-quality GNSS receivers, they may be capable of RTK on the fly or recording data for post processing. Post-processed position through PPK or PPP could be used to help improve the accuracy with limited GCPs. It is noted that RTK and PPK could both produce centimeter-level accuracy [19]. PPK would be more accurate than RTK, but less than using GCPs, especially in the vertical direction. In [23], the authors further compared PPK with PPP. Since PPP does not need an additional local reference GNSS receiver, it is more convenient and flexible. However, it was found that PPP produced worse accuracy in the vertical direction than RTK (10 cm error reported for PPP). Further, RTK requires a live data link between a reference station and the airborne receiver, which is not always possible or necessary.

Although the approaches above claimed that GCPs were not necessary if PPK positions were available for the cameras, it would be challenging to directly register the point cloud with just PPK. SFM with PPK can produce precise point clouds only in the camera body frame. Since the PPK position does not directly solve the orientation of the camera or the point cloud, an additional step is needed to align the point cloud in the correct direction.

Therefore, it is more practical to use a few GCPs even with PPK. Ref. [24] showed that a PPK–SFM solution workflow could provide a consistent, repeatable point cloud over time, with an accuracy of a few centimeters. A vertical bias could be corrected using one single GCP. The results were used to estimate centimeter-level topographical change detection. PPK-SFM could accurately and quickly achieve a very high spatial and temporal resolution.

As the main manufacturer of commercial small UAVs, DJI also stated similar conclusions [2]. The new UAV supports both RTK and PPK solutions. Although it could potentially reduce the required amount of GCPs to 0, DJI mentioned the use of ‘fewer GCPs’ and a reduction in GCP set-up time.

4.2. LIDAR and Direct Geo-Referencing Errors

Although a UAV LIDAR may have lower sensor quality than a more capable airborne laser scanner (ALS), both follow the same principle for measurements. The existing error analysis approach of ALS is based on direct geo-referencing and is largely applicable to UAV LIDAR. LIDAR measurement error, navigation and timing error, and modeling error can all contribute to the error in the LIDAR point cloud.

In this review, ‘LIDAR measurement error’ refers to the single point position error in the body frame. It is dependent on the beam width (or divergence), the reflecting surface, and the angular and range measurement made with the laser beam [25]. Beam divergence and the possible uncertainty in the scan angle are both considered angular errors in the LIDAR, whereas the reflecting surface and the measurement noise both contribute to the ranging error along the laser beam. In [26], the angular and ranging errors are both modeled as random processes. The magnitude of these errors depends on the LIDAR manufacturer. In a downward-looking laser beam, ranging error primarily contributes to the vertical position error. In practice, ranging error could also have a systematic component, such as a bias. It needs to be calibrated or bounded.

Some LIDARs are designed with narrow beams (1 or several milliradians; 1 milliradian is approximately 0.06 degrees) to minimize the uncertainty, such as in [27]. Others believe that a wider beam is more robust (~10 milliradians) for a UAV LIDAR, such as in [28]. With multiple returns measured on the same beam, a wide beam may get returns on the target

or the ground after it hits occlusion due to dust, rain, and other objects [28]. Therefore, it has the potential to measure the distance to targets and the ground in a harsh environment.

The small angular error in LIDAR is scaled with the distance to the ground, which contributes to horizontal position error in a downward-looking laser beam. However, since the laser beam would have a slant angle on a sloped object even with a downward-looking LIDAR, it will also contribute to the vertical uncertainty.

The position of laser return points in the LIDAR body frame cannot be directly used in a 3D model if the LIDAR is mobile or airborne. The absolute position and orientation of the LIDAR itself in the global world frame need to be accurately measured, which should be synchronized with the measurement time of each point in the LIDAR point cloud.

The position of LIDAR is not directly measured. Instead, it is inferred from the location of the GPS/GNSS antenna measured with RTK, PPK, or PPP. The accuracy of RTK, PPK, or PPP had been discussed in the previous section, which is in the range of 1 cm to 10 cm. It must be noted that the navigation system used for UAV LIDAR should be GPS/GNSS tightly coupled with the onboard inertial measurement unit since it is mandatory for the LIDAR system to be accompanied by accurate orientation measurements. The post-processed solution with integrated GNSS and an inertial measurement unit can be less noisy than PPK or PPP alone. The typical error magnitude is 1 cm horizontal and 2 cm vertical in [29] or, similarly, 2–5 cm in [30]. The actual values are sensor specific.

The antenna position is combined with the lever arm between the antenna and the LIDAR center of measurement to compute the LIDAR position. Any errors in the lever arm, which is typically at the millimeter level, become biases in the point cloud.

Similarly, the navigation system measures the orientation of the UAV in the world frame. It is transferred into the LIDAR orientation via known boresighting of the LIDAR. Boresighting errors can be calibrated, and any residual error will contribute to the angular errors discussed below. Ref. [31] showed that successful calibration could reduce error magnitude down to the centimeter level.

The navigation system can be very accurate at measuring roll and pitch angles: typical values are much lower than 1 degree (0.008 degrees [29] or 0.015 degrees [30]). The actual values are also sensor specific.

However, the reported true heading angle accuracy for these sensors could be overly optimistic and misleading. The nominal accuracy, typically close to 0.1 degrees, is achieved only after maneuvers of the UAV and the fine alignment of the heading. The maneuvers may not always be possible for small UAVs with a short flight time, or for the operational environment at a small urban worksite. Without that, the heading is initialized by vehicle velocity, gyro-compassing, compassing, or manual input, which has the accuracy of a few degrees as reported in [32]. These heading accuracy levels are applicable to most high-end navigation systems that can fit on a small UAV.

A true heading error of a few degrees is a major concern for UAV LIDAR, although it is not a big issue for SFM. As discussed above, the SFM point cloud is calculated from overlapping images. The points from SFM are precisely located with respect to each other within the camera body frame, and the relative precision does not depend on the absolute orientation in the world frame. In fact, camera orientation can be precisely solved by matching point features in images [33].

The same does not apply to the LIDAR point cloud. In processing raw LIDAR data, the points are geo-located independently from each other. There is no relative precision as in SFM. As a result, a large angular error, such as the heading offset, causes each point to be out of its place. A point cloud formed in this case could be distorted so much that it could no longer represent the geometric shape of the target or the terrain. Therefore, the point cloud becomes meaningless with large angular errors. Smaller heading and boresighting errors would cause the points measured in different parts of a UAV flight or from different flights to be inconsistent [34].

Unfortunately, the operator of small UAVs may not know if the UAV has completed enough maneuvers to guarantee the desired heading accuracy. In the navigation industry,

measuring true heading in real-time has always been a challenge. A possible solution for airborne and ground vehicles is to use a dual-antenna system. For example, VectorNav has a dual antenna system that can measure the relative location of both antennas in the GPS coordinate frame. The vector between both antennas thus provides an absolute heading, with the error of 0.3 degrees 1 sigma [35]. However, the accuracy is achieved by placing both antennas at least 1 m away from each other. Unfortunately, the heading error would be inversely proportional to the distance between both antennas. If installed on a small UAV, the maximum distance between antennas is typically much shorter than 1 m, and the heading error approaches 1 degree 1 sigma. Therefore, the dual antenna solution could not help with a lot of small UAVs.

In addition, the timing error in the navigation system is often overlooked. Ideally, the LIDAR orientation at the exact moment of measuring every single point in the point cloud must be recorded. Sometimes, the geo-registration process is simplified by using the same orientation for a batch of points, which leaves a small uncertainty in time, at the millisecond level. Any UAV rotation and vibration experienced within a few milliseconds are therefore not compensated, which contributes to the overall angular error.

Finally, the LIDAR point cloud will be processed and registered. In some applications, LIDAR points will be compared against a known model and fit with the known model [36]. In this case, the location of the fit 3D model would not directly reflect the noise level on each point. Instead, it could be affected by the bias and systematic errors in the LIDAR point cloud.

In summary, the position errors observed in the navigation system are typically limited, and the orientation errors could be significant. In an ideal case, the orientation errors would mainly affect the horizontal locations of the individual points in the LIDAR point cloud. For example, an angular error of 0.1 degrees is equivalent to horizontal errors of 5 cm at 30 m away. The expected vertical error is also around the level of several centimeters. An analytical example can be found in [25], and a similar behavior and performance were observed in [37].

4.3. Additional Error Reduction Methods

If the angular error magnitude or the flight altitude increases, centimeter-level accuracies cannot be guaranteed anymore. Some of the error sources are in fact systematic, which result in bias in the point cloud with respect to the truth and discrepancies among subsets of the LIDAR point cloud measured from different flight paths. An ALS point cloud was faced with similar problems [34].

Overlapped observation of the same terrain or target is not necessary to form a LIDAR point cloud, but it helps correct the self-discrepancies. The overlapped area between the footprint of different flight paths (also called 'strips') can be used to correct the subsets of the point cloud, which makes the entire point cloud more precise in a relative sense. Ref. [34] mentioned the data-driven approach to minimize the differences between strips for a given transformation model.

Points and geometric features can be extracted from LIDAR data and matched with ground control points or features with surveyed locations. This approach makes the point cloud accurate in an absolute sense [34]. These points and features could be calibration targets purposely distributed in the area, which makes them equivalent to GCPs, or common objects with recognizable shapes, such as sidewalks.

5. UAV-Based Remote Sensing Construction Management Applications

5.1. UAV-Based Photogrammetry Applications

Infrastructure and materials conditions are estimated by various types of simulation models. To obtain more detailed information, UAV-based sensing systems have been widely used for various types of operations and applications in the construction industry [38]. The main capabilities of a UAV-based imaging system include 2D surveying, 3D mapping and modeling, progress control, onsite monitoring, inspection, and assessment. They are

applicable to buildings, bridges, transportation areas, and other infrastructure systems and help improve infrastructure sustainability. A summary of these applications can be found in [39].

Ref. [40] discussed applications for a safety inspection on construction sites. UAV imagery could be used to identify non-compliances with the safety requirements established. With improved visualization of the working conditions, UAVs could help improve the safety inspection process on job sites by means of better visualization of working conditions. Ref. [40] developed a set of procedures and guidelines for data collecting, processing, and analyzing safety requirements based on 2D imagery.

Construction progress monitoring could also benefit from using small UAVs. Most of the construction progress is simulated with computational models [41]. Instead of relying on the manual input and observation of each and every phase of the construction projects, which is costly and time-consuming, [42] proposed integrating building information modeling (BIM), UAVs, and real-time cloud-based data modeling and analysis. This enabled an accurate comparison between the as-planned and UAS-based as-built states of the project. The limitation of this approach lies in the fact that the data generated are currently qualitative with a visualization of the project's progress. A software approach to automatically align and compare the BIM model and the point cloud was needed to produce quantitative and measurable data for project control and performance monitoring. Ref. [43] proposed an industry foundation classes (IFC)-based solution for UAV-enabled as-built and as-is BIM development, quality control, and smart inspections. It enabled the automated integration of as-built and as-is conditions into BIM. However, it was based on 2D images only.

Structural damage assessment could be done with 2D or 3D imagery. Ref. [44] showed examples of building scanning and monitoring using a small rotary-wing UAV. Two-dimensional UAV images were stitched together to become a high-resolution imagery map. It allowed damages and cracks to be observed in the millimeter range. Additional algorithms and processing software were developed to recognize and highlight the cracks based on 2D edge detection. In [36], a 3D point cloud was formed from the multi-perspective, overlapping, very high-resolution oblique images collected with UAVs. The 3D point cloud was collected for the entire building and was combined with a detailed object-based image analysis (OBIA) of façades and roofs. Major damages could be identified in the 3D point cloud, whereas other cases are by OBIA-based damage indicators. However, it was recognized that the 3D point cloud was collected for individual parts of the building. It required an additional algorithm to aggregate the information from these parts.

Three-dimensional mapping with UAV photogrammetry is the main application to be covered in this review. A review of relevant technologies can be found in [45]. In general, UAV photogrammetry can reduce the cost and the risks of mapping and surveying tasks in harsh environments. Centimeter-level accuracy is achievable, and rotatory-wing UAVs are better choices for small sites. However, the durability of small UAVs may be a potential issue considering weather and wind conditions.

Ref. [46] demonstrated the use of UAV imagery and SFM on modeling the surface and volume of earthwork in a field-realistic environment. This study also incorporated the use of autonomous flight of the UAV with pre-programmed waypoints. The methodology used for this was based on the Mikrokopter Flight Planning Tool, and the new computer program was specifically designed for surveying aspects of aerial photogrammetry that are relevant for civil engineering. It was found that 70% longitudinal coverage and 40% traversal coverage are recommended. Although UAV was much more convenient than traditional methods, it was recognized that the volumetric measurements could bear large errors. The authors noted that error sources needed to be identified and mitigated. The DEM of a designated area could be created from UAV imagery and SFM [47]. The horizontal and vertical accuracy falls within the desirable threshold according to the National Standard for Spatial Data Accuracy. The DEM was used to choose a proper siting for dam construction. The authors concluded that the terrain model created in this approach was robust enough for planning purposes in construction and engineering applications.

Ref. [48] compared the efficiency of 3D mapping in terms of the easiness of model development, data quality, usefulness, and limitations on two typical building cases. The easiness of model development took into consideration the accessibility of the worksite for takeoff and landing; physical barriers for UAV flights; disruption on the worksite; and software processing time. The data quality considerations included the footprint, spatial resolution and overlap of the images, and visual inconsistency between images due to distortion, shadowing, and gaps. The usefulness and limitations were defined for the users of the data product. The users interviewed in this work noted that the 3D maps were useful for logistics, monitoring work progress, planning, and visualization. However, these maps could not provide details in a close range, and there were parts of the buildings that could not be modeled (such as the inside and top). Due to safety considerations and regulations, the UAV flight could not cover certain parts of the site to create a full 3D point cloud.

Ref. [49] demonstrated the use of UAVs for augmenting bridge inspections, using the Placer River Trail Bridge in Alaska as an example. The authors produced a 3D model of the bridge using UAV imagery and a hierarchical dense SFM algorithm. The UAV design, data capture, and data analysis were optimized together for a dense 3D model, and the results were compared against models generated through laser scanning. The 3D models created with UAV imagery did provide the accuracy to resolve defects and support the needs of infrastructure managers.

5.2. LIDAR Applications

LIDAR-based solutions are raising some interest within the construction industry as well [50]. UAV-based LIDAR is a relatively new technology for construction management, especially for improving construction and infrastructure sustainability. Users in this industry are more familiar with terrestrial laser scanners (TLS), mobile laser scanners (MLS) mounted on ground vehicles, and ALS mounted on large, manned aircraft.

5.2.1. TLS Applications

Ref. [51] showcased how a TLS point cloud is integrated with total station surveying to create BIM models for existing buildings. The point cloud-based BIM model provided the ability to detect and define facade damage on buildings. It also provided the ability to detect discrepancies between the existing drawings and the real situation captured with the TLS point cloud. Limitations of this method were also pointed out, including (i) the difficulty in manipulating point cloud data; (ii) the lack of a best fitting algorithm; (iii) the lack of the ability to enforce known shapes of openings such as windows in the point cloud; and (iv) the lack of a standard in managing data. Ref. [52] as well as [53] emphasize that, in general, the maximum range of a scanner should be taken into account before collecting data, as the low-density point clouds taken at the maximum distance range may not be sufficient for all surveying needs. Ref. [54] focused on TLS application on bridge inspection, involving geometric documentation, surface defect determination, and corrosion evaluation. Workflows based on TLS data were proposed to measure cracks and vertical deflection. They could save up to 90% of the time and could detect cracks between 1.6 mm and 4.8 mm.

TLS data are also able to assist with assessments of the saturation of building materials, which can be used for several civil engineering applications, such as monitoring bridges, landslides, dams, and tunnels [55]. Changes in roughness and color should be taken into consideration with the analysis of structure moisture content. In [56], the authors were able to use TLS to assess the deformation of bridge structures, suggesting that it is a viable method for construction inspection. The TLS data collected were processed using a shape information model and octree algorithm. It was found that this method is effective in detecting deflections of greater than 4 mm. TLS data have also been effective in measuring the thickness of concrete pavement on construction sites. Ref. [57] found that surveying construction sites before and after the addition of concrete may be a more

accurate and time-efficient alternative to traditional core sampling methods conducted at construction sites.

With regards to construction site management, surface profiles have been created with TLS point cloud data by attaching a 2D profilometer to an excavator machine. This method is not commonly found in the literature but has been found to have an accuracy of better than 10 mm, and the advantages of this technique include accuracy, a high update rate, real-time measurements of the site, and construction without moving parts [58]. With the correct algorithms, there is potential for the excavator to be fully autonomous through the use of machine learning.

5.2.2. ALS Applications

TLS measures the point cloud from a fixed location, which is inconvenient in a lot of applications. LIDAR can be installed on airborne and ground vehicles and can measure point clouds while the vehicles are moving. As aforementioned, these types of LIDARs would require high-quality navigation sensors (typically differential GPS/GNSS and an inertial measurement unit [15]) to measure the position and orientation of the LIDAR.

ALS has been widely used to survey the ground and create topographical models, although normally it would not be used to survey construction worksites, due to cost and other practical limitations. The authors of [59] noted in their comparison of ALS, satellite imagery, and USGS models that LIDAR technology is not the most accurate choice when surveying in areas with steep slopes, ridges, or ditches. Ref. [60] described the use of aerial photography and ALS to estimate individual tree heights in forests. The main challenge of modeling the forest-covered terrain was to differentiate the LIDAR returns from the tree and the ground. This process depended on multiple returns of the laser beam, since the first return is usually from the treetops, and the last strong return is from the ground. However, due to the low density of ALS returns (3–4 returns per m^2) and the small footprint of the laser beam (10 cm^2), the tree models were not as accurate as one had hoped for with LIDAR measurements. Only meter-level accuracy was achieved. Airborne LIDAR may be effectively used for structural damage assessments. For example, airborne LIDAR has been evaluated for the damage assessment of buildings caused by hurricanes [61]. However, only severely damaged structures are able to be detected with this method, and high-density point cloud data are necessary.

5.2.3. MLS Applications

The application of MLS is similar to that of TLS. For example, [62] proposed using MLS in monitoring progress. MLS point cloud data and 4D design models were used to identify deviations of the performed work from the planned work. The proposed framework was tested using as-built data acquired from an ongoing bridge construction project. The percentage of completion for the as-built bridge elements was calculated and compared with the as-planned values. The differences for every element on a specific scan date were used for assessing the performance of the proposed framework. The obtained difference ranged from -7% to 6% for most elements.

Since MLS is mounted on ground vehicles, it can offer similar high data density as the TLS (higher than that of ALS), similar accuracy levels (millimeter to centimeter), and is more flexible than TLS. MLS is becoming a popular choice for mapping urban environments [15]. Available commercial systems today can produce close to or more than one million points per second and a few hundred-meter range. The manufacturers of these LIDARs include Faro, Velodyne, Riegl, Sick, Optech, and Leica. They have been used in mapping transportation infrastructure, building information modeling, utility surveying, and vegetation. Road markings, zebra crossings, center lines, and other features could be automatically identified from the integrated LIDAR-imagery data product. For example, the authors of [63] were able to extract road surface features from terrestrial mobile LIDAR point cloud data using an algorithm. This effectively resulted in the creation of an index of roadway features with greater than 90% correctness, suggesting that TLS data

are useful in surface reconstruction situations [63]. The challenges identified in using MLS include: (1) classification and recognition of objects, (2) data integration and registration, and (3) city modeling.

The issue with data integration and registration is the most relevant to this work. Although the MLS point cloud can be directly geo-referenced, errors in navigation (position and orientation) can cause discrepancies among the point cloud data sets, since the position and orientation are non-stationary. In particular, the authors from [15] noted that ‘the misalignment among sensors needs to be carefully calibrated (through either indirect or direct sensor orientation), and their time needs to be rigorously synchronized’. This was because orientation and timing errors could cause a great offset in the location of the point cloud, the same as in ALS. The MLS point cloud could be registered with respect to other sensor data, such as a reference point cloud and imagery. Multiple sets of MLS point clouds could also be registered and stitched together. However, different data sets often had to be manually registered into the same coordinate system due to navigation errors. Special shaped artificial targets were used in the process. The precision of the MLS point cloud was verified via registration, which was around 4–5 cm.

Ref. [15] provided a summary of how urban objects could be modeled with a LIDAR point cloud from TLS, MLS, and ALS. Building roofs and façades could be modeled with ALS or ground-based LIDAR. The modeling process could be data-driven, which extracted models from the point cloud; or model-driven, which verified a hypothetical model with a point cloud; or a hybrid between the two. The choice of models was a balance between geometry, topology, and semantics. Power lines could be better modeled with ALS and geometric models (a more detailed example can be found in [24]). Road surfaces could be modeled with ALS or MLS, and with various types of models. Ref. [15] called for more research into LIDAR-based bridge models.

Ref. [15] also recognized that it was more challenging to model free-form objects, such as statues, towers, fountains, and certain types of buildings. Various types of surface reconstruction methods were discussed in this work, and it was certainly possible to extract robust and accurate (centimeter-level) representation from the point cloud. However, the accuracy depended on the surface characteristics and the input data.

Although there has not been much literature on the application of UAV-based ALS, the remote sensing industry has started to pay more attention to it. UAV LIDARs were developed based on adapted versions of ALS [64] and MLS [27,28,65]. As with ALS and MLS, the UAV LIDARs were tightly integrated with navigation systems, such as Trimble/ Applanix [30] and NovAtel [29]. Attempts have also been made to use a hybrid form of TLS data and UAV-based image processing. This technique is thought to be most useful at large earthwork sites to improve the cost-effectiveness and means of efficiency of construction management [66].

Due to constraints in cost, power, size, and weight, the low-cost UAV LIDAR systems had limitations in range, point cloud density, ranging accuracy, and navigation accuracy. For example, the Hokuyo LIDAR in [65] has a nominal range of 30 m. While UAV LIDAR can be of use for capturing data over huge land areas, ground-based LIDAR is superior in capturing the specific details of an area [67]. UAV LIDAR is typically only suitable for ground vehicles and UAVs flying very low to the ground. GPS/GNSS receivers with RTK or differential corrections could produce large position errors, which translates to large 3D position errors in the point cloud. The orientation of the low-cost IMU sensors produced substantial angular errors, especially in the heading. As a result, the accuracy and resolution of low-cost UAV LIDARs were rather limited. Remote sensing experts had argued that UAV LIDARs were not as effective as UAV photogrammetry in construction management not too long ago [68]. Despite these constraints, a BIM–UAV LIDAR combination approach was found to be effective for construction project monitoring and quality control. This system provides real-time information which can assist in early defects detection on construction sites. The use of technology can be considered advantageous over traditional quality

control checks when taking into consideration the safety, accessibility, and efficiency of the BIM–LIDAR system [69,70].

It is easier to obtain a high-density point cloud with photogrammetry, and high-resolution cameras are much more cost-effective than high-density LIDARs. While LIDAR sensors may be more costly and heavier than high-resolution cameras, [71] note that the results may improve the overall quality of construction project management. More importantly, the relative precision of the 3D point cloud from SFM photogrammetry is based on the consistency within imagery. It is relatively more convenient to achieve centimeter-level relative precision with sufficient imagery coverage. The absolute accuracy is dependent on GCPs. With sufficient GCPs, centimeter-level absolute accuracy can also be achieved. On the other hand, the LIDAR point cloud is always using direct geo-referencing. As discussed above, the accuracy is highly dependent on the navigation sensors, especially angular measurements. As a result, the errors in the 3D point cloud are amplified with distance. Limited by accuracy and range, low-cost UAV LIDARs often have to take measurements close to the ground (tens of meters). Therefore, it was argued that low-cost UAV LIDARs could only help when SFM or GCPs are not available [68].

However, it was pointed out that there could be several types of environments where UAV LIDAR would enable projects to be delivered that may not have been possible otherwise [72]. These projects included those that involved steep topography, a linear-based survey, or sites covered by dense vegetation. LIDAR direct geo-referencing minimizes the need for GCPs and therefore is suitable in environments where it is either too expensive or impossible to place GCPs. Ref. [73] tested the possibility of autonomous beyond visual range (BVR) flights in unknown environments with LIDAR. The three qualities that this study found to be necessary for autonomous long-distance UAV flights were BVR waypoint navigation flight, ground detection/terrain following, and obstacle detection and avoidance. More importantly, some LIDARs have multiple return capabilities [27]. The LIDAR beams are sometimes wide enough that they can be reflected by multiple surfaces and objects, including dust, rain, foliage, and the actual target (ground). It becomes possible for LIDAR to see through to the ground. Therefore, the main advantage of using LIDAR is potentially differentiating the ground from vegetation.

Furthermore, recent developments in the remote sensing and navigation industries have made available higher density UAV LIDARs at a greater range (a few hundred meters) and better inertial measurement units that can measure orientation more precisely. They could be used to take volumetric or topographic measurements of the ground, with or without vegetation cover, and model roads, cuts and other surfaces, and even buildings [37].

In the last few years, custom-built LIDAR systems have been reported that were specially designed for modeling the terrain or vegetation, such as in [74]. Commercial solutions are becoming more available, such as in [75]. Obviously, UAV-based photogrammetry (SFM) and LIDAR have different limitations and requirements on the hardware (UAV airframe and sensors) and the operational environment. The expected quality of the data product also differs between both technologies. In general, the SFM point cloud is expected to have a higher precision and higher density than that of UAV-LIDAR. For example, Figure 1 shows a tent-shaped calibration target placed on the ground. The target was designed by the authors of this paper to quantify the errors in SFM and the LIDAR point cloud. It has a base of approximately 1 m by 1 m, and the height is about 0.4 m. The surface of the target was covered with white canvas and painted with blue stripe patterns. The SFM and LIDAR point clouds have been illustrated in Figures 2 and 3, respectively. The SFM point cloud was formed with imagery collected with a GoPro camera installed on a DJI Inspire UAV, and processed in Agisoft Metashape. This point cloud was geo-registered in a local North-East-Up frame. Each point in this point cloud has been assigned with a color extracted from the airborne imagery. A custom UAV-LIDAR system based on a Sick UAV LIDAR and a DJI Matrice 600 Pro UAV was used to collect the point cloud in Figure 3. The point cloud was displayed in the same North-East-Up frame as in Figure 2. The points in Figure 3 were not colored with imagery, since the UAV LIDAR does not have color-based

returns. Instead, the colors in Figure 3 are simply used to illustrate height, such that the target can be visually differentiated from the ground. Both point clouds are accurately geo-referenced and can be aligned with each other. However, Figure 2 shows more 3D details of the target, with a higher density and colored points. On the other hand, the target in Figure 3 appears coarse and noisy, with a lower density.



Figure 1. Airborne imagery of the calibration target.

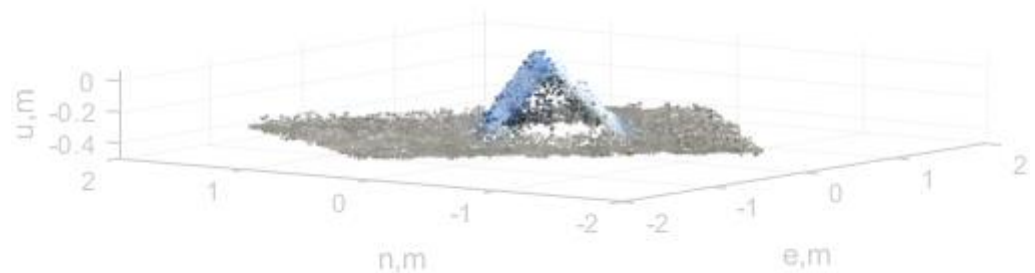


Figure 2. SFM point cloud of the calibration target (courtesy of Mr. Nicholas Hill).

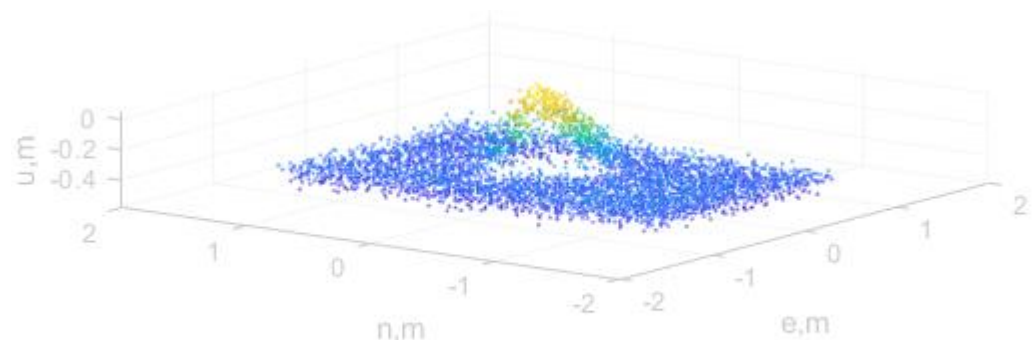


Figure 3. LIDAR point cloud of the calibration target.

UAV LIDARs and ALS are capable of measuring terrain and surfaces, with or without vegetation cover, via direct geo-referencing. The point cloud density and accuracy decrease with flight altitude. Therefore, it may not provide the same level of details that UAV imagery can. However, the absolute accuracy of SFM is dependent on the GCPs, and is more likely to be limited by the operational environment. The UAV used in this example circled around the target at different altitude levels for multiple times, to ensure that there were sufficient coverage and overlap between images, and that images were collected from multiple view angles. It took several minutes to scan this small target. The LIDAR SFM requires no GCP, and the UAV only needed one overhead flight in this example. It only took a few seconds in a flight to capture the point cloud in Figure 3. The pros and cons of

both technologies have been summarized in Table 2, in terms of hardware, operations, and data quality.

Table 2. A comparison between UAV-based SFM and UAV-based LIDAR point cloud.

| | UAV-SFM | UAV-LIDAR |
|--------------------------------------|----------|-----------|
| Hardware | | |
| GCP | Yes | Optional |
| GNSS-IMU | Optional | Yes |
| Airframe | Any | Large |
| Cost | Low | High |
| Operations | | |
| Robustness (light/ground conditions) | Low | High |
| Flight altitude | Various | Low |
| Flight time | Long | Short |
| Data Quality | | |
| Precision | mm-cm | cm |
| Density | High | Medium |
| Imagery | Yes | No |

Since SFM and LIDAR each have unique strengths, they can complement each other in some applications. A data fusion method can be used to merge two types of point clouds to obtain and analyze data in construction settings. Ref. [76] examines the compatibility of aligning data sources from different types of point cloud collection methods. MLS and ALS data are easily aligned through geo-referencing methods [76]. TLS data may be better in smaller scanning areas compared to MLS, and are able to be combined with ALS point cloud data. This process involves finding matching pairs of objects between the two-point cloud datasets and creating Laplacian matrices and finding the resulting correlation coefficients [76]. Point cloud data can also be overlaid with original design models as a way of determining construction progress [77]. Similarly, the overlapping of point clouds from consecutive days is a possibility as a way of assessing progress [77].

Overlaying point cloud data with imagery is an additional technique that may be used effectively. Ref. [78] examined the concept of automatic change detection with UAV image-based point clouds in the context of assessing landslide sites over time. This approach allows for the comparison of a large number of images from different dates without the necessity of having extensive ground control point information [78]. Construction progress may also be monitored by superimposing two-dimensional photographs with 3D point models. Ref. [79] utilized this technique in order to visualize the construction progress schedule. For example, aspects of a building site that were considered on the schedule were color-coded one color while entities that were behind schedule were coded a separate color for clear distinction [79]. This allowed for easily visible progress reports in the construction process. Alternatively, the LIDAR point cloud can be fused with available imagery to construct 3D models. The fusion will be based on direct geo-referencing and can still provide more details. Ref. [80] proposed an approach to register images with an ALS point cloud for urban models. OpenGL and graphics hardware were used in the optimization process for efficient registration. Ref. [16] discussed a hybrid intensity-based approach that utilizes both statistical and functional relationships between images, particularly in the case of registering aerial images and 3D point clouds. Statistical dependence of mutual information or functional relationships of correlation ratio alone was not sufficient to register photos to LIDAR reliably. However, the proposed method used both of them and performed a robust registration of urban areas. Ref. [81] discussed registering SFM 3D point clouds, 3D meshes, and geo-referenced orthophoto imagery in a fully automated manner. The data product could be used in disaster relief response and construction progress monitoring.

Ref. [82] focused more on road maintenance. This work combined a TLS point cloud with UAV photogrammetry. The authors acknowledged the difficulties faced with road

maintenance using TLS alone: (1) As passengers and cars use the road being surveyed during measurements, and available space for instrumentation setup is limited, it is sometimes difficult to set up TLS. (2) TLS can only provide high-density measurements in a limited range (10 m). Part of the road that was surveyed used UAV photogrammetry and SFM. The point cloud was combined with that from TLS, which was used to scan a bridge, including sides and lower works. The inaccuracy for the bridge was an effective length of 1.2 cm and an effective width of 1.9 cm, and the three-dimensional data described the structure of the bridge with high accuracy. The combined point cloud could be used to develop a road maintenance management system that accumulates data and refers to the inspection results and repair information in three dimensions.

The existing literature mainly covered the registration of imagery with TLS and ALS. The fusion and registration of UAV LIDAR with imagery collected by an onboard camera has not been well documented yet. It is one of the emerging technologies that will soon find more applications in construction and civil engineering.

6. Safety and Risk Considerations

Additional risks arise primarily from operating in construction applications. Ref. [83] noted that ‘about 30 incidents of near-misses or crashes leading to human injury have been reported associated with the use of recreational UAVs. Unstable flying conditions, operator errors, and faulty equipment may represent potential hazards to nearby workers from the commercial use of UAVs’. This work described the use of UAVs in construction, the potential risks of their use to workers, and approaches for risk mitigation, including ‘prevention-through-design’ for small UAVs, the adequate training of operators, and updating occupational safety regulations.

Risks of small UAVs could result from a number of technical reasons, including (but not limited to) power, communications, navigation, and control. UAV operations may be autonomous, semi-autonomous, or remote-controlled [84]. In a fully autonomous or semi-autonomous operation, the low-level control is governed by the onboard flight controller and navigator, which relies on GNSS (or an equivalent sensor) as aforementioned. If the UAV follows a pre-loaded flight plan without the need for human intervention, it is considered fully autonomous. In a semi-autonomous operation, sometimes also referred to as a GNSS-assisted operation, the UAV follows the guidance of a remote controller, with commands transmitted via a communication channel. In a remote-controlled operation, the user directly performs low-level control functions, such as attitude or velocity control, without using on-board GNSS.

When a UAV is close to a building or other structure, it may lose communication with the operator. The quality of GNSS positioning in the vicinity of a construction site could also suffer from blockage and multipath. In an autonomous operation where GNSS has been corrupted, the onboard flight controller could command erroneous operations. A properly designed UAV system will attempt to stop the operation, by landing or returning to the home location, upon the loss of communications or GNSS. Without the ability to ‘sense and avoid’, the UAV could potentially cause damage during this process. An obvious way to prevent communication loss is for users to remain in the line of sight when operating UAVs, as often required in various regulations, including FAA part 107 (FAA 2016). Autonomous operations should be enabled only when GNSS (or equivalent) is available. Small UAVs with redundant navigation systems, payload capabilities, redundant rotors, and battery capability in case of a rotary-wing UAV provide additional safety protection. Furthermore, small UAVs with GNSS-denied and indoor navigation capabilities, and sense and avoid capabilities, are also available now.

Ref. [85] recognized that the construction industry had the potential to greatly increase safety and efficiency on the job site, particularly in safety inspections. This article discussed the opinions of safety managers and their thoughts on the implementation of UAVs. In 2019, the construction industry was found to be the second-highest economic market sector for UAVs, with agriculture coming first. It was found that various monitoring tasks, such as

for cranes in the proximity of overhead power lines, are the most important safety-related tasks that might benefit from using UAVs on a construction project. It was also found that the three most important technical features of the UAV were the camera movability, sense and avoid capability, and a real-time video communication feed. A list of state regulations can be found in [86]. FAA part 107 guidelines [87] must be followed when operating small UAVs for these applications.

7. Conclusions

UAV-based remote sensing and inspections have been used widely in construction and civil fields. This paper summarizes the up-to-date performance and applications of UAV-based photogrammetry and LIDAR technologies. UAV-based technologies have demonstrated their unique advantages, especially in helping with construction and infrastructure sustainability, although there are also limitations in some of the applications. With the recent development of sensing technologies and their application in UAV-based systems, some of the limitations will be overcome soon. Although the operation of UAVs could potentially raise risks at a construction site, especially in fully autonomous operations, they can also improve the safety, efficiency, and sustainability of construction operations.

Author Contributions: Literature view, S.G., Z.Z. and G.W.; writing, S.G., Z.Z. and G.W.; editing, S.G., Z.Z. and G.W. All authors have read and agreed to the published version of the manuscript.

Funding: The authors would like to thank the North Carolina Department of Transportation (award number: RP 2020-35) for their assistance in supporting this research.

Institutional Review Board Statement: Not applicable.

Informed Consent Statement: Not applicable.

Conflicts of Interest: The authors declare no conflict of interest. The content of the information provided in this publication does not necessarily reflect the position or the policy of the United States government, and no official endorsement should be inferred.

References

1. Tao, C.; Watts, B.; Ferraro, C.C.; Masters, F.J. A multivariate computational framework to characterize and rate virtual Portland cements. *Comput.-Aided Civ. Infrastruct. Eng.* **2019**, *34*, 266–278. [CrossRef]
2. DJI. Next Generation Mapping—Saving Time in Construction Surveying with Drones. Available online: <https://enterprise.dji.com/news/detail/next-generation-mapping> (accessed on 12 January 2019).
3. Triggs, B.; McLauchlan, P.F.; Hartley, R.I.; Fitzgibbon, A.W. Bundle adjustment—A modern synthesis. In *International Workshop on Vision Algorithms*; Springer: Berlin/Heidelberg, Germany, 1999; pp. 298–372.
4. Agisoft. Tutorial (Beginner Level): Orthomosaic and DEM Generation with Agisoft PhotoScan Pro 1.3 (with GCPs). Available online: [https://www.agisoft.com/pdf/PS_1.3%20-Tutorial%20\(BL\)%20-%20Orthophoto,%20DEM%20\(GCPs\).pdf](https://www.agisoft.com/pdf/PS_1.3%20-Tutorial%20(BL)%20-%20Orthophoto,%20DEM%20(GCPs).pdf) (accessed on 12 January 2019).
5. Trimble. Inpho UASMaster. Available online: <https://geospatial.trimble.com/products-and-solutions/trimble-inpho-uasmaster> (accessed on 12 January 2019).
6. Pix4D Home Page. Available online: <https://pix4d.com> (accessed on 4 January 2022).
7. Yasutaka Furukawa, Jean Ponce CMVS-PMVS. Available online: <https://github.com/pmoulon/CMVS-PMVS> (accessed on 12 January 2019).
8. von Übel, M. Affordable and Easy 3D Scanning 2019 Best Photogrammetry Software. Available online: <https://all3dp.com/1/best-photogrammetry-software> (accessed on 12 January 2019).
9. Agisoft Technical Support. Algorithms Used in Photoscan. Available online: <https://www.agisoft.com/forum/index.php?topic=89.0> (accessed on 4 January 2022).
10. Lowe, D.G. Object recognition from local scale-invariant features. In Proceedings of the Seventh IEEE International Conference on Computer Vision, Kerkyra, Greece, 20–27 September 1999; pp. 1150–1157.
11. Leica. Cyclone 3D Point Cloud Processing Software. Available online: <https://leica-geosystems.com/en-us/products/laser-scanners/software/leica-cyclone> (accessed on 4 January 2022).
12. Autodesk Help. Registering Unstructured Scans. Available online: <https://knowledge.autodesk.com/support/recap/learn-explore/caas/CloudHelp/cloudhelp/2018/ENU/Reality-Capture/files/GUID-AF55A2EB-FCE8-4982-B3D6-CEAD5732DF03-htm.html> (accessed on 4 January 2022).
13. Meshlab Homepage. Available online: <http://www.meshlab.net> (accessed on 4 January 2022).

14. CloudCompare. 3D Point Cloud and Mesh Processing Software. Available online: <https://www.danielgm.net/cc> (accessed on 12 January 2019).
15. Wang, R.; Peethambaran, J.; Chen, D. Lidar point clouds to 3-D urban models: A review. *IEEE J. Sel. Top. Appl. Earth Obs. Remote Sens.* **2018**, *11*, 606–627. [[CrossRef](#)]
16. Parmehr, E.G.; Fraser, C.S.; Zhang, C.; Leach, J. Automatic Registration of Aerial Images with 3D LiDAR Data Using a Hybrid Intensity-Based Method. In Proceedings of the 2012 International Conference on Digital Image Computing Techniques and Applications (DICTA), Fremantle, WA, Australia, 3–5 December 2012; pp. 1–7.
17. Nasrullah, A.R. Systematic Analysis of Unmanned Aerial Vehicle (UAV) Derived Product Quality. Master's Thesis, University of Twente, Enschede, The Netherlands, 2016.
18. Natan, M.; Jim, C.H.; Lane, S.N. Structure from Motion (SfM) Photogrammetry. In *Geomorphological Techniques*; British Society of Geomorphology: London, UK, 2015; Chapter 2.
19. Pix4D. Do RTK/PPK Drones Give You Better Results than GCPs? Available online: https://assets.ctfassets.net/go54bjdzbrgi/2VpGjAxJC2aaYlpsmFswD/3bcd8d512ccfe88ff63168e15051baee/BLOG_rtk-ppk-drones-gcp-comparison.pdf (accessed on 4 January 2022).
20. Ground Control Points for Drone Mapping. Creating Quality GCPs for Mapping Contour Lines. Available online: <https://www.groundcontrolpoints.com/mapping-contour-lines-using-gcps> (accessed on 12 January 2019).
21. Shaw, L.; Helmholz, P.; Belton, D.; Addy, N. Comparison of UAV Lidar and imagery for beach monitoring. *Int. Arch. Photogramm. Remote Sens. Spat. Inf. Sci.* **2019**, *42*, 589–596. [[CrossRef](#)]
22. Sanz-Ablanedo, E.; Chandler, J.H.; Rodríguez-Pérez, J.R.; Ordóñez, C. Accuracy of unmanned aerial vehicle (UAV) and SfM photogrammetry survey as a function of the number and location of ground control points used. *Remote Sens.* **2018**, *10*, 1606. [[CrossRef](#)]
23. Grayson, B.; Penna, N.T.; Mills, J.P.; Grant, D.S. GPS precise point positioning for UAV photogrammetry. *Photogramm. Rec.* **2018**, *33*, 427–447. [[CrossRef](#)]
24. Zhang, R.; Yang, B.; Xiao, W.; Liang, F.; Liu, Y.; Wang, Z. Automatic extraction of high-voltage power transmission objects from UAV lidar point clouds. *Remote Sens.* **2019**, *11*, 2600. [[CrossRef](#)]
25. Guan, S.; Zhu, Z. UAS-Based 3D Reconstruction Imagery Error Analysis. *Struct. Health Monit.* **2019**. [[CrossRef](#)]
26. May, N.C.; Toth, C.K. Point positioning accuracy of airborne LiDAR systems: A rigorous analysis. *Int. Arch. Photogramm. Remote Sens. Spat. Inf. Sci.* **2007**, 19–21. Available online: https://scholar.google.co.jp/scholar?q=.+Point+positioning+accuracy+of+airborne+LiDAR+systems:+A+rigorous+analysis.&hl=zh-TW&as_sdt=0&as_vis=1&oi=scholar (accessed on 10 April 2022).
27. Velodyne. VLP-16 User Manual63-9243 Rev. D. Available online: https://github.com/UCSD-E4E/aerial_lidar/blob/master/Datasheets%20and%20User%20Manuals/velodyne%20lidar%20datasheets/**VLP-16%20User%20Manual%20and%20Programming%20Guide%2063-9243%20Rev%20A.pdf (accessed on 12 January 2019).
28. Weber, H. Sick AG Whitepaper. Available online: https://cdn.sick.com/media/docs/2/22/322/Whitepaper_SICK_AG_Whitepaper_Select_the_best_technology_for_your_vision_application_en_IM0063322.PDF (accessed on 4 January 2022).
29. NovAtel. SPAN IMU-CPT. Available online: <https://www.novatel.com/assets/Documents/Papers/IMU-CPT.pdf> (accessed on 4 January 2022).
30. Applanix. APX-20 UAV High Performance GNSS-Inertial Solution with Dual IMU'S. Available online: https://www.applanix.com/downloads/products/specs/APX20_UAV.pdf (accessed on 4 January 2022).
31. Ravi, R.; Lin, Y.J.; Elbahnasawy, M.; Shamseldin, T.; Habib, A. Bias impact analysis and calibration of terrestrial mobile lidar system with several spinning multibeam laser scanners. *IEEE Trans. Geosci. Remote Sens.* **2018**, *56*, 5261–5275. [[CrossRef](#)]
32. Mostafa, M.; Hutton, J.; Reid, B.; Hill, R. GPS/IMU products—The Applanix approach. In *Photogrammetric Week*; Wichmann: Berlin/Heidelberg, Germany, 2001; Volume 1, pp. 63–83.
33. Hartley, R.; Zisserman, A. *Multiple View Geometry in Computer Vision*; Cambridge University Press: Cambridge, UK, 2003.
34. Toth, C.; Grejner-Brzezinska, D.A. *Airborne LiDAR Reflective Linear Feature Extraction for Strip Adjustment and Horizontal Accuracy Determination*; No. FHWA/OH-2008/15; Ohio State University: Columbus, OH, USA, 2009.
35. VectorNav. Industrial Series. Available online: [https://www.vectornav.com/docs/default-source/product-brochures/industrial-series-product-brochure-\(12-0009\).pdf](https://www.vectornav.com/docs/default-source/product-brochures/industrial-series-product-brochure-(12-0009).pdf) (accessed on 4 January 2022).
36. Fernandez Galarreta, J.; Kerle, N.; Gerke, M. UAV-based urban structural damage assessment using object-based image analysis and semantic reasoning. *Nat. Hazards Earth Syst. Sci.* **2015**, *15*, 1087–1101. [[CrossRef](#)]
37. Geocue. Drone LIDAR Systems (Drone LIDAR Considerations). Available online: <http://www.geocue.com> (accessed on 12 January 2019).
38. Tao, C.; Kutchko, B.G.; Rosenbaum, E.; Massoudi, M. A review of rheological modeling of cement slurry in oil well applications. *Energies* **2020**, *13*, 570. [[CrossRef](#)]
39. Dastgheibifard, S.; Asnafi, M. A review on potential applications of unmanned aerial vehicle for construction industry. *Sustain. Struct. Mater.* **2018**, *1*, 44–53.
40. De Melo, R.R.S.; Costa, D.B.; Álvares, J.S.; Irizarry, J. Applicability of unmanned aerial system (UAS) for safety inspection on construction sites. *Saf. Sci.* **2017**, *98*, 174–185. [[CrossRef](#)]
41. Tao, C.; Kutchko, B.G.; Rosenbaum, E.; Wu, W.T.; Massoudi, M. Steady flow of a cement slurry. *Energies* **2019**, *12*, 2604. [[CrossRef](#)]

42. Moeini, S.; Oudjehane, A.; Baker, T.; Hawkins, W. Application of an interrelated UAS-BIM system for construction progress monitoring, inspection and project management. *PM World J.* **2017**, *6*, 1–13.
43. Hamledari, H.; Davari, S.; Azar, E.R.; McCabe, B.; Flager, F.; Fischer, M. UAV-enabled site-to-BIM automation: Aerial robotic-and computer vision-based development of as-built/as-is BIMs and quality control. In *Construction Research Congress*; ASCE: New Orleans, LA, USA, 2018; pp. 336–346.
44. Eschmann, C.; Kuo, C.M.; Kuo, C.H.; Boller, C. Unmanned aircraft systems for remote building inspection and monitoring. In *Proceedings of the 6th European Workshop on Structural Health Monitoring (EWSHM 2012)*, Dresden, Germany, 3–6 July 2012.
45. Nex, F. UAV photogrammetry for mapping and 3d modeling—Current status and future perspectives. *Int. Arch. Photogramm. Remote Sens. Spat. Inf. Sci.* **2011**, *38*, 25–31.
46. Siebert, S.; Teizer, J. Mobile 3D mapping for surveying earthwork projects using an Unmanned Aerial Vehicle (UAV) system. *Autom. Constr.* **2014**, *41*, 1–14. [[CrossRef](#)]
47. Ajayi, O.G.; Palmer, M.; Salubi, A.A. Modelling farmland topography for suitable site selection of dam construction using unmanned aerial vehicle (UAV) photogrammetry. *Remote Sens. Appl. Soc. Environ.* **2018**, *11*, 220–230. [[CrossRef](#)]
48. Álvares, J.S.; Costa, D.B.; de Melo, R.R.S. Exploratory study of using unmanned aerial system imagery for construction site 3D mapping. *Constr. Innov.* **2018**, *18*, 301–320. [[CrossRef](#)]
49. Khaloo, A.; Lattanzi, D.; Cunningham, K.; Dell’Andrea, R.; Riley, M. Unmanned aerial vehicle inspection of the Placer River Trail Bridge through image-based 3D modelling. *Struct. Infrastruct. Eng.* **2018**, *14*, 124–136. [[CrossRef](#)]
50. Knight, R. LiDAR: Going Beyond Photogrammetry. Inside Unmanned Systems. Available online: <https://insideunmannedsystems.com/lidar-going-beyond-photogrammetry> (accessed on 12 January 2019).
51. Mill, T.; Alt, A.; Liias, R. Combined 3D building surveying techniques—terrestrial laser scanning (TLS) and total station surveying for BIM data management purposes. *J. Civ. Eng. Manag.* **2013**, *19* (Suppl. S1), S23–S32. [[CrossRef](#)]
52. Kiziltas, S.; Akinci, B.; Ergen, E.; Tang, P.; Gordon, C. Technological assessment and process implications of field data capture technologies for construction and facility/infrastructure management. *J. Inf. Technol. Constr. (ITcon)* **2008**, *13*, 134–154.
53. Randall, T. Construction engineering requirements for integrating laser scanning technology and building information modeling. *J. Constr. Eng. Manag.* **2011**, *137*, 797–805. [[CrossRef](#)]
54. Truong-Hong, L.; Laefer, D.F. Application of terrestrial laser scanner in bridge inspection: Review and an opportunity. In *Engineering for Progress, Nature and People, Proceedings of the 37th IABSE Symposium: Engineering for Progress, Nature and People, Madrid, Spain, 3–5 September 2014*; International Association for Bridge and Structural Engineering (IABSE): Zurich, Switzerland, 2014.
55. Suchocki, C.; Katzer, J. Terrestrial laser scanning harnessed for moisture detection in building materials—Problems and limitations. *Autom. Constr.* **2018**, *94*, 127–134. [[CrossRef](#)]
56. Cha, G.; Park, S.; Oh, T. A terrestrial LiDAR-based detection of shape deformation for maintenance of bridge structures. *J. Constr. Eng. Manag.* **2019**, *145*, 04019075. [[CrossRef](#)]
57. Walters, R.; Jaselskis, E.; Zhang, J.; Mueller, K.; Kaewmorachoen, M. Using scanning lasers to determine the thickness of concrete pavement. *J. Constr. Eng. Manag.* **2008**, *134*, 583–591. [[CrossRef](#)]
58. Niskanen, I.; Immonen, M.; Makkonen, T.; Keränen, P.; Tyni, P.; Hallman, L.; Hiltunen, M.; Kolli, T.; Louhisalmi, Y.; Kostamovaara, J.; et al. 4D modeling of soil surface during excavation using a solid-state 2D profilometer mounted on the arm of an excavator. *Autom. Constr.* **2020**, *112*, 103112. [[CrossRef](#)]
59. Karan, E.P.; Sivakumar, R.; Irizarry, J.; Guhathakurta, S. Digital modeling of construction site terrain using remotely sensed data and geographic information systems analyses. *J. Constr. Eng. Manag.* **2014**, *140*, 04013067. [[CrossRef](#)]
60. Suárez, J.C.; Ontiveros, C.; Smith, S.; Snape, S. Use of airborne LiDAR and aerial photography in the estimation of individual tree heights in forestry. *Comput. Geosci.* **2005**, *31*, 253–262. [[CrossRef](#)]
61. Zhou, Z.; Gong, J.; Hu, X. Community-scale multi-level post-hurricane damage assessment of residential buildings using multi-temporal airborne LiDAR data. *Autom. Constr.* **2019**, *98*, 30–45. [[CrossRef](#)]
62. Puri, N.; Turkan, Y. Bridge construction progress monitoring using lidar and 4D design models. *Autom. Constr.* **2020**, *109*, 102961. [[CrossRef](#)]
63. Guo, J.; Tsai, M.J.; Han, J.Y. Automatic reconstruction of road surface features by using terrestrial mobile lidar. *Autom. Constr.* **2015**, *58*, 165–175. [[CrossRef](#)]
64. Riegl. ‘Downward-Looking’ LiDAR Sensor for Unmanned Laser Scanning. Available online: <http://www.riegl.com/products/unmanned-scanning/riegl-minivux-1dl> (accessed on 12 January 2019).
65. Hokuyo. Scanning Laser Range Finder UTM-30LX/LN Specification. Available online: <https://www.hokuyo-aut.jp/search/single.php?serial=169> (accessed on 12 January 2019).
66. Moon, D.; Chung, S.; Kwon, S.; Seo, J.; Shin, J. Comparison and utilization of point cloud generated from photogrammetry and laser scanning: 3D world model for smart heavy equipment planning. *Autom. Constr.* **2019**, *98*, 322–331. [[CrossRef](#)]
67. Guo, F.; Jahren, C.T.; Hao, J.; Zhang, C. Implementation of CIM-related technologies within transportation projects. *Int. J. Constr. Manag.* **2020**, *20*, 510–519. [[CrossRef](#)]
68. Geocue. Drone Mapping—SfM Versus Low Precision LIDAR. Available online: <https://support.geocue.com/drone-mapping-sfm-versus-low-precision-lidar> (accessed on 12 January 2019).
69. Wang, J.; Sun, W.; Shou, W.; Wang, X.; Wu, C.; Chong, H.Y.; Liu, Y.; Sun, C. Integrating BIM and LiDAR for real-time construction quality control. *J. Intell. Robot. Syst.* **2015**, *79*, 417–432. [[CrossRef](#)]

70. Li, Y.; Liu, C. Applications of multirotor drone technologies in construction management. *Int. J. Constr. Manag.* **2019**, *19*, 401–412. [[CrossRef](#)]
71. Zhou, S.; Gheisari, M. Unmanned aerial system applications in construction: A systematic review. *Constr. Innov.* **2018**, *18*, 453–468. [[CrossRef](#)]
72. Tompkinson, W. Professional UAV Lidar Is (Finally) Focusing on the Ground. Available online: <https://www.geoweeknews.com/blogs/professional-uav-lidar-is-finally-focusing-on-the-ground> (accessed on 17 June 2019).
73. Merz, T.; Kendoul, F. Beyond visual range obstacle avoidance and infrastructure inspection by an autonomous helicopter. In Proceedings of the 2011 IEEE/RSJ International Conference on Intelligent Robots and Systems, San Francisco, CA, USA, 25–30 September 2011; pp. 4953–4960.
74. Guo, Q.; Su, Y.; Hu, T.; Zhao, X.; Wu, F.; Li, Y.; Liu, J.; Chen, L.; Xu, G.; Lin, G.; et al. An integrated UAV-borne lidar system for 3D habitat mapping in three forest ecosystems across China. *Int. J. Remote Sens.* **2017**, *38*, 2954–2972. [[CrossRef](#)]
75. Microdrones. Fully Integrated Systems for Professionals. Available online: <https://www.microdrones.com/en/integrated-systems/mdlidar/mdlidar3000dl> (accessed on 12 January 2019).
76. Yang, B.; Zang, Y.; Dong, Z.; Huang, R. An automated method to register airborne and terrestrial laser scanning point clouds. *ISPRS J. Photogramm. Remote Sens.* **2015**, *109*, 62–76. [[CrossRef](#)]
77. Naai-Jung, S.H.I.H.; Ming-Chang, W.U. *A 3D Point-Cloud-Based Verification of As-Built Construction Progress*; Springer: Vienna, Australia, 2005.
78. Al-Rawabdeh, A.; Moussa, A.; Foroutan, M.; El-Sheimy, N.; Habib, A. Time series UAV image-based point clouds for landslide progression evaluation applications. *Sensors* **2017**, *17*, 2378. [[CrossRef](#)]
79. Golparvar-Fard, M.; Peña-Mora, F.; Savarese, S. D4AR—A 4-dimensional augmented reality model for automating construction progress monitoring data collection, processing and communication. *J. Inf. Technol. Constr.* **2009**, *14*, 129–153.
80. Mastin, A.; Kepner, J.; Fisher, J. Automatic registration of LIDAR and optical images of urban scenes. In Proceedings of the 2009 IEEE Conference on Computer Vision and Pattern Recognition, Miami, FL, USA, 20–25 June 2009; pp. 2639–2646.
81. Thuy, C.T.; Watanabe, A.; Wakutsu, R. Cloud-based 3d data processing and modeling for uav application in disaster response and construction fields. In *Geotechnics for Sustainable Infrastructure Development*; Springer: Singapore, 2020; pp. 1177–1182.
82. Kubota, S.; Ho, C.; Nishi, K. Construction and usage of three-dimensional data for road structures using terrestrial laser scanning and UAV with photogrammetry. In Proceedings of the International Symposium on Automation and Robotics in Construction, Banff, AB, Canada, 21–24 May 2019; IAARC Publications: London, UK, 2019; Volume 36, pp. 136–143.
83. Howard, J.; Murashov, V.; Branche, C.M. Unmanned aerial vehicles in construction and worker safety. *Am. J. Ind. Med.* **2018**, *61*, 3–10. [[CrossRef](#)] [[PubMed](#)]
84. Wang, G.; Hollar, D.; Sayger, S.; Zhu, Z.; Buckeridge, J.; Li, J.; Chong, J.; Duffield, C.; Ryu, D.; Hu, W. Risk considerations in the use of unmanned aerial vehicles in the construction industry. *J. Risk Anal. Crisis Response* **2016**, *6*, 165–177. [[CrossRef](#)]
85. Gheisari, M.; Esmaeili, B. Applications and requirements of unmanned aerial systems (UASs) for construction safety. *Saf. Sci.* **2019**, *118*, 230–240. [[CrossRef](#)]
86. UAVCoach. Master List of Drone Laws. Available online: <https://uavcoach.com/drone-laws> (accessed on 12 January 2019).
87. FAA. Part 107 of the Federal Aviation Regulations. Available online: https://www.faa.gov/news/fact_sheets/news_story.cfm?newsId=20516 (accessed on 12 January 2019).

Review

sUAS Monitoring of Coastal Environments: A Review of Best Practices from Field to Lab

Shanyue Guan ¹, Hannah Sirianni ^{2,*}, George Wang ³ and Zhen Zhu ¹ 

¹ Department of Engineering, East Carolina University, Greenville, NC 27858, USA; guans18@ecu.edu (S.G.); zhuz@ecu.edu (Z.Z.)

² Department of Geography, Planning & Environment, East Carolina University, Greenville, NC 27858, USA

³ Department of Construction Management, East Carolina University, Greenville, NC 27858, USA; wangg@ecu.edu

* Correspondence: siriannah21@ecu.edu

Abstract: Coastal environments are some of the most dynamic environments in the world. As they are constantly changing, so are the technologies and techniques we use to map and monitor them. The rapid advancement of sUAS-based remote sensing calls for rigorous field and processing workflows so that more reliable and consistent sUAS projects of coastal environments are carried out. Here, we synthesize the best practices to create sUAS photo-based surveying and processing workflows that can be used and modified by coastal scientists, depending on their project objective. While we aim to simplify the complexity of these workflows, we note that the nature of this work is a craft that carefully combines art, science, and technology. sUAS LiDAR is the next advancement in mapping and monitoring coastal environments. Therefore, future work should consider synthesizing best practices to develop rigorous field and data processing workflows used for sUAS LiDAR-based projects of coastal environments.

Keywords: drone; UAS; coastal; coastal environments; data collection; data processing; structure from motion; workflow



Citation: Guan, S.; Sirianni, H.; Wang, G.; Zhu, Z. sUAS Monitoring of Coastal Environments: A Review of Best Practices from Field to Lab. *Drones* **2022**, *6*, 142. <https://doi.org/10.3390/drones6060142>

Academic Editor: David R. Green

Received: 12 May 2022

Accepted: 6 June 2022

Published: 8 June 2022

Publisher's Note: MDPI stays neutral with regard to jurisdictional claims in published maps and institutional affiliations.



Copyright: © 2022 by the authors. Licensee MDPI, Basel, Switzerland. This article is an open access article distributed under the terms and conditions of the Creative Commons Attribution (CC BY) license (<https://creativecommons.org/licenses/by/4.0/>).

1. Introduction

Coastal zones are land surfaces that are influenced by marine processes, which is why they are some of the most dynamic environments in the world. Both marine (e.g., waves and tides) and atmospheric (e.g., precipitation and winds) processes create a variety of landforms ranging from gently sloping sandy beaches to high rocky cliffs. Coastal zones are important because they support many different complex ecosystems from tidal swamps and marshes that extend from the landward limit of waves to coral reefs that extend to the seaward limit where the waves interact with the seabed. Coastal zones not only provide essential ecosystem services, such as shoreline protection, improved water quality, fisheries resources, and food and habitat to wildlife, but they are also attractive to human populations for their recreational opportunities [1]. For this reason, coastal scientists, engineers, and managers prioritize mapping and monitoring these changing environments.

As our coastal environments are constantly changing, so are the technologies and techniques that we use to map and monitor them. Traditionally, passive sensors mounted on satellites and occupied aircraft were used to monitor coastal environments [2]. However, with the rapid advancement of small Unoccupied Aircraft Systems (sUAS), coastal monitoring is now more affordable and efficient [3–7]. This makes sUAS highly attractive “on-demand remote sensing devices” [7]. The ability to choose sensors and to control temporal resolutions with a sUAS makes them excellent for mapping and monitoring small coastal areas. For example, many coastal habitats need on-demand remote sensing monitoring devices to capture data at certain phases of the tide, such as oyster reef beds exposed

A.4 Literature Review Paper 2 (published 2022)

at low tide [8–10]. In addition, on-demand remote sensing monitoring is needed to understand the behavior of sea life, such as rays [6], sea turtles [11,12], and whales [9]. In addition to the ability to control temporal resolution, sUAS help to reduce the time needed to collect in situ data in challenging coastal environments (e.g., by as much as a week) [4,6,7]. While sUAS have other benefits, such as the ability to provide high resolution imagery, dense point clouds, and the ability to capture data simultaneously with in situ measurements, the use of these technologies can be especially challenging in coastal environments. These challenges include but are not limited to environmental conditions such as the weather, sun glint on water, turbidity [8], distribution, and placement of Ground Control Points (GCPs) [5,6], the phase of the tide [4–8], battery capacity limiting sUAS projects to small coastal areas [6,7,13], and technical issues related to the computer power and skill needed for image processing [5,7].

To address these challenges, this review article aims to synthesize and illustrate best practices used to collect and process the sUAS data of coastal environments. To assist with this objective, we reviewed recent review articles that focus on sUAS applications in coastal environments and include topics such as regulations, sensors, platforms, calibration, validation, and data processing. Based on the best practices identified from these review articles in addition to the current literature, we illustrate a step-by-step workflow that can be used for either conducting sUAS surveys or sUAS data processing, or both. It is anticipated that this review will assist coastal scientists, engineers, and managers by providing flexible workflows that help guide consistent and reliable sUAS projects of coastal environments.

2. Previous Reviews of sUAS Monitoring of Coastal Environments

The rapid advancement of sUAS-based remote sensing has resulted in several recent review articles with a focus on coastal environments. Two academic research databases were used in this study to locate these articles. A Scopus search was conducted using the terms ‘coastal’, and ‘drone’, where 353 results were found. A Google Scholar search was also conducted using these terms, where 33,800 results were found. Both database searches were then limited to review documents, which produced 16 articles from Scopus and 665 articles from Google Scholar. We examined each abstract to verify each review article related to our overall goal of understanding the current sUAS applications in coastal environments. We were interested in synthesizing and illustrating the best practices used to collect and process sUAS data in coastal environments.

It should be noted that several of the review articles focused on other topics not related to our goals. Some articles from the Scopus search included a short discussion of how sUAS can be used in coastal environments, such as for non-destructive testing of bridges [14], to benefit marine citizen science [15], or to study human behavior such as recreational fishing or visitor use to public land [16]. Other articles from Scopus reviewed a different topic altogether, such as the application of space-borne synthetic aperture radar to offshore wind sources [17]. The Google Scholar search results were similar, in that some articles reviewed a different topic such as the application of sUAS for protected areas [18], monitoring marine environments with autonomous underwater vehicles [19], and the use of sUAS to conduct water sampling in freshwater environments [20]. These articles were removed from the literature bases, and afterwards five remained from Scopus and an additional four remained from Google Scholar. After thoroughly examining each article, a review article was identified in the references that was not categorized accordingly in the search engine [3]. All 10 of these articles focused on our interests above [3–9,11–13].

2.1. sUAS Regulations

Most of the review articles mention that a critical component to any sUAS project is the employment of a commercial pilot who is knowledgeable with the current flight restrictions and regulations placed by their respective country’s aviation authorities [3–7,9,11]. The authors of [6] expands on this requirement to include that a commercial pilot should be knowledgeable on the three common approaches to sUAS regulations, which include: (1) the Outright or

Effective Ban, as used in countries such as Cuba to ban sUAS flights completely; (2) the Visual Line of Sight (VLOS)-dependent approach, as used by Australia and the European Union to limit the sUAS flight to be within the pilot's VLOS; and (3) the Permissive approach, where regulations are reasonable and less restrictive, such as in Sweden. Since flight restrictions vary across the globe and continue to change as the technology advances, it is often difficult for commercial pilots to keep up with these changes [11,13]. This is especially the case for countries such as the United States that implement the VLOS-dependent approach that requires scientific pilots to obtain a license. Once qualified as a commercial pilot for a respective country, it is good practice to periodically check the sUAS regulations to ensure no changes were implemented, especially if flights are not conducted on regular basis (e.g., once, or twice a year). Regulations for the VLOS-dependent approach can be found at each aviation authority's website, such as the United States (<https://www.faa.gov/uas/> (accessed on 7 May 2022)), Costa Rica (<https://www.dgac.go.cr/> (accessed on 7 May 2022)), the European Union (<https://www.easa.europa.eu/domains/civil-drones> (accessed on 7 May 2022)), New Zealand (<https://www.aviation.govt.nz/> (accessed on 7 May 2022)), and Japan (<https://www.mlit.go.jp/en/koku/index.html> (accessed on 7 May 2022)).

2.2. Cameras and Platforms

The choice of a camera sensor should depend on the sUAS project objectives, although this can be limited, based on the project's budget costs and aircraft (multirotor or fixed-wing). The review articles cover a range of camera sensors including basic Red, Green, Blue (RGB), and more advanced sensors capable of measuring wavelengths not visible to the human eye such as multispectral (red edge and near infrared), hyperspectral, and thermal infrared. Basic camera RGB sensors are most often used because they are suitable for most coastal applications due to their low-cost, light weight, and high resolution [4,5]. The visible RGB bands of the electromagnetic spectrum are effective at capturing the behavior of marine vertebrates [6,9,11,12], as well as accurate 3D changes in coastal geomorphology derived from structure-from-motion (SfM) photogrammetry techniques. However, additional portions of the electromagnetic spectrum are needed to capture certain phenomena. For example, multispectral and hyperspectral sensors can capture the health and distribution of different wetland [3–5,7,8] and coral species [3,9], algal blooms, and water quality [4]. Thermal infrared cameras provide images of temperature, which are used to assess animal populations and water quality [4,6,8,9,11,13]. While the choice of sensor should depend on the sUAS project objectives, the choice of platform should depend on its ability to carry the sensor and meet the project's quality specifications (e.g., image resolution and accuracy).

sUAS are either multirotors with propellers, or fixed wings. Fixed wings are the most efficient at surveying large coastal areas due to the increased flight time, while multirotors are best for small coastal areas because the flight height and speed are easier to control [3–5,7]. However, if surveying several kilometers of coastline, the efficiency of fixed wings goes down while the project costs go up. The higher payload and better stabilization offered by multirotors makes them better suited for mounting more complex sensors, such as hyperspectral cameras [3,7]. Nonetheless, the technology is advancing, and complex sensors are now being designed specifically for fixed wings, such as the senseFly Parrot Sequoia+.

2.3. Calibration Procedures

Calibration is an important process that needs to be considered when conducting a sUAS project. Calibration is performed by comparing a test measurement with a calibration measurement standard of known accuracy. Calibration can refer to the platform, RAW (uncompressed, which is preferred) imagery, camera, and the final products (i.e., orthomosaics, 3D dense clouds, Digital Elevation Models (DEMs)). In terms of the platform itself, the Inertial Measurement Unit (IMU), compass, and gimble need to be calibrated often to ensure that the sUAS operates within the software tolerances. The IMU corrects for the platform's yaw, pitch, and roll allowing it to balance while moving in different directions. One review article mentions that multirotors often calibrate their IMU at startup, which can

be a problem if launching from a moving platform, such as a boat [9]. This issue can often be resolved by first launching the aircraft on land using motion-boot or boat-mode calibration sequences [9]. None of the review articles mention compass or gimbal calibration, which are important for accuracy and safety. Compass calibration aligns the platform's flight system with the Earth's magnetic north. We prefer to calibrate our platforms' compass prior to each flight to help prevent unwelcoming flyaways and unstable landings. The gimbal's motors support and stabilize the camera about an axis so it is not restricted from movement when taking images at different angles that increase the image network's geometry. We typically calibrate our gimbal after any rough handling of the platform, such as a harsh landing or even after an unwanted crash. A commercial pilot can often perform these calibrations using the respective platform's software.

In addition to platform calibration, both image and camera calibration need to be acknowledged. Image calibration, or radiometric calibration, is necessary when using multispectral and hyperspectral cameras because the raw Digital Numbers (DN) must be converted into reflectance spectra. Radiometric calibration is also required when conducting repeat flights where weather conditions are different so that the imagery is in a common scale based on reflectance spectra, such as when using multispectral, hyperspectral and RGB cameras. Sensor noise can also contribute to radiometric variability [7]. We note that radiometric calibration is required when comparing reflectance spectra data through time, such as when monitoring different vegetation communities. However, if the sUAS project goal is to monitor topographic changes, as derived from SfM techniques, 3D point clouds are compared and not the reflectance spectra data. While radiometric calibration is an important process to consider in many sUAS projects, only 2 out of the 10 review articles discussed radiometric calibration procedures [4,7]. These include the use of calibration targets that are distributed prior to the sUAS survey, so that the corresponding imagery (test measurement) can be used with the calibration target (calibration measurement of standard accuracy) [4,7]. Spectroradiometers are also used in flight or in the field to collect upwelling radiance and downwelling irradiance data [4]. Some camera manufacturers offer calibration targets, such as MicaSense, and software available for radiometric calibration to consider include Agisoft and Pix 4D.

A discussion on camera calibration is missing from all of the 10 review articles. Camera calibration is a process used to describe the camera parameters needed to reliably relate the 2D image coordinate system with a 3D real-world coordinate system. The camera model can be determined using a pre-calibration or self-calibration procedure. Pre-calibration is more involved because it requires capturing images taken at many different angles of a calibration pattern whose geometry in 2D or 3D space is precisely known [21], which is performed prior to the bundle adjustment in the SfM workflow [21,22]. A workflow for determining a pre-calibration camera model using a 2D geometric pattern is available using MATLAB (<https://www.mathworks.com/help/vision/ug/using-the-single-camera-calibrator-app.html> (accessed on 7 May 2022)) and Agisoft (<https://agisoft.freshdesk.com/support/solutions/articles/31000160059-lens-calibration-using-chessboard-pattern-in-metashape> (accessed on 7 May 2022)). A caveat is that the geometric pattern should be captured at a distance that is roughly equal to the flight height, which is not suitable for long-range capturing scenarios. On the other hand, self-calibration procedures are more flexible because they do not require an observation of a geometric pattern and are carried out automatically during the bundle adjustment. However, this approach also has its cons, as many parameters need to be estimated that do not always obtain accurate results [21]. The pre-calibration and self-calibration approaches each have their pros and cons, and, regardless of which approach is used for a sUAS project, we agree with [23] that sufficient image metadata such as the camera make and model, ISO, shutter speed, aperture, and focal length need to be reported to allow confidence and reproducibility in the results.

Geometric calibration (also known as georeferencing) is the process used to relate the 2D image coordinate system with a 3D real-world coordinate system. The calibration measurements of known accuracy relative to an established 3D coordinate system are referred

to as GCPs. GCPs are often surveyed with Real-time Kinematic Global Navigation Satellite Systems (RTK-GNSS) prior to or after a sUAS survey, so that the corresponding imagery (test measurement) can be matched up with their 3D ground coordinates (calibration measurement of standard accuracy) in the SfM workflow. Only 1 out of the 10 review articles mention the use of GCPs for registering the sUAS imagery to a 3D coordinate system [7]. In addition to accurate measurements of GCPs, their number and distribution throughout the study area depends on the quality specifications of the sUAS project. The number of GCPs should be sufficient where half are designated as control (calibration) and the other half are designated as quality (validation) to assess the reliability of the georeferencing [24].

2.4. Validation Procedures

Validation is the process of determining whether the test measurement meets the standard requirements for an intended sUAS project's purpose. A total of 3 out of the 10 review articles discussed validation as the process of comparing the RTK-GNSS locations of field samples of the phenomenon to be mapped (e.g., coastal habitat, water quality, etc.) with the classified coastal habitat or predicted water quality values [4,5,7]. Validation in this context is used to assess, for example, how well a machine learning model makes new predictions on unseen data to predict the water quality. However, before we can validate such a model, we must validate the geometric calibration results.

2.5. Literature Review Gaps

The best practices used to conduct sUAS surveys as well as process sUAS photo-based data in coastal environments are missing from the review literature. Table 1 emphasizes the gaps as data collection, calibration, validation, data processing, and software. We intend to fill this gap by presenting two workflows to help guide coastal scientists. The following section compiles the current best practices as a series of activities necessary to complete a successful sUAS field campaign as well as a workflow to process sUAS photo-based data.

Table 1. Major topics either reviewed or not reviewed by each of the 10 review articles identified in this study. Topics marked by a check in the box indicate the topic was covered. The topics least reviewed are data collection, calibration, validation, data processing, and software.

| Reference | Regulations | Sensors | Platforms | Collection | Calibration | Validation | Processing | Software | Challenges | Benefits | Applications |
|-------------------------------|-------------------------------------|-------------------------------------|-------------------------------------|-------------------------------------|-------------------------------------|-------------------------------------|--------------------------|-------------------------------------|-------------------------------------|-------------------------------------|-------------------------------------|
| Morgan et al. (2022) [7] | <input type="checkbox"/> | <input checked="" type="checkbox"/> | <input checked="" type="checkbox"/> | <input checked="" type="checkbox"/> | <input checked="" type="checkbox"/> | <input checked="" type="checkbox"/> | <input type="checkbox"/> | <input type="checkbox"/> | <input checked="" type="checkbox"/> | <input checked="" type="checkbox"/> | <input type="checkbox"/> |
| Adade et al. (2021) [5] | <input type="checkbox"/> | <input checked="" type="checkbox"/> | <input checked="" type="checkbox"/> | <input type="checkbox"/> | <input type="checkbox"/> | <input checked="" type="checkbox"/> | <input type="checkbox"/> | <input checked="" type="checkbox"/> | <input checked="" type="checkbox"/> | <input type="checkbox"/> | <input checked="" type="checkbox"/> |
| Kandrot et al. (2021) [13] | <input checked="" type="checkbox"/> | <input type="checkbox"/> | <input checked="" type="checkbox"/> | <input type="checkbox"/> | <input type="checkbox"/> | <input checked="" type="checkbox"/> | <input type="checkbox"/> | <input type="checkbox"/> | <input checked="" type="checkbox"/> | <input type="checkbox"/> | <input checked="" type="checkbox"/> |
| Oleksyn et al. (2021) [6] | <input checked="" type="checkbox"/> | <input type="checkbox"/> | <input type="checkbox"/> | <input type="checkbox"/> | <input type="checkbox"/> | <input type="checkbox"/> | <input type="checkbox"/> | <input type="checkbox"/> | <input checked="" type="checkbox"/> | <input checked="" type="checkbox"/> | <input checked="" type="checkbox"/> |
| Ridge and Johnston (2020) [8] | <input type="checkbox"/> | <input checked="" type="checkbox"/> | <input checked="" type="checkbox"/> | <input type="checkbox"/> | <input type="checkbox"/> | <input type="checkbox"/> | <input type="checkbox"/> | <input type="checkbox"/> | <input checked="" type="checkbox"/> | <input checked="" type="checkbox"/> | <input checked="" type="checkbox"/> |
| Johnston et al. (2019) [9] | <input checked="" type="checkbox"/> | <input checked="" type="checkbox"/> | <input checked="" type="checkbox"/> | <input type="checkbox"/> | <input checked="" type="checkbox"/> | <input type="checkbox"/> | <input type="checkbox"/> | <input type="checkbox"/> | <input checked="" type="checkbox"/> | <input type="checkbox"/> | <input checked="" type="checkbox"/> |
| Schofield et al. (2019) [12] | <input type="checkbox"/> | <input type="checkbox"/> | <input type="checkbox"/> | <input type="checkbox"/> | <input checked="" type="checkbox"/> | <input checked="" type="checkbox"/> |
| Kislik (2018) [4] | <input checked="" type="checkbox"/> | <input checked="" type="checkbox"/> | <input checked="" type="checkbox"/> | <input type="checkbox"/> | <input checked="" type="checkbox"/> | <input checked="" type="checkbox"/> | <input type="checkbox"/> | <input checked="" type="checkbox"/> | <input checked="" type="checkbox"/> | <input checked="" type="checkbox"/> | <input checked="" type="checkbox"/> |
| Rees et al. (2018) [11] | <input checked="" type="checkbox"/> | <input type="checkbox"/> | <input type="checkbox"/> | <input checked="" type="checkbox"/> | <input type="checkbox"/> | <input type="checkbox"/> | <input type="checkbox"/> | <input type="checkbox"/> | <input checked="" type="checkbox"/> | <input checked="" type="checkbox"/> | <input checked="" type="checkbox"/> |
| Klemas (2015) [3] | <input checked="" type="checkbox"/> | <input type="checkbox"/> | <input checked="" type="checkbox"/> | <input type="checkbox"/> | <input type="checkbox"/> | <input type="checkbox"/> | <input type="checkbox"/> | <input type="checkbox"/> | <input checked="" type="checkbox"/> | <input checked="" type="checkbox"/> | <input checked="" type="checkbox"/> |

3. sUAS Photo-Based Surveys of Coastal Environments: Best Practices

3.1. sUAS Photo-Based Surveys

Good data can easily be lost due to poor field protocols. Here, we expand on the existing literature and create a Red, Green, Blue (RGB) workflow organized in three phases using best practices (Figure 1). This workflow can be modified to map and monitor different coastal phenomena such as coastal habitats, beach nesting species, topographic and nearshore bathymetry.

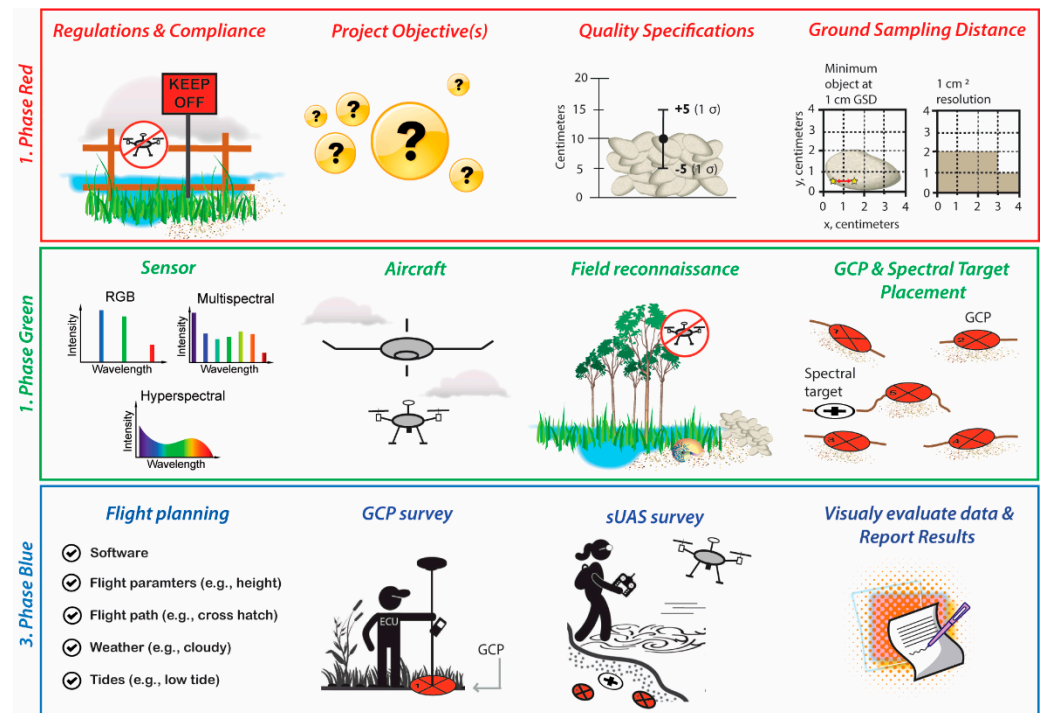


Figure 1. Red, Green, Blue (RGB) workflow organized in three phases using best practices for conducting sUAS photo-based surveys of coastal environments.

In phase red of the workflow, the scientific pilot follows sUAS regulations while obtaining any special permissions from landowners and managers to access the survey area [25,26]. While sUAS regulations differ among nations, [26] identified three general aspects of sUAS regulations, which include: (1) targeting regulated use of airspace; (2) imposing operational limitations; and (3) administration of flight permissions, pilot licenses, and authorization of data collection. This demonstrates the importance of knowing these rules before beginning a sUAS survey. The next step in phase red is to determine the project objective(s). In our example, the project objective is to conduct repeat annual surveys to monitor vertical changes in newly restored oyster reefs. With the project objective identified, the quality specifications of minimum vertical accuracy (mean bias) and precision (1σ or Root Mean Square Error (RMSE)) assuming data follow a normal distribution) requirements can be justified. This requires some background knowledge of the features being mapped. In our example, intertidal oyster reefs can grow 10 to 13 cm yr^{-1} vertically [27], so one approach is to determine the required precision by dividing the minimum annual expected vertical change of 10 cm by two ($10/2 = 5\text{ cm}$). The required mean bias should be zero. This allows the minimum expected annual vertical change of 10 cm to be measured more reliably. The next step in phase red of the workflow is to determine the optimal resolution based on the minimum object to be mapped, which, in our example, is a $2 \times 4\text{ cm}$ oyster. Traditionally, the Minimum Mapping Unit (MMU), which is the smallest feature to be mapped, is useful when considering the Ground Sampling Distance (GSD) [28]. The GSD can be illustrated as the distance between the center of two cells when using an orthogonal plane. In our

example, the GSD should be at a maximum 1 cm, so that the shape and size of an oyster can be resolved. GSD is a result of flight height, focal length, and sensor resolution, which can automatically be calculated in most flight planning software, such as DJI GS Pro.

Once regulations, project objective(s), quality specifications, and GSD are defined in phase red, the next phase in the workflow is phase green, where the first step is to identify the appropriate sensor. RGB sensors with fine resolutions (≥ 20 MP), a wide range in global shutter speed, lens aperture, and ISO should be considered for accurate topographic mapping [16]. An RGB sensor is a reasonable choice for our example project objective, to monitor vertical changes in oyster reefs. Currently, multispectral, and hyperspectral sensors produce non-aligned bands and low-resolution images [26,29] making them less suitable for fine resolution topographic mapping. However, if our project objective was to classify coastal vegetation at the species level or estimate water quality, multispectral or hyperspectral sensors would be preferred because they provide more spectral information for training a machine or deep learning classification model. Although vendors typically carry out sensor calibration, an ongoing assessment in the lab is also necessary [26]. The next step in phase green of the workflow is to determine the aircraft on which the sensor will be mounted. Multicopters are best suited for our example project, due to their vertical takeoff and landing in complex coastal terrain, their ability to fly slowly and stop to capture imagery (reducing motion blur), hover at low flight heights for close data capture of small objects, and the project's small spatial coverage (e.g., < 2 ha), which is suitable for a low battery capacity.

A field reconnaissance of the survey site is critical for safety, which is the next step in phase green. This visual ground assessment helps to identify any flight obstacles, potential takeoff and landing sites, and accessible areas with full visibility of GCPs [26]. It is also useful to take good field notes that map out these safety concerns to assist with proper placement of the GCPs and geometric calibration targets (if comparing spectral information). Important considerations in GCP placement include the number (more GCPs tend to reduce vertical errors), an even spatial distribution that also reflects the variations in topography, and accurate and precise measurement, such as with RTK-GNSS [26]. One helpful tool for managing the placement of GCPs is the open-source PhenoFly Planning Tool [26,30]. The combination of this tool with field reconnaissance notes maximizes careful GCP planning in the coastal zone. Additional considerations for our example project objective are the use of semi-permanent elevated GCPs on a platform [7] on the marsh-side and seaward-side of the oyster reefs. Additionally, the dimension of the GCPs should be about 10 times the GSD [26,31]. With our required GSD of 1 cm, GCP dimensions should be no less than 10 cm in dimension. In addition to the GCPs, radiometric calibration target(s) should be considered if comparing reflectance spectra data through time, such as when monitoring different vegetation communities.

Once the sensor, aircraft, field reconnaissance, and GCP placement are determined in phase green of the workflow, the last phase in the workflow is the blue phase, which involves planning and conducting the sUAS surveys. The first step in phase blue is flight planning, which can be performed a few days before or on the day of the survey. The options for flight planning software are well covered in the literature [5,7,26]. The open-source PhenoFly Planning Tool is unique because, in addition to planning the number and placement of GCPs, the software allows for flight mission planning that considers many important parameters, such as sensor and lens, flight height needed to achieve the required GSD, exposure value due to a sunny or cloudy day, side and end lap, motion blur, and flight path [30]. The choice of autopilot software, such as DJI GS Pro and DroneDeploy, should be made, based on its compatibility with the aircraft and pilot control over as many of these parameters as possible. In setting the GSD, the software optimizes flying speed and height, based on the aircraft and camera. To reduce motion blur, we use a capture mode of hover and capture at each point. For homogenous coastal areas, such as beaches and sandy bottoms in the intertidal zone, we prefer a cross flight pattern, a tilted camera, and an 80% front and side overlap (this requires more images and longer flights). These parameter

settings help mitigate fewer tie points from being identified in the SfM process and improve the self-calibration process [26]. Another important consideration in this step is to set the image file format as a RAW file rather than a JPEG file, because RAW files do not compress information that leads to lower quality imagery [28]. It is wise to save the mission in the autopilot software and adjust as needed when in the field.

Additional considerations in the blue phase include weather and tides, which should be checked prior to and on the day of the survey. Many aircraft cannot sustain winds over 20 mph, nor should they be flown in the rain. We prefer a calm cloudy day to reduce shadows amongst objects on the surface. In addition, the flight needs to be timed right at low tide when collecting data in the intertidal zone. There are useful apps that can be used to check airspace notifications, weather, and tides prior to and during flight operations. In the US, there are the notices to airmen (NOTAMs; identifies where a pilot can fly), the aviation weather report (METAR), and the terminal aerodrome forecast (TAF) from the National Weather Service Aviation Weather Center at www.aviationweather.gov (accessed on 7 May 2022). Tides can be predicted far in advance with a high degree of accuracy, and tidal predictions in the US can be obtained from the National Oceanic Atmospheric Administration's Tide Alert app or for free at: <https://tidesandcurrents.noaa.gov/> (accessed on 7 May 2022). The next steps in phase blue are to conduct the GCP survey and flights. For safety and efficiency, a preliminary checklist should be followed and is provided in Appendix A by [26] including aircraft calibration procedures. In the final step of phase blue, the procedures, settings, and parameters are documented and shared with the data products and any results derived from them. We recommend following Appendix B by [26] for creating metadata associated with the sUAS survey, which are critical for reproducibility and confidence in the results.

3.2. sUAS Photo-Based Processing of Dense Point Clouds, DEMs and Orthomosaics

A sUAS photo-based workflow is created in this study by combining the best practices of several proven data processing approaches into one (Figure 2). We expand on the workflow provided by [24] (see Figure 3), focusing more in detail on the processing of sUAS photo-based data.

Step 1 of the workflow requires the use of radiometrically calibrated images when conducting repeat sUAS surveys where the spectral data are compared through time (e.g., classifying coastal vegetation). The Empirical Line Method (ELM) is commonly used due to its accuracy and simplification [32], which was further simplified by [33]. However, in projects that require dense point clouds to be compared through time, radiometric calibration may be less necessary. This is because radiometric calibration is not directly related to the performance of SfM photogrammetry used to derive dense point clouds [34]. The next step in the workflow is to determine the processing software and removal of poorly focused images. Agisoft Photoscan/Metashape (Metashape) is the leading software used by coastal scientists for geometric calibration, orthomosaic, and dense point cloud generation [4,7]. Therefore, Metashape is used here to illustrate the sUAS photo-based processing workflow. In Step 2, poorly focused images are excluded because they can negatively impact image alignment. Metashape offers an automatic image quality feature that calculates a value, based on the sharpness of the most focused area of an image [35]. While images with a value less than 0.5 units are recommended for removal, a unit of 0.8 was found to be a more conservative estimate [24].

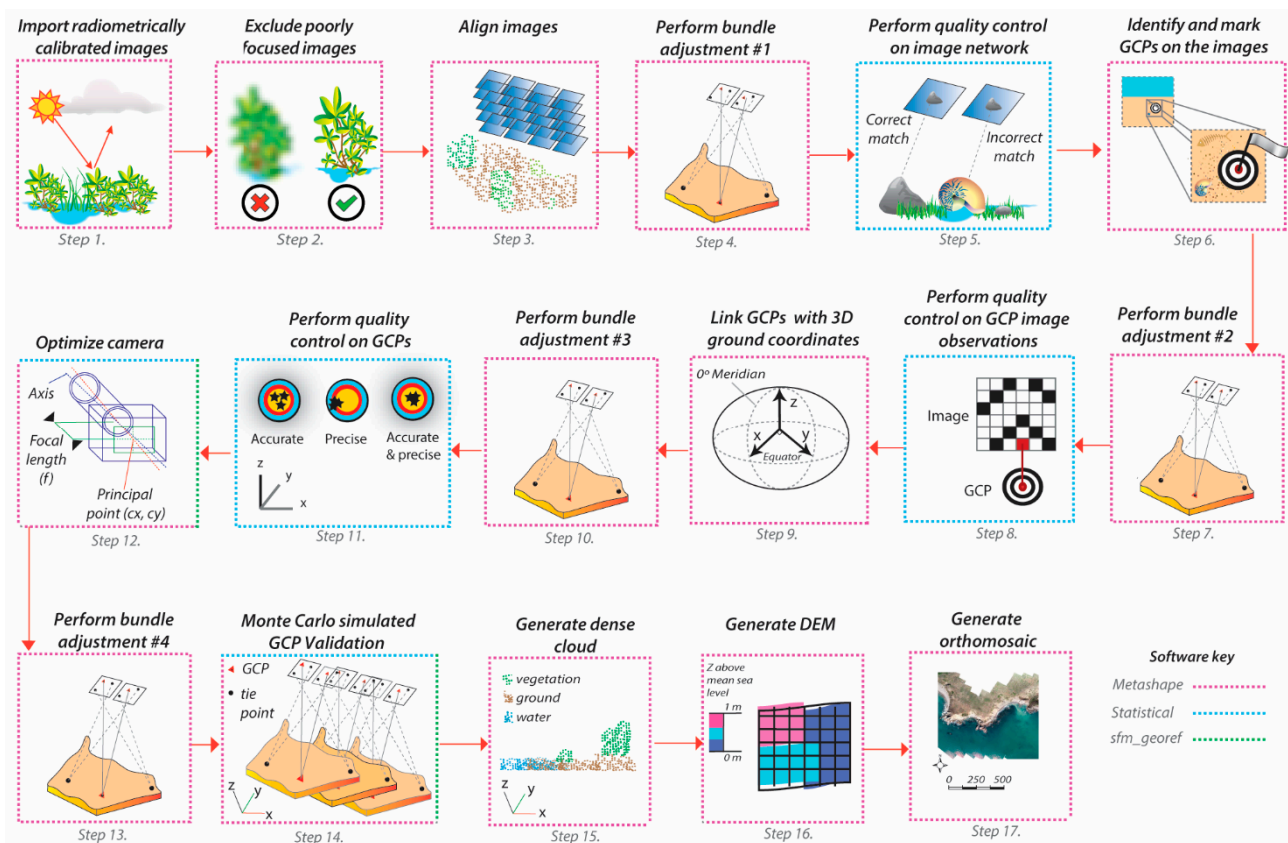


Figure 2. A 17-step workflow using best practices for processing sUAS photo-based surveys of coastal environments.

Step 3 in the processing workflow is image alignment. This involves SfM to reconstruct 3D geometry by identifying and matching common features on overlapping images into tie points. In Step 4, a bundle adjustment is carried, which uses a least-squares global optimization approach to reduce image residuals by adjusting camera parameters, camera orientations, and the 3D point positions [36,37]. The output from this procedure results in a more reliable, aligned image network based on the estimated camera positions from the imagery alone and a resulting sparse cloud. Step 5 involves performing a quality control assessment on the image network by checking for errors in the potential mismatching of tie points [24,37]. At this step, the RMSE between the projected reconstructed tie points and their corresponding original projections detected on the photos are calculated for each photo in the network and the results visualized in a statistical software, such as open-source R v4.1.3. This helps to identify any photos with high image residuals that may need removal from the image network [24,37].

Step 6 in the workflow involves the process of hand marking GCPs on the images. The GCPs are then added to the image network without setting them as a control, followed by another bundle adjustment (Step 7) [24,37]. This allows for the quality of the GCPs to be captured in pixels (Step 8). In Step 9, georeferencing to an established coordinate system is achieved by linking the GCPs with their 3D ground coordinates. This is followed by another bundle adjustment, using all GCPs as control (Step 10). A Python script is then executed in Metashape [37] to export the GCP errors into a statistical software, so that the RMSE between the estimated positions and GCP 3D coordinates can be calculated (Step 11).

The next step in the processing workflow is camera model optimization (Step 12). A camera model can be determined either by a pre-calibration or self-calibration procedure during the bundle adjustment. The pre-calibrated procedure involves determining the intrinsic geometry and distortion camera model parameters prior to camera model optimization, such as through a common checkboard routine [22]. Self-calibration is where

the camera model parameters are determined during the bundle adjustment. It should be noted that capturing imagery at various angles during the survey (e.g., different crosshatch flight patterns and gimbal pitches) increases the image geometry and can minimize error in the dense point clouds when self-calibrating [38]. Whether using a pre-calibrated or self-calibrated procedure, a suitable camera model is determined by evaluating different camera models (i.e., different combinations of camera parameters such as focal length, principal point, etc.) to determine which provides the lowest RMSE [38]. To test a camera model, half of the GCPs are randomly selected as control when running many Monte Carlo simulations in Metashape [24], using the Python script provided by [37]. The Monte Carlo results are then compiled in the open source `sfm_georef v.3.0` [39] and brought into a statistical software to estimate the RMSE where the camera model with the lowest RMSE prevails. Then another bundle adjustment is performed, but this time, all GCPs are set as control so the reprojection RMSE, GCP image RMSE, and GCP ground RMSE are captured (Step 13). These parameter values are important for any coastal scientist to report, as they are used in the final calculation of the reported error for the derived dense point clouds and orthomosaics.

For Step 14 in the processing workflow, Step 12 is repeated but this time the camera model is set because it is already optimized, and the errors calculated in step 13 are used in many Monte Carlo simulations, each followed by a bundle adjustment [37]. The Monte Carlo results are then compiled in `sfm_georef v.3.0` and brought into a statistical software to estimate the control and quality of the GCP RMSEs. With a high-quality image network, a dense point cloud is generated (Step 15), but first, all of the GCPs are selected as control, the errors calculated in Step 13 are included, and the camera model is set followed by a bundle adjustment. Dense point clouds are generated using “high” quality and “aggressive” depth filtering, followed by automatic and manual classification [24]. The workflow is concluded by generating a high resolution and accurate DEM (Step 16), and orthomosaic (Step 17).

4. Discussion

Our analysis of recent review articles on sUAS-based remote sensing of coastal environments demonstrates the need for workflows to help guide coastal scientists in carrying out consistent and reliable sUAS projects from field to lab. The art and science of capturing and processing accurate sUAS data involves field survey requirements and rigorous photogrammetric workflows to compensate for the potential shortcomings in sUAS-derived products [24]. Traditionally, geographers and remote sensing scientists are trained in the use of such technologies and data processing. However, with the accessibility and affordability of these on demand remote sensing devices for real-time monitoring, coastal scientists from a variety of backgrounds are taking advantage of their benefits. While the workflows presented in Sections 3.1 and 3.2 of this study aim to provide helpful guidance on the steps needed to carry out reliable and repeatable sUAS projects in coastal environments, we acknowledge the detail and complexity of the workflows, which is a part of the craft.

The sUAS survey workflow illustrated in this article was divided into three phases to help simplify the process. In phase 1 of the workflow, the requirement of a licensed pilot who is knowledgeable of the scientific questions that are being addressed is required. Phase 1 in the workflow ultimately relies on the pilot’s ability to carry out phase 2, where the choice of sensor and aircraft are determined, along with a field reconnaissance to ensure the survey can be conducted efficiently and safely. Otherwise, the ability to address the sUAS objectives may be compromised. The sUAS survey workflow illustrated in this article demonstrates that there is more to simply being a commercial pilot when carrying out sUAS projects for science.

Although we also attempted to help simplify a sUAS data processing workflow that results in data products that meet strict sUAS project quality specifications (see Figure 2), the need for coastal scientists with advanced technical skills persists. The 17-step processing workflow illustrates that sUAS photo-based data processing requires special attention to the image network, GCP image observations, and camera model optimization procedures

to prevent propagation of errors into the resulting data products. This requires knowledge of the SfM process as well as of many different software packages.

Currently, there is not one single software that can carry out all the steps provided in the sUAS processing workflow. Instead, a combination of Metashape SfM photogrammetry software, open-source programming such as Python, and statistical software such as R, and `sfm_georef` [39] are used (see Figure 2). However, coastal scientists with minimum programming experience can use the Python script provided by [37], because basic information such as the file path and version of Metashape require basic re-scripting. The Python scripting associated with each version of Metashape is also provided by the software's scripting reference [40]. For coastal scientists that do not have access to Metashape, another option is the open-source photogrammetry software MicMac [41]. Future work may consider modifying our sUAS data processing workflow using MicMac instead of Metashape to allow accessibility to all coastal scientists regardless of budget.

While this article focused on sUAS photo-based data collection and processing, future work is needed to create reliable sUAS LiDAR-based workflows used for surveying coastal environments. sUAS LiDAR is the next advancement in coastal mapping and monitoring [3–5,7]. sUAS LiDAR-based surveys are faster than sUAS photo-based surveys, which require multiple flight paths at different angles and large image overlap (e.g., 70–80%). When compared to sUAS photo-based data, sUAS LiDAR-based data are more reliable at estimating ground, vegetation height, and density in coastal marshes [42]. While sUAS photo-based surveys seem promising for the measurement of nearshore bathymetry, they are limited to areas with distinct visible features on the seafloor and do not perform well in homogeneous sandy bottoms. sUAS LiDAR-based surveys, on the other hand, have proven effective at measuring homogenous sandy bottoms [43]. Many of the reviews converge on sUAS-based LiDAR as the next advancement in coastal mapping and monitoring [3–5,7].

5. Conclusions

We assessed the current state of review articles on the use of sUAS in coastal environments [3–9,11–13]. These review articles covered a wide range of topics including sUAS photo-based regulations, sensors, platforms, calibration, validation, software, challenges, benefits, and applications. Table 1 emphasizes the major gaps as data collection, calibration, validation, and processing. We expanded on these review articles to create both a sUAS survey and sUAS processing workflow, using several proven data collection and processing techniques.

sUAS photo-based surveys require more time than sUAS LiDAR-based surveys, and this poses a challenge for pilots tasked with collecting data at certain phases of the tide. The sUAS survey workflow presented in this study can be modified to fit other sUAS projects to ensure more reliable and rapid data are captured during sensitive time constraints. For example, the sUAS survey workflow helps prepare the scientific pilot with knowledge of sUAS regulations, the project objective along with its quality specifications, the layout of the survey site, and the GCP placement. With data collected using reliable field protocols, rigorous photogrammetric workflows can be carried out to compensate for the potential shortcomings in the final sUAS-derived products. The sUAS processing workflow presented in this study is rigorous, so that accurate and reliable products are produced. Key steps include performing quality and control assessments on the image network, GCPs, and camera calibration model.

While this article focused on sUAS photo-based surveys due to the current rapid advance of technology, future work should focus on developing rigorous field and processing workflows for using sUAS LiDAR in coastal environments. sUAS LiDAR is the next important advancement in mapping and monitoring coastal environments. We hope that this study will stimulate the application of sUAS photo-based and sUAS LiDAR-based best practices in coastal environments.

A.5 LIDAR Error Model Paper 1 (published 2022)

Author Contributions: Conceptualization, S.G., H.S. and Z.Z.; methodology, H.S.; writing—original draft preparation, H.S.; writing—review and editing, H.S.; illustrations, H.S.; funding acquisition, Z.Z., S.G., G.W. and H.S. All authors have read and agreed to the published version of the manuscript.

Funding: The authors would like to thank the North Carolina Department of Transportation (Award Number: RP 2020-35) (Z.Z., S.G. and G.W.), and the Department of Interior—National Park Service (Award Number: P19AC01091) (H.S.) for their assistance in supporting this research. This project is also funded, in part, by the US Coastal Research Program (USCRP) (H.S.) as administered by the US Army Corps of Engineers (USACE), Department of Defense. The authors acknowledge the USACE and USCRP’s support of their effort to strengthen coastal academic programs and address coastal community needs in the United States.

Institutional Review Board Statement: Not applicable.

Informed Consent Statement: Not applicable.

Data Availability Statement: Not applicable.

Conflicts of Interest: The authors declare no conflict of interest. The content of the information provided in this publication does not necessarily reflect the position or the policy of the United States government, and no official endorsement should be inferred.

References

1. Leven, L.A.; Boesch, D.F.; Covich, A.; Dahm, C.; Erséus, C.; Ewel, K.C.; Kneib, R.T.; Moldenke, A.; Palmer, M.A.; Shelgrove, P.; et al. The function of marine critical zone transition zones and the importance of sediment biodiversity. *Ecosystems* **2001**, *4*, 430–451. [[CrossRef](#)]
2. Matthews, M.W. A current review of empirical procedures of remote sensing in inland and near-coastal transitional waters. *Int. J. Remote Sens.* **2011**, *32*, 6855–6899. [[CrossRef](#)]
3. Klemas, V.V. Coastal and environmental remote sensing from unmanned aerial vehicles: An overview. *J. Coast. Res.* **2015**, *31*, 1260–1267. [[CrossRef](#)]
4. Kislik, C.; Dronova, I.; Kelly, M. UAVs in support of algal bloom research: A review of current applications and future opportunities. *Drones* **2018**, *2*, 35. [[CrossRef](#)]
5. Adade, R.; Aibinu, A.M.; Ekumah, B.; Asaana, J. Unmanned Aerial Vehicle (UAV) applications in coastal zone management—A review. *Environ. Monit. Assess.* **2021**, *193*, 1–12. [[CrossRef](#)]
6. Oleksyn, S.; Tosetto, L.; Raoult, V.; Joyce, K.E.; Willimason, J.E. Going Batty: The challenges and opportunities of using drone to monitor the behavior and habitat use of rays. *Drones* **2021**, *5*, 12. [[CrossRef](#)]
7. Morgan, G.R.; Hodgson, M.E.; Wang, C.; Schill, S.R. Unmanned aerial remote sensing of coastal vegetation: A review. *Ann. GIS* **2022**, 1–15. [[CrossRef](#)]
8. Ridge, J.; Seymour, A.; Rodriguez, A.B.; Dale, J.; Newton, E.; Johnston, D.W. Advancing UAS Methods for Monitoring Coastal Environments. In Proceedings of the AGU Fall Meeting, New Orleans, LA, USA, 11–15 December 2017.
9. Johnston, D.W. Unoccupied Aircraft Systems in Marine Science and Conservation. *Annu. Rev. Mar. Sci.* **2019**, *11*, 439–463. [[CrossRef](#)]
10. Windle, A.E.; Poulin, S.K.; Johnston, D.W.; Ridge, J.T. Rapid and accurate monitoring of intertidal Oyster Reef Habitat using unoccupied aircraft systems and structure from motion. *Remote Sens.* **2019**, *11*, 2394. [[CrossRef](#)]
11. Rees, A.F.; Avens, L.; Ballorain, K.; Bevan, E.; Broderick, A.C.; Carthy, R.R.; Christianen, M.J.A.; Duclos, G.T.; Heithaus, M.R.; Johnston, J.W.; et al. The potential of unmanned aerial systems for sea turtle research and conservation: A review and future directions. *Endang. Species Res.* **2018**, *35*, 81–100. [[CrossRef](#)]
12. Schofield, G.; Esteban, N.; Katselidis, K.A.; Hays, G.C. Drones for research on sea turtles and other marine invertebrates—A review. *Biol. Conserv.* **2019**, *238*, 108214. [[CrossRef](#)]
13. Kandrot, S.; Hayes, S.; Holloway, P. Applications of Uncrewed Aerial Vehicles (UAV) Technology to Support Integrated Coastal Zone Management and the UN Sustainable Development Goals at the Coast. *Estuaries Coast.* **2021**, 1–20. [[CrossRef](#)] [[PubMed](#)]
14. Khedmatgozar Dolati, S.S.; Caluk, N.; Mehrabi, A.; Khedmatgozar Dolati, S.S. Non-destructive testing applications for steel bridges. *Appl. Sci.* **2021**, *11*, 9757. [[CrossRef](#)]
15. Garcia-Soto, C.; Seys, J.J.C.; Zielinski, O.; Busch, J.A.; Luna, S.I.; Baez, J.C.; Domegan, C.; Dubsky, K.; Kotynska-Zielinska, I.; Loubat, P.; et al. Marine Citizen Science: Current State in Europe and New Technological Developments. *Front. Mar. Sci.* **2021**, *8*, 621472. [[CrossRef](#)]
16. Nowlin, M.B.; Roady, S.E.; Newton, E.; Johnston, D.W. Applying unoccupied aircraft systems to study human behavior in marine science and conservation programs. *Front. Mar. Sci.* **2019**, *6*, 567. [[CrossRef](#)]
17. Beaucage, P.; Glazer, A.; Choisnard, J.; Yu, W.; Bernier, M.; Benoit, R.; Lafrance, G. Wind assessment in a coastal environment using synthetic aperture radar satellite imagery and a numerical weather prediction model. *Can. J. Remote Sens.* **2007**, *33*, 368–377. [[CrossRef](#)]

18. Seier, G.; Hodl, C.; Abermann, J.; Schottl, S.; Maringer, M.; Hofstadler, D.N.; Probstl-Haider, U.; Lieb, G.H. Unmanned aircraft systems for protected areas: Gadgetry or necessity? *J. Nat. Conserv.* **2021**, *64*, 126078. [[CrossRef](#)]
19. Ciaccio, F.; Troisi, S. Monitoring marine environments with Autonomous Underwater Vehicles: A bibliometric analysis. *Res. Eng.* **2021**, *9*, 100205.
20. Lally, H.; O'Connor, I. Can drone be used to conduct water sampling in aquatic environments? A review. *Sci. Total Environ.* **2019**, *20*, 569–575. [[CrossRef](#)]
21. Zhang, Z. A flexible new technique for camera calibration. *IEEE Trans. Pattern Anal. Mach. Intell.* **2000**, *22*, 1330–1334. [[CrossRef](#)]
22. Griffiths, D.; Burningham, H. Comparison of pre- and self-calibrated camera calibration models for UAS-derived nadir imagery for a SfM application. *Prog. Phys. Geog.* **2019**, *43*, 215–235. [[CrossRef](#)]
23. Oconner, P.L.; Smith, M.J.; James, M.R. Cameras and settings for aerial surveys in the geosciences: Optimising image data. *Prog. Phys. Geog.* **2017**, *41*, 325–344. [[CrossRef](#)]
24. Cooper, H.M.; Wasklewicz, T.; Zhu, Z.; Lewis, W.; Lecompte, K.; Heffentrager, M.; Smaby, R.; Brady, J.; Howard, R. Evaluating the ability of multi-sensor techniques to capture topographic complexity. *Sensors* **2021**, *21*, 2105. [[CrossRef](#)] [[PubMed](#)]
25. Cruzan, M.B.; Weinstein, B.G.; Grasty, M.R.; Kohn, B.F.; Hendrickson, E.C.; Arredondo, T.M.; Thompson, P.G. Small unmanned aerial vehicles (micro-UAVs, drones) in plant ecology. *Appl. Plant Sci.* **2016**, *4*, 1600041. [[CrossRef](#)] [[PubMed](#)]
26. Tmušić, G.; Salvator, M.; Helge, A.; James, M.R.; Goncalves, G.; Ben-Dor, E.; Brook, A.; Polinova, M.; Arranz, J.J.; Mészáros, J.; et al. Current practices in UAS-based environmental monitoring. *Remote Sens.* **2020**, *12*, 1001. [[CrossRef](#)]
27. Rodriguez, A.B.; Fodrie, F.J.; Ridge, J.T.; Lindquist, N.L.; Theuerkauf, E.J.; Coleman, S.E.; Grabowski, J.H.; Brodeur, M.C.; Gittman, R.K.; Keller, D.A.; et al. Oyster reefs can outpace sea-level rise. *Nat. Clim. Change* **2014**, *4*, 493–497. [[CrossRef](#)]
28. Singh, K.K.; Frazier, A.E. A meta-analysis and review of unmanned aircraft system (UAS) imagery for terrestrial applications. *Int. J. Remote Sens.* **2018**, *39*, 5078–5098. [[CrossRef](#)]
29. Aasen, H.; Bolten, A. Multi-temporal high-resolution imaging spectroscopy with hyperspectral 2D imagers—From theory to application. *Remote Sens. Environ.* **2018**, *205*, 374–389. [[CrossRef](#)]
30. Roth, L.; Hund, A.; Aasen, H. PhenoFly Planning Tool: Flight planning for high-resolution optical remote sensing with unmanned aerial systems. *Plant Methods* **2018**, *14*, 116. [[CrossRef](#)]
31. Assmann, J.J.; Kerby, J.T.; Cunlie, A.M.; Myers-Smith, I.H. Vegetation monitoring using multispectral sensors—Best practices and lessons learned from high latitudes. *J. Unmanned Veh. Syst.* **2019**, *7*, 54–75. [[CrossRef](#)]
32. Smith, G.M.; Milton, E.J. The use of the empirical line method to calibrate remotely sensed data to reflectance. *Int. J. Remote Sens.* **1999**, *20*, 2653–2662. [[CrossRef](#)]
33. Iqbal, F.; Lucieer, A.; Barry, K. Simplified radiometric calibration for UAS-mounted multispectral sensor. *Eur. J. Remote Sens.* **2018**, *51*, 301–313. [[CrossRef](#)]
34. Conte, P.; Girelli, V.A.; Mandanici, E. Structure from Motion for aerial thermal imagery at city scale: Pre-processing, camera calibration, accuracy assessment. *ISPRS J. Photogramm. Remote Sens.* **2018**, *146*, 320–333. [[CrossRef](#)]
35. Agisoft LLC. *Agisoft Metashape User Manual; Professional Edition, Version 1.8*; Agisoft LLC: St. Petersburg, Russia, 2022.
36. Granshaw, S.I. Bundle adjustment methods in engineering photogrammetry. *Photogram. Rec.* **1980**, *56*, 181–207. [[CrossRef](#)]
37. James, M.R.; Robson, S.; Smith, M.W. 3-D uncertainty-based topographic change detection with structure-from-motion photogrammetry: Precision maps for ground control and directly georeferenced surveys. *Earth Surf. Process. Landf.* **2017**, *42*, 1769–1788. [[CrossRef](#)]
38. Wackrow, R.; Chandler, J.H. Minimizing systematic error surfaces in digital elevation models using oblique convergent imagery. *Photogram. Rec.* **2011**, *26*, 16–31. [[CrossRef](#)]
39. James, M.R.; Robson, S. Straightforward reconstruction of 3D surfaces and topography with a camera: Accuracy and geoscience application. *J. Geophys. Res.* **2012**, *117*, F03017. [[CrossRef](#)]
40. Agisoft LLC. *Metashape Python Reference, Release 1.8.2*; Agisoft LLC: St. Petersburg, Russia, 2022.
41. Rupnik, E.; Daakir, M.; Deseiligny, P. MicMac—A free, open-source solution for photogrammetry. *Open Geospat. Data Softw. Stand.* **2017**, *2*, 14. [[CrossRef](#)]
42. Pinton, D.; Canestrelli, A.; Wilkenson, B.; Ifju, P.; Ortega, A. Estimating ground elevation and vegetation characteristics in coastal salt marshes using UAV-based LiDAR and digital aerial photogrammetry. *Remote Sens.* **2021**, *13*, 4506. [[CrossRef](#)]
43. Wang, D.; Xing, S.; He, Y.; Yu, J.; Xu, Q.; Li, P. Evaluation of new lightweight UAV-borne topo-bathymetric LiDAR for shallow water bathymetry and object detection. *Sensors* **2022**, *22*, 1379. [[CrossRef](#)]

Article

An Error Prediction Model for Construction Bulk Measurements Using a Customized Low-Cost UAS-LIDAR System

Shanyue Guan ¹, Yilei Huang ² , George Wang ², Hannah Sirianni ³ and Zhen Zhu ^{1,*} ¹ Department of Engineering, East Carolina University, Greenville, NC 27858, USA; guans18@ecu.edu² Department of Construction Management, East Carolina University, Greenville, NC 27858, USA; huangy21@ecu.edu (Y.H.); wangg@ecu.edu (G.W.)³ Department of Geography, Planning & Environment, East Carolina University, Greenville, NC 27858, USA; siriannah21@ecu.edu

* Correspondence: zhuz@ecu.edu

Abstract: Small unmanned aerial systems (UAS) have been increasingly popular in surveying and mapping tasks. While photogrammetry has been the primary UAS sensing technology in other industries, construction activities can also benefit from accurate surveying measurements from airborne LIDAR. This paper discusses a custom-designed low-cost UAS-based LIDAR system that can effectively measure construction excavation and bulk piles. The system is designed with open interfaces that can be easily upgraded and expanded. An error model was developed to predict the horizontal and vertical errors of single point geo-registration for a generic UAS-LIDAR. This model was validated for the proposed UAS-LIDAR system using calibration targets and real-world measurements from different scenarios. The results indicated random errors from LIDAR at approximately 0.1 m and systematic errors at or below centimeter level. Additional pre-processing of the raw point cloud can further reduce the random errors in LIDAR measurements of bulk piles.

Keywords: UAS; LIDAR; point cloud; construction; error model



Citation: Guan, S.; Huang, Y.; Wang, G.; Sirianni, H.; Zhu, Z. An Error Prediction Model for Construction Bulk Measurements Using a Customized Low-Cost UAS-LIDAR System. *Drones* **2022**, *6*, 178. <https://doi.org/10.3390/drones6070178>

Academic Editor: Giordano Teza

Received: 22 June 2022

Accepted: 18 July 2022

Published: 19 July 2022

Publisher's Note: MDPI stays neutral with regard to jurisdictional claims in published maps and institutional affiliations.



Copyright: © 2022 by the authors. Licensee MDPI, Basel, Switzerland. This article is an open access article distributed under the terms and conditions of the Creative Commons Attribution (CC BY) license (<https://creativecommons.org/licenses/by/4.0/>).

1. Introduction

A successful construction project depends on many quantitative and qualitative surveying measurements, including both the fine dimensions for building structures and the bulk measurements for civil infrastructures. Traditional construction surveying equipment includes total stations and GNSS devices [1] and their accuracy of measurements varies depending on the equipment calibration, jobsite environment, and the specific surveying application. For example, the accuracy standard of earthwork measurements is more tolerant than that of the locations of pile foundations. The accuracy requirements typically range from a minimum of 1:2500 up to 1:20,000, as set forth by construction professional organizations, such as the American Society for Photogrammetry and Remote Sensing, the American Society of Civil Engineers, the American Congress on Surveying and Mapping, and the American Land Title Association [2].

With the rapid advancement of technology, the construction industry has embraced many new surveying and mapping techniques for better work efficiency and more consistent levels of accuracy. These new surveying technologies include terrestrial, aerial, and satellite imaging, which acquire planimetric, topographic, hydrographic, or feature attribute data for photogrammetry, as well as terrestrial and aerial light detection and ranging (LIDAR) that directly captures 3D point clouds of objects and surfaces. One of the most promising approaches for the implementation of these new surveying technologies is using a small unmanned aerial system (UAS). Due to the significant improvements in their flight time, payload capability, and affordability in the last decade, the small UAS has been

increasingly applied in broader surveying areas, such as agriculture, civil infrastructure, and disaster management [3]. While photogrammetry has been the primary UAS sensing technology in these areas, the construction industry, on the other side, can also benefit from accurate surveying measurements from a UAS-based LIDAR. The level of accuracy and error prediction of UAS-based LIDAR measurements, however, have been less studied for construction uses. Consequently, there is a knowledge gap regarding UAS-based LIDAR technology and its application in construction projects.

This paper presents the design of a custom UAS-based LIDAR system that is capable of effectively measuring construction excavation and bulk piles. The system mainly consists of a commercial small UAS equipped with a video camera, an industrial image camera, a LIDAR sensor, a GNSS receiver, an inertial measurement unit, and three embedded computers. The onboard GNSS receiver is paired to an onsite GNSS base station for post-processed navigation measurements. The effectiveness of the overall system was validated with point clouds collected from three different measurement scenarios using surveyed results as the truth reference.

Using this system as an example, a robust and generic error prediction model is developed to estimate the position accuracy of individual point in the LIDAR point cloud. With this model, systematic and random error components have been estimated, respectively. The model shows that the random error is the dominant component for a low-flying UAS-based LIDAR, and the error level is tolerable for construction applications, such as excavation and bulk pile measurements. The random error in the vertical direction could be further reduced in post processing. The UAS-LIDAR systems and the error model could have significant potential for the civil engineering and construction industries.

2. Background

The accurate and efficient surveying of the construction site and construction materials is critical to the safety, quality, and overall success of the construction process. Several different approaches exist to perform construction surveying and measuring activities, including traditional manual tools, such as tape measures, straight edges, levels, and transits for lengths, angles, areas, and volume quantities [4,5]; and modern automated equipment, such as total stations, GNSS, and cameras for spatial positions, coordinates, and 3D digital models [6–8]; as well as a combination of different types of measuring equipment [9]. Nevertheless, all the conventional techniques or their combinations have certain disadvantages, which have limited their overall applications. For example, the robotic total station is one of the commonly used pieces of surveying equipment due to its efficiency in capturing the information of multiple locations within a short amount of time [10,11]. However, a robotic total station is usually cost-prohibitive and is heavy and bulky to transport, making it inconvenient to use for large areas. GNSS receivers have also been used frequently for construction surveying activities due to their high accuracy in measurements and rapid relocation in large areas [12]. However, GNSS applications are often limited by the conditions of their operational environment, especially in urban areas with obstructed view of the sky, electromagnetic shielding, multipath reflection, etc., which can significantly reduce the accuracy of measurements [13,14].

Furthermore, conventional building and construction surveying activities in most cases require the equipment operators to physically enter the structure or site to be able to perform such activities. With considerations of safety, efficiency, approachability, and practicality, it is imperative to implement new technologies with less or no human labor at the site [15–17]. In response to this demand, different types of innovative devices have been developed during the last decade for construction surveying, such as robotic platforms [18,19]. Due to their own limitations, however, most of these systems have not yet been used widely in construction projects.

UAS-based surveying equipment is another type of innovative device that can address some of the drawbacks and limitations faced by traditional surveying technologies. With the recent technological advancement in materials, batteries, sensors, navigation, and flight

control, the performance of small UASs has improved dramatically. In the meantime, their cost has decreased considerably. As a result, small UASs have been increasingly used for forest inventory, package delivery, and agriculture growth monitoring [20–23]. At the same time, the improvements of payload capability and flight time of small UAS have enabled their uses in many types of civil and construction applications, such as the post-disaster assessment of infrastructure [24–26], construction site planning [27–30], construction process monitoring [31], and infrastructure inspections [32,33]. Small UASs deployed for construction applications use either a fixed-wing airframe or a rotary-wing airframe. Fixed-wing airframes provide much longer flight time whereas rotary-wing airframes do not require a special taking off/landing pad and are thus more versatile [34,35].

Vision-based sensors are most commonly equipped on UAS for general purposes, including high-definition image cameras and video cameras [36–39]. To conduct civil and construction surveying applications, a LIDAR system or other active ranging/imaging devices are proven to provide better performance [20]. Operations at night or in low visibility scenarios require infrared or thermal sensors to detect structural conditions [40]. Other types of sensors, such as ultrasound or compact continuous-wave radar, can also be deployed with a small UAS for specific purposes [41,42]. Sophisticated tasks and operations often require a small UAS to carry multiple types of sensors simultaneously to perform comprehensive measurements. Due to the limited UAS payload and the challenges in integrating different sensing systems, however, it is still challenging to find a capable small UAS with integrated multiple sensor modalities for civil engineering and construction surveying applications.

It is well proven that a ground-based LIDAR system, such as a terrestrial laser scanner (TLS), can provide a dense and accurate point cloud for construction measurements. The same however does not apply to UAS-based LIDAR, because the position and orientation of the UAS constantly change during a flight. As a result, the point clouds captured by LIDAR cannot be geo-referenced as that of a stationary TLS. Instead, raw point cloud measurements from the airborne LIDAR must be integrated and synchronized with the UAS navigation measurements during pre-processing, which is typically a challenge and roadblock. The accuracy of geo-registration in airborne LIDAR point cloud has been studied for large, manned aircraft systems. It has been recognized that the errors in the navigation system, LIDAR installation, laser beam, and ranging can all contribute to the geo-registration error [43]. The general error model can also apply to UAS-based systems [44]. A UAS typically flies at a lower altitude and has a lower-grade navigation system than manned aircraft. The LIDAR equipped on a UAS can have lower power and shorter range as well. Therefore, the error in a UAS-LIDAR point cloud may manifest itself in a way that is slightly different from ALS. In practice, the observed error magnitude and pattern is related to the target application as well. For example, errors have been assessed for forestry [45], meadow steppe [46], mountainous areas [47], flood plains [48], and different vegetation levels [49]. The focus of this work is on the vertical error on bulk measurements, such as piles or excavation.

3. System Design

3.1. Hardware Components

The presented UAS-LIDAR system uses a commercial rotary-wing small UAS, DJI Matrice 600 Pro, equipped with an auxiliary sensing system, including the following components:

- A GoPro Hero 5 video camera;
- An IDS uEye industrial RGB image camera;
- A SICK LD-MRS LIDAR sensor;
- A NovAtel SPAN GNSS receiver with an integrated inertial measurement unit (IMU);
- Three Raspberry Pi III-embedded computers;
- A rigid lightweight cage to mount all the components above.

In addition, the GNSS receiver can use both the US constellation GPS and the Russian constellation Global Navigation Satellite System (GLONASS). This receiver is paired with

an onsite GNSS base station (NovAtel OEM 6 receiver) for post-processed navigation measurements. A close-up look of the major components of the sensing system is shown in Figure 1.

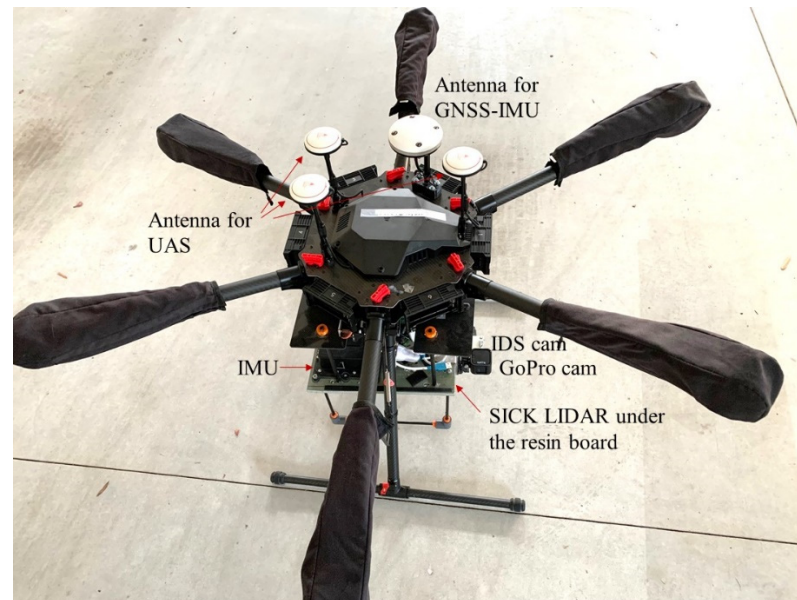


Figure 1. Major Components of the UAS Sensing System.

The cage attached to the bottom of the airframe is made of a rigid resin board supported by carbon fiber and 3D printed components. The system components are mounted on both sides of the board to conserve space and at the same time improve the rigidity of lever arms between the sensors. The total weight of the sensing system is approximately 3.6 kg and the maximum flight time of the UAS with this configuration is approximately 17 min.

Two lightweight cameras are mounted onboard, a GoPro video camera and an IDS industrial RGB image camera. The video camera captures continuous video frames of the flight that can be used for 2D imaging and 3D mapping via Structure from Motion (SfM), which operates independently from the other sensors. By contrast, the image camera is tightly integrated with navigation and LIDAR sensors. The image camera collects images with a global shutter triggered by the navigation system, which is also synchronized to the LIDAR. Consequently, the image camera is effectively synchronized to the LIDAR and provides 2D imagery of the point cloud observed by it. The imagery was only used to identify targets from the LIDAR point cloud and was therefore not incorporated into the point cloud in the results reported in this work.

The LIDAR is a SICK LD-MRS unit capable of scanning four layers simultaneously with a field of view of approximately 110° facing downwards at the ground. The aperture size is no greater than $\pm 0.4^\circ$ in one direction and $\pm 0.04^\circ$ in the other, corresponding to 0.23° and 0.023° in standard deviations, respectively. The LIDAR scans at 0.125° of angular resolution with a frequency of 12.5 Hz, and it takes approximately 10 ms to complete one sweep of the field of view, collecting around 3000 ground points. It is assumed that all points from a single scan will be collected simultaneously, which is timestamped by the navigation system through a synchronization mechanism, although the precise scanning time of each point could be retrieved if needed. Therefore, the potential discrepancy in timing is up to ± 5 ms for each point and is considered part of the error sources. SICK provides an estimation of nominal ranging accuracy for the LD-MRS unit, which includes a noise level of a single point at $\sigma_{eR} \approx 0.1$ m (quantization step 0.04 m) and a systematic bias ≈ 0.3 m (estimated ahead of time and removed from the data). It is noted from field testing that the specified noise level is rather conservative compared with results from actual observations, which ranges between 0.04 m and 0.1 m. This unit cost approximately USD

10,000 in 2018, which is significantly lower than the price of other UAS-LIDAR systems on the market (estimated average cost USD 23,000 [50]). However, more low-cost UAS-LIDARs are expected to become available commercially.

The NovAtel SPAN GNSS-inertial integrated receiver is used as the primary navigation system for data collection over the native flight control system of Matrice 600 Pro, due to the superior performance in limiting potential systematic error [51]. The GNSS receiver is paired with a GNSS base station to record raw data for accurate post-processed kinematic (PPK) solutions without relying on a live real-time kinematic (RTK) solution. The GNSS measurements are also tightly coupled with the integrated IMU, which enables precise position, velocity, and orientation measurements at a high update rate. Nevertheless, any residual uncertainty in the position and orientation from the GNSS-IMU will propagate to raw data of all the attached sensors, which becomes part of the systematic error. Figure 1 shows four GNSS antennas mounted on top of the airframe, of which three are used by the UAS for the redundancy and safety of flight control, and the fourth is part of the GNSS-IMU system.

The LIDAR and the GNSS receiver are both powered by a 3-cell lithium-polymer battery, which supplies approximately 12VDC. Both sensors can accept a wide range of voltage level and their performance is not dependent on the voltage [52,53]. As illustrated in Figure 2, the battery voltage is also converted into 5VDC through a DC–DC voltage converter, to support the onboard embedded computers for data recording. The sensor power system is completely separated from the airframe batteries, such that they do not interfere with each other.

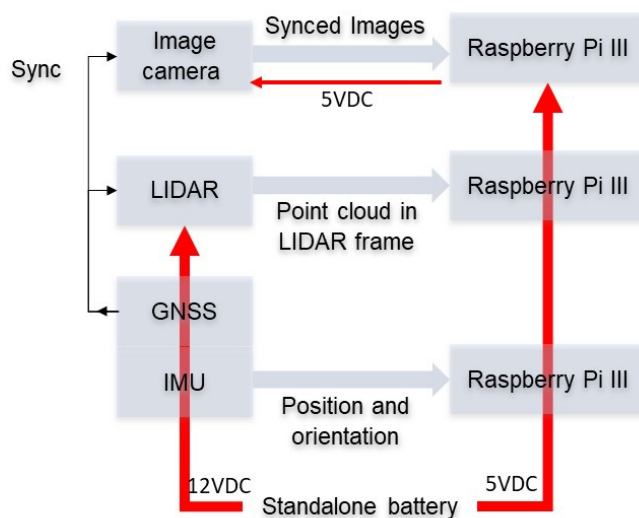


Figure 2. Synchronization and Power Schematics of the UAS-LIDAR System.

3.2. System Synchronization

The time synchronization function is the core mechanism of sensor integration in the UAS-LIDAR system, also shown in Figure 2. Naturally, GNSS is synchronous to GPS time, which also enables additional timing services via input and output triggers to the receiver. The GNSS receiver in the UAS-LIDAR system triggers the shutter of the image camera and receives a timing trigger from the LIDAR. Raw data with corresponding timing information recorded by the image camera, LIDAR, and GNSS-IMU are streamed into three onboard Raspberry Pi-embedded computers, which also control and initialize all the sensors. Due to the time-sensitivity of data collection, each computer records the raw data from only one sensor and stores it on a separate SD card for post-processing, avoiding onboard processing to allow sufficient throughput capability.

The configuration of the sensing system can be easily adjusted for other applications. As illustrated in Figure 2, the various sensors use a parallel configuration: the GNSS-IMU sensors establish the accurate position, orientation, and timing, which is essential to the

system, whereas other sensors can be either replaced or expanded as long as they can be synchronized via a triggering mechanism.

3.3. Post-Processed Navigation Measurements

The NovAtel Inertial Explorer software was used to process the raw data recorded by the GNSS and IMU sensors. GNSS carrier phase-based differential solution needs to be computed with respect to a nearby reference GNSS station, which could be either an onsite setup or from a local reference station, such as a Continuously Operating Reference Station (CORS). In this study, an onsite GNSS base station was set up and the positioning accuracy was defined based on the uncertainty of absolute positioning, which refers to the position geo-registered in a global frame. The positioning error from post-processing typically does not exceed centimeter level. The orientation accuracy was computed separately and differently. While the roll and pitch angles from the IMU are typically accurate and stable, the accuracy of true heading (geographic north instead of magnetic north), however, depends on the flight trajectory of the UAS. Since the IMU used in this work cannot directly sense the true heading, it must be inferred from an accurate position measurement while the UAS is moving. Therefore, the UAS must perform specific maneuvers at the beginning of each data collection flight to gain an accurate heading.

3.4. Pre-Processed Point Clouds

The point clouds collected by the LIDAR are referenced in the LIDAR body frame (L frame), which is constructed with Forward, Right, Down (FRD) directions. Since the LIDAR is constantly moving and rotating in the air, the point clouds cannot be directly geo-referenced in a global frame (G frame). The conversion between the two frames relies on the accurate position, orientation, and true heading of the LIDAR, as well as the accuracy in relative timing between each LIDAR scan point and the GNSS receiver.

When a LIDAR point in the L frame is synchronized to GNSS time, it can be geo-referenced into a G frame based on the reference GNSS station. For example, if the reference station is located with World Geodetic System (such as WGS-84) coordinates, the G frame will use local North, East, Down (NED) coordinates based on the WGS-84 coordinates. The potential positioning error in the reference station is ignored in this study.

The following algorithm of frame conversion was implemented in a custom code in MATLAB.

1. Record the 3D position of a static ground point x in L frame, $P_x^L(t)$, at time t . The position error $\epsilon P_x^L(t)$ is caused by LIDAR ranging error and beam angular error (aperture size);
2. Convert $P_x^L(t)$ into the G frame:

$$P_x^G = C_L^G(t')P_x^L(t) + P_L^G(t') \quad (1)$$

where P_x^G is the static position of this point in the G frame (no longer a function of time), C_L^G reflects the rotation from L frame to G frame, and P_L^G stands for the LIDAR position.

t' is the time of measurement of this LIDAR point perceived by the system, which could be slightly different from the actual time of measurement t . This time difference exists because the position and rotation of the LIDAR are computed based on measurements from the GNSS and IMU sensors at t' instead of t . The LIDAR timing error is thus specified as $\epsilon t = t' - t$ and could be up to 5 ms in a single scan point in the presented UAS-LIDAR system, as noted before.

C_L^G is not directly measurable and is computed via the real-time IMU orientation and relative orientation of LIDAR from the IMU, also known as boresighting [54]:

$$C_L^G(t) = C_V^G(t)C_L^V \quad (2)$$

where C_L^V is the fixed rotation from L frame to the vehicle frame (V) and $C_V^G(t)$ reflects the rotation from the vehicle frame (IMU in this system) to G frame.

\mathbf{P}_L^G is not directly measurable either. The GNSS antenna location on the UAS \mathbf{P}_{ant}^G is measured at time t , and the lever arm between the antenna and the LIDAR is measured in the vehicle frame as $\mathbf{P}_L^V - \mathbf{P}_{ant}^V$. Thus,

$$\mathbf{P}_L^G(t) = C_V^G(t) \left[\mathbf{P}_L^V - \mathbf{P}_{ant}^V \right] + \mathbf{P}_{ant}^G(t) \quad (3)$$

3. Finally, the geo-referenced location of point x is found using

$$\mathbf{P}_x^G = C_V^G(t) C_L^V \mathbf{P}_x^L(t) + C_V^G(t) \left[\mathbf{P}_L^V - \mathbf{P}_{ant}^V \right] + \mathbf{P}_{ant}^G(t) \quad (4)$$

4. Error Prediction Model

The error prediction model introduced in this work follows the same principles of ALS [43,44], which includes errors in position, orientation, lever arm, and boresighting. It can be expanded to include synchronization errors as well. More importantly, this model can be used to understand and differentiate the random and relative errors from the systematic and absolute errors.

4.1. Measurement Error Prediction

Errors in t , $C_V^G(t)$, C_L^V , $\mathbf{P}_L^V - \mathbf{P}_{ant}^V$ and $\mathbf{P}_{ant}^G(t)$ can contribute to the overall system error. It is further assumed in this study that with a rigorous calibration procedure in place, errors, such as the ones found in boresighting, are at least one order of magnitude smaller than those from IMU orientation. For simplicity of analysis, boresighting errors were not modeled in this study. Similarly, it is assumed that the lever arm error is also negligible. Therefore, the contributions of UAS orientation, positioning, timing, and LIDAR are considered in the error prediction model.

First, smaller angular errors in UAS roll ($\varepsilon\varphi$), pitch ($\varepsilon\theta$), and heading ($\varepsilon\psi$) angles are considered. In addition, a rotating or vibrating airframe will experience additional angular errors due to uncertainties in time, such that

$$\Delta^T = [\varepsilon\varphi \ \varepsilon\theta \ \varepsilon\psi] + \left[\frac{d\varphi}{dt} \ \frac{d\theta}{dt} \ \frac{d\psi}{dt} \right] \varepsilon t \quad (5)$$

$$\varepsilon C_V^G(t) = \Delta_{\times} C_V^G(t) \quad (6)$$

where Δ_{\times} is a skew-symmetric matrix. Ideally, $\varepsilon\psi$ is at a sub-degree level for the sensor used in the system, whereas $\varepsilon\varphi$ and $\varepsilon\theta$ are substantially smaller.

Next, the UAS position error, including the impact from the timing uncertainties, is represented with $\varepsilon t \frac{d\mathbf{P}_{ant}^G(t)}{dt} + \varepsilon \mathbf{P}_{ant}^G(t)$, where $\frac{d\mathbf{P}_{ant}^G(t)}{dt}$ is the velocity of the antenna in the G frame.

Finally, $\varepsilon \mathbf{P}_x^L$ is considered in the L frame in forward, right, and down directions. Since the LIDAR is pointing to the ground, the LIDAR forward direction is the vehicle down direction. The position error without timing error is

$$\varepsilon \mathbf{P}_x^L(t) = [0 \ \delta_r \ \delta_d]_{\times} \mathbf{P}_x^L(t) + \varepsilon R \frac{\mathbf{P}_x^L(t)}{|\mathbf{P}_x^L(t)|} \quad (7)$$

where $\varepsilon R \frac{\mathbf{P}_x^L(t)}{|\mathbf{P}_x^L(t)|}$ represents the LIDAR ranging error projected onto the direction of point x . δ_r and δ_d indicate right and downward angular errors with respect to LIDAR.

The error in x is thus modeled with

$$\varepsilon \mathbf{P}_x^G = \left[\varepsilon C_V^G(t) \right] C_L^V \mathbf{P}_x^L(t) + \left[\varepsilon C_V^G(t) \right] \left[\mathbf{P}_L^V - \mathbf{P}_{ant}^V \right] + C_V^G(t) C_L^V \cdot \left[\varepsilon \mathbf{P}_x^L(t) \right] + \varepsilon \mathbf{P}_{ant}^G(t) + \varepsilon t \frac{d\mathbf{P}_{ant}^G(t)}{dt} \quad (8)$$

Equation (8) can be used to predict the 3D error magnitude in a global frame for individual scan points. Noticeably, the LIDAR errors (δ_r , δ_d and εR) are not considered

systematic errors. Instead, εP_x^L from Equation (7) is modeled as a random process, which is uncorrelated either among multiple points within the same scan or among repeated scans of the same point from a moving LIDAR. The other components from Equation (8) may be correlated among the points within the same scan but are likely uncorrelated among repeated scans. Therefore, the total errors in εP_x^G are expected to include a major component of random errors and a minor component of systematic errors. Since the random error component is caused by the LIDAR, it is considered a relative error, whereas the systematic error component was largely related to errors in the G frame, which is an absolute error.

In a set of points X that are approximately collocated in the G frame horizontally, the vertical dimension can be estimated based on all the points, P_X^G . In this study, the points were computed with a mean or median value. Therefore, a dense raw point cloud could be preprocessed, decimated, and turned into a more accurate elevation model. The expected accuracy can be significantly improved with the number of points. For example, the down-sampled point $P_{X,v}^G$ could be an average of all the points, as shown in Equation (9).

$$P_{X,v}^G = \text{mean}\{P_{x,v}^G, \forall x \in X\} \quad (9)$$

The standard deviation of vertical errors in $P_{X,v}^G$ is reduced by the square root of the number of points in X . With a sufficiently large number of points in X , the random and relative errors in $P_{X,v}^G$ will approach zero, and therefore the systematic and absolute errors will dominate.

Alternatively, $P_{X,v}^G$ can be calculated based on the median value of all the points in X . Median values are less likely to be affected by outliers in the set. An implicit assumption is made that all the points in the set share similar heights in a small horizontal neighborhood (centimeter to decimeter level), which is a valid assumption for most smooth surfaces. The median value shown in Equation (10) is expected to be a robust estimation. To better find all the points, some optimization methods will be applied in future work [55].

$$P_{X,v}^G = \text{median}\{P_{x,v}^G, \forall x \in X\} \quad (10)$$

While the error model can predict horizontal and vertical errors separately, it is independent of the target surface. The texture, smoothness, and slope of a surface can contribute to the errors in the point cloud. For instance, a horizontal error can be perceived as a vertical error in a sloped surface. Vegetation on the surface could also result in additional uncertainty and, as a result, the optimal choice of the down-sampling method, i.e., mean vs. median values, may be dependent on the target surface. In general, the UAS-LIDAR system can measure a smooth and flat surface that is not covered by any vegetation with lower errors.

Furthermore, this error model is generic and would be applicable to any UAS-LIDAR system that has LIDAR synchronized to an onboard navigation system. However, in order to implement Equation (8), it does require intermediate data, such as the error models of navigation and synchronization, which may not be available from a commercial system.

4.2. An Illustrative Example of Error Prediction Model

The presented error model helps with the quantification of the contribution of individual error sources in a single point in a LIDAR point cloud. As an illustrative example, consider a typical slow and smooth flight (speed = 5 m/s, no vibration or vertical velocity considered), where the UAS holds a constant altitude of 15 m above ground. The UAS flight control is often based on a standalone GNSS receiver, which can only achieve meter-level accuracy. For example, the 3D position error of GPS alone is 4.5 m (95% value) [56]. However, the UAS is not required to fly at a precise altitude. Instead, the precise position of the UAS and the LIDAR will be computed in the PPK solution. Since the UAS flights discussed in this work all had open sky conditions, typically there are at least 15 GNSS satellites from

GPS and GLONASS combined. The number of satellites has always been sufficient for a successful PPK or RTK solution. The precise LIDAR position, instead of the approximate flight altitude, will be used to compute a point cloud as shown in Equation (1).

Based on the typical performance provided by the manufacturer in [52], it is assumed that $[\varepsilon\varphi \ \varepsilon\theta \ \varepsilon\psi] = [0.01, 0.01, 0.1]^\circ$ (1 standard deviation) and $\varepsilon\mathbf{P}_{ant}^G = [0.01, 0.01, 0.02]\text{m}$ for positioning errors (1 standard deviation). The lever arm between the LIDAR and the antenna $|\mathbf{P}_L^V - \mathbf{P}_{ant}^V| = 0.17\text{ m}$. The LIDAR is pointing downward, thus $C_L^V = \begin{bmatrix} 0 & 0 & -1 \\ 0 & 1 & 0 \\ 1 & 0 & 0 \end{bmatrix}$.

It is further assumed that the UAS is leveled and facing north, thus $C_V^G(t) = \begin{bmatrix} 1 & 0 & 0 \\ 0 & 1 & 0 \\ 0 & 0 & 1 \end{bmatrix}$.

The error magnitude on a ground point x right underneath the LIDAR ($\mathbf{P}_x^L(t) = [15\text{ m}, 0, 0]^T$) is analyzed and illustrated below:

Let $\varepsilon\mathbf{P}_{x,\Delta}^G$ represent the error component contributed by the orientation uncertainty. In a leveled flight with little vibration, it is assumed that there is unsensed orientation change within εt , so that $\left[\frac{d\varphi}{dt} \ \frac{d\theta}{dt} \ \frac{d\psi}{dt}\right] \varepsilon t = 0$. Although this assumption may be too optimistic for the UAS in some practical flight conditions, it would be acceptable for the presented sensing system since the vibration of the sensing system could be damped or separated from the vibration of the UAS airframe. In this case, the orientation error has a simplified model $\Delta^T = [\varepsilon\varphi \ \varepsilon\theta \ \varepsilon\psi]$.

Since the distance between x and the LIDAR is much greater than the lever arm, i.e., $|\mathbf{P}_x^L(t)| \gg |\mathbf{P}_L^V - \mathbf{P}_{ant}^V|$, the main contribution from the orientation error will be based on the term $[\varepsilon C_V^G(t)] C_L^V \mathbf{P}_x^L(t)$. Recall that $\varepsilon C_V^G(t) = \Delta_\times C_V^G(t)$; therefore,

$$\varepsilon\mathbf{P}_{x,\Delta}^G = \Delta_\times C_V^G(t) C_L^V \mathbf{P}_x^L(t) = [0.0026, -0.0026, 0]^T \text{m}. \tag{11}$$

where $\varepsilon\mathbf{P}_{x,\Delta}^G$ is a component of the overall error, $\varepsilon\mathbf{P}_x^G$, which is caused by the orientation uncertainty Δ . The errors are provided in North, East, and vertical directions, respectively.

Similarly, the error component caused by UAS positioning can be estimated by

$$\varepsilon\mathbf{P}_{x,P}^G = \varepsilon\mathbf{P}_{ant}^G = [0.010, 0.010, 0.020]^T \text{m}. \tag{12}$$

In this simplified model, the contribution of timing error is purely horizontal and is only proportional to UAS velocity. The magnitude is limited by

$$|\varepsilon\mathbf{P}_{x,t}^G| = \left| \frac{d\mathbf{P}_{ant}^G(t)}{dt} \cdot \varepsilon t \right| \leq 0.025\text{ m}. \tag{13}$$

A greater contribution comes from LIDAR error $\varepsilon\mathbf{P}_x^L(t)$. As aforementioned, $\delta_r = 0.023^\circ$, $\delta_d = 0.23^\circ$, and $\varepsilon R = 0.1\text{ m}$ (a conservative error level) are assumed for this LIDAR.

$$\varepsilon\mathbf{P}_x^L(t) = [0 \ \delta_r \ \delta_d]_\times \mathbf{P}_x^L(t) + \varepsilon R \frac{\mathbf{P}_x^L(t)}{|\mathbf{P}_x^L(t)|} = [0.10, 0.06, -0.006]^T \text{m} \tag{14}$$

which contributes to the overall error via

$$\varepsilon\mathbf{P}_x^G = C_V^G(t) C_L^V \cdot [\varepsilon\mathbf{P}_x^L(t)] = [0.006, 0.06, 0.10]^T \text{m}. \tag{15}$$

It is evident from comparing Equations (11)–(15) that the LIDAR is the dominant error source ($\varepsilon\mathbf{P}_x^L$) for point x . Since the majority of $\varepsilon\mathbf{P}_x^G$ is considered a random process that is independent among points, as mentioned earlier, the integration and synchronization with the navigation measurements does not introduce substantial systematic errors in the

LIDAR point. As a result, the error magnitude is on the order of 0.1 m for both horizontal and vertical directions in a typical low-altitude flight.

5. Error Model Validation

5.1. Validation of Random Errors

The vertical and horizontal performance of raw point measurements P_x^G can be validated with customized calibration targets. The error prediction model was first validated for random errors with a flat surface cardboard box. The dimensions of this target can be found in Table 1. The box target was placed on flat paved ground with a reference GNSS antenna next to it to record raw data for post-processing. The UAS scanned the target at different heights from 20 m to 40 m above the target (~21 m to ~41 m above ground) with 5 m intervals. Figure 3 illustrates the raw point cloud collected at 20 m above target with both the target and the reference antenna. The exact height of the UAS above ground during this flight was measured with the PPK solution, which can be found in Figure 4.

Table 1. Box Target Dimensions.

| Width | Depth | Height | Volume |
|--------|--------|--------|---------------------|
| 1.24 m | 0.94 m | 0.95 m | 1.11 m ³ |

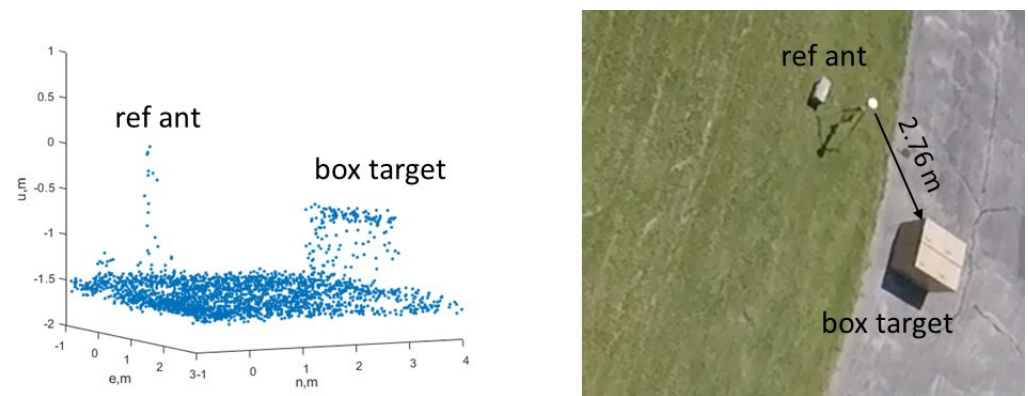


Figure 3. Left: Raw Point Cloud of Box Target and Reference GNSS Antenna. Right: Image from Onboard Camera. Collected at 20 m above target (~21 m above ground).

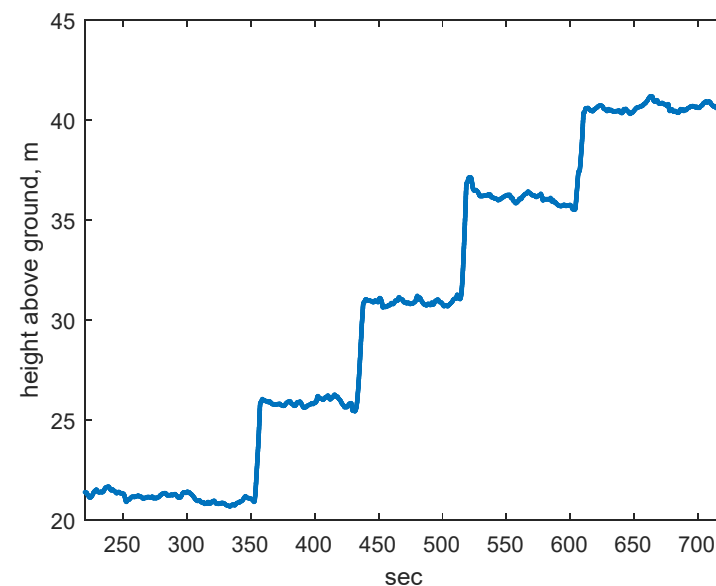


Figure 4. UAS Height Above Ground.

To improve the heading accuracy, the UAS performed initialization maneuvers immediately after taking off. After the flight, raw data were retrieved from the SD cards from both the UAS and the reference receivers. The data were post-processed, and the accuracy has been summarized in Table 2.

Table 2. Post-Processed Error Level for Flat Surfaces, Averaged over the Entire Flight.

| Error Level | Positioning | | | Orientation | | |
|-------------|-------------|---------|---------|---------------|---------------|--------------|
| | North | East | Down | Roll | Pitch | Heading |
| 1σ | 0.006 m | 0.007 m | 0.008 m | 0.006° | 0.007° | 0.02° |

The vertical and horizontal errors in P_x^G were assessed with the consistency of raw point cloud data collected from the top surface and one side surface of the box target, which contains mainly random and relative errors. As aforementioned, the vertical root mean square error (RMSE) of the raw point cloud is expected to be between 0.04 m and 0.1 m regardless of the height above the target, which was verified with results presented in Figure 5. On the other hand, Equation (8) indicates that the horizontal error would grow proportionally with the distance to target as it is mainly contributed by angular uncertainties. As demonstrated in Figure 6, the observed RMSE in the horizontal direction closely follows the estimated nominal error level.

The box target used to validate the single point error model described in Equation (8) has known flat surfaces that are either vertical or horizontal. The error magnitude presented in Figures 5 and 6 are representative of the vertical and horizontal error components of individual scan points, which are dominated by random errors contributed to by the LIDAR. Figure 4, however, does not include the potential contribution of horizontal errors. On a box-shaped target, the horizontal errors of points on the edge of a surface could result in greater vertical errors, which will be discussed next.

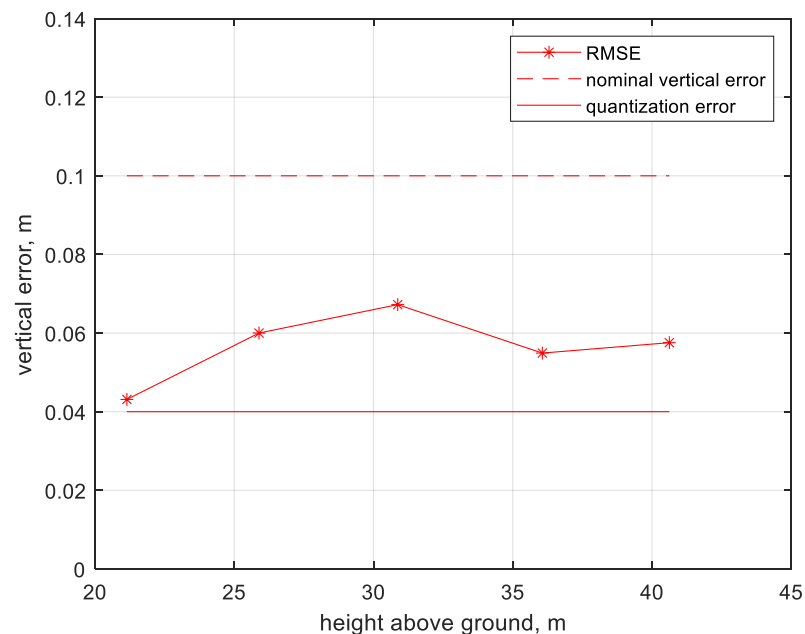


Figure 5. Vertical Error of Raw Point Cloud of the Box Target.

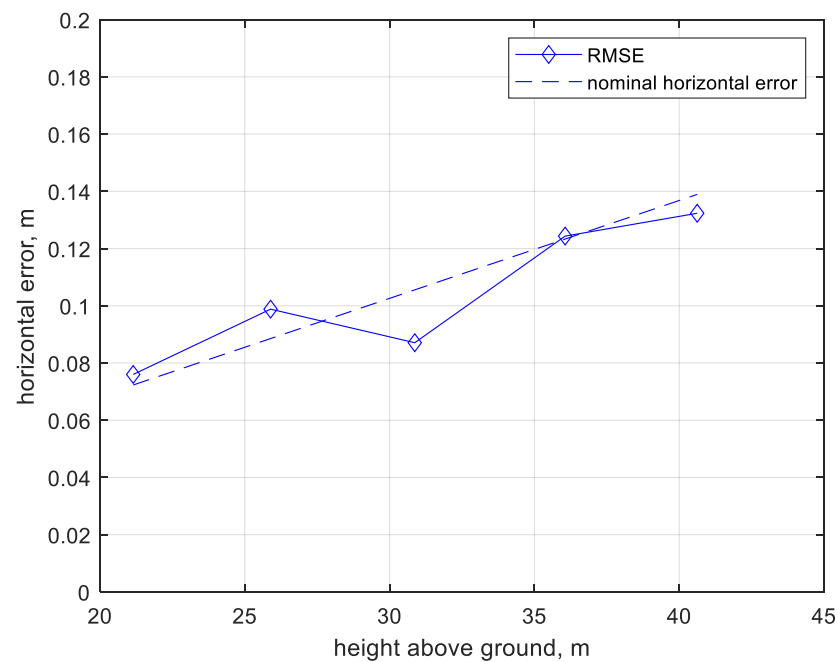


Figure 6. Horizontal Error of Raw Point Cloud of the Box Target.

5.2. Validation of Systematic Errors

Next, the magnitude of random and systematic errors was validated respectively, using a point cloud dataset with slope surfaces and survey points. Two tent-shape target objects were placed on flat paved ground, each with two smooth planar surfaces covered by white canvas, as shown in Figure 7. Both targets are identical and their dimensions have been provided in Table 3. The UAS hovered at approximately 15 m to 17 m above the ground and scanned the targets multiple times. The navigation data were post-processed, and the accuracy is summarized in Table 4.



Figure 7. Experimental Setup for Model Validation with Tent Targets (Width = 0.90 m).

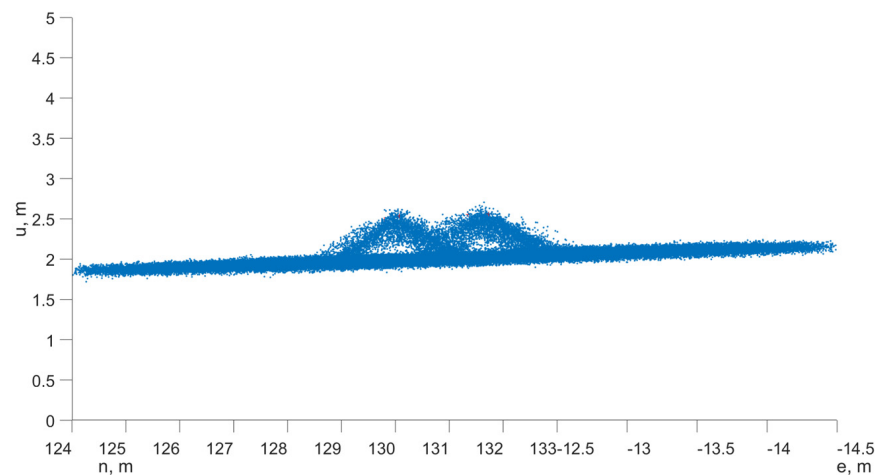
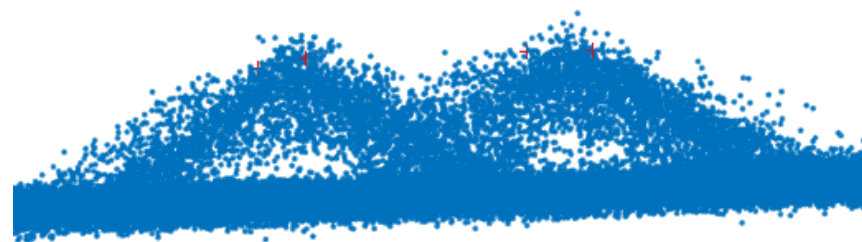
Table 3. Tent Target Dimensions.

| Left Side | Right Side | Width | Depth | Height | Volume |
|-----------|------------|--------|--------|--------|---------------------|
| 0.70 m | 0.64 m | 0.90 m | 0.90 m | 0.50 m | 0.20 m ³ |

Table 4. Post-Processed Error Level for Slope Surfaces, Averaged over the Entire Flight.

| Error Level | Positioning | | | Orientation | | |
|-------------|-------------|---------|---------|---------------|---------------|--------------|
| | North | East | Down | Roll | Pitch | Heading |
| 1σ | 0.007 m | 0.006 m | 0.001 m | 0.007° | 0.008° | 0.07° |

The raw LIDAR point cloud georeferenced in a G frame (NED) is shown in Figure 8, and Figure 9 provides a zoomed-in view with the two corners of both tent targets marked, which were surveyed separately by post-processed GNSS with an accuracy of 0.005 m, 0.005 m, 0.01 m in NED. The raw point cloud included laser returns from the open ends of both targets, which appear lower than the surface. Therefore, the side view of the point cloud will include more noisy points between the target surfaces and the ground. This artifact is excluded from the error analysis in this section. If both targets were piles of bulk materials, there would be no open ends, and the point cloud would not include these points.

**Figure 8.** Raw Point Cloud of Tent Targets, Georeferenced in A Local G Frame (NED).**Figure 9.** Zoomed-In View of Raw Point Cloud of Tent Targets with Four Survey Points Marked.

In this dataset, raw point cloud ($P_{x,v}^G$) reports 0.04 m relative vertical error (1σ) on a flat ground surface, which is consistent with the results reported in Figure 5. However, the vertical error observed on the tent targets was expected to be greater. Since the slope on both sides of the targets is approximately 45° , a portion of the horizontal errors was mapped onto the vertical direction at a 1:1 ratio. In other words, the observed vertical error from a raw LIDAR point cloud would be a combination of the actual horizontal and vertical error components. As a result, the absolute vertical error of raw point cloud on slope surfaces is approximately 0.1 m (1σ), which is also consistent with the error prediction model in Equation (8).

Although the UAS-LIDAR system can collect relatively dense point clouds, it is not guaranteed that all surfaces of the target will be captured directly in the raw point cloud during a flight. As a result, it should not be assumed that the entire target will be included

in the raw point cloud. Instead, the system is able to extract the geometry of targets from the raw point cloud in addition to measurements. The systematic error component of the point cloud can be estimated by using known geometric information of the target, such as shape and dimensions, and the target location from GNSS surveys. The geometric features of the target, such as planar surfaces, can then be extracted from a partial point cloud, and it is more convenient and robust to identify and extract planar features than point features on small-scale objects.

The average height of an object can be estimated from two planar features that are extracted from all points measured by the UAS-LIDAR system, and the absolute positioning error on a point reflects the magnitude of systematic and absolute error. The measurements from one of the two tent targets are validated here as a demonstration. Figure 10 illustrates 8280 points from Target 2 that are projected onto a 2D plane perpendicular to the ridgeline of the target. These points form the cross-section shape of the tent target as a triangle, and its left side and right side, colored in red and blue, respectively, represent all the points from both planar surfaces. An orthogonal linear fit is applied to each side to recover the shape of the triangle. The top of the triangle is then compared against its GNSS survey reference projected onto the same plane. As shown in Table 5, the LIDAR measurement of the height of Target 2 is 2.504 m whereas the GNSS measurement is 2.512 m (averaged between two corners), resulting in a vertical difference of 0.008 m. Since this difference is smaller than the GNSS survey accuracy of 0.01 m, it may not accurately represent the actual vertical error. Nonetheless, the absolute systematic error is indeed much smaller than the overall vertical error of 0.1 m, as predicted in Equation (8).

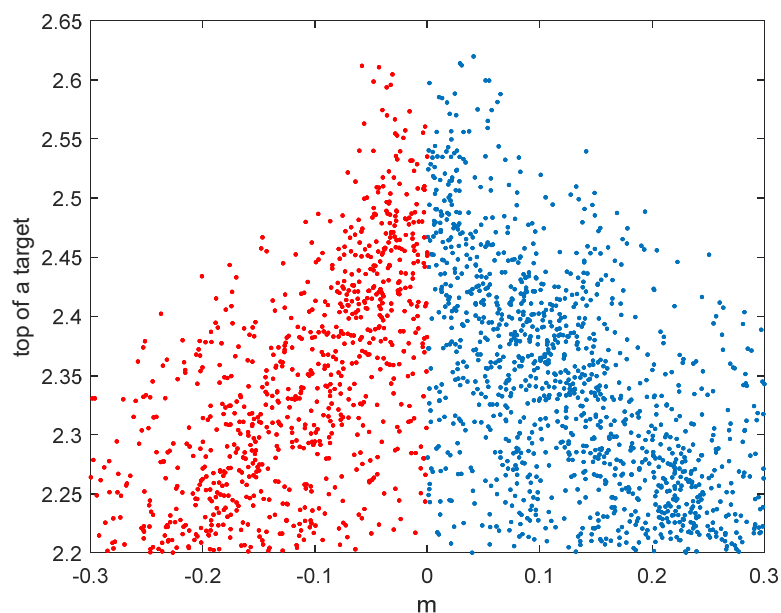


Figure 10. Raw Point Cloud of Tent Target 2 Projected onto A 2D Perpendicular Plane.

Table 5. Height of Tent Target 2 Measured by LIDAR and GNSS Survey.

| Target 2 | LIDAR | GNSS Survey | Difference | GNSS Accuracy (1σ) |
|----------|---------|-------------|------------|------------------------------|
| Height | 2.504 m | 2.512 m | 0.008 m | 0.01 m |

LIDAR measurements of bulk piles will face the same challenges as the tent targets, and it would be impractical to directly extract the height, surface, and volume from a noisy raw point cloud. Instead, an averaged, down-sampled point cloud will be more reliable, assuming that the errors on single points are mostly independent of each other, which has been validated in this dataset. The vertical errors can be effectively reduced by pre-processing based on mean or median values introduced in Equations (9) and (10).

As a demonstration, the pre-processed point cloud of the tent targets shown in Figure 11 appears much less noisy than the raw data point cloud in Figure 8.

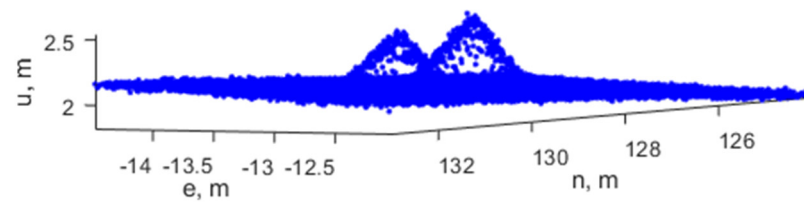


Figure 11. Pre-Processed Point Cloud of Tent Targets.

5.3. Test Site Bulk Measurements

Finally, the presented system was validated with bulk materials at a test site located by Town Creek in Greenville, North Carolina. The UAS-LIDAR system scanned a stretch of the creek (approximately 100 m long) multiple times at a speed of approximately 5 m/s or lower, where a bulk pile of rock stairs was built on a dry riverbed as part of the creek drainage system. An image of the test site from the synchronous camera is shown in Figure 12.

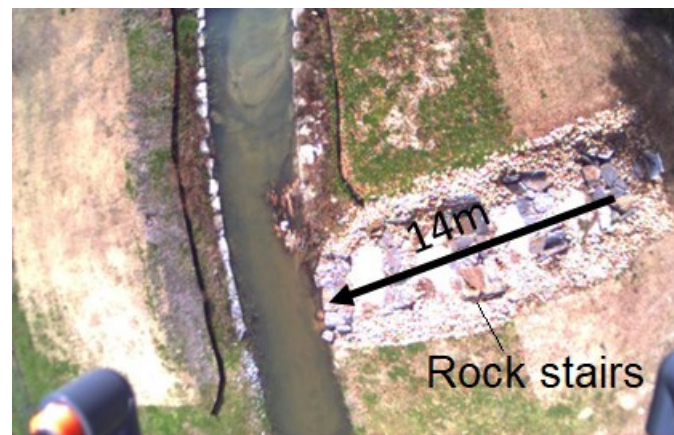


Figure 12. UAS Image of Test Site with Bulk Materials (Length of Rock Stairs: 14 m).

In this test, the collected raw point cloud was pre-processed and decimated into a lower resolution. The site was divided into small cells of 0.05 m by 0.05 m, and a single point P_X^G was reported for every cell following Equation (9). The magnitude of random error in point cloud would be reduced by the down-sampling process, whereas the systematic error is expected to remain the same. The processed point cloud of the site with rock stairs is presented in Figure 13. The navigation performance of this flight is shown in Table 6.

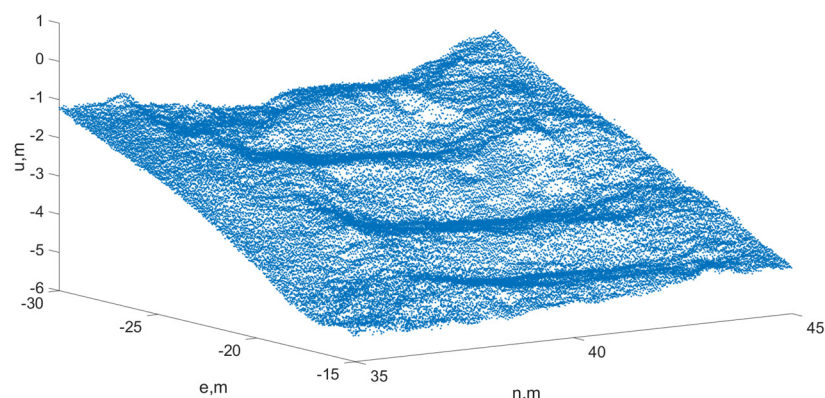


Figure 13. Point Cloud of Test Site with Bulk Materials.

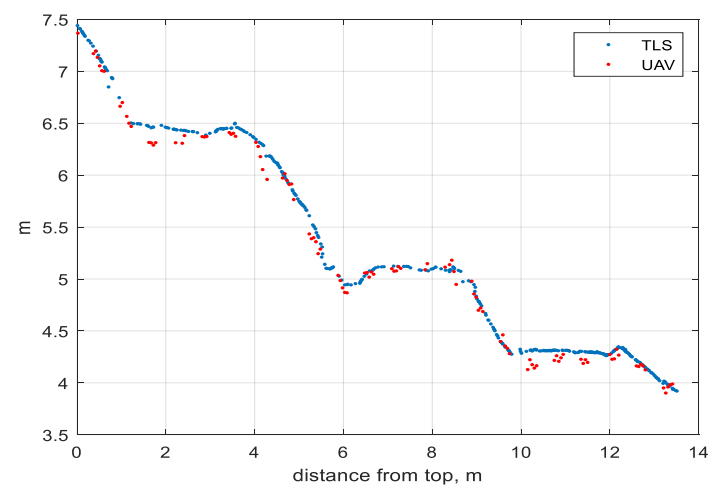
Table 6. Post-Processed Error Level for Test Site, Averaged over the Entire Flight.

| Error Level | Positioning | | | Orientation | | |
|-------------|-------------|---------|--------|-------------|--------|---------|
| | North | East | Down | Roll | Pitch | Heading |
| 1 σ | 0.007 m | 0.006 m | 0.01 m | 0.007° | 0.008° | 0.07° |

A terrestrial laser scan (TLS) of the test site was performed separately [57], where a Leica ScanStation P40 with a 3 mm (1σ) accuracy at 50 m was used. In this validation of the test site, the TLS point cloud was used as a true reference for the comparison with a vertical profile of down-sampled UAS-LIDAR point cloud collected on the rock stairs at the test site. As shown in Table 7, the difference between the measurements from the two sensors was 0.055 m in 1σ with a 0.064 m mean, and the maximum observed difference was 0.24 m. The vertical profiles measured by the TLS and UAS-LIDAR are illustrated in Figure 14, where deviation between the two profiles can be seen at a few locations. It is likely due to the changes in horizontal locations that can contribute to vertical errors in UAS-LIDAR measurements, as previously discussed. At this test site, the rock stairs have irregular rock shapes with steep slopes on the edge, resulting in a substantial level of mean and maximum error. Nevertheless, the overall error is still consistent with the predictions suggested by the presented error model. Designated calibration targets placed in a controlled environment can be used to compare the performance of bulk measurement with both technologies in the future.

Table 7. Measurements Difference of Rock Stairs between TLS and UAS-LIDAR.

| TLS-UAS Difference | Mean | 1 σ | Max |
|--------------------|---------|------------|--------|
| Rock Stairs | 0.055 m | 0.064 m | 0.24 m |

**Figure 14.** Comparison of Point Cloud Vertical Profile of Rock Stairs between TLS and UAS-LIDAR Measurements.

6. Conclusions

Technology advancement in the last decade has given the construction industry many new approaches for traditional daily jobs, among which using a small UAS for surveying and mapping tasks has been increasingly adopted due to its unparalleled efficiency. A custom-designed high-accuracy UAS-LIDAR system is discussed in this work. It is equipped with a combination of camera and LIDAR sensors that are synced to an onboard GNSS-IMU navigation system to enable precise time-stamping and geo-referencing. The presented UAS-LIDAR system also provides the flexibility of upgrading existing sensors

or including additional sensors for other civil and construction applications, thanks to its parallel sensor configuration with a core navigation and timing system.

A robust error model was developed for a generic UAS-LIDAR system to predict the horizontal and vertical errors of single point geo-registration. The contributions of errors from different components, such as navigation, timing, and LIDAR are all considered.

This model was validated for the proposed UAS-LIDAR system with calibration targets and real-world data from three different measurement scenarios: a box target with smooth flat surfaces for random error validation, targets of known sloped surfaces for systematic error validation, and a test site rock stair pile for bulk measurement validation. The test results indicated that the random errors from raw LIDAR point cloud reach approximately 0.1 m in the horizontal and vertical directions, respectively, during typical low-altitude flight conditions.

Some of the error sources, such as angular error from navigation or boresighting, are considered systematic. Other error sources, such as LIDAR ranging error, are modeled as random errors. This error model can be used to estimate the magnitude for each error type individually. Different strategies can be developed to reduce the overall error level based on that. For example, systematic errors could leave a bias in the point cloud, which affects the absolute accuracy. It can be limited by a carefully designed calibration process. It has been shown in these flights that the systematic errors are at or below centimeter-level, suggesting that the presented UAS-LIDAR had introduced negligible systematic errors. Random errors affect the relative precision. Random errors can be reduced via the pre-processing of the raw point cloud.

The comprehensive validation of the system has proven the capability and effectiveness of a downward-looking UAS-LIDAR system in construction applications, such as excavation and bulk pile measurements, and therefore has significant potential for civil engineering and construction projects. The prediction model currently focuses on the errors originated from the UAS and the LIDAR and can be further expanded to include characteristics of the target surfaces, such as material, texture, smoothness, and slope in future work.

Author Contributions: Literature review, S.G., H.S., Y.H., G.W. and Z.Z.; Writing, S.G., H.S., Y.H., G.W. and Z.Z.; Editing, S.G., H.S., Y.H., G.W. and Z.Z. All authors have read and agreed to the published version of the manuscript.

Funding: The authors would like to thank the North Carolina Department of Transportation (Award Number: RP 2020-35) for their assistance in support this research.

Institutional Review Board Statement: Not applicable.

Informed Consent Statement: Not applicable.

Data Availability Statement: The data is available from the corresponding author upon request.

Conflicts of Interest: The authors declare no conflict of interest. The content of the information provided in this publication does not necessarily reflect the position or the policy of the United States government, and no official endorsement should be inferred.

References

1. Bondrea, M.V.; Naş, S.; Fărcaş, R.; Dîrja, M.; Sestraş, P. Construction survey and precision analysis using RTK technology and a total station at axis stake-out on a construction site. *Int. Multidiscip. Sci. GeoConference SGEM* **2016**, *2*, 155–161.
2. Liu, Q.; Duan, Q.; Zhao, P.; Ren, H.; Duan, H.; Liu, G.; Wang, Z.; Duan, Z.; Qin, L. Summary of calculation methods of engineering earthwork. *J. Phys. Conf. Ser.* **2021**, *1802*, 032002. [[CrossRef](#)]
3. Chen, A.Y.; Huang, Y.N.; Han, J.Y.; Kang, S.C.J. A review of rotorcraft unmanned aerial vehicle (UAV) developments and applications in civil engineering. *Smart Struct. Syst.* **2014**, *13*, 1065–1094.
4. Dib, H.; Adamo-Villani, N.; Garver, S. An Interactive Virtual Environment for Teaching “Triangulations and Coordinates Calculations” to Surveying Students. In Proceedings of the 2013 IEEE 17th International Conference on Information Visualisation, London, UK, 16–18 July 2013; pp. 445–450.
5. Thomas, H.; Kennedy, M.A. A new methodology for accurate digital planning of archaeological sites without the aid of surveying equipment. *J. Archaeol. Sci. Rep.* **2016**, *10*, 887–892. [[CrossRef](#)]

6. Bohn, J.S. Benefits and Barriers of Construction Project Monitoring Using Hi-Resolution Automated Cameras. Ph.D. Thesis, Georgia Institute of Technology, Atlanta, GA, USA, 2009.
7. Kizil, U.; Tisor, L. Evaluation of RTK-GPS and Total Station for applications in land surveying. *J. Earth Syst. Sci.* **2011**, *120*, 215–221. [[CrossRef](#)]
8. Chekole, S.D. Surveying with GPS, Total Station and Terrestrial Laser Scanner: A Comparative Study. Master's Thesis, Royal Institute of Technology, Stockholm, Sweden, 2014.
9. Dampagama, K.P.; Abesinghe, A.M.L.K.; Dinusha, K.A.; Vandebona, R. Comparative study on methods for 3d modelling with traditional surveying technique and total station technique. In Proceedings of the 11th International Research Conference, Rathmalana, Sri Lanka, 13–14 September 2018.
10. Marsh, J.G.; Douglas, B.C.; Klosko, S.M. A global station coordinate solution based upon camera and laser data-GSFC 1973. In Proceedings of the Intern Symposium on the Use of Artificial Satellites for Geodesy and Geodyn, Athens, Greece, 14–21 May 1973. No. X-592-73-171.
11. El-Ashmawy, K.L. A comparison between analytical aerial photogrammetry, laser scanning, total station and global positioning system surveys for generation of digital terrain model. *Geocarto Int.* **2015**, *30*, 154–162. [[CrossRef](#)]
12. Pradhananga, N.; Teizer, J. Automatic spatio-temporal analysis of construction site equipment operations using GPS data. *Autom. Constr.* **2013**, *29*, 107–122. [[CrossRef](#)]
13. Cucurull, L. Improvement in the use of an operational constellation of GPS radio occultation receivers in weather forecasting. *Weather Forecast.* **2010**, *25*, 749–767. [[CrossRef](#)]
14. Aparicio, J.M.; Laroche, S. Estimation of the added value of the absolute calibration of GPS radio occultation data for numerical weather prediction. *Mon. Weather Rev.* **2015**, *143*, 1259–1274. [[CrossRef](#)]
15. Zucca, J.J.; Carrigan, C.; Goldstein, P.; Jarpe, S.; Sweeney, J.; Pickles, W.L.; Wright, B. Signatures of testing: On-site inspection technologies. In *Monitoring a Comprehensive Test Ban Treaty*; Springer: Dordrecht, The Netherlands, 1996; pp. 123–134.
16. Ngan, C.C.; Tam, H.Y. A non-contact technique for the on-site inspection of molds and dies polishing. *J. Mater. Process. Technol.* **2004**, *155*, 1184–1188. [[CrossRef](#)]
17. Ashour, R.; Taha, T.; Mohamed, F.; Hableel, E.; Kheil, Y.A.; Elsalamouny, M.; Kadadha, M.; Rangan, K.; Dias, J.; Seneviratne, L.; et al. Site inspection drone: A solution for inspecting and regulating construction sites. In Proceedings of the 2016 IEEE 59th International Midwest Symposium on Circuits and Systems (MWSCAS), Abu Dhabi, United Arab Emirates, 16–19 October 2016; pp. 1–4.
18. Tunstel, E.; Dolan, J.M.; Fong, T.; Schreckenghost, D. Mobile robotic surveying performance for planetary surface site characterization. In *Performance Evaluation and Benchmarking of Intelligent Systems*; Springer: Boston, MA, USA, 2009; pp. 249–268.
19. Lachat, E.; Landes, T.; Grussenmeyer, P. Investigation of a combined surveying and scanning device: The trimble SX10 scanning total station. *Sensors* **2017**, *17*, 730. [[CrossRef](#)] [[PubMed](#)]
20. Wallace, L.; Lucieer, A.; Watson, C.; Turner, D. Development of a UAV-LiDAR system with application to forest inventory. *Remote Sens.* **2012**, *4*, 1519–1543. [[CrossRef](#)]
21. Czaplicka, A.; Hołyst, J.A.; Sloot, P. Stochastic resonance for information flows on hierarchical networks. *Eur. Phys. J. Spec. Top.* **2013**, *222*, 1335–1345. [[CrossRef](#)]
22. Adão, T.; Hruška, J.; Pádua, L.; Bessa, J.; Peres, E.; Morais, R.; Sousa, J.J. Hyperspectral imaging: A review on UAV-based sensors, data processing and applications for agriculture and forestry. *Remote Sens.* **2017**, *9*, 1110. [[CrossRef](#)]
23. Ribeiro-Gomes, K.; Hernández-López, D.; Ortega, J.F.; Ballesteros, R.; Poblete, T.; Moreno, M.A. Uncooled thermal camera calibration and optimization of the photogrammetry process for UAV applications in agriculture. *Sensors* **2017**, *17*, 2173. [[CrossRef](#)] [[PubMed](#)]
24. Bendea, H.; Boccoardo, P.; Dequal, S.; Giulio Tonolo, F.; Marenchino, D.; Piras, M. Low cost UAV for post-disaster assessment. *Int. Arch. Photogramm. Remote Sens. Spat. Inf. Sci.* **2008**, *37*, 1373–1379.
25. Adams, S.M.; Friedland, C.J. A survey of unmanned aerial vehicle (UAV) usage for imagery collection in disaster research and management. In Proceedings of the 9th International Workshop on Remote Sensing for Disaster Response, Stanford, CA, USA, 15–16 September 2011; Volume 8, pp. 1–8.
26. Torok, M.M.; Golparvar-Fard, M.; Kochersberger, K.B. Image-based automated 3D crack detection for post-disaster building assessment. *J. Comput. Civ. Eng.* **2014**, *28*, A4014004. [[CrossRef](#)]
27. Nex, F.; Remondino, F. UAV for 3D mapping applications: A review. *Appl. Geomat.* **2014**, *6*, 1–15. [[CrossRef](#)]
28. Siebert, S.; Teizer, J. Mobile 3D mapping for surveying earthwork projects using an Unmanned Aerial Vehicle (UAV) system. *Autom. Constr.* **2014**, *41*, 1–14. [[CrossRef](#)]
29. Goessens, S.; Mueller, C.; Latteur, P. Feasibility study for drone-based masonry construction of real-scale structures. *Autom. Constr.* **2018**, *94*, 458–480. [[CrossRef](#)]
30. Wang, Z.; He, W.; Zhang, X.; Wang, Y.; Wu, B.; Wang, Y. Lane-based vehicular speed characteristics analysis for freeway work zones using aerial videos. *Can. J. Civ. Eng.* **2021**, *48*, 274–283. [[CrossRef](#)]
31. Leite, F.; Cho, Y.; Behzadan, A.H.; Lee, S.; Choe, S.; Fang, Y.; Akhavian, R.; Hwang, S. Visualization, information modeling, and simulation: Grand challenges in the construction industry. *J. Comput. Civ. Eng.* **2016**, *30*, 04016035. [[CrossRef](#)]
32. Seo, J.; Duque, L.; Wacker, J. Drone-enabled bridge inspection methodology and application. *Autom. Constr.* **2018**, *94*, 112–126. [[CrossRef](#)]

33. Sohn, H.; Farrar, C.R.; Hemez, F.M.; Shunk, D.D.; Stinemates, D.W.; Nadler, B.R.; Czarnecki, J.J. *A Review of Structural Health Monitoring Literature: 1996–2001*; Los Alamos National Laboratory: Los Alamos, NM, USA, 2003; Volume 1.
34. Çetinsoy, E.; Dikyar, S.; Hançer, C.; Oner, K.T.; Sirimoglu, E.; Unel, M.; Aksit, M.F. Design and construction of a novel quad tilt-wing UAV. *Mechatronics* **2012**, *22*, 723–745. [[CrossRef](#)]
35. Li, Y.; Liu, C. Applications of multirotor drone technologies in construction management. *Int. J. Constr. Manag.* **2019**, *19*, 401–412. [[CrossRef](#)]
36. Lee, J.J.; Fukuda, Y.; Shinozuka, M.; Cho, S.; Yun, C.B. Development and application of a vision-based displacement measurement system for structural health monitoring of civil structures. *Smart Struct. Syst.* **2007**, *3*, 373–384. [[CrossRef](#)]
37. Rathinam, S.; Kim, Z.W.; Sengupta, R. Vision-based monitoring of locally linear structures using an unmanned aerial vehicle. *J. Infrastruct. Syst.* **2008**, *14*, 52–63. [[CrossRef](#)]
38. Huang, W.; Kovacevic, R. A laser-based vision system for weld quality inspection. *Sensors* **2011**, *11*, 506–521. [[CrossRef](#)]
39. Neogi, N.; Mohanta, D.K.; Dutta, P.K. Review of vision-based steel surface inspection systems. *EURASIP J. Image Video Process.* **2014**, *2014*, 50. [[CrossRef](#)]
40. Essock, E.A.; Sinai, M.J.; McCarley, J.S.; Krebs, W.K.; DeFord, J.K. Perceptual ability with real-world nighttime scenes: Image-intensified, infrared, and fused-color imagery. *Hum. Factors* **1999**, *41*, 438–452. [[CrossRef](#)]
41. Lanza Discalea, F.; Matt, H.; Bartoli, I.; Coccia, S.; Park, G.; Farrar, C. Health monitoring of UAV wing skin-to-spar joints using guided waves and macro fiber composite transducers. *J. Intell. Mater. Syst. Struct.* **2007**, *18*, 373–388. [[CrossRef](#)]
42. Guan, S.; Bridge, J.A.; Li, C.; DeMello, N.J. Smart radar sensor network for bridge displacement monitoring. *J. Bridge Eng.* **2018**, *23*, 04018102. [[CrossRef](#)]
43. Schaer, P.; Skaloud, J.; Landtwing, S.; Legat, K. Accuracy estimation for laser point cloud including scanning geometry. In Proceedings of the 5th International Symposium on Mobile Mapping Technology, Padova, Italy, 29–31 May 2007.
44. Pilarska, M.; Ostrowski, W.; Bakula, K.; Górski, K.; Kurczyński, Z. The potential of light laser scanners developed for unmanned aerial vehicles—the review and accuracy. The International Archives of the Photogrammetry, Remote Sensing and Spatial Information Sciences. In Proceedings of the 2016 11th 3D Geoinfo Conference, Athens, Greece, 20–21 October 2016; Volume XLII-2/W2.
45. Wallace, L.; Lucieer, A.; Turner, D.; Watson, C. Error assessment and mitigation for hyper-temporal UAV-borne LiDAR surveys of forest inventory. In Proceedings of the SilviLaser, Hobart, Tasmania, 16–20 October 2011; pp. 1–13.
46. Zhao, X.; Su, Y.; Hu, T.; Cao, M.; Liu, X.; Yang, Q.; Guan, H.; Liu, L.; Guo, Q. Analysis of UAV lidar information loss and its influence on the estimation accuracy of structural and functional traits in a meadow steppe. *Ecol. Indic.* **2022**, *135*, 108515. [[CrossRef](#)]
47. Chen, Z.; Li, J.; Yang, B. A strip adjustment method of UAV-borne lidar point cloud based on DEM features for mountainous area. *Sensors* **2021**, *21*, 2782. [[CrossRef](#)]
48. Muller, A. Assessment of Vertical Accuracy from UAV-LiDAR and Structure from Motion Point Clouds in Floodplain Terrain Mapping. Ph.D. Thesis, Portland State University, Portland, OR, USA, 2021.
49. Salach, A.; Bakula, K.; Pilarska, M.; Ostrowski, W.; Górski, K.; Kurczyński, Z. Accuracy assessment of point clouds from LiDAR and dense image matching acquired using the UAV platform for DTM creation. *ISPRS Int. J. Geo-Inf.* **2018**, *7*, 342. [[CrossRef](#)]
50. Van Tassel, C. Defining the True Cost Behind Implementing Lidar Systems into Your Business. 2021. Available online: <https://candrone.com/blogs/news/the-real-cost-of-starting-a-lidar-drone-business> (accessed on 5 July 2022).
51. Guan, S.; Zhu, Z. UAS-based 3D Reconstruction Imagery Error Analysis. *Struct. Health Monit.* **2019**. [[CrossRef](#)]
52. NovAtel. SPAN-IGM-A1 Product Sheet. 2016. Available online: <https://hexagondownloads.blob.core.windows.net/public/Novatel/assets/Documents/Papers/SPAN-IGM-A1-PS/SPAN-IGM-A1-PS.pdf> (accessed on 5 July 2022).
53. Sick. Operating Instructions of LDMRS 3D LIDAR Sensors. 2017. Available online: <https://www.sick.com/us/en/detection-and-ranging-solutions/3d-LIDAR-sensors/ld-mrs/c/g91913> (accessed on 5 July 2022).
54. May, N.C.; Toth, C.K. Point positioning accuracy of airborne LiDAR systems: A rigorous analysis. In Proceedings of the International Archives of Photogrammetry, Remote Sensing and Spatial Information Sciences, Munich, Germany, 19–21 September 2007; pp. 19–21.
55. Tao, C.; Watts, B.; Ferraro, C.C.; Masters, F.J. A multivariate computational framework to characterize and rate virtual Portland cements. *Comput. Aided Civ. Infrastruct. Eng.* **2019**, *34*, 266–278. [[CrossRef](#)]
56. Hegarty, C.J.; Kaplan, E.D. *Understanding GPS: Principles and Applications*; Artech House: London, UK, 2006.
57. Cooper, H.M.; Wasklewicz, T.; Zhu, Z.; Lewis, W.; LeCompte, K.; Heffentrager, M.; Smaby, R.; Brady, J.; Howard, R. Evaluating the ability of multi-sensor techniques to capture topographic complexity. *Sensors* **2021**, *21*, 2105. [[CrossRef](#)]

Typical positioning accuracy

| | GPS/GNSS | RTK | PPK* | PPP+ |
|----------------------------|----------|---------------|---|--|
| Horizontal error (1 sigma) | 1 m | 2 cm | 1 cm | 6 cm |
| Vertical error (1 sigma) | 2 m | 3 cm | 2 cm | 15 cm |
| Additional equipment/data | | Live datalink | Recorded data from UAV and a reference nearby; Data from a network of reference stations (such as CORS) | Data from a network of reference stations (such as CORS) |

*Post-processed kinematic: post processed version of RTK. It will use better satellite orbit and clock data, and will be more accurate than RTK.

+Precise Point Positioning (PPP): post processed single point positioning. It will use data from a network of reference stations.

Typical orientation accuracy*

| | Live/recorded | Post-processed |
|---------------------------|-------------------------------------|--|
| Roll/pitch (1 sigma) | 0.02 deg | 0.01 deg |
| Heading (1 sigma) | 0.1 deg | 0.04 deg |
| Additional equipment/data | May need live datalink if using RTK | Recorded data from UAV and a reference nearby if using PPK; Data from a network of reference stations (such as CORS) |

*They are based on a good commercial IMU[1]. The error levels may be different with other IMUs[2,3].

Typical geo-referencing accuracy of point cloud

| | Error (1 sigma) | Ground control points |
|---|--|----------------------------------|
| UAV SFM | cm level | dense; surveyed with RTK or PPK |
| UAV SFM with RTK or PPK[4] | cm level | sparse; surveyed with RTK or PPK |
| UAV LIDAR with RTK or PPK and orientation | cm level (usually no smaller than SFM) | None |

References

[1]<https://hexagondownloads.blob.core.windows.net/public/Novatel/assets/Documents/Papers/SPAN-CPT7-PS/SPAN-CPT7-PS.pdf>

[2]<https://hexagondownloads.blob.core.windows.net/public/Novatel/assets/Documents/Papers/PwrPak7-E1-Product-Sheet/PwrPak7-E1-Product-Sheet.pdf>

[3]https://2w6vmg3m8cv83pn80b2dfi9f-wpengine.netdna-ssl.com/wp-content/uploads/SPAN-IGM-A1_DS.pdf

[4]https://assets.ctfassets.net/go54bjdzbrgi/2VpGjAxJC2aaYIipsmFswD/3bcd8d512ccfe88ff63168e15051baee/BLOG_rtk-ppk-drones-gcp-comparison.pdf

A.6 Workshop slides



Training and Case Studies for UAV- based LIDAR and Imaging Systems (2020-35)

ZHEN ZHU, GEORGE WANG AND SHANYUE GUAN

EAST CAROLINA UNIVERSITY

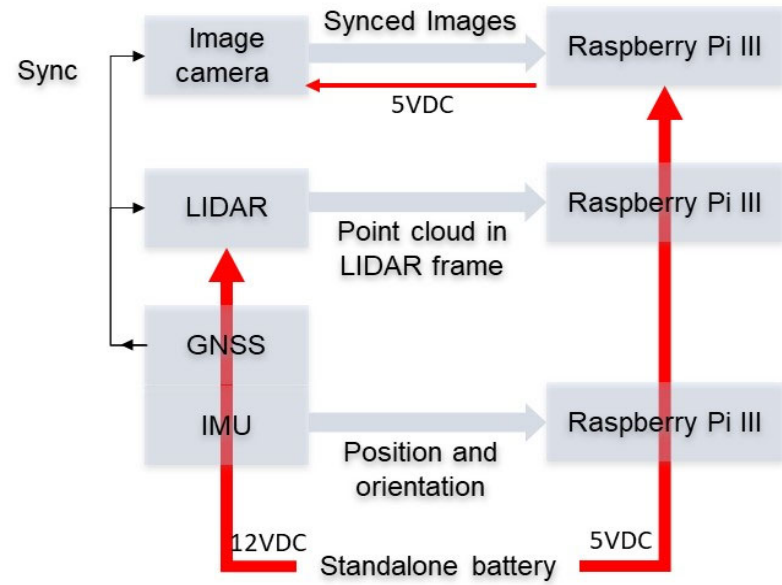
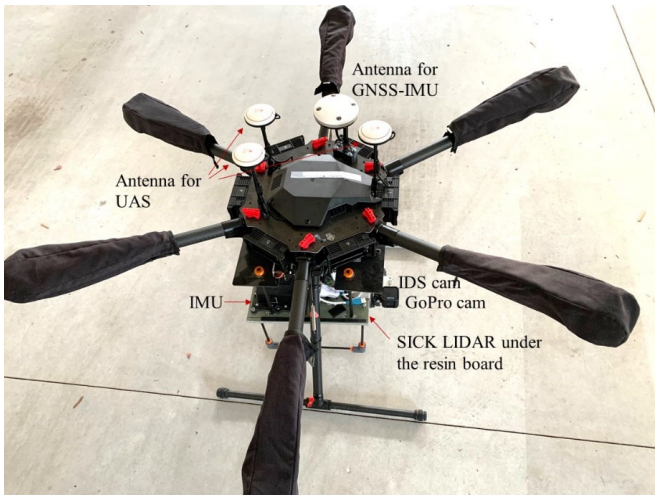
What will we cover

- ▶ What is a UAS-LIDAR system and how does it work?
- ▶ How can it help with construction and disaster management projects?
- ▶ LIDAR vs. SFM
- ▶ LIDAR vs. GNSS survey



UAS-LIDAR

UAS-LIDAR



Airframe

Aircraft

| | |
|---|--|
| Diagonal Wheelbase | 1133 mm |
| Dimensions | 1668 mm × 1518 mm × 727 mm with propellers, frame arms and GPS mount unfolded (including landing gear) 437 mm × 402 mm × 553 mm with propellers, frame arms and GPS mount folded (excluding landing gear) |
| Package Dimensions | 525 mm × 480 mm × 640 mm |
| Weight (with six TB47S batteries) | 9.5 kg ← |
| Weight (with six TB48S batteries) | 10 kg |
| Max Takeoff Weight Recommended | 15.5 kg ← |
| Hovering Accuracy (P-GPS) | Vertical: ±0.5 m, Horizontal: ±1.5 m |
| Max Angular Velocity | Pitch: 300°/s, Yaw: 150°/s |
| Max Pitch Angle | 25° |
| Max Wind Resistance | 8 m/s |
| Max Ascent Speed | 5 m/s |
| Max Descent Speed | 3 m/s |
| Max Service Ceiling Above Sea Level | <ul style="list-style-type: none"> • 2170R propellers: 2500 m; • 2195 propellers: 4500 m |
| Max Speed | 40 mph / 65 kph (no wind) |
| Hovering Time* (with six TB47S batteries) | No payload: 32 min, 6 kg payload: 16 min ← |
| Hovering Time* (with six TB48S batteries) | No payload: 38 min, 5.5 kg payload: 18 min |

Navigation system (orientation)

| IMU type | Navigation grade (near) | Tactical grade | Commercial grade |
|----------|-------------------------|----------------|------------------|
| Roll | 0.003° | 0.004° | 0.01° |
| Pitch | 0.003° | 0.004° | 0.01° |
| Heading | 0.004° | 0.01° | 0.05° |



<https://en.calameo.com/read/001915796d1d051759463?authid=gKG8EjL5yKMt>

Typical values from post processing. Requires initialization maneuver.
Practical error budget 0.01° 0.01° 0.1°.

Navigation system (position)

| Solution Type | RTK | PPK | PPP |
|---------------|-------|-------|-------|
| East-North | 0.02m | 0.01m | 0.06m |
| Up | 0.03m | 0.01m | 0.15m |



<https://hexagondownloads.blob.core.windows.net/public/Novatel/assets/Documents/Papers/IMU-IGM-A1-PS/IMU-IGM-A1-PS.pdf>

Practical error budget 0.01m, 0.01m, 0.02m.

Real Time Kinematic (RTK), Post-Processed Kinematic (PPK), Precise Point Positioning (PPP)



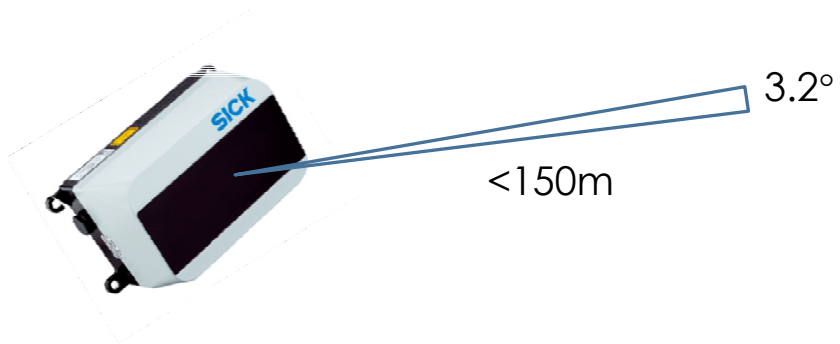
SICK LIDAR

LD-MRS420201

- ▶ $\pm 0.4^\circ$ by 0.04° narrow aperture (divergence)
- ▶ 0.125° angular resolution, 12.5 Hz
- ▶ 4 layers of laser beam, 3.2° vertical FOV
- ▶ 10 ms per sweep of the FOV (90°)
- ▶ 300,000 points per second.
- ▶ 150 m range



SICK LIDAR



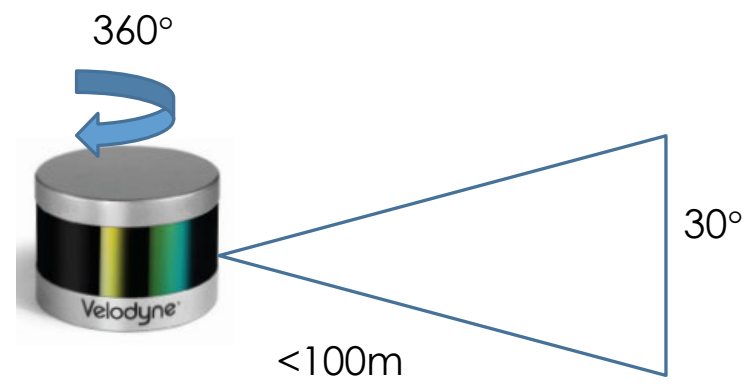
Velodyne LIDAR

VLP-16

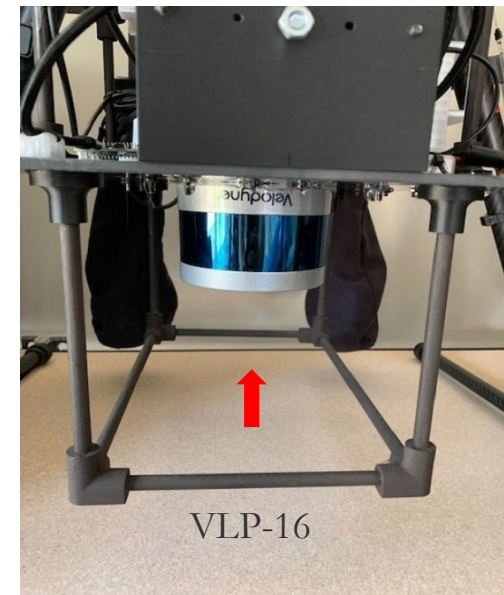
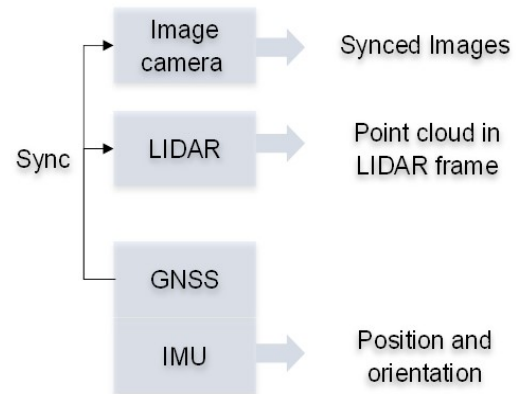
- ▶ +/- 0.09° aperture(divergence)
- ▶ 16 layers of laser beams (30° vertical FOV)
- ▶ 50 to 200 ms per rotation, 360° FOV
- ▶ 0.1° to 0.4° angular resolution
- ▶ 3,000,000 points per second
- ▶ 150 m range



Velodyne LIDAR



Sensor system



LIDAR error model

Angular error

$$\varepsilon \mathbf{P}_x^G = [\varepsilon C_V^G(t')] C_L^V \mathbf{P}_x^L(t) + [\varepsilon C_V^G(t')] [\mathbf{P}_L^V - \mathbf{P}_{ant}^V] +$$

$$C_V^G(t) C_L^V \cdot [\varepsilon \mathbf{P}_x^L(t)] + \varepsilon \mathbf{P}_{ant}^G(t) + \varepsilon t \frac{d\mathbf{P}_{ant}^G(t)}{dt}$$

LIDAR error
GNSS/PPK error
Timing error

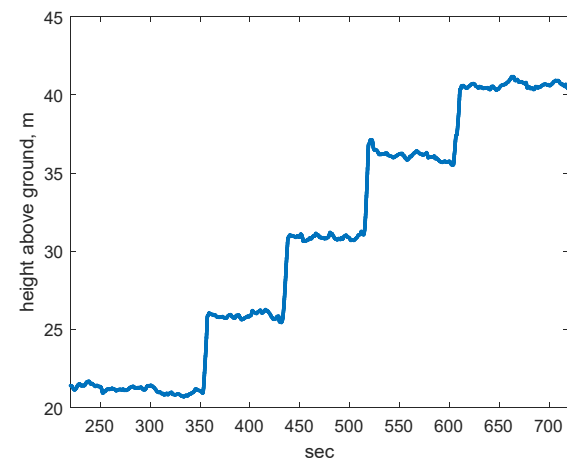
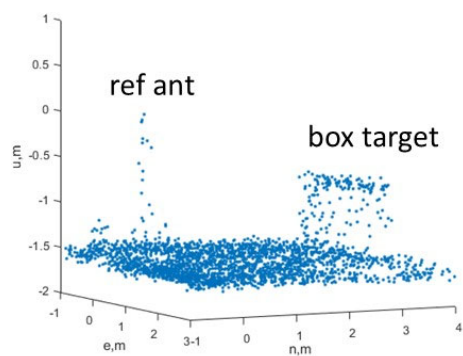
Error control

- ▶ Random errors:
 - ▶ GNSS/PPK position, LIDAR
 - ▶ Can be reduced by post-processing redundant measurements
- ▶ Systematic errors:
 - ▶ Angular errors from IMU (orientation) and boresighting; Lever arm
 - ▶ Can be reduced by calibration and in-flight initialization
 - ▶ Low altitude (short distance to target)
 - ▶ In flight validation
- ▶ Synchronization error:
 - ▶ Sync mechanism
 - ▶ Low speed, less vibration

LIDAR Installation

| | Synchronization error | Range error | Beam angular uncertainty | Lever arm X | Lever arm Y | Lever arm Z |
|---------|-----------------------|-------------|--------------------------|-------------|------------------|-------------|
| 1 sigma | 1ms | 0.05m | 0.1° | 0.001m | 0.001m | 0.001m |
| | Boresighting Roll | | Boresighting Pitch | | Boresighting Yaw | |
| 1 sigma | 0.01° | | 0.01° | | 0.1° | |

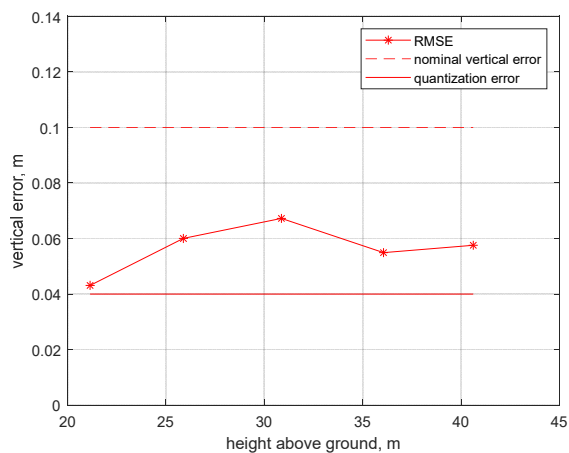
Verification of error model



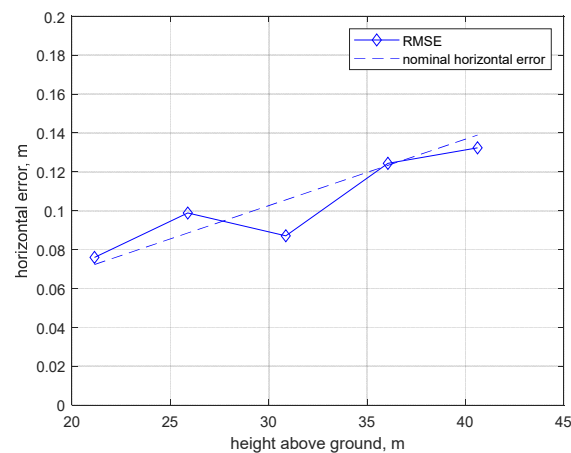
Test vertical and horizontal precision with a box target at different height.

Precision model verified at different heights

Vertical error is almost constant



Horizontal error grows with height



For downward-looking LIDAR, the vertical random error is almost constant. Minimum vertical systematic error <math><0.01\text{m}</math>.

Flight control

1. Take off and hover at ~15 m above ground.
2. Initialization maneuvers for ~ 3 min: including accelerations in horizontal directions. Make circular and figure-8 patterns.
3. Fly over calibration targets (optional). The target can be the antenna and the tripod of the ground reference GNSS receiver.
4. Fly over worksite, ~15 m above target, ~5 m/s.
5. Fly over calibration targets (optional).
6. Land.



Flight



Ground targets and/or antenna are used for validation.

Butner, NC, 02/20

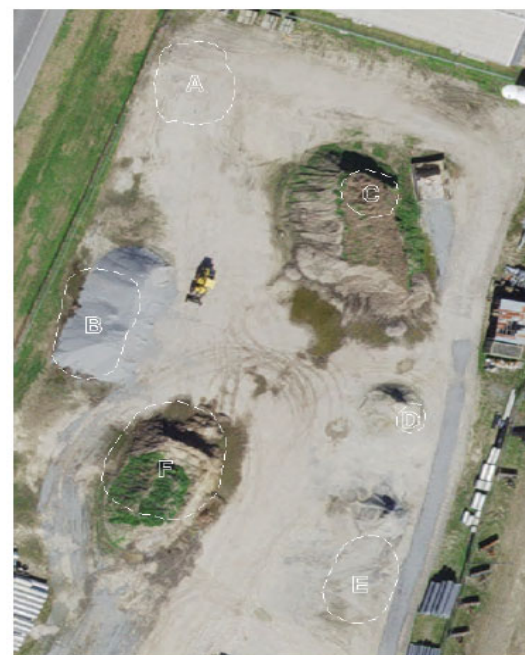
Onboard video camera



UAS-LIDAR
applications in
construction
management

Piles and bulk measurements

Pitt County Maintenance Yard



Pitt County Maintenance Yard



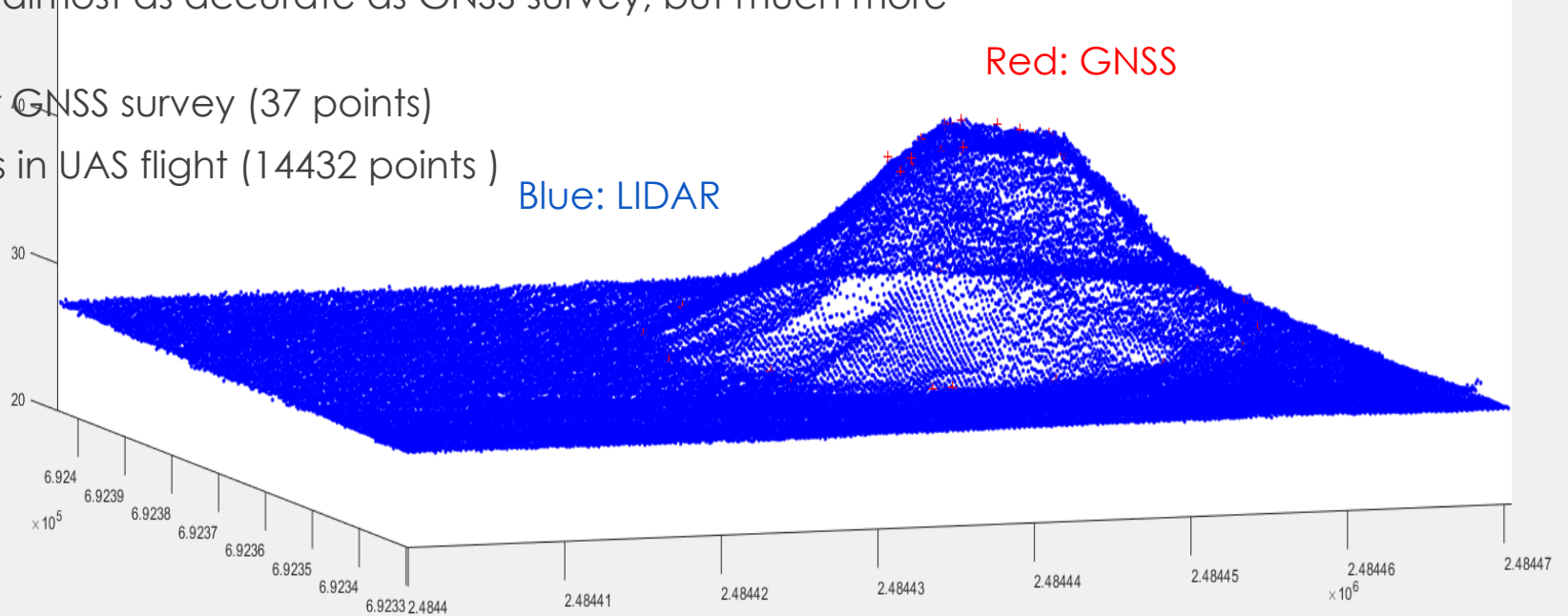
Greenville, NC
09/20

UAS-LIDAR performance

- ▶ Downward-looking LIDAR, low altitude
- ▶ Accurate orientation with initial maneuver
- ▶ Verified accuracy of each flight every year
- ▶ For individual points: ~ 0.06 m random error; < 0.01 m systematic error (bias)
- ▶ Same performance every year

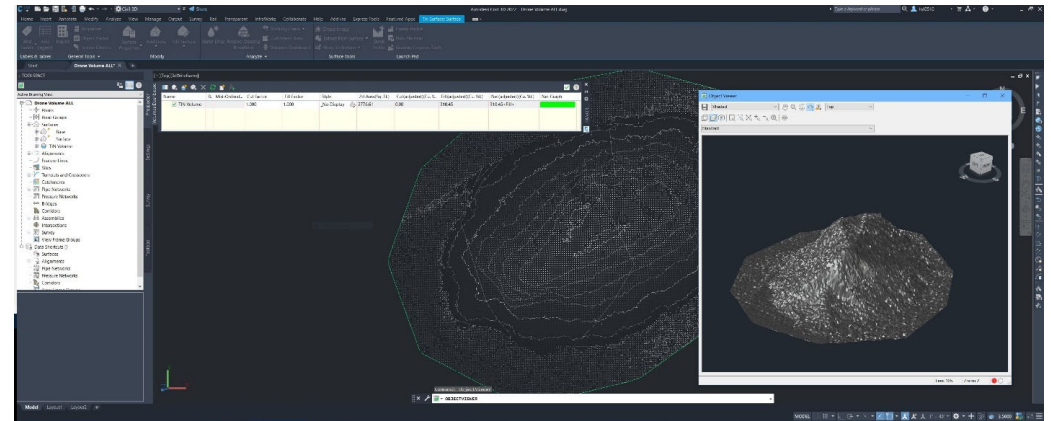
Point accuracy: LIDAR and GNSS

- ▶ UAS-LIDAR is almost as accurate as GNSS survey, but much more efficient.
- ▶ 15-30 min for GNSS survey (37 points)
- ▶ Few seconds in UAS flight (14432 points)



Volumetric measurement

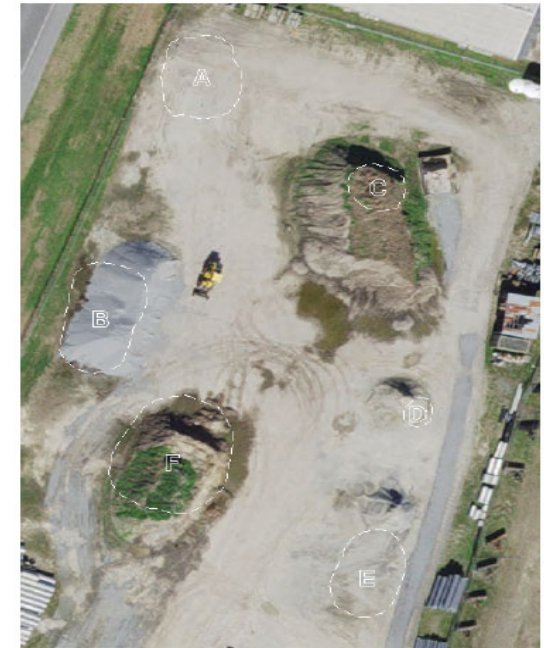
- ▶ GNSS and LIDAR points can both be processed in commercial software, such as Civil3D or Bentley MicroStation
- ▶ Both use Triangulated irregular network (TIN) model
 - ▶ Choice of model and ground points affects absolute volume only
 - ▶ Volume change is always precise.
- ▶ Difference: 10% volume
 - ▶ Due to resolution.



Volumetric measurement

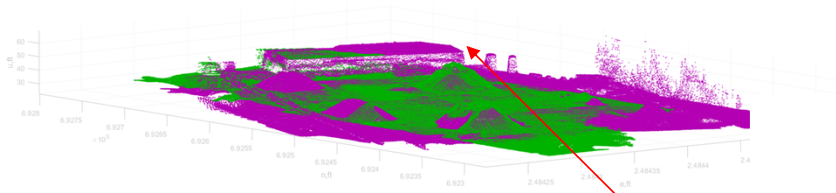
- ▶ A Sparse LIDAR point cloud can be used instead.
 - ▶ 0.1m vs 0.5m grid size.
- ▶ May save time in manual processing
- ▶ UAS can fly higher and faster, which may save time for a bigger site.
 - ▶ Current flights <60ft, 5 m/s, due to nearby airport

| Pile | UAS-LIDAR | Diff % (0.5 m vs. 0.1m) |
|------|-----------|-------------------------|
| A | 370.81 | 0.48 |
| B | 461.69 | 0.006 |
| C | 95.95 | 0.15 |
| D | 13.23 | 1.8 |
| E | 346.54 | 0.017 |
| F | 865.75 | 0.03 |



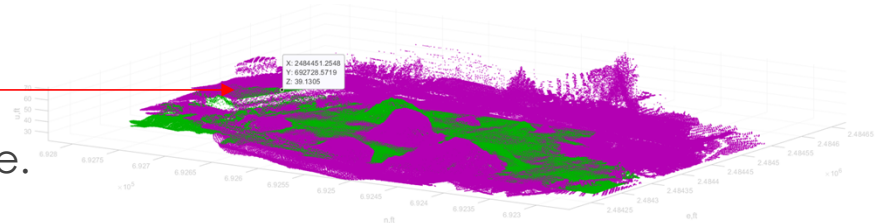
Long-term monitoring

2021 (r) vs 2020 (g)



UAS-LIDAR is very precise in measuring volumetric changes.

2022 (r) vs 2020 (g)



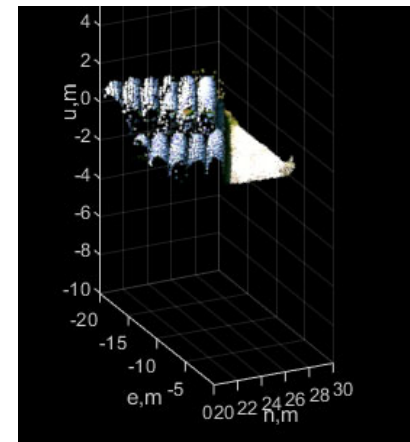
Minimal systematic bias (cm-level) in year-to-year comparison, verified with antenna and fixed structure.

UAS-LIDAR vs. SFM

1. UAS-LIDAR does not require any GCPs over the worksite, but can benefit from having one or few for validation purposes.
2. SFM needs a relatively dense network of GCPs.
3. UAS-LIDAR data collection is faster than SFM.
4. UAS-LIDAR can collect data over low-texture surfaces (sand or soil).
5. Usually UAS-LIDAR does **not** create an imagery surface.
6. Image can be superimposed on point cloud.

Imagery on point cloud

Image from sync camera can be **automatically** superimposed onto point cloud.



Questions

- ▶ Data product (point cloud and volume) format
- ▶ Visualization
- ▶ Software compatibility

Other applications

Borrow pits

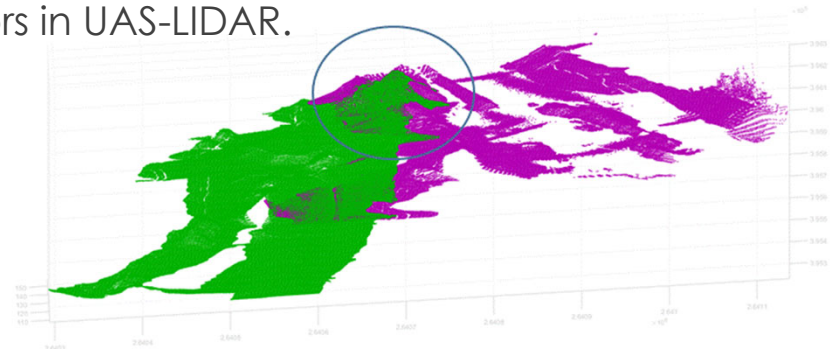
Buildings



Courtesy from Balfour Beatty

Borrow pit

- ▶ UAS-LIDAR can measure the volume or changes of borrow pit precisely.
- ▶ Neither LIDAR nor SFM measures stationary water surface.
 - ▶ Pits must be measured before ground water build up.
- ▶ Certain flight patterns will increase systematic errors in UAS-LIDAR.

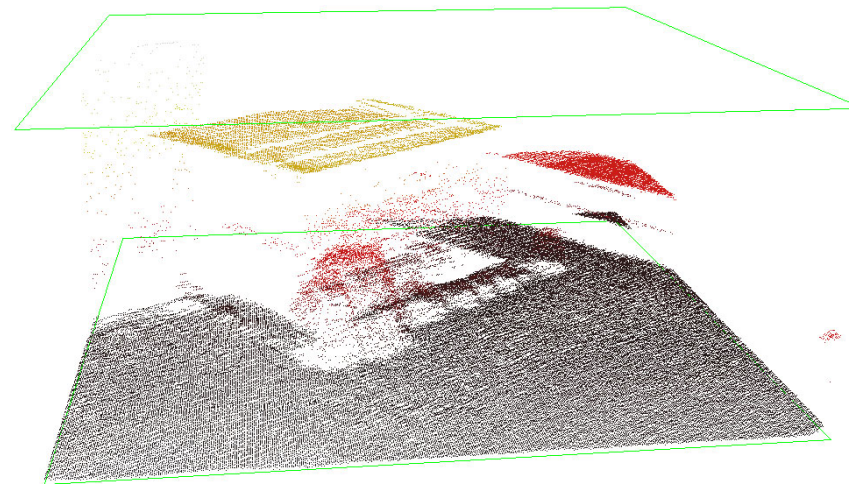
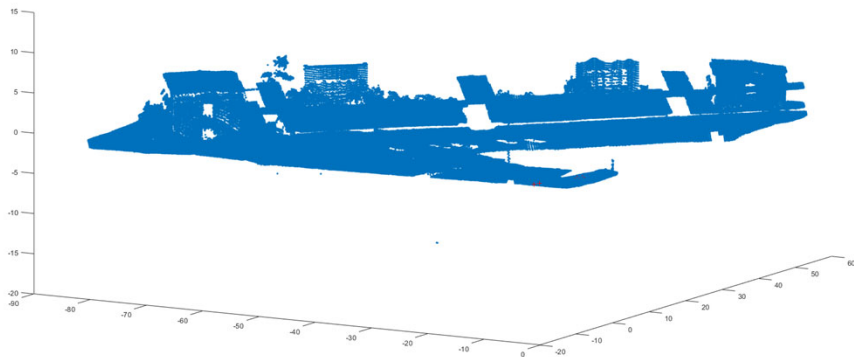


Havelock, NC

First flight: green; 12 m above ground. Second flight: pink; 24 m above ground.

Building

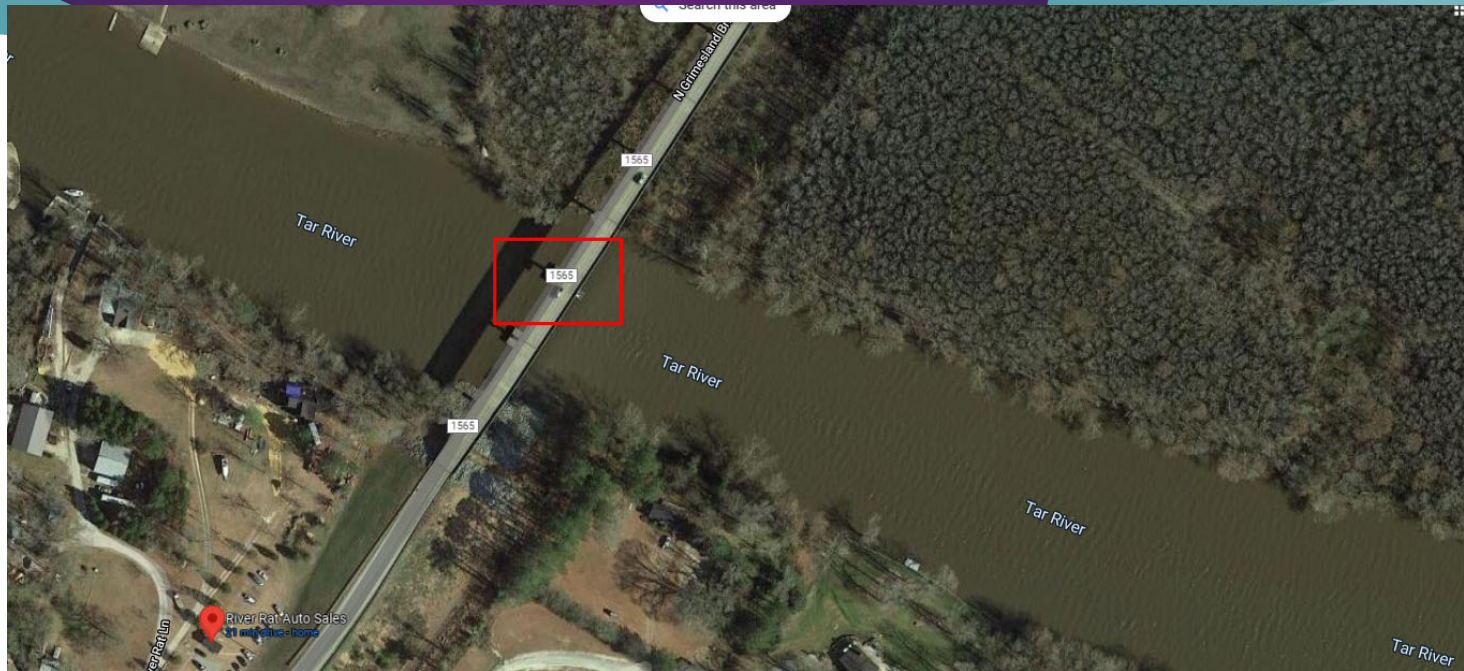
- ▶ UAS-LIDAR point cloud can measure buildings and other structures.
- ▶ LIDAR provides higher absolute accuracy. SFM provides better relative precision and resolution.





UAS-LIDAR
applications in
disaster management

Bridge



UAS-LIDAR flight

UAS initialization flight



South Grimesland Road,
Pitt County, NC

360 deg side-view LIDAR

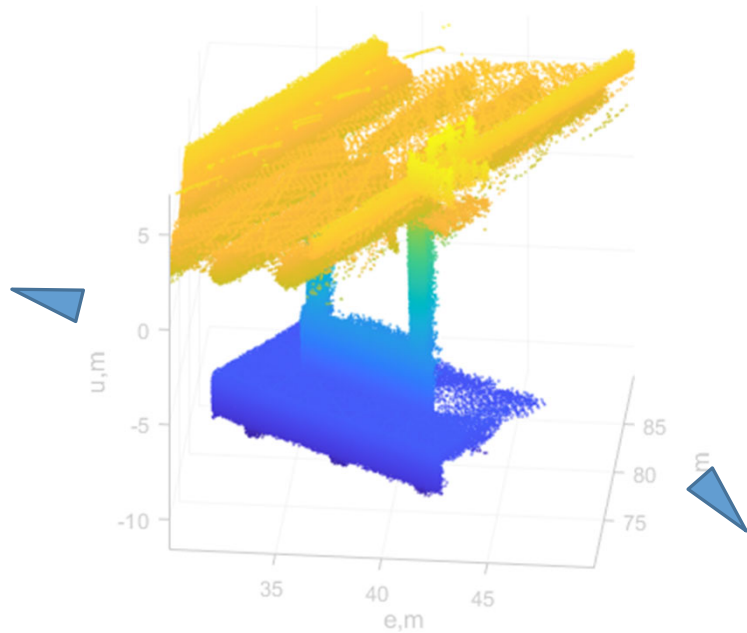
- ▶ Dataset set with Velodyne VLP-16
- ▶ Quickly scans the side of a bridge, <1 min for a 20 m by 20 m area.



Bridge point cloud

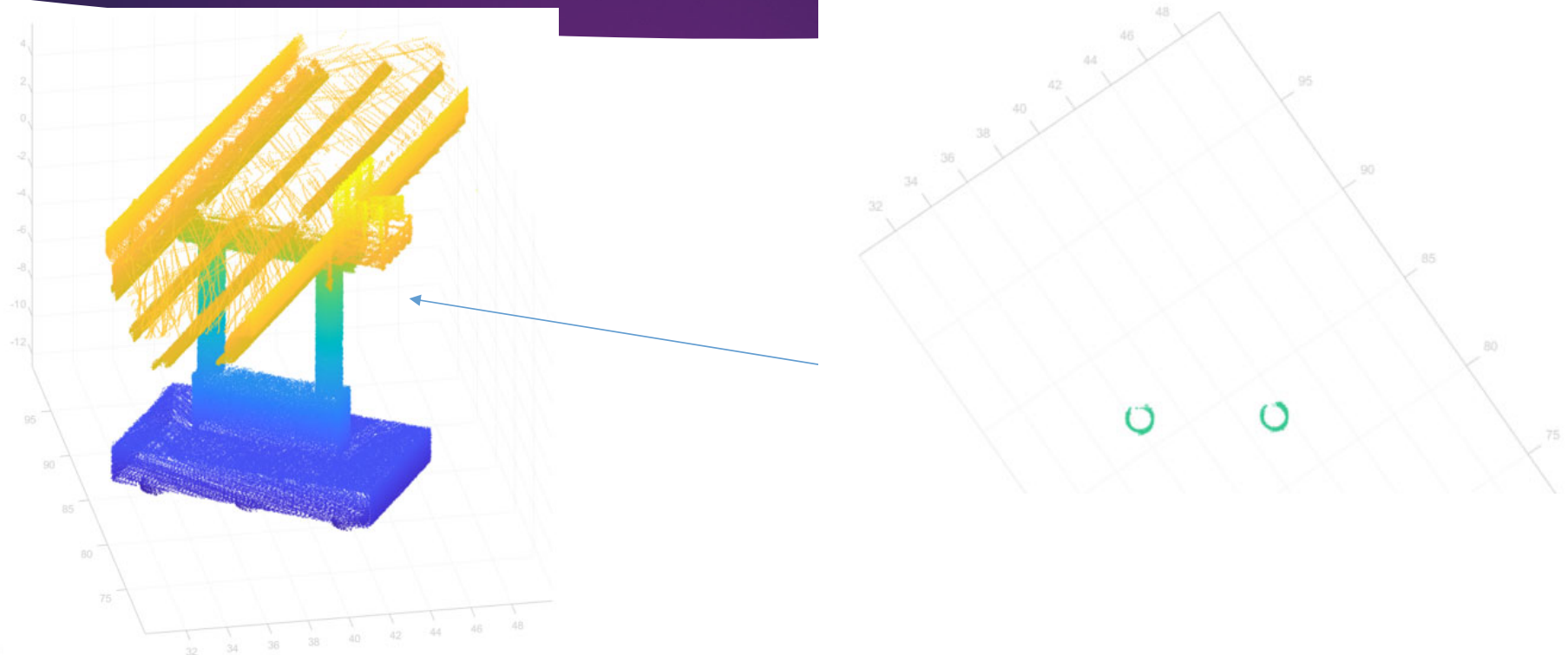


Potential issues

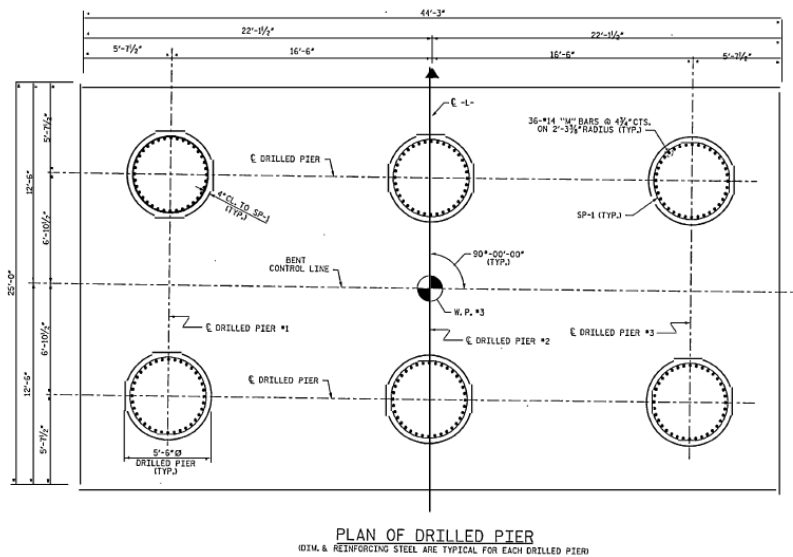
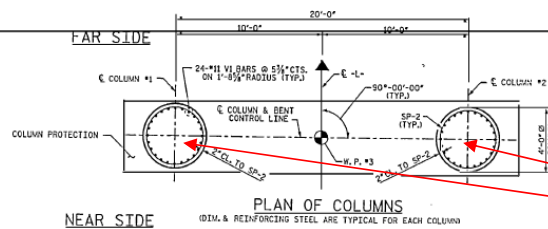


- ▶ Small systematic error (several cm), caused by angular errors, can cause shift of point cloud from different angles.
- ▶ Systematic error can be limited by distance and calibration; can be removed by manual calibration.
- ▶ It does not affect precision, but may affect absolute geo-registration.
- ▶ Onsite validation with antenna can be helpful.

Measurements with LIDAR



Measurements with LIDAR



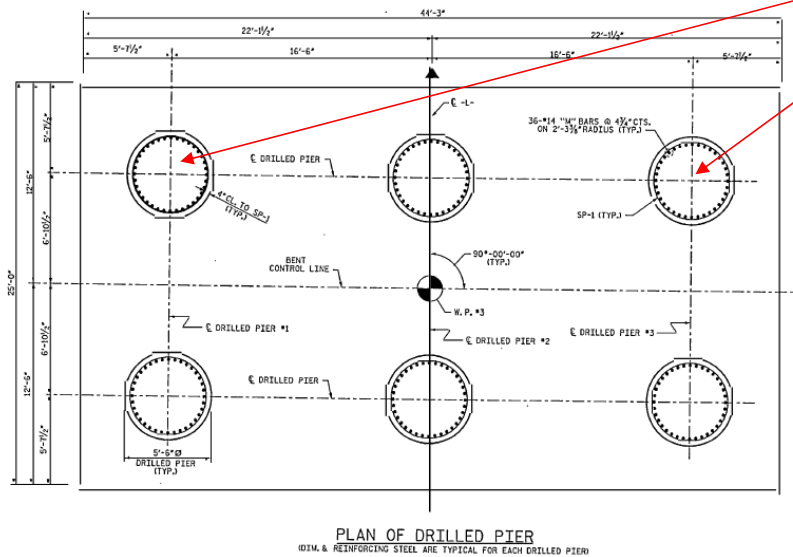
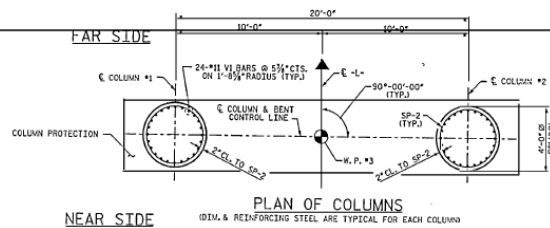
Design: 20 ft
 LIDAR measurement 6.125 m or 20.09 ft
 Random error: 1 sigma ~ 3 cm
 Systematic error: 1 sigma ~ 3 cm



Measurements with LIDAR



Measurements with LIDAR



Design: 33 ft
 LIDAR measurement 10.099 m or 33.13 ft
 Random error: 1 sigma ~ 3 cm
 Systematic error: 1 sigma ~ 3 cm



Questions

- ▶ How to use the point cloud measurement
- ▶ SFM with RTK vs. LIDAR for bridges
- ▶ Other structures

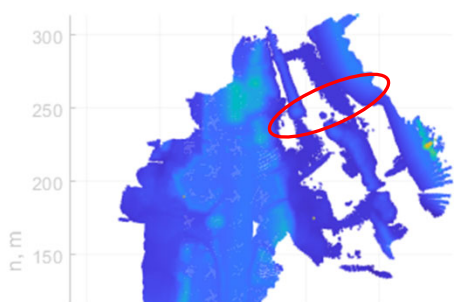
Other applications

Seashore

Riverbed

Road

Havelock borrow pit scan



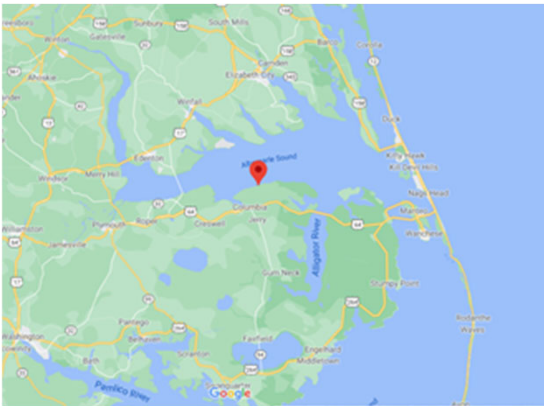
Few returns from smooth water surface.

Albemarle Sound

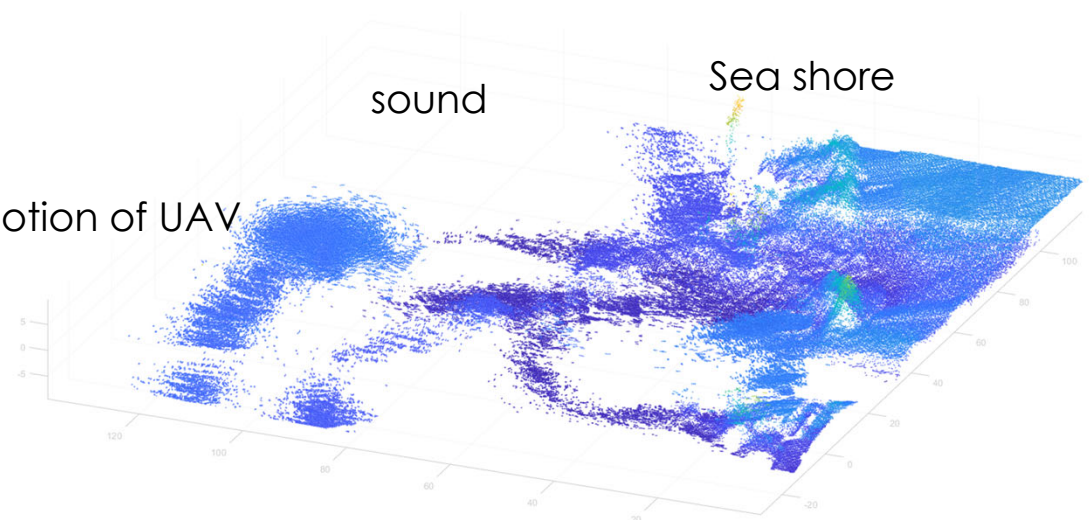


LiDAR over water

At 40-60m above water, even calm water surface with 1 ft wave from sound can be measured with SICK LIDAR (narrow aperture).



Circular motion of UAV



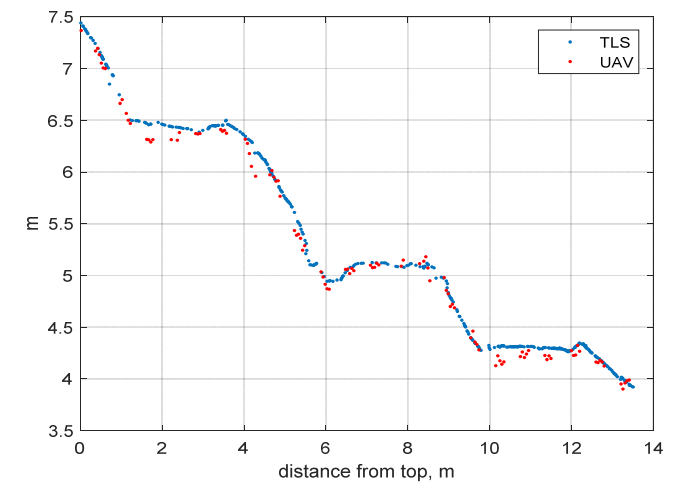
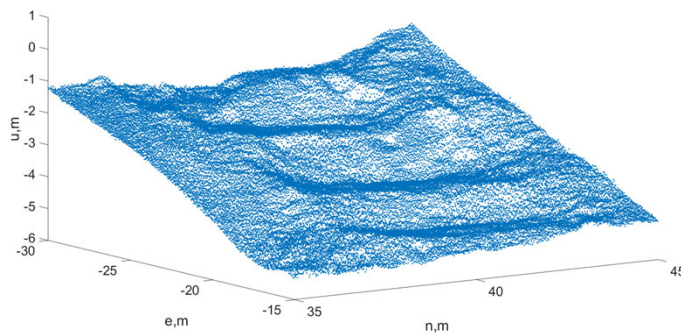
LIDAR about 50 m above water

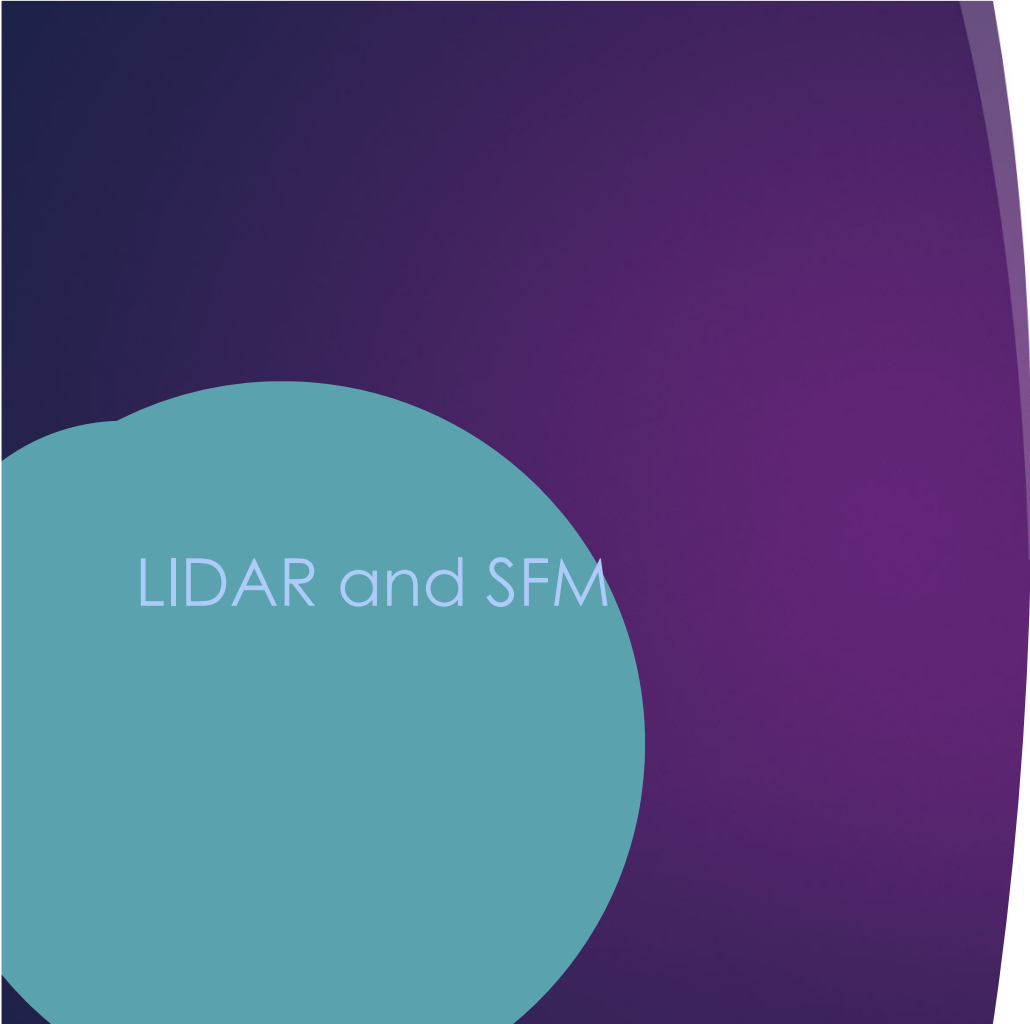
Towncreek



UAS-LIDAR vs TLS

- ▶ UAS-LIDAR has cm-level accuracy.
- ▶ UAS-LIDAR may not always agree with TLS due to resolution and perspective.





LIDAR and SFM

SFM with navigation system

- ▶ Camera can be integrated with precise positioning and/or orientation.
 - ▶ For orientation, SFM can only benefit from a high-quality IMU.

| IMU type | Navigation grade (near) | Tactical grade | Commercial grade |
|----------|-------------------------|----------------|------------------|
| Roll | 0.003° | 0.004° | 0.01° |
| Pitch | 0.003° | 0.004° | 0.01° |
| Heading | 0.004° | 0.01° | 0.05° |

- ▶ SFM can benefit from precise positioning alone, but camera has to be in sync with navigation (ms-level).

SFM with RTK (PPK)

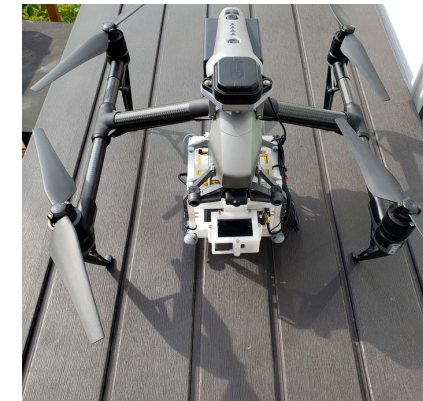
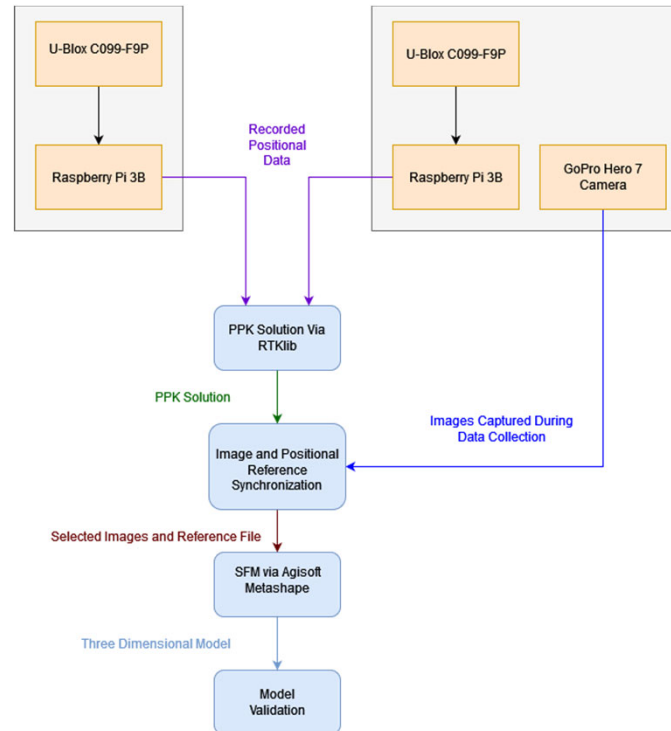


DJI Inspire 2 pro, Gopro Hero 7 camera,
UBLOX GNSS, sync mechanism, recording
computer

SFM with PPK



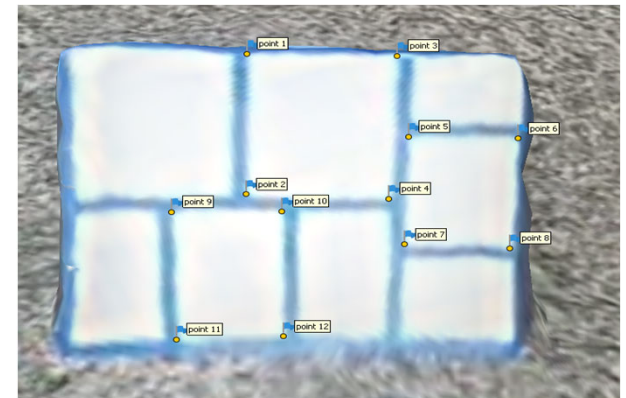
Ground station
No real-time data link
needed for PPK



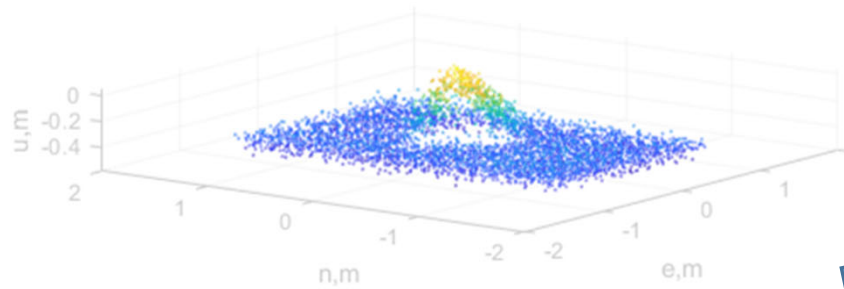
DJI Inspire 2 pro

SFM with PPK

- ▶ No GCP needed for relative measurements
 - ▶ dimension, scale, distance, size, etc.
- ▶ Precision: 3-8mm 1 sigma
- ▶ Need few GCPs for absolute geo-location (in GPS frame)
 - ▶ Since PPK does not measure orientation of camera
- ▶ GCPs can be targets or LIDAR point cloud.



LIDAR vs. SFM: point cloud

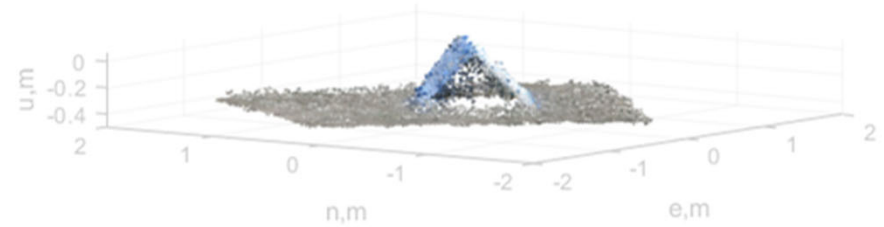


Difference: 4 cm
1 sigma

SICK LIDAR, no imagery



SFM/PPK



LIDAR vs. SFM: data quality

| | UAS-LIDAR | SFM | SFM-RTK(PPK) |
|---|---------------------|-----------------|-----------------|
| Relative precision (typical values, 1 sigma) | <0.1m | Depends on GCPs | <0.01m |
| Absolute accuracy (typical values, 1 sigma) | <0.1m | Depends on GCPs | Depends on GCPs |
| Resolution / point density | Medium | High | High |
| Visualization | Need external image | Yes | Yes |

SFM flight and operation

- ▶ Capture the whole subject first, and then the detail, ensuring that occlusions are captured adequately .
- ▶ Appropriate coverage. Basic principle: every point on the subject must appear on at least three images acquired from spatially different locations and mixed altitude.
- ▶ Static scene. Consistent light. Avoid overexposed and underexposed images.
- ▶ Avoid transparent, reflective or homogeneous surfaces.
- ▶ **Without** PPK, an evenly spaced dense network (such as 40 per squared kilometer) of GCPs are needed.

UAS-LIDAR flight

- ▶ UAS-LIDAR must have accurate orientation.
 - ▶ Orientation accuracy is dependent on IMU quality and initialization.
 - ▶ There are other methods of getting absolute heading accuracy, such as duo-antenna or gyrocompassing. They are less feasible for small UAS.
 - ▶ Low altitude, overhead flight.
1. Rotation
 2. Figure-8
 3. Waypoints and rectangular patterns
 4. Straight
 5. Hover
 6. Spin
- } in-flight initialization and data collection
- } avoid to reduce systematic error

Flight patterns - circle



Flight patterns – figure8



Flight patterns – rectangular



Flight patterns - straight



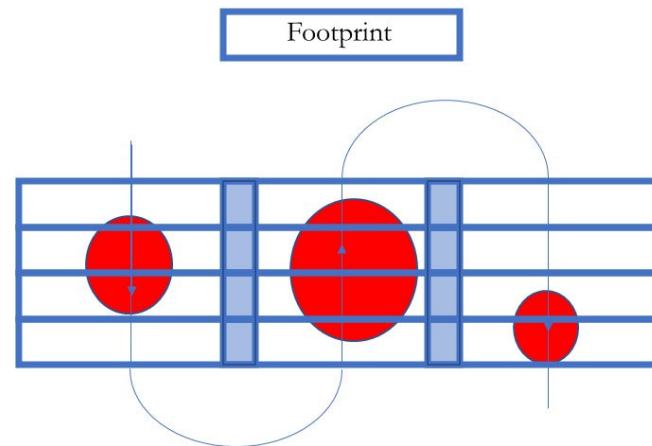
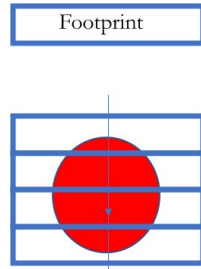
Flight patterns - hover



Flight patterns - spin



LIDAR coverage and footprint



LIDAR vs. SFM: flight requirement for data collection

| | UAS-LIDAR | SFM | SFM-RTK(PPK) |
|-----------------------|------------------|----------|--------------|
| Flight duration | Short | Long | Long |
| Flight pattern | Straight (short) | Circles | Circles |
| Desired flight height | Low | Multiple | Multiple |
| In flight calibration | Yes | No | No |

LIDAR vs. SFM: environment requirement

| | UAS-LIDAR | SFM | SFM-RTK(PPK) |
|---------------------------------|----------------------------|------------------------|------------------------|
| GCPs or ground reference points | Few, optional | Dense, onsite | Sparse, onsite |
| Light condition | Not sensitive | Sensitive | Sensitive |
| Shadow | Not sensitive | Sensitive | Sensitive |
| Surface texture | Not sensitive | Sensitive [#] | Sensitive [#] |
| Vegetation on surface | Not sensitive [*] | Sensitive | Sensitive |
| Dusty or foggy environment | Not sensitive [*] | Sensitive | Sensitive |
| Still water surface | No | No | No |
| Moving water surface | Yes ⁺ | No | No |

*Wide laser beam and multiple returns are helpful.

+Wide laser beam is helpful.

#High camera resolution is helpful.

LIDAR vs. SFM: cost

| | UAS-LIDAR | SFM | SFM-RTK(PPK) |
|-------------------------|---------------|--------------|--------------------|
| Hardware (typical cost) | High (>\$20K) | Low (<\$10K) | Medium (\$10K~20K) |
| Software | Medium | High | High |
| Operation (Labor) | Low | High | High |
| Post-processing (Labor) | Medium | High | High |

For typical commercial systems, not ECU systems.

LIDAR vs. SFM: application

| | UAS-LIDAR | SFM | SFM-RTK(PPK) |
|----------------------|-----------|-----|--------------|
| Piles | Yes | Yes | Yes |
| Pit with no water | Yes | Yes | Yes |
| Pit with water | No | No | No |
| Buildings | Yes | Yes | Yes |
| Bridge | Yes | No | TBD |
| Road | Yes | Yes | Yes |
| Beach and sand dunes | Yes | Yes | Yes |
| Seashore/riverbank | Yes | Yes | Yes |
| Sea/river water | Yes | No | No |



General
recommendations

Airframe

| | Fixed-wing | Rotary-wing |
|-----------------|------------|-------------|
| Takeoff/landing | Hard | Easy |
| Distance | Long | Short |
| Height | High | Various |
| Maneuverability | Low | High |
| Payload | High | Low |

RTK or PPK

| | RTK | PPK (Post Processed RTK) |
|--------------------------------|------|--------------------------|
| Base station | Yes | Optional |
| Datalink required | Yes | No |
| Results available in real time | Yes | No |
| Accuracy | Good | Best |

Flight control for LIDAR

| | Manual control | Pre-planned |
|-----------|----------------------|-------------|
| Height | <30m | >30m |
| Worksite | Small (100m by 100m) | Large |
| Waypoints | No | Yes |

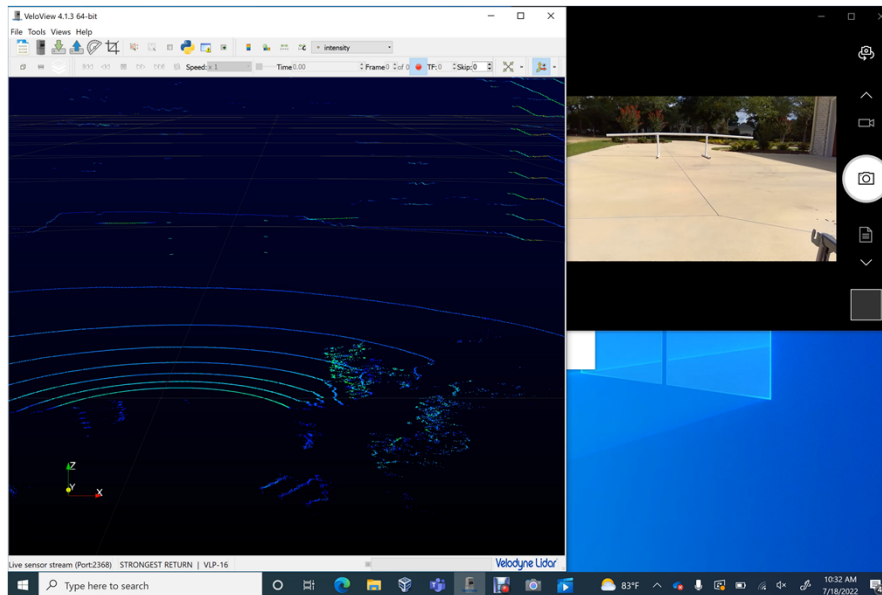
LIDAR vs. GNSS for piles and borrow pits

| | UAS-LIDAR | GNSS-Survey |
|-----------------------|---|--------------------------------------|
| Point density | Thousands per pile | Tens per pile |
| Data collection speed | Minutes for a site with multiple piles; 2-person team | Hours for a site with multiple piles |
| Accuracy | centimeter-level | centimeter-level |
| Difference in volume | ~10%, due to point density | |

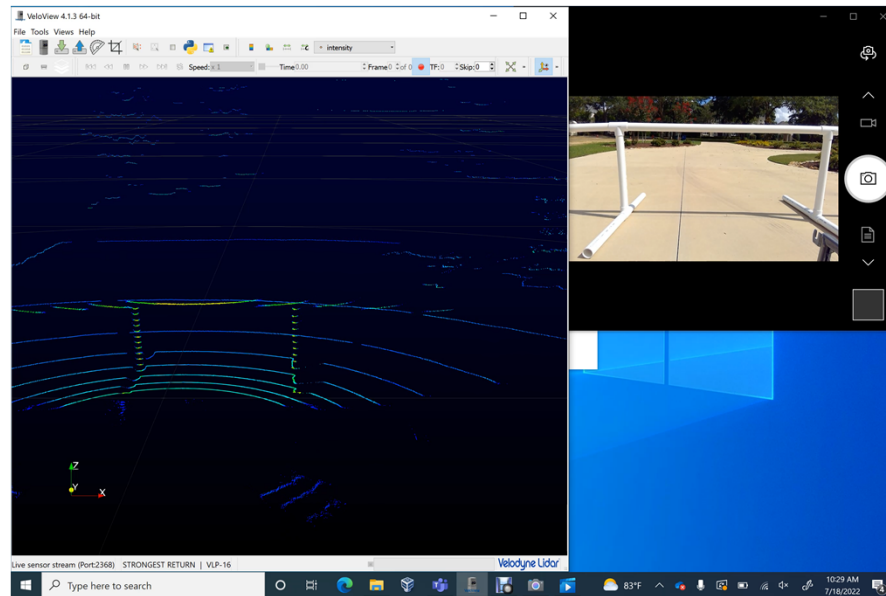


LIDAR sensor demo

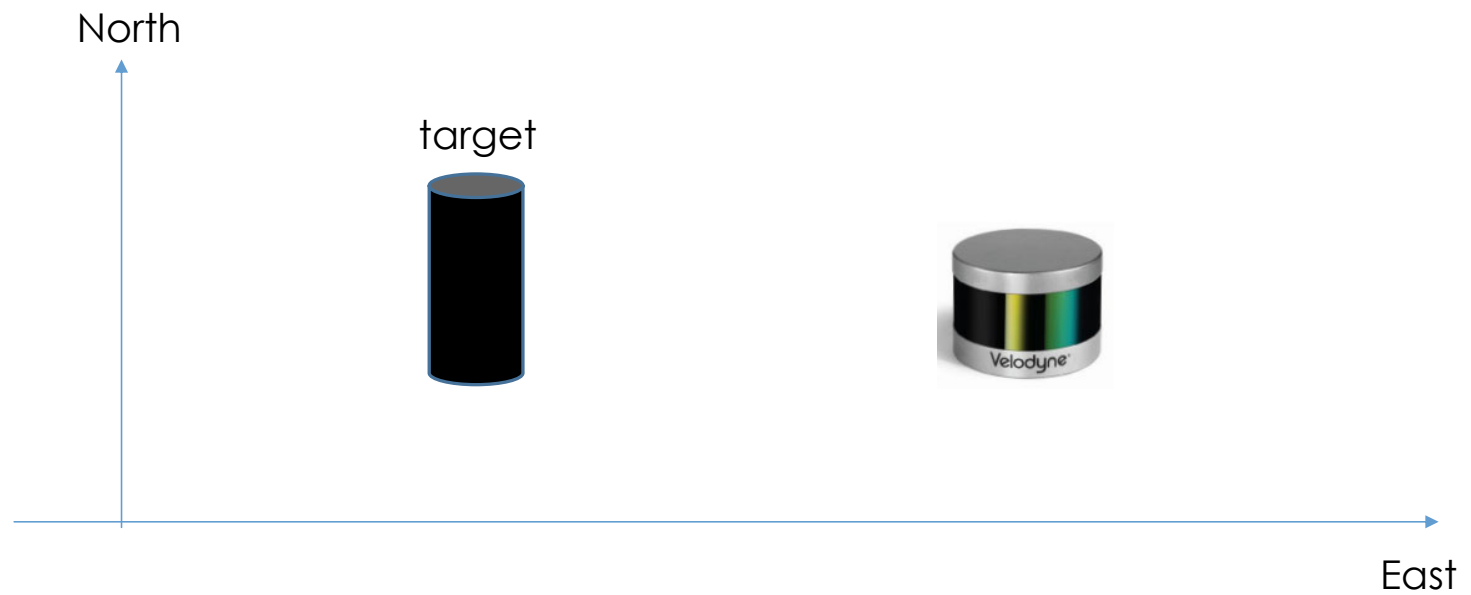
A ground test of VLP16



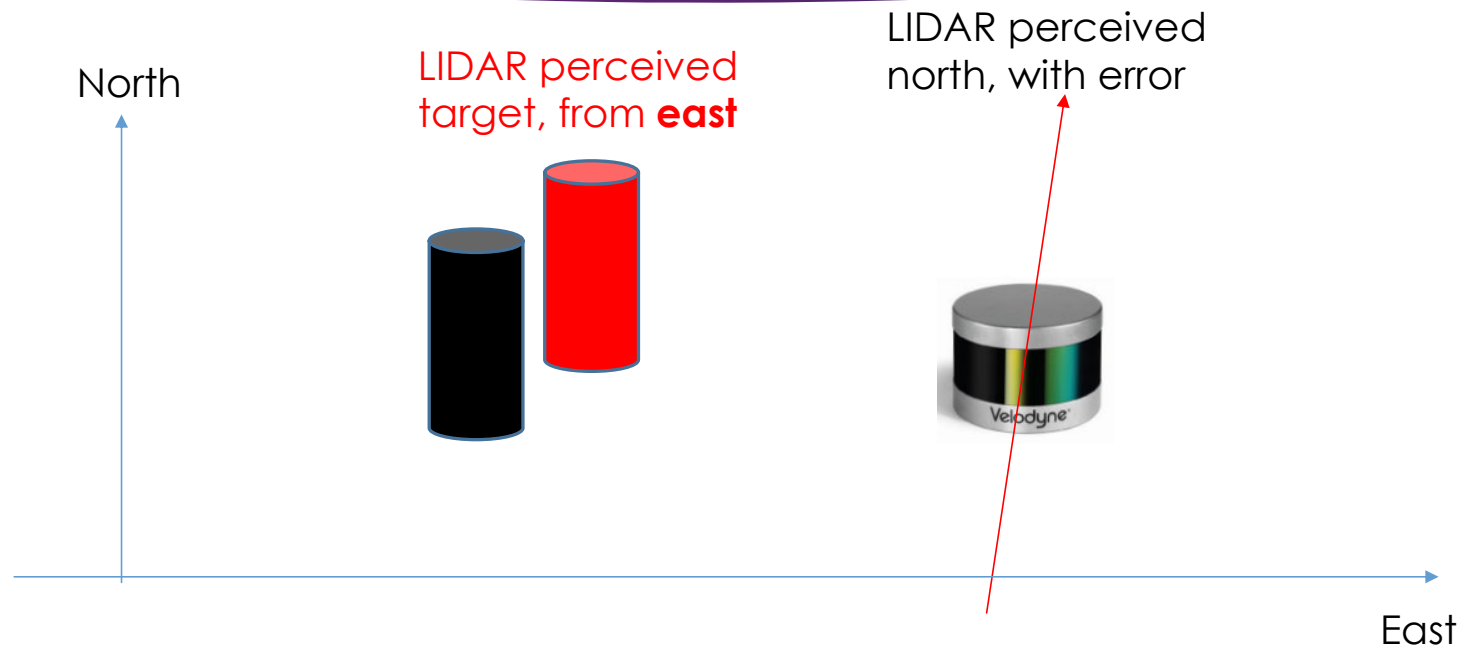
Angular errors



Bias and systematic error



Bias and systematic error

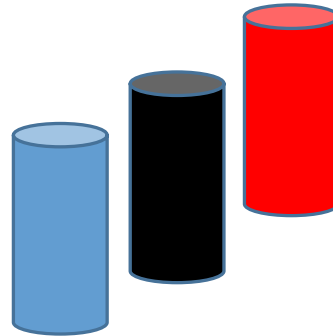


Bias and systematic error

LIDAR perceived north, with the **same** error

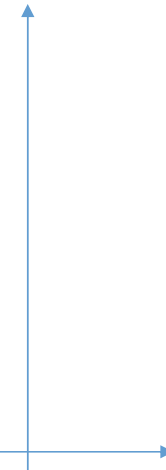


LIDAR perceived target, from **east**



LIDAR perceived target, from **west**

North



East

Bias and systematic error

- ▶ Boresighting angular bias is constant.
 - ▶ Systematic error in point cloud will change with LIDAR location.
 - ▶ Repeatable in every flight, can be calibrated.
- ▶ Navigation angular bias could slowly vary over time.
 - ▶ Systematic error in point cloud will change with LIDAR location and time.
 - ▶ Not repeatable, can be corrected manually.